PL-TR-96-2233

SPACE SYSTEM ENVIRONMENT INTERACTIONS INVESTIGATION

M. J. Mandell
G. A. Jongeward
R. A. Kuharski
V. A. Davis

Maxwell Laboratories, Inc.
S-Cubed Division
P. O. Box 1620
La Jolla, California 92038-1620
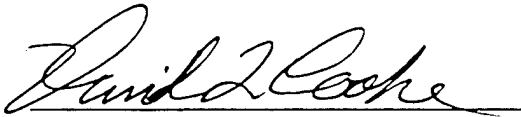
July 1996

Scientific Report No. 1

19971202 018
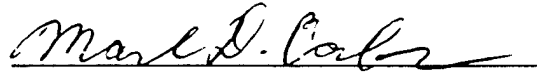
Approved for Public Release; Distribution Unlimited.

PHILLIPS LABORATORY
Directorate of Geophysics
AIR FORCE MATERIEL COMMAND
HANSCOM AFB, MA 01731-3010
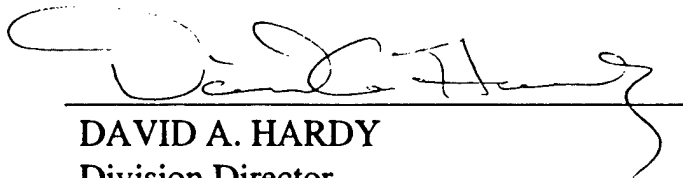
DTIC QUALITY INSPECTED 8

"This technical report has been reviewed and is approved for publication"

DAVID L. COOKE
Contract Manager

MARK D. CONFER, Maj. USAF
Branch Chief

DAVID A. HARDY
Division Director

This report has been reviewed by the ESC Public Affairs Office (PA) and is releasable to the National Technical Information Service (NTIS).

Qualified requestors may obtain additional copies from the Defense Technical Information Center (DTIC). All others should apply to the National Technical Information Service (NTIS).

If your address has changed, if you wish to be removed from the mailing list, or if the addressee is no longer employed by your organization, please notify PL/IM, 29 Randolph Road, Hanscom AFB, MA, 01731-3010. This will assist us in maintaining a current mailing list.

Do not return copies of this report unless contractual obligations or notices on a specific document require that it be returned.

REPORT DOCUMENTATION PAGE

Public reporting burden for this collection of information is estimated to average 1 hour per response, including the time for reviewing instructions, searching existing data sources, gathering and maintaining the data needed, and completing and reviewing the collection of information. Send comments regarding this burden estimate or any other aspect of this collection of information, including suggestions for reducing this burden, to Washington Headquarters Services, Directorate for Information Operations and Reports, 1215 Jefferson Davis Highway, Suite 1204, Arlington VA 22202-4302, and to the Office of Management and Budget, Paperwork Reduction Project (0704-0188), Washington, DC 20503.

1. AGENCY USE ONLY *(Leave blank)*	2. REPORT DATE July 1996	3. REPORT TYPE AND DATES COVERED Scientific Report No. 1

4. TITLE AND SUBTITLE Space System-Environment Interactions Investigation	5. FUNDING NUMBERS PE 63410F PR S327 TA 01 WU AA
6. AUTHOR(S) M. J. Mandell, G. A. Jongeward, R. A. Kuharski, V. A. Davis	Contract F19628-91-C-0187

7. PERFORMING ORGANIZATION NAME(S) AND ADDRESS(ES) S-Cubed A Division of Maxwell Laboratories, Inc. P.O. Box 1620 La Jolla, CA 92038-1620	8. PERFORMING ORGANIZATION REPORT NUMBER SSS-DPR-92-15486
9. SPONSORING/MONITORING AGENCY NAME(S) AND ADDRESS(ES) Phillips Laboratory 29 Randolph Road Hanscom AFB, MA 01731-3010 Contract Manager: Dr. David Cooke/GPSG	10. SPONSORING/MONITORING AGENCY REPORT NUMBER PL-TR-96-2233

11. SUPPLEMENTARY NOTES

12a. DISTRIBUTION/AVAILABILITY STATEMENT Approved for public release; distribution unlimited.	12b. DISTRIBUTION CODE

13. ABSTRACT *(Maximum 200 words)*

This report describes work conducted for the first 4 1/2 years of a contract to support research into the interactions of space systems with the space environment. This report covers theoretical and calculational research in support of the SPEAR 3 program using the EPSAT and DynaPAC computer codes. Analysis of CHAWS and PASP Plus flight data is discussed.

14. SUBJECT TERMS Spacecraft, Space Environment, SPEAR, EPSAT, DynaPAC, CHAWS, PASP Plus, Solar Arrays, Wakes, Parasitic Current Collection	15. NUMBER OF PAGES 192
	16. PRICE CODE

17. SECURITY CLASSIFICATION OF REPORT UNCLASSIFIED	18. SECURITY CLASSIFICATION OF THIS PAGE UNCLASSIFIED	19. SECURITY CLASSIFICATION OF ABSTRACT UNCLASSIFIED	20. LIMITATION OF ABSTRACT SAR

NSN 7540-01-280-5500

Standard Form 298 (Rev. 2-89)
Prescribed by ANSI Std. Z39-18
298-102

TABLE OF CONTENTS

TABLE OF CONTENTS (cont.)

1. INTRODUCTION

This report is a summary of technical work performed from inception (December 1991) through June 1996 on contract F19628-91-C-0187 entitled "Space System-Environment Interactions Investigation." It is the ninth of a series of interim reports to be produced every six months. Each report includes an update of the material of the previous report, deleting obsolete material, and adding the work performed during the two most recent quarters. In that way, a single volume will always suffice as a technical summary of the work.

The objectives of this contract are to support, with theoretical and modeling studies, research into the interactions of space systems with the space environment that are of interest to the Air Force. During this period, work was performed in support of the SPEAR-III rocket flight experiment, the PASP Plus orbital experiment, the CHAWS shuttle experiment, and the SPREE shuttle experiment.

SPEAR III

Dr. Myron Mandell and Dr. Gary Jongeward made presentations at the following conferences and SPEAR-III project meetings:

Meeting Name	Location	Date
Science Meeting	Arlington, VA	17-18 December 1991
Mid-Point Review	Logan, UT	14-16 January 1992
CDR	Logan, UT	14-16 April 1992
Science Meeting	Sandusky, OH	9-10 July 1992
Mock-up Data Review	Arlington, VA	2 September 1992
AGU Fall 1992	San Francisco, CA	7-11 December 1992
High Voltage Workshop	Dayton, OH	20-21 October 1992
SPEAR-III Data Review	Logan, UT	20-21 April 1993
IEEE Plasma Physics	Vancouver, B.C.	7-9 June 1993

In addition, SPEAR-III information was exchanged by telephone and telefax. The presentations at these meetings, along with some telephone and telefax information, have been reorganized into chapters titled:

2. EPSAT Calculations in Support of Maintaining a High Apogee for SPEAR-III.

3. DynaPAC Calculations for SPEAR-III Floating Potentials and Currents.

4. DynaPAC Calculations for ESA Currents and Angles

5. Neutral Densities Produced by the NGRS (Neutral Gas Release System)

6. NGRS-Induced Breakdown of the SPEAR-III Negative Body Sheath

7. Modeling of SPEAR III Mock-up.

The quarterly reports for this contract contain the actual presentation material.

A review of our examination of the SPEAR-III flight data appears in Appendix C.

PUBLICATIONS

Three prospective publications have been supported by this contract. The S-Cubed contribution to the SPEAR-II products report received its final set of revisions under this contract, and appears as Appendix A. A paper based on a presentation on the DynaPAC computer code at the DNA Numerical Methods Symposium (Menlo Park, April 1992) was published in the conference proceedings, and appears as Appendix B. A paper describing our review of the SPEAR III flight data was prepared for the AIAA Aerospace Sciences Meeting in Reno, NV and appears in Appendix C. A paper describing our preliminary review of the PASP Plus data and included in the SPRAT XIV Conference proceedings is in Appendix D.

We submitted the paper "Modeling of Parasitic Current Collection by Solar Arrays in Low Earth Orbit" to Physics of Plasmas for publication. We wrote a paper on PASP Plus current collection flight data for presentation at the 31st Intersociety Energy Conversion Engineering Conference in August. This paper will appear in the conference proceedings.

CHAWS

We did a statistical analysis of CHAWS data from the flights of the Wake Shield Facility (WSF). The analysis is described in Chapter 8 of this report.

We did a preliminary calculation of the current collected by CHAWS while WSF was in the wake of the shuttle. This involved making a geometric model of the WSF and shuttle system.

We made a presentation on comparing calculations with experiment values of the wake side currents from the CHAWS experiment at the Spring AGU meeting in May. The presentation is included in the quarterly report for the appropriate period.

SPREE

We made a geometric model of SPREE in the shuttle bay.

PASP Plus

We presented the paper "Parasitic Collection by PASP-Plus Solar Arrays" at the Space Photovoltaic Research and Technology 1995 Conference. The paper prepared for this conference is in Appendix D.

We submitted the paper "Modeling of Parasitic Current Collection by Solar Arrays in Low Earth Orbit" to Physics of Plasmas for publication.

We examined the floating potential of APEX.

We examined the effect of the magnetic field on PASP Plus current collection. No systematic effect could be seen.

We made a presentation at the Space Power Workshop in Manhattan Beach, CA. The presentation is included in the quarterly report for the appropriate period.

We wrote a paper on PASP Plus current collection flight data for presentation at the 31st Intersociety Energy Conversion Engineering Conference in August. This paper will appear in the conference proceedings.

2. EPSAT CALCULATIONS IN SUPPORT OF MAINTAINING A HIGH APOGEE FOR SPEAR-3

In January, 1992, as the SPEAR-3 payload had grown in length and weight, concern was expressed that its apogee would fall well below the desired 300 km altitude. A presentation based on EPSAT calculations was given, showing that the mission objectives would be severely impacted should the apogee fall well below 300 km.

Figure 1 shows the trajectories for 250, 300, and 350 km apogees, assuming rocket burnout at about 125 km. As the apogee drops, the time above a given altitude decreases. The figure indicates that the time above 200 km is 200, 280, and 350 seconds for the three orbits.
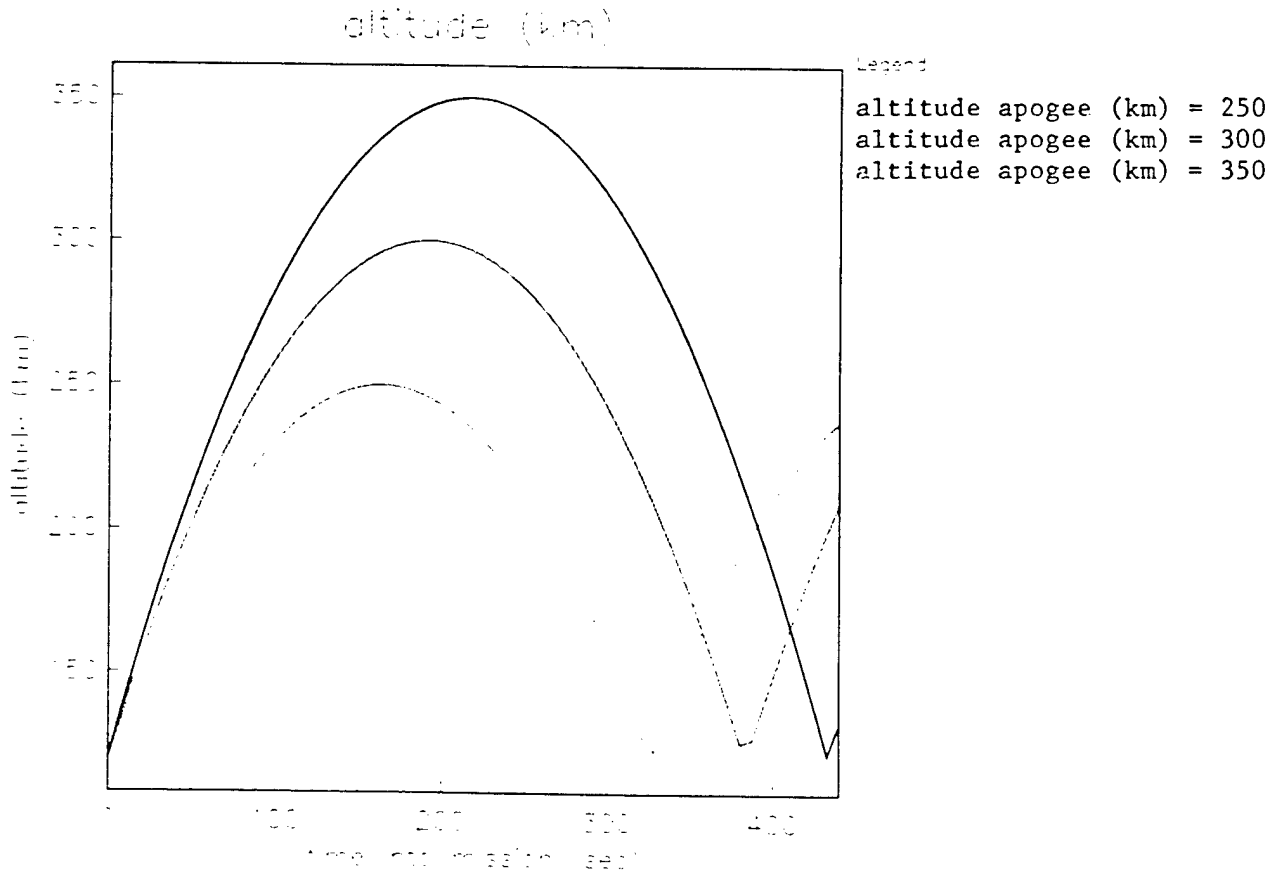

Figure 1. SPEAR-3 trajectories for 250, 300, and 350 km apogee missions.

Figure 2 shows the IRI model plasma density for the same three orbits. For the 300 and 350 km orbits there is an extended period of roughly constant plasma density. For the 250 km orbit the peak density is never reached, the plasma density is usually varying fairly rapidly, and the higher plasma densities occur early in the flight, when outgassing may not be complete.
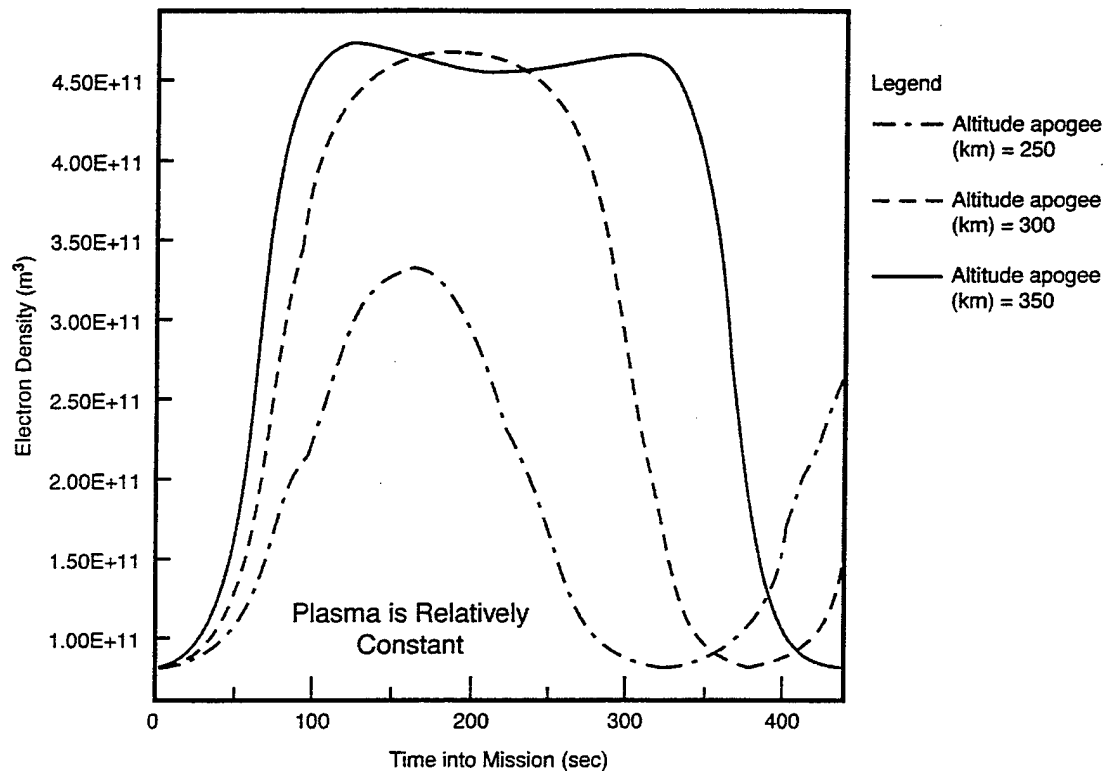

Figure 2. IRI model plasma density profiles for three SPEAR-3 orbits.

It is important to reach a high plasma density to avoid spontaneous breakdown. Figure 3 shows that the sheath radii about the sphere and the rocket increase sharply below 200 km, increasing ionization paths and enhancing the likelihood of spontaneous breakdown.
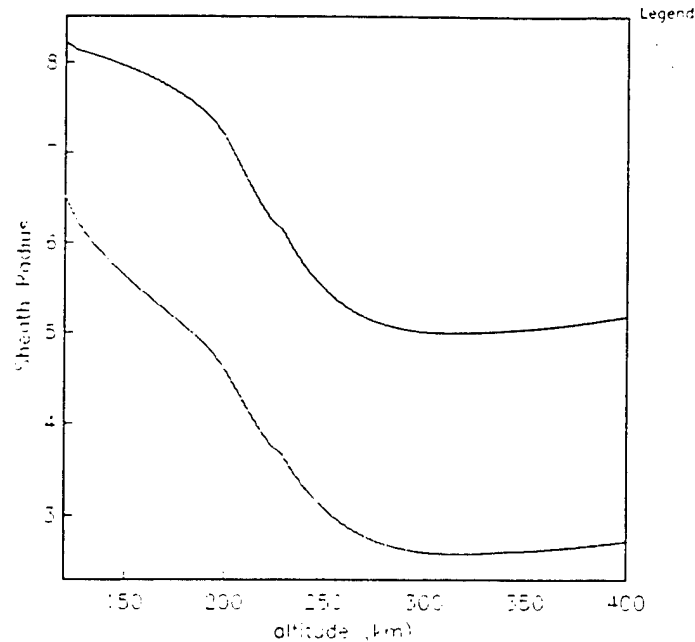
Figure 3. Sheath radii about the SPEAR-3 sphere and body, calculated using IRI predicted plasma density at specified altitude.

Figure 4 shows the MSIS86 predicted neutral densities for the three orbits. We expect breakdown to be likely when the ambient density exceeds a few times 1016 m⁻³. Again, for the 250 km orbit we fall well below this threshold for a shorter time than would be the case for a higher orbit.
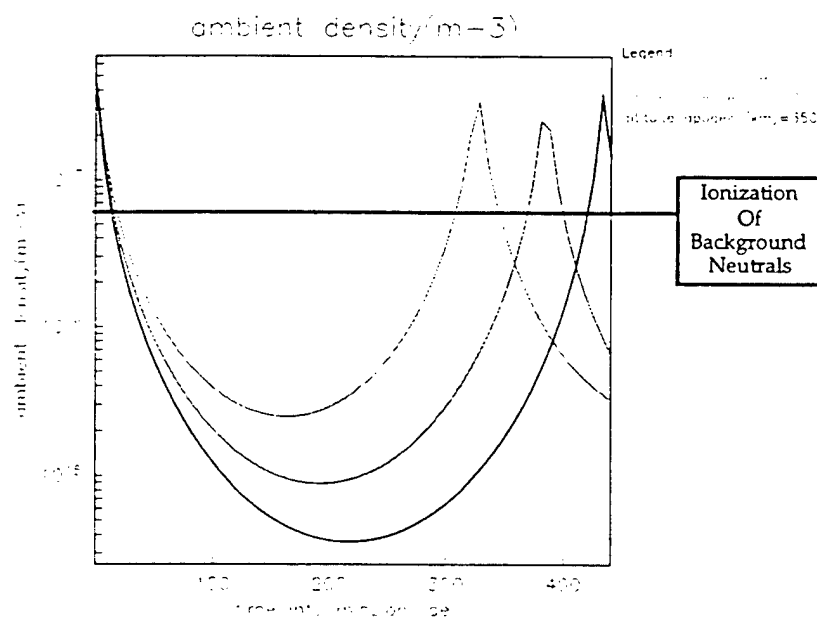

Figure 4. MSIS86 neutral density profiles for the three SPEAR-3 orbits.

3. DYNAPAC CALCULATIONS FOR SPEAR-3 FLOATING POTENTIALS AND CURRENTS

The floating potential of SPEAR-3 results from a balance between electron current collected on the positively biased sphere and secondary-electron-enhanced ion current collected by the negative rocket body. Simple models, which assume Parker-Murphy collection by the sphere and Langmuir-Blodgett collection by the rocket, generally predict that the bulk of the applied voltage will appear on the negative body. Results of these simple models are incorrect because (1) they neglect the effects of the interaction between the sphere and body sheaths, and (2) neither a sphere nor a cylinder gives a satisfactory estimate for the body sheath current.

Experience in calculating the floating potential of SPEAR-I gives us confidence that we know how to proceed. NASCAP/LEO calculations for SPEAR-I calculated floating potentials and currents by tracking ions and electrons in an assumed constant magnetic field and non-self-consistent potentials in which space charge is estimated by a nonlinear analytic screening formula. Using DynaPAC gives results with higher confidence levels because electrons will not be scattered by discontinuous electric fields.

Figure 5 shows the DynaPAC model for SPEAR-3. In addition to the essential cylinder-boom-graded boom-sphere configuration, the model includes the floating probe and its boom, the solar cell experiment, and some additional flush-mounted experiments. For the calculations of this chapter, all the experiments are assumed to be at rocket body potential, the plastic boom is assumed to be a plasma potential (despite having a grounded cable shield running along the outside), and the graded boom is in four sections biased at 1/8, 3/8, 5/8, and 7/8 of the capacitor voltage.
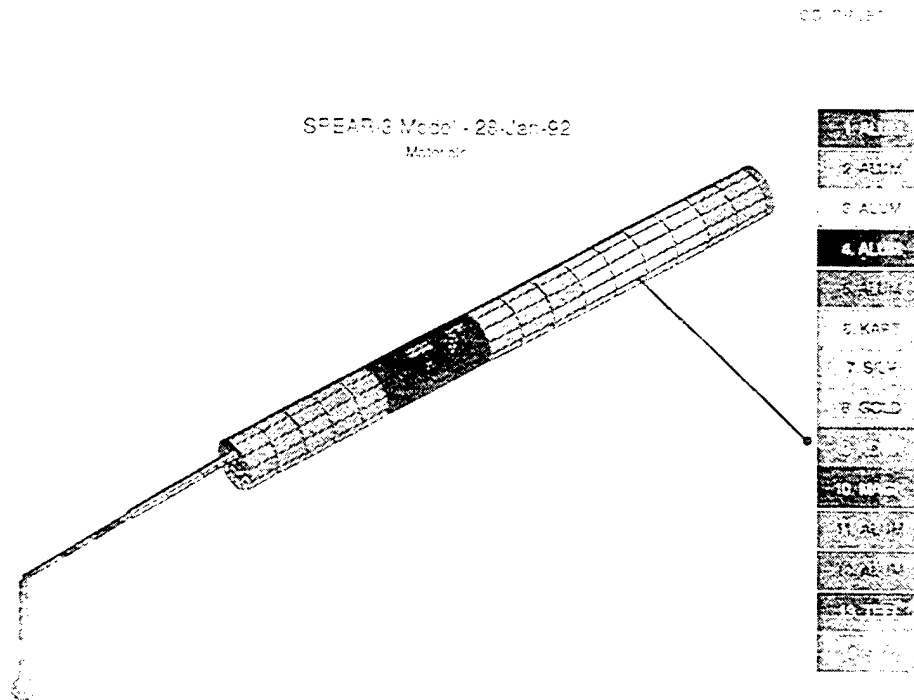
Figure 5. DynaPAC geometrical model for SPEAR-3.

The ionosphere model used in this chapter is given in Table 1.

Table 1. Ionospheric plasma properties assumed in this chapter.

Plasma Property	Value
Maximum Density	2×10^{11} m^{-3}
Minimum Density	1×10^9 m^{-3}
Plasma Temperature	0.1 eV
Magnetic Field	0.4 gauss
Ion Species	O$^+$

The effect of the sheath overlap differs depending on whether the overlap is weak or strong. Figure 6 shows a weak overlap case. Electrons that E x B drift along the sheath contour into the high electric field overlap region receive a waiver from the regulations of Parker and Murphy, so that they can contribute to the collected electron current. This effect is strongest when the magnetic field is normal to the plane of the figure (Science Attitude 1), and weakest when the

8

magnetic field is parallel to the rocket axis (which minimizes the intersection of the drift orbits with the sheath overlap region). The collected electron current exceeds the Parker-Murphy bound for all three magnetic field orientations.
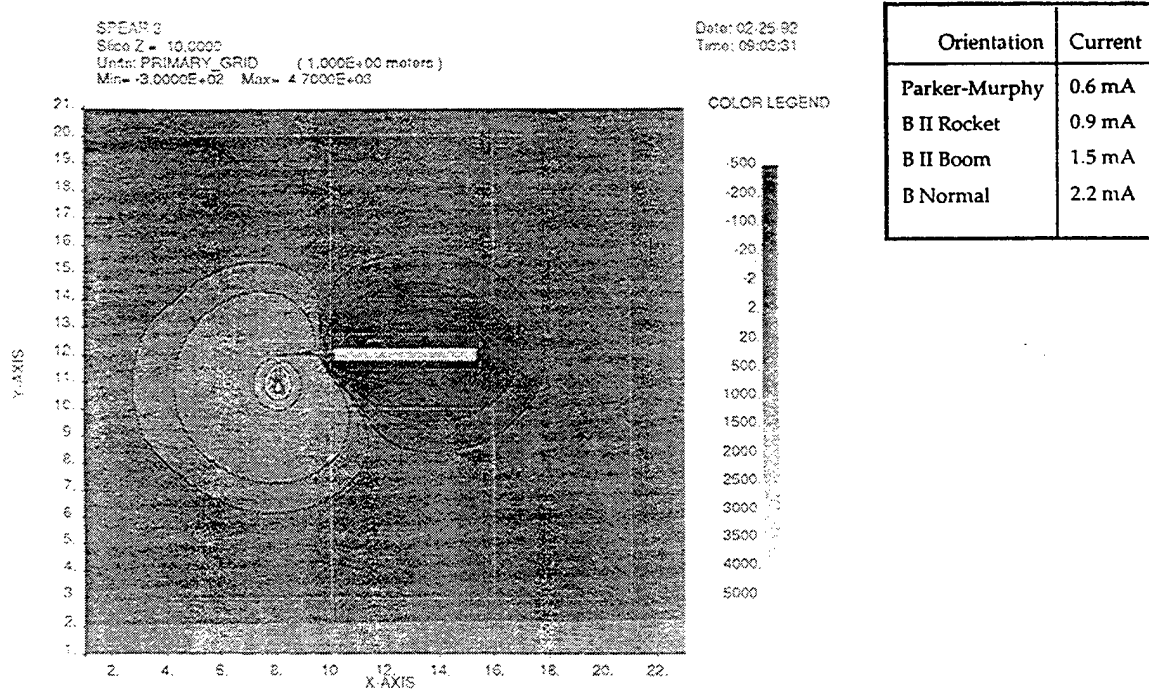

SPEAR 3
Slice Z = 10.0000
Units: PRIMARY_GRID   (1.000E+00 meters)
Min= -3.0000E+02   Max= 4.7000E+03

Date: 02-25-92
Time: 09:03:31

COLOR LEGEND

-500
-200
-100
-20
-2
2
20
500
1000
1500
2000
2500
3000
3500
4000
5000

Orientation	Current
Parker-Murphy	0.6 mA
B II Rocket	0.9 mA
B II Boom	1.5 mA
B Normal	2.2 mA

Figure 6. DynaPAC calculated electrostatic potentials about SPEAR-3, illustrating a case of weak sheath overlap.

Figure 7 illustrates the case of strong sheath overlap. Here the body sheath nearly overwhelms the sphere sheath, which is both reduced in size and partially blocked by the immense negative potential region. This reduces the collected electron current well below the Parker-Murphy bound. The highest current now occurs when the magnetic field is parallel to the rocket body, since these experience the least blockage by electrostatic barriers.
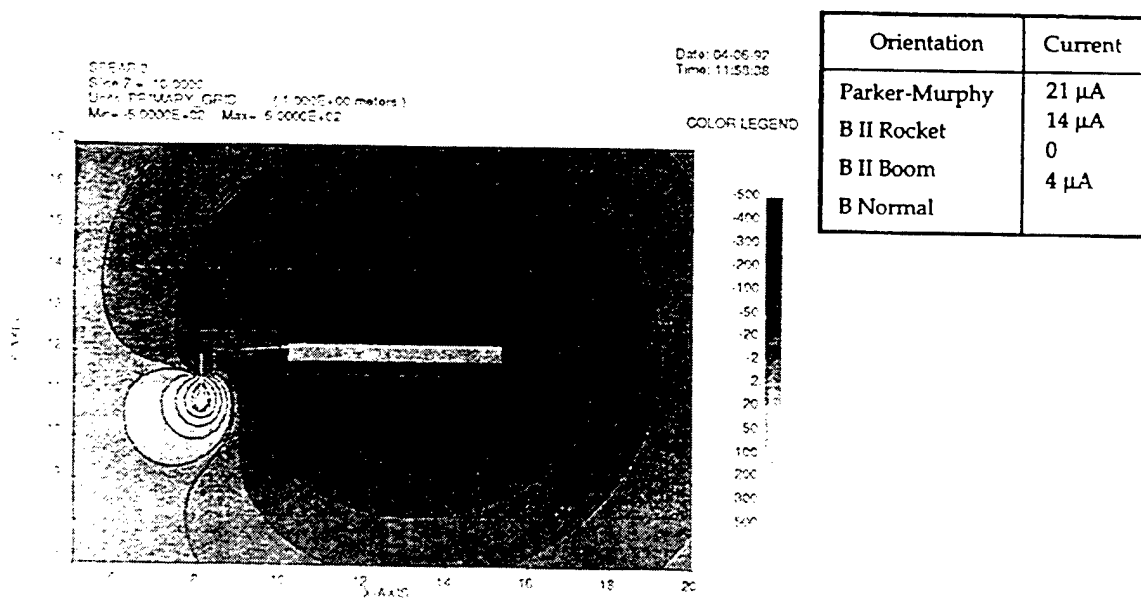
9

Figure 7. DynaPAC calculated electrostatic potentials about SPEAR-3, illustrating a case of strong sheath overlap.

Figure 8 shows the current variation as a function of assumed floating potential for the case of 16 kV capacitor voltage and 2×10^{11} m-3 plasma density. It is fairly typical that the floating potential occurs near the switch from weak to strong sheath overlap, so that there is only a weak dependence of floating potential and circuit current on magnetic field.
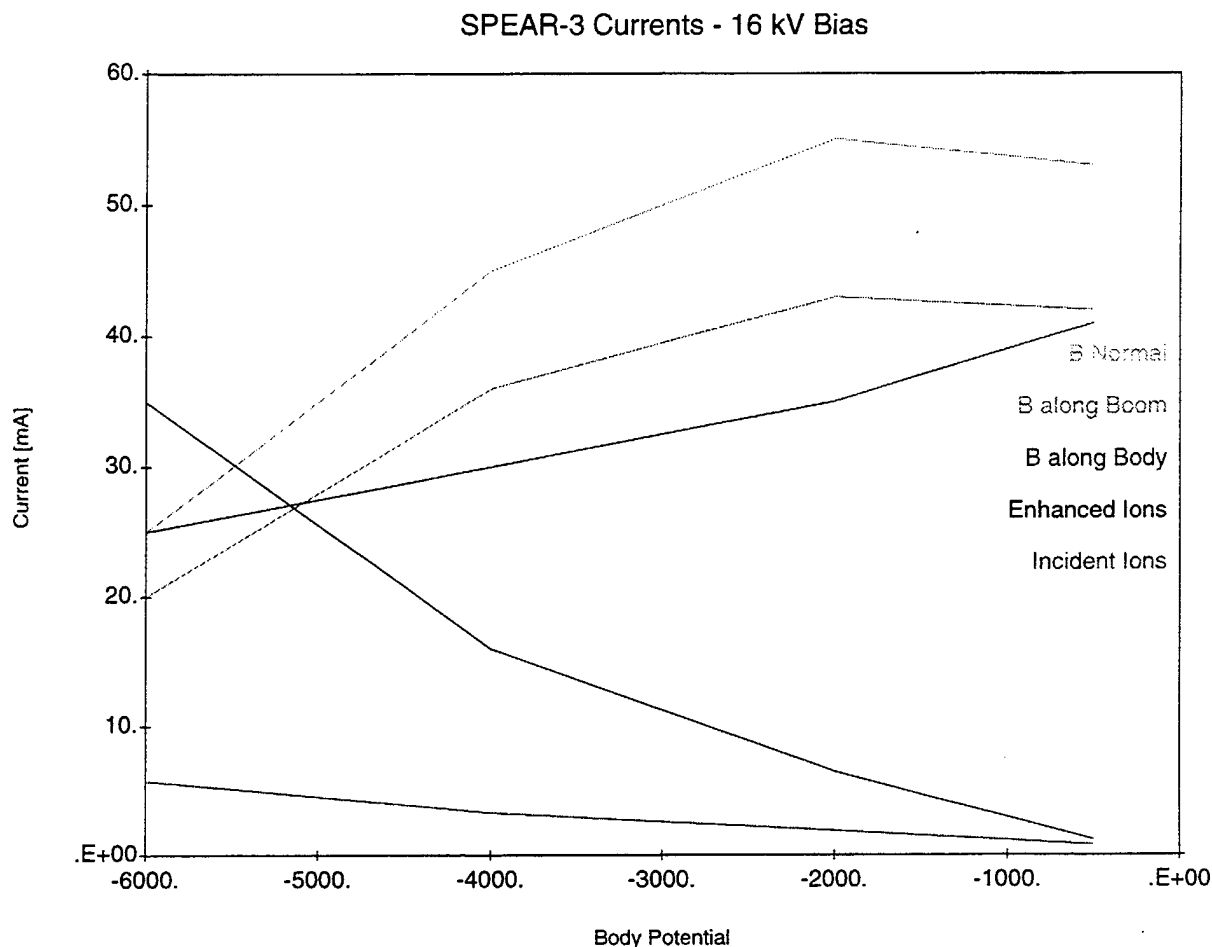
SPEAR-3 Currents - 16 kV Bias

Figure 8. Variation of sphere and body currents as a function of assumed floating potential for 16 kV capacitor voltage, 2×10^{11} m^{-3} plasma density, and various magnetic filed orientations.

Figure 9 shows a list of calculations performed with capacitor voltages of 1, 5, 10, and 16 kV, plasma densities in the range indicated in Table 1, and various assumed body potentials. Floating potentials inferred from these calculations are replotted in Figure 10 in terms of the fraction of the applied voltage which appears on the body. We see that this fraction decreases with applied voltage, and increases with plasma density. For high applied voltages (> 5 kV) about one-third of the voltage typically appears on the body. At lower applied voltages (~1 kV) this fraction rises to one-half or more. Figure 11 shows the same floating potential information, but with circuit current values (milliamperes) indicated. We expect currents in the 10 milliampere range at the high end of the plasma density range, and in the 0.1 milliampere range at the lowest plasma densities.
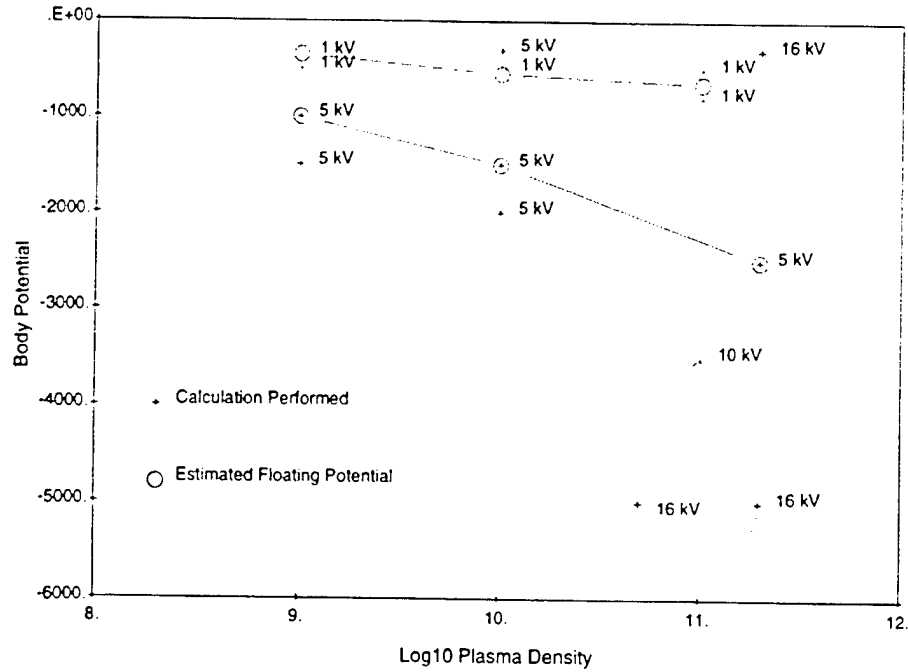
11

Figure 9. DynaPAC calculations performed ("+") for various capacitor voltages (noted on figure), plasma densities, and assumed body potentials. Circles represent estimated floating potentials.
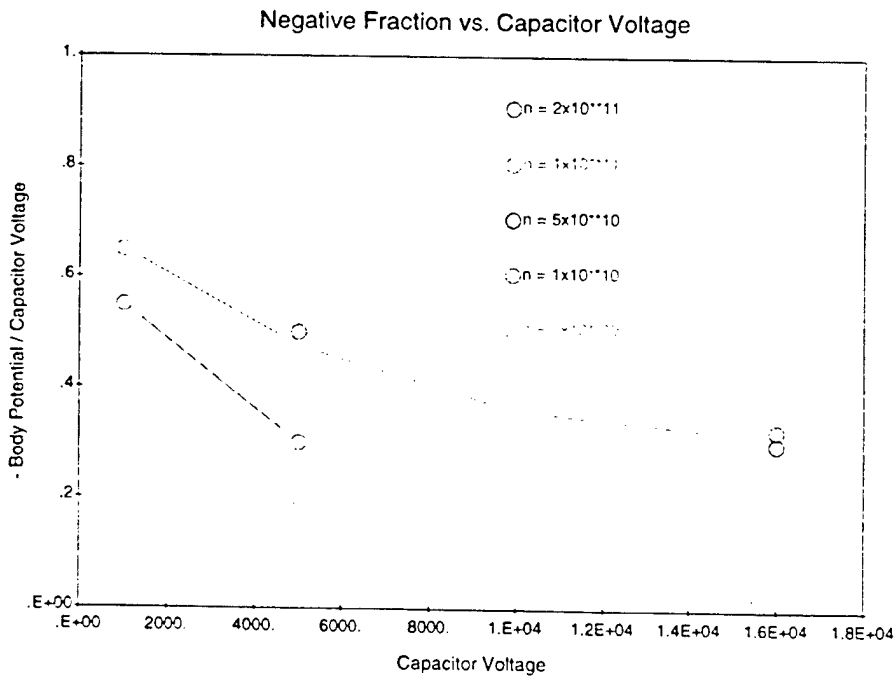

Figure 10. SPEAR-3 predicted floating potentials (expressed as the fraction of capacitor voltage appearing on the body) for various plasma densities. The lines represent plasma densities of 10^{11} m^{-3} (top), 10^{10} m^{-3} (middle), and 10^9 m^{-3} (bottom).
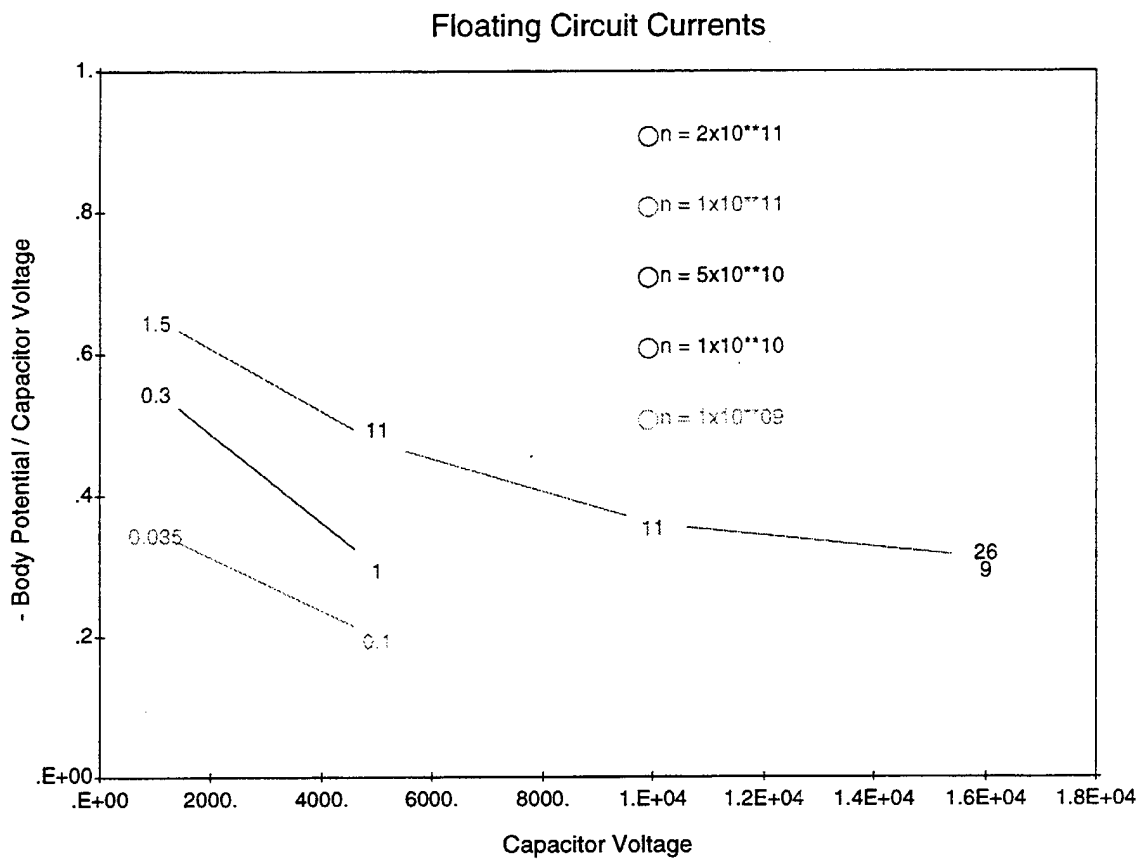
12

Figure 11. SPEAR-3 predicted plasma currents (milliamperes) in the same format as Figure 10.

4. DYNAPAC CALCULATIONS FOR ESA CURRENTS AND ANGLES

The DynaPAC calculations described in the previous chapter also allow us to calculate the distribution of sheath ion current over the body. This is important in order to be sure that there are sheath ions impacting the location of the Electrostatic Analyzer (particle detector), and to estimate the ion current and angular distribution to the detector in order to optimize the detector sensitivity.

Figure 12 shows a typical selection of ion trajectories from a sheath contour to the rocket. The first point to notice is that some portions of the rocket skin receive no ions, as they are totally electrostatically shadowed by the sphere sheath. The shadowed region typically covers nearly half of the boomward side of the rocket, and one-fourth to one-third of the side opposite the boom. The ESA is located just above the middle of the rocket (approximately 0.57 of the way from the bottom of the adapter ring to the top of the high voltage module) on the side opposite the boom. In no case of interest have we observed electrostatic shadowing of the particle detector position.
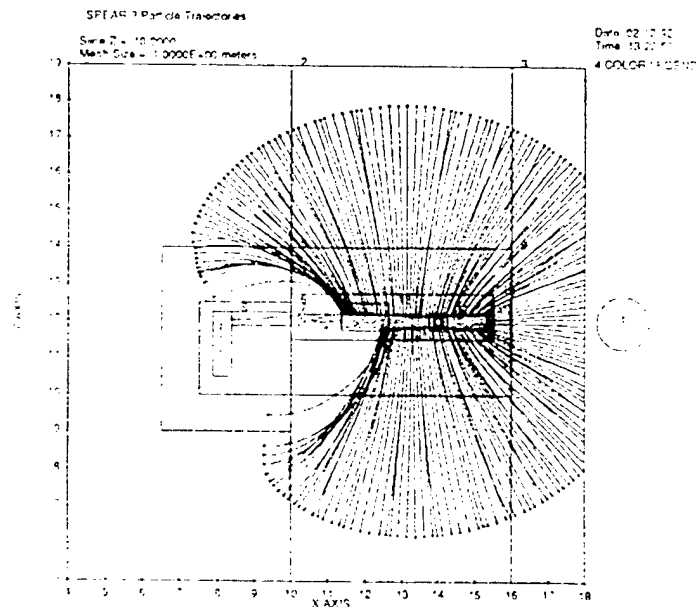

Figure 12.   Typical ion trajectories from a sheath contour to the SPEAR-3 rocket body.

The second point to notice on Figure 12 is that the first several trajectories to the anti-boom side of the rocket cross, indicating focusing to a "hot spot". Figure 13 shows the flux to the entire rocket surface (for plasma density 1×10^{11} m^{-3}, 5 kV capacitor voltage, and -1.5 kV body potential). Over most of the rocket (excluding the electrostatically shadowed portion) the ion flux (for this case) is about 0.1 milliamperes per square meter, but a hot spot with flux of 0.3 milliamperes per square meter is clearly seen near the transition from the electrostatically shadowed region.

SPEAR-3 Model - 28-Jan-92
Flux (Amps/m**2) --- Min= 0.00E+00 Max= 2.88E-04

COLOR LEGEND

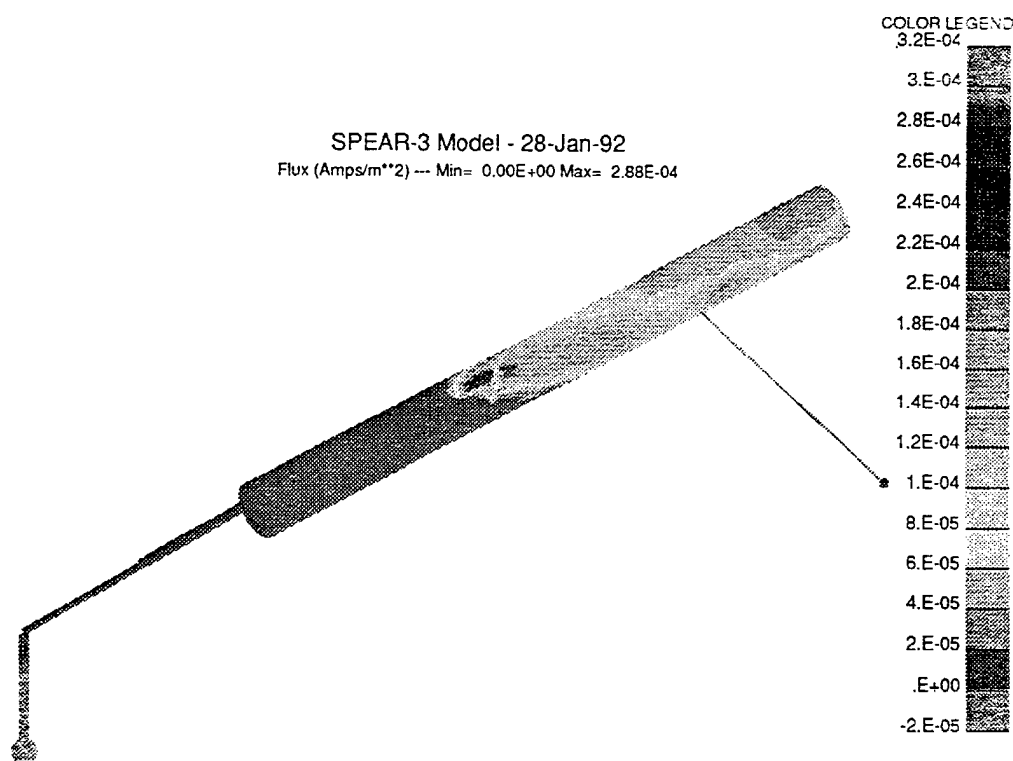|	
3.2E-04	
3.E-04	
2.8E-04	
2.6E-04	
2.4E-04	
2.2E-04	
2.E-04	
1.8E-04	
1.6E-04	
1.4E-04	
1.2E-04	
1.E-04	
8.E-05	
6.E-05	
4.E-05	
2.E-05	
.E+00	
-2.E-05	

Figure 13. Ion flux density to the SPEAR-3 rocket surface.

Figure 14 shows the calculated current densities at the ESA location for the calculations indicated in Figure 9. The predicted current densities range over nearly two orders of magnitude (from nearly one milliampere per square meter down to about 10 microamperes per square meter), and correlate strongly with plasma density and less strongly with body potential. There is also appreciable variation due to the strong gradients of flux density (due to focusing effects) near the ESA location.
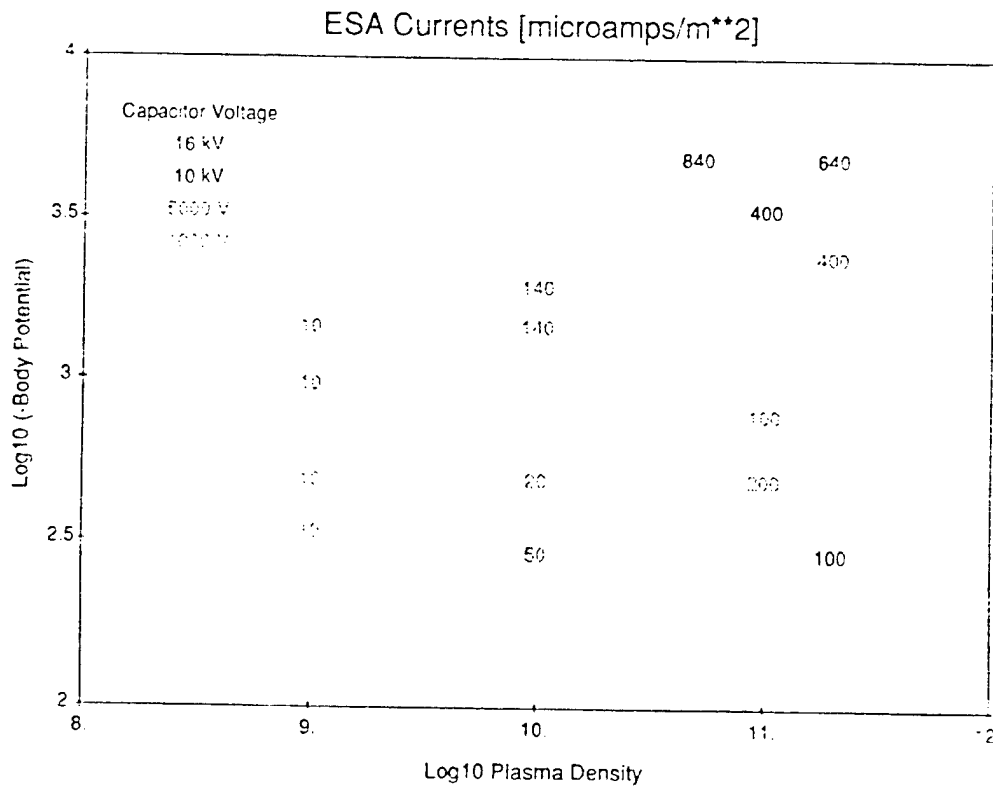
ESA Currents [microamps/m**2]

Capacitor Voltage
16 kV
10 kV
5000 V

Log10 (-Body Potential)

Log10 Plasma Density

Figure 14. DynaPAC calculated flux densities to the ESA location for various plasma densities, body potentials, and capacitor voltages.

The angle of incidence of sheath ions to the particle detectors is also of concern, since the ESA's have limited angular range, and the proposed instruments do not scan in angle. Previous calculations (reverse trajectory calculations with DynaPAC) showed that the velocity component normal to the rocket axis was broadly distributed, corresponding to a broad distribution of the corresponding angle. However, the velocity component along the rocket axis was narrowly distributed, suggesting an angular distribution spanning only a few degrees.
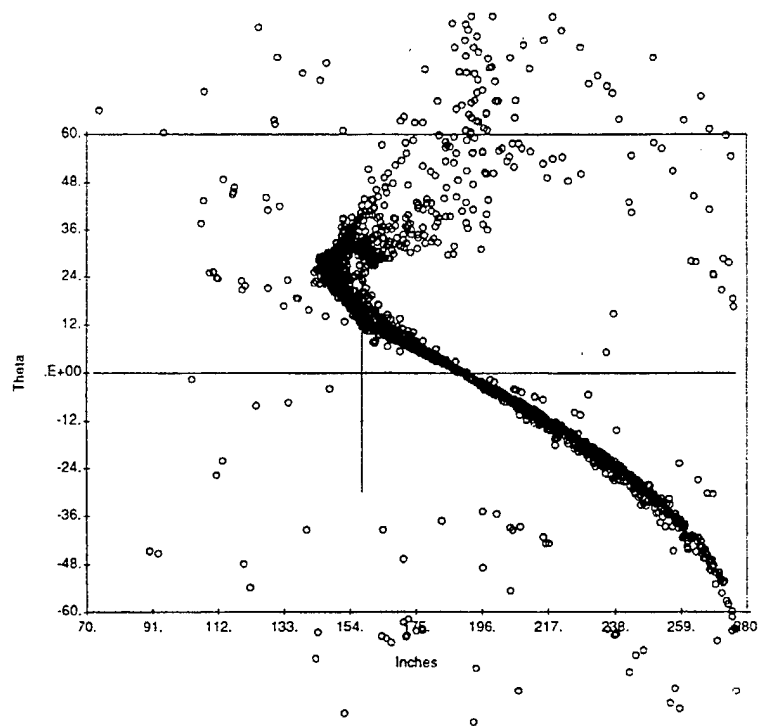
Figure 15. Incident angle (relative to surface normal) of ions striking the anti-boom side of the SPEAR-3 rocket body.

Figure 15 shows the incident angle of ion macroparticles impacting the anti-boom side of the rocket (as a function of position on the rocket) for the same case as Figure 13. At the particle detector position (vertical line) the incident angle of the main beam is seen to be about 12 degrees off normal. (Note also the vertical distribution just above the particle detector position, indicating focusing to the hot spot.) Figure 16 shows the incident angles (as a function of plasma density and body potential) according to the same scheme as Figure 14. In general, the predicted angle increases with increasing sheath size, i.e., with more negative body potential or with lower plasma density.
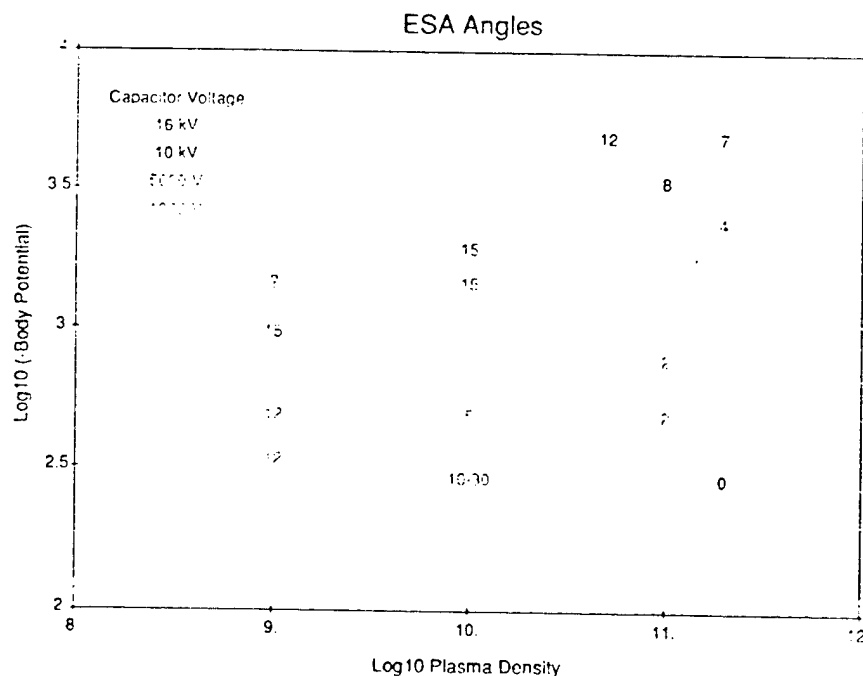
17

ESA Angles

Figure 16. DynaPAC calculated incident angles at the ESA location for various plasma densities, body potentials, and capacitor voltages.

To compare with these predictions, Dr. R. C. Olsen (Naval Postgraduate School) reviewed the measurements by the ESA's on SPEAR-I. The SPEAR-I measurements indicated that the incident ions were broadly distributed in both energy and angle. The integrated current corresponded, at least roughly, to DynaPAC predictions. The energy distribution was a constant count rate up to the inferred spacecraft potential, with a high energy falloff characterized by a temperature of about one-tenth the inferred spacecraft potential. There was little angular dependence, except that, where charging peaks did occur, they tended to be at angles where DynaPAC would have predicted no incident flux. No plausible physical mechanisms have been proposed for degrading the sharp peak in energy and angle predicted by simple theory to the broad distribution observed by SPEAR-I.

On the basis of the DynaPAC calculations, we recommended ESA aperture diameters as shown in Table 2. The recommendations take into account the detector saturation at 1.6 picoamperes, and assume that one-fourth of the flux enters the detector (due to limited range in azimuthal angle). The recommended aperture diameter is then given by

18

$$d = 2.85 \times 10^{-6} \, J^{-1/2}$$

where J is the expected current density. Because the SPEAR-I results indicated a broad distribution of incident current, larger apertures (corresponding to 10^{14} and 10^{12} ster^{-1} cm^{-2} s^{-1} E^{-1}) were adopted.

Table 2

Energy Range	Flux Range	Design Flux	Aperture Diameter [microns]	Aperture Diameter [inches]
High	High	1×10^{-3} Am^{-2}	90	0.0035
High	Low	3×10^{-5} Am^{-2}	520	0.020
Low	High	2×10^{-4} Am^{-2}	200	0.008
Low	Low	1×10^{-5} Am^{-2}	900	0.035

Finally, it was suggested that ions produced in the sphere sheath might be seen in the particle detector measurements. Figure 17 shows trajectories of ions generated within the sphere sheath. Most are rapidly expelled from the spacecraft vicinity. While a minor fraction of the ions from the sphere sheath did impact the rocket body, none reached the particle detector location. This leads to the preliminary result that ions produced in the sphere sheath should not cause any problem for the ESA's.
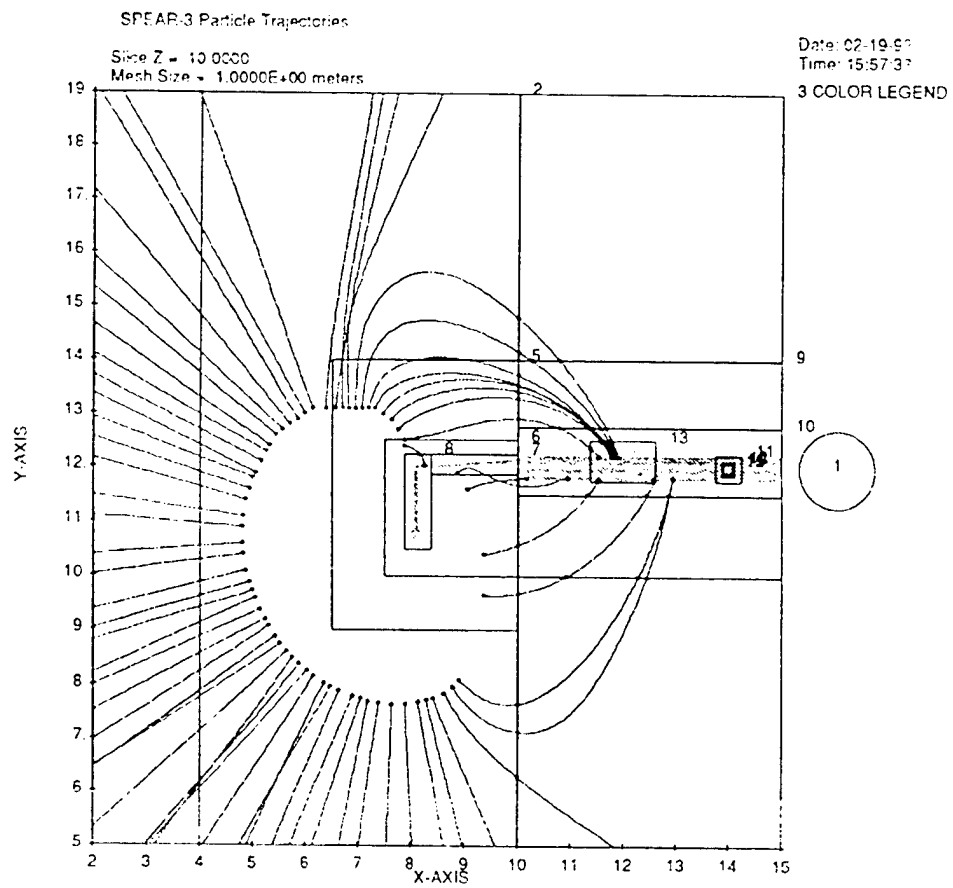
Figure 17. Trajectories of ions generated within the sphere sheath.

5. NEUTRAL DENSITIES PRODUCED BY THE NGRS (NEUTRAL GAS RELEASE SYSTEM)

The EPSAT model for nozzle plume and backflow density are being used under this contract to provide neutral densities to be used to calculate grounding of the rocket by the NGRS. Table 3 shows the input parameters for the nozzle as modeled by EPSAT.

Table 3 Nozzle Parameters

Nozzle length	.001
Exit radius	.00274
Exit mach #	7
Stagnation temp	.0223
Stagnation press	2×10^6
Throat radius	2.685×10^{-4}
Thrust	0.782
Area ratio	104
Number flow rate	2.16×10^{22}
Mass flow rate	1.005×10^{-3}
Gamma	1.4
Species	N2

A coarse plot of the effluent densities around the rocket is shown in Figure 18. The high voltage sphere is in the region of the nozzle backflow. We see that there is a substantial region near the nozzles with density exceeding 10^{19} m^{-3}, but the density falls to 3×10^{16} m^{-3} in the neighborhood of the sphere. This neutral density is probably low enough to avoid sphere breakdown, but with less safety margin than would be desirable.
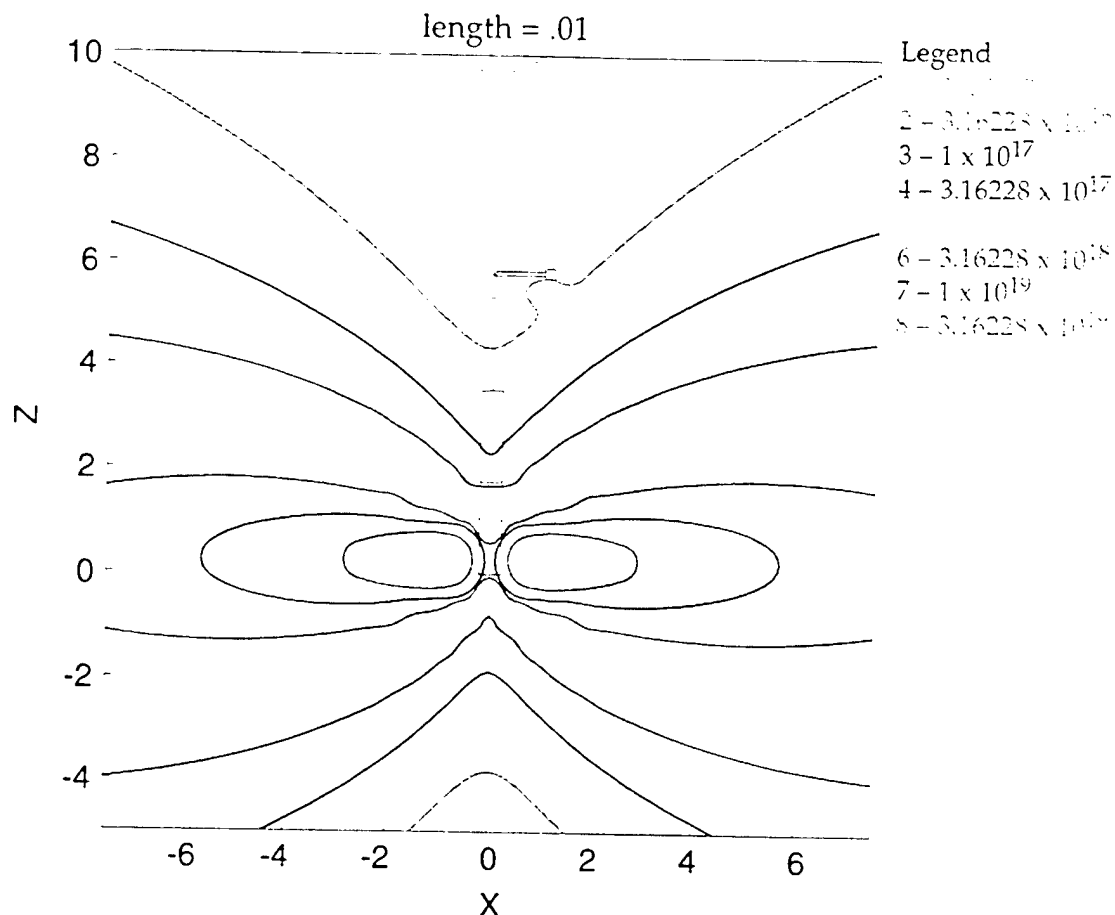
Figure 18. EPSAT plot of neutral density [m⁻³] about SPEAR-3 resulting from four nozzles.

Figure 19 shows the density at three positions on the rocket as a function of flow rate, with the breakdown regime indicated to begin at a density of 10^{17} m⁻³. The high voltage sphere appears to be safe for flow rates below ten grams per second, but the safety factor is not high. Increasing the mach number of the flow should improve the situation with regard to sphere breakdown.
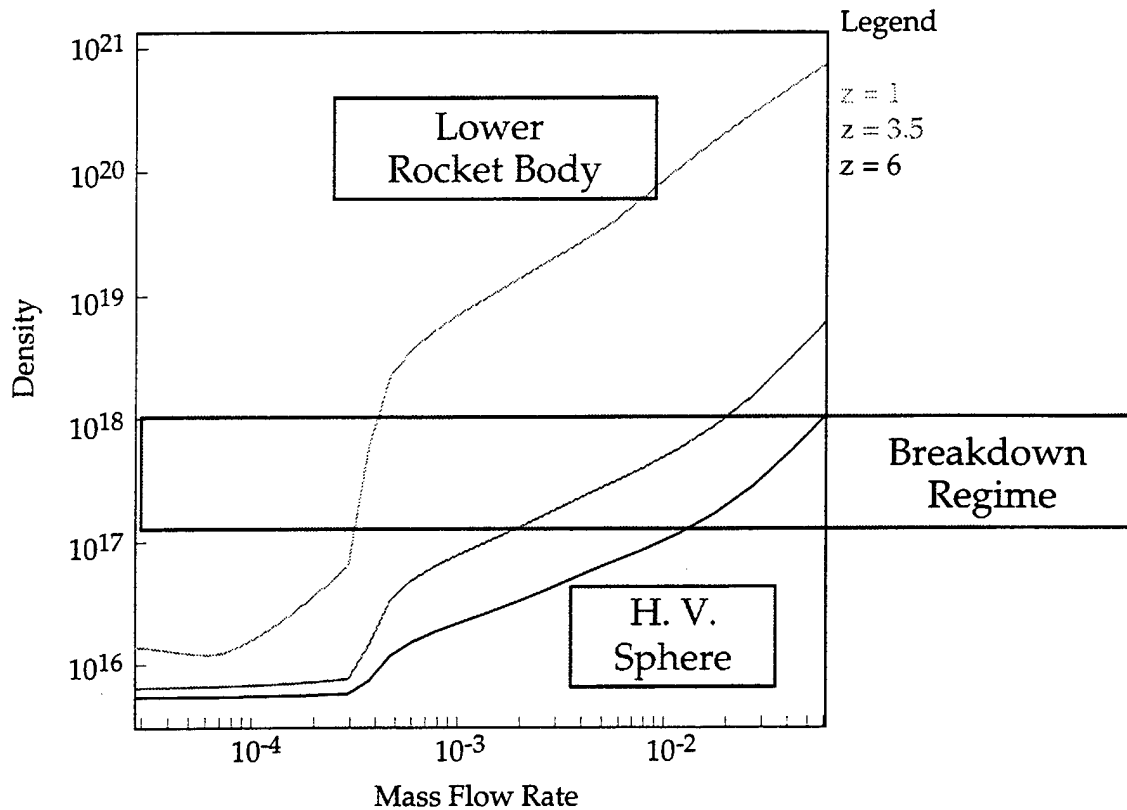
Figure 19. EPSAT-calculated neutral densities near the lower rocket body, top of rocket body, and high voltage sphere. Sphere breakdown is expected for densities above about 10^{17} m^{-3}.

The EPSAT generated density field has been incorporated into DynaPAC for use in three-dimensional calculations. Figures 20 (a and b) show two views of the density field plotted using DynaPAC software. The highest densities occur at the nozzle, but radial paths pass quickly through these very high densities. On the other hand, radial paths along the nozzle direction see modest densities for very long distances.
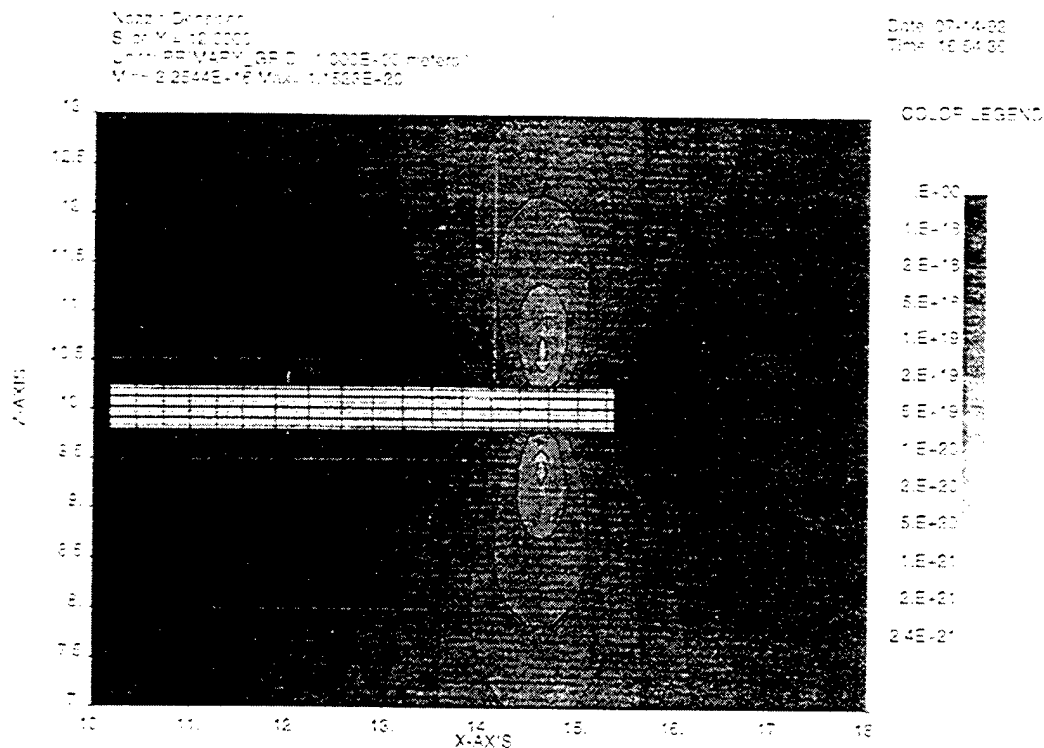
Figure 20. (a) EPSAT-calculated neutral density about SPEAR-3 plotted using DynaPAC: (a) Plane containing rocket axis and nozzle flow direction.
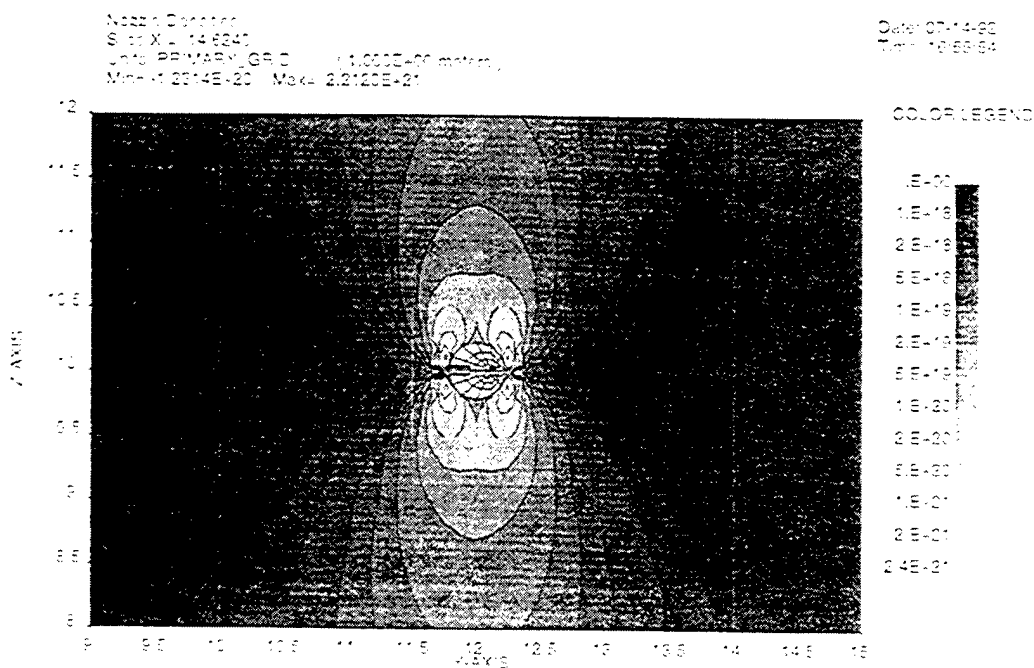

Figure 20. (b) Plane normal to rocket axis at nozzle location.

This is further illustrated in Figures 21 (a and b), with show column densities and linear gains along radial paths. Conventional phenomenology (Paschen curves) suggest that breakdown takes place along paths with column densities of one half to one torr-cm. The torr-cm plot shows that most paths satisfying this criterion occur not at the nozzle location, but 45 to 90 degrees away, passing either along the plume or obliquely through the plume. The "linear amplification" plot delineates the number of secondary electrons produced by the process of an electron leaving the rocket surface, producing ions without slowing down, and having those ions return to the rocket without charge exchanging. The regions of high gain match well the regions where column density is well-suited to breakdown.
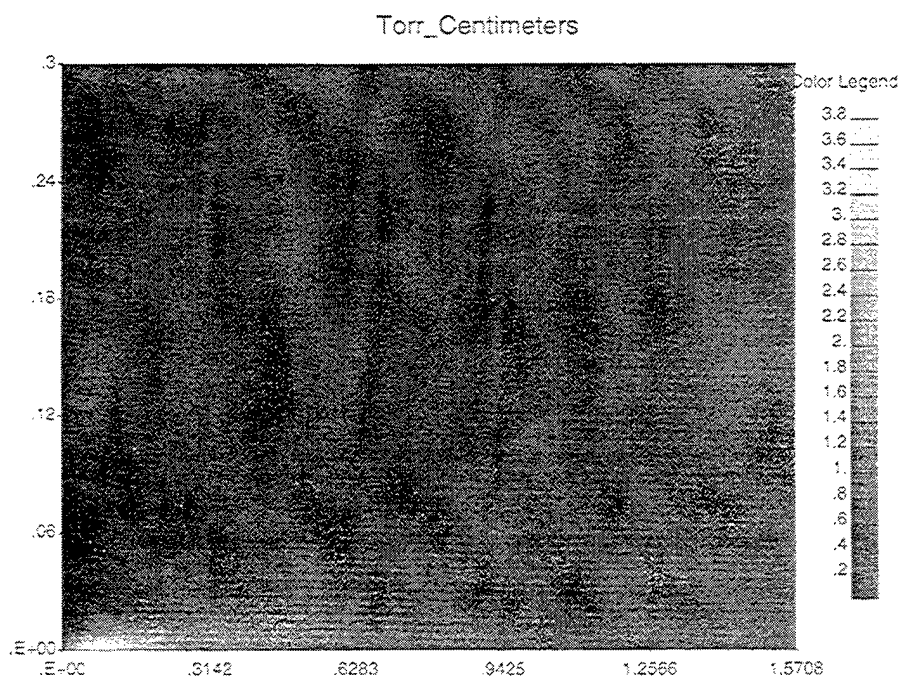

Torr_Centimeters

Figure 21. (a) Properties of the plasma plume obtained by integrating along a radial path. On the left side of the figure, the path passes through the nozzle location normal to the flow direction. On the right side of the figure the path parallels the flow direction. (a) Integral of neutral density (column density) expressed in units of torr-cm.

25

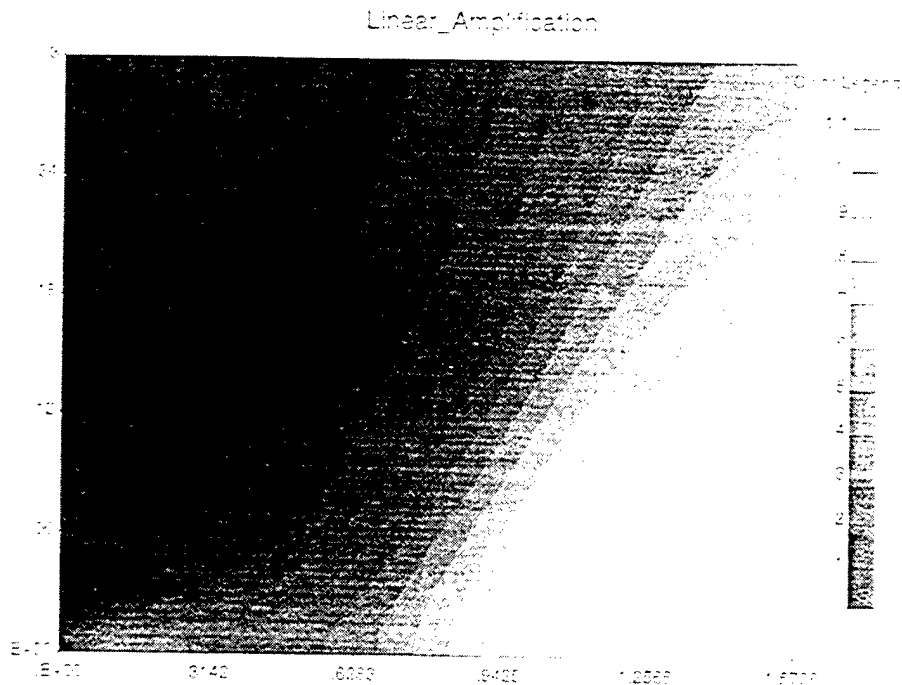**Figure 21.** (b) Integral of neutral density time ionization cross-section times secondary emission coefficient.

This analysis depends on conventional phenomenology, which deals with constant densities and electric fields. Also, the importance of charge exchange remains to be assessed. Three-dimensional trajectory effects may also impact the likelihood of breakdown. This work will progress in the next period.

6. NGRS-INDUCED BREAKDOWN OF THE SPEAR-3 NEGATIVE BODY SHEATH

This chapter describes preliminary three-dimensional considerations for NGRS-induced breakdown calculated using DynaPAC, and a dynamic, two-dimensional breakdown calculation using Gilbert. In this chapter we consider the neutral species to be molecular nitrogen, although argon will actually be used in the SPEAR-3 NGRS. These results were presented at NASA Plum Brook Station in July, 1992.

6.1. Three-Dimensional Considerations

Figure 22 illustrates the processes of ionization breakdown for negative potentials. An electron leaving the surface interacts with a neutral to yield an ion and an electron. The ion is accelerated back to the surface and creates secondary electrons. This process scales linearly with the neutral density. The newly created electron may interact with another neutral. Because two neutral collisions are involved, the number of secondary electrons produced as a result of second collisions scales quadratically with the neutral density. While we consider primarily the linear order processes in this chapter, higher order processes are important in achieving breakdown.

27

Breakdown Is Initiated When:

Each Electron Emitted From Surface Produces <u>At Least One</u> New Electron From The Surface
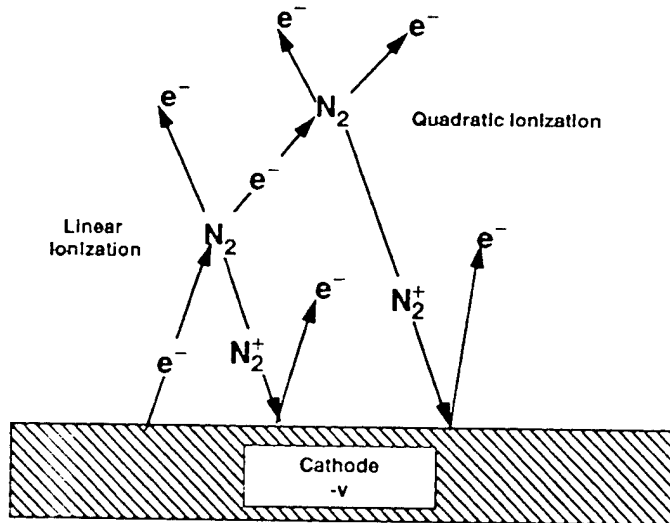
- **Each electron Generates**

  $\Gamma \approx e^{\langle \rho \sigma \ell \rangle} - 1$ **Ions**

- **Each generated ion produces** γ **surface secondary electrons**

- **When** $\gamma \Gamma = 1$ **the system is unstable and an exponential buildup of ionization occurs**

> **Positive Feedback**, $\gamma \Gamma \geq 1$, **Causes Breakdown Initiation**

Figure 22. Breakdown initiation process for a negatively biased system.

Suppose that the dominant collisions occur more than one radius from the rocket. Ionizing electrons have then been accelerated to nearly the full rocket potential, and returning ions gain this energy as well. The number of secondary electrons is proportional to the ionization cross-section for this energy times the ion-induced secondary yield. These two functions, with their product, are shown in Figure 23. The product rises sharply in the 500 to 1000 volt range, suggesting that a stable breakdown phase can occur. This is valid only for low gas densities, as we have neglected the effects of charge exchange.
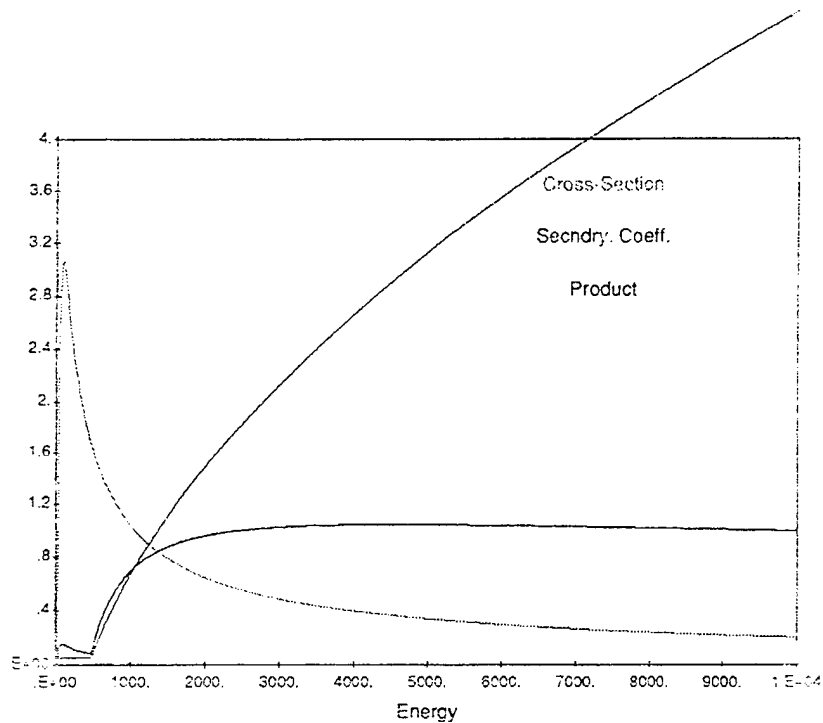
Figure 23. Ionization cross-section (for electrons on N_2), ion-induced secondary emission coefficient, and their product.

We set out to calculate the linear amplification process for actual SPEAR-3 potentials and nozzle densities. The potential field used is shown in Figure 24. It corresponds to 10 kV capacitor potential and a plasma density of 1×10^{11} m^{-3}, at the estimated floating potential of -3.5 kV. Electrons were tracked outward from the center of each surface cell on the rocket model. Ions were created in proportion to the ionization cross-section for the electron energy times the neutral density. The created ions were then tracked back to the rocket where they created secondary electrons. Electron energy loss mechanisms were neglected (under the assumption that the number of ions per electron would be small). Ion charge exchange was neglected (under the assumption of small neutral density).
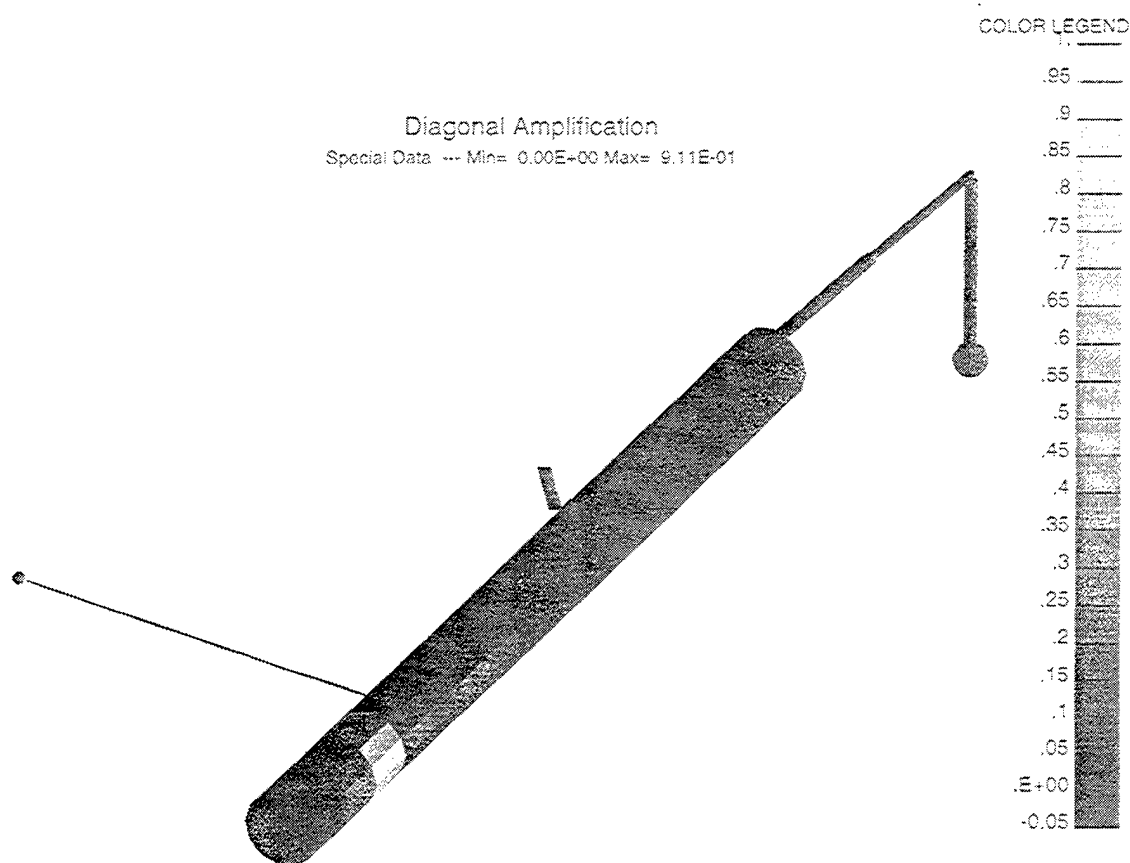
29

Figure 24. Potential field used for three-dimensional ionization calculations, corresponding to 10 kV capacitor voltage, -3.5 kV body potential, and 10^{11} m^{-3} plasma density.

In order to sustain breakdown, the secondary electrons must be created at the approximate location where the primary was emitted. As a first cut, we take this to mean the same surface cell of the DynaPAC model. Figure 25 shows the number of secondary electrons produced (by the process described above) at the same cell as the emitted primary. The cells with substantial values are in the neighborhood of the nozzles, and face the nozzle flow direction. The maximum of this diagonal secondary production term was 0.91. Some of the properties of the trajectory having this maximum are shown in Table 4.

Figure 25. Secondary electron production resulting from primary electron emitted from same cell.

Three dimensional effects tend to reduce the diagonal amplification. Because emitted electrons receive their initial acceleration near the rocket, where fields are radially outward, their trajectories are approximately radially outward. Ions, however, are created far from the rocket, where electric fields have a substantial component toward the rocket center. This causes an incipient electron avalanche to migrate toward the rocket center, where it fizzles for lack of neutral density. However, the magnetic field can play a role in reducing this effect. In the case of the cell with maximum diagonal secondary production, the magnetic field (for science attitude 1) deflects electrons toward the rear of the rocket. Still, on average, secondary electrons are produced nearly five inches from the site of primary emission. For a neighboring cell located similarly and symmetrically, but for which magnetic deflection is toward the top of the rocket, displacement of secondary production grows to seven inches.

31

For the most interesting surface cell, we also calculated the quadratic ion production, i.e., ions produced by ionization-produced electrons. The number of quadratic ions (see Table 4) was, for this density, greater than the number of first generation ions.

Table 4

For cell with maximum likelihood of breakdown:	
Direction	Nearly along flow direction
First generation ions	1.36
First generation sec. electrons	1.2
Diagonal sec. electrons	0.91
Mean ion impact distance	5.5 cm
Mean secondary production	11.7 cm
Second generation ions	1.75
For neighboring cell (magnetic field effect)	
Mean ion impact distance	8.85 cm
Mean secondary production	17.7 cm

6.2. Two Dimensional Breakdown Calculation

Two-dimensional calculations of breakdown induced by nozzle flow were done using the Gilbert code. The purpose of these calculations was to develop the experience, techniques, and expertise needed to successfully attack the three-dimensional problem.

The rocket was represented as a sphere with radius 0.57 cm. The neutral density was obtained by taking densities corresponding to the 1 gram per second flow rate nozzle firing tangentially to the sphere, and rotating the densities (in the plane formed by the nozzle axis and the sphere center) about the sphere diameter (passing through the nozzle). (Angle-averaging the density provided by two such nozzles gave insufficient neutral density to cause breakdown.) The neutral species was N_2. Electrons were taken with their true mass and with mass enhanced by 100, and runs were done with initial potentials of -3.5 kV and -2 kV.

32

Two new features were introduced for these calculations. First, an energy-dependent slowing down field (for electrons) was developed in order to reproduce the high density side of a Paschen curve. The slowing-down field is

$$E_{slow} = B\,N/\log\,(A/\sigma\,(\epsilon))$$

where

N = Neutral Density [m^{-3}]

$A = 3.43 \times 10^{-20}$ m^2

$B = 1 \times 10^{-18}$ volt -m^2

ϵ = electron energy

σ = ionization cross-section

The second improvement was to introduce an implicit algorithm (similar to those which have appeared in the literature) capable of handling very high plasma densities. The algorithm replaces Poisson's equation with

$$- \text{div}\,[1 + 1/2\,(\omega_p\,(r)\,\delta t)^2]\,\text{grad}\,\phi = \rho_A\,/\,\epsilon_0$$

where ρ_A is the "free streaming" charge density, i.e., the charge density calculated after moving particles at constant velocity for δt. (The plasma frequency is also calculated using the free-streaming densities.) The algorithm consists of (1) doing the free-streaming pre-push, (2) solving for the implicit potentials, and (3) performing the actual particle push. It is not necessary to ever solve for the actual potentials. Particle deposition must be accounted for in the pre-push, but particle emission need not be done in the pre-push.

Table 5 shows the time dependence of the discharge. (Times up to 12 μs are for real mass electrons. The heavy electron run behaved similarly, but with some modest changes in the dynamics.) The run was started with the sphere at -3500 volts and emitting a small current of seed electrons. Significant ion return began at about two μs, and the ion- generated secondaries soon dominated the problem. A peak potential of -120 volts was reached but could not be sustained. The final steady state oscillated about a potential of -850 volts, with excursions of ± 200 V and a frequency of about 20 kHz.

33

Table 5

Time [μs]	
0	Sphere at -3500 volts
2	Significant ion return current begins
6	Total space charge peaks
7	Steady ion return current of 20 mA reached
8	Peak ion space charge
9	Ion current begins to drop
9	Peak electron space charge
11	Peak secondary electron current
12	Peak potential of -120 volts
20-60	Mean ion return current of 2.5 mA
25	Total space charge has minimum
70	Equilibrium reached at -850 volts
	Mean secondary emission coefficient ~0.15
>100	Oscillations ±200 V, ~20 kHz

As we expected for the three-dimensional case, discharge was predominantly along a path passing obliquely through the nozzle plume. A quasi-neutral, dense plasma region was formed where the greatest ionization took place. Figures 26 show the electrostatic potential, ion density, and electron density during the discharge. The regions of high electron and ion density coincide, and a cathode fall region, with increased electric field, is created between the sphere surface and the quasi-neutral region.
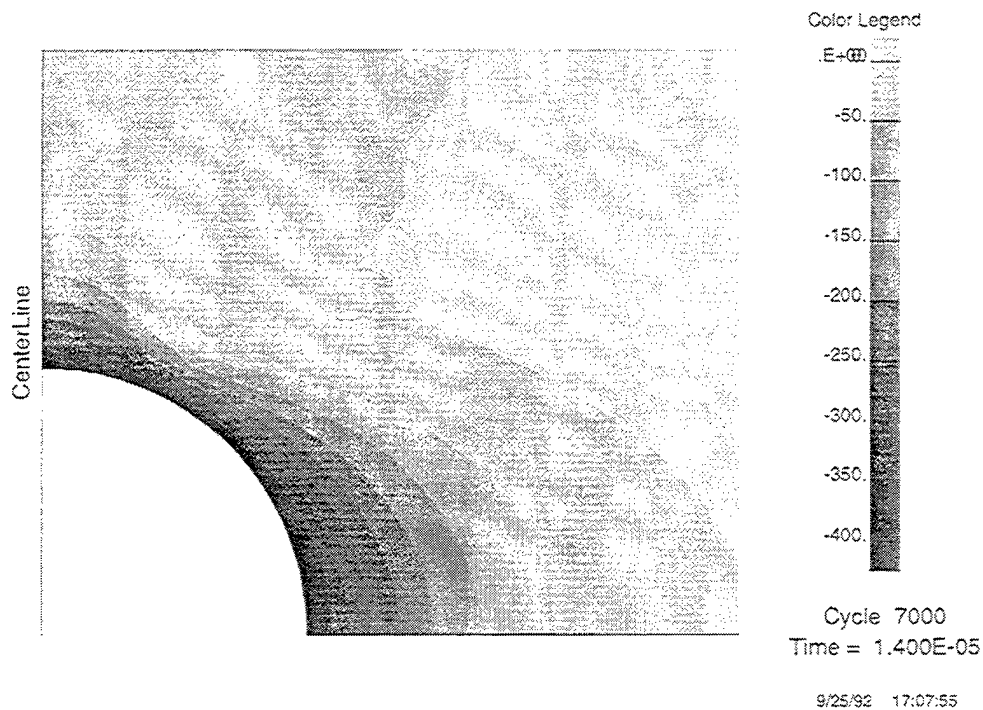
Figure 26. (a) Electrostatic potentials during breakdown, showing localized cathode fall region.
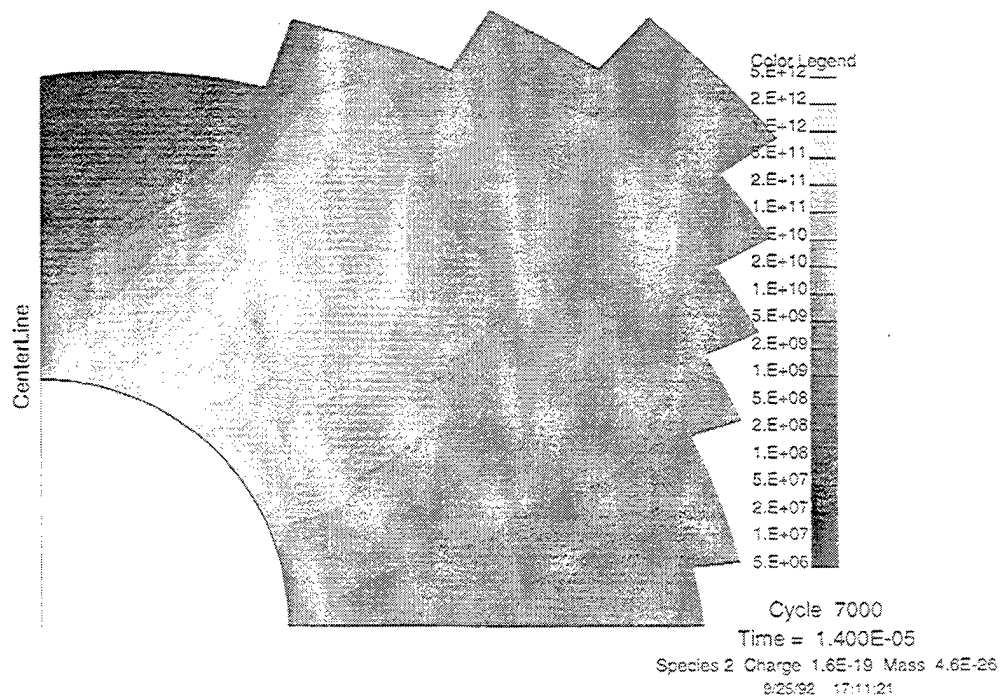

Figure 26. (b) Plasma ion density during breakdown, showing formation of a high density region at an oblique angle to the nozzle flow.
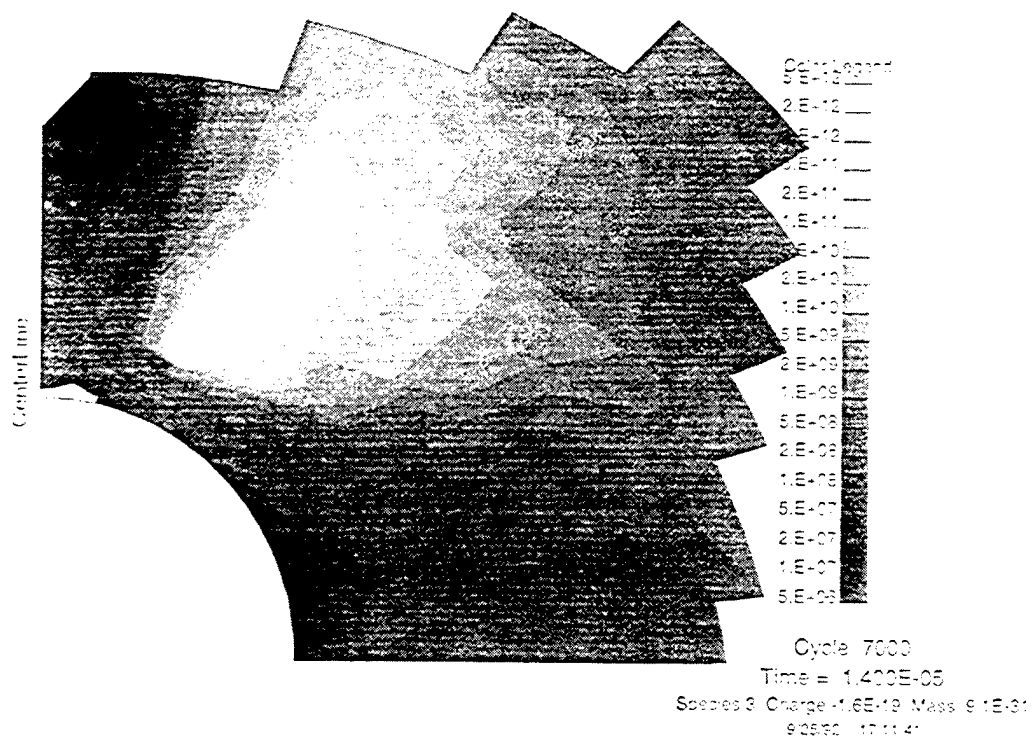
Figure 26. (c) Plasma electron density during breakdown, showing high electron density coincident with the ion density.

6.3. Continuous Slowing Down Approximation

The importance of estimating the required gas flow for the SPEAR-3 neutral gas release system led us to pursue yet another approach to calculating breakdown in the neutral plume (shown in Figure 20). This approach was to calculate the number of electron-ion pairs produced as a result of one electron emitted from the rocket and traveling a radial path (i.e., following the electric field) through the three-dimensional gas plume. The ions produced return to the rocket at low energy due to charge exchange, and thus have a secondary electron coefficient in the range 0.05 to 0.1. If their number is sufficient to reproduce the original electron by secondary emission, breakdown will occur.

Analytic formulas were fit to published cross-section and energy loss data for electron impact on neutral Argon. The ionization cross section fit is

$$\sigma(E) = 1.1 \times 10^{-16} \frac{E - 15.8}{(100 + E)^2} m^2$$

The energy loss fit is

$$L(E) = 4 \times 10^{-16} \frac{E - 12}{100 + E} V\, m^2$$

The electron macroparticles generate electron-ion pairs and loose energy independently.

This approach reproduces the Paschen curves for parallel plate geometry. Figure 27 shows the inverse of the second Townsend coefficient as a function of the the voltage and the column density for the parallel plate geometry.
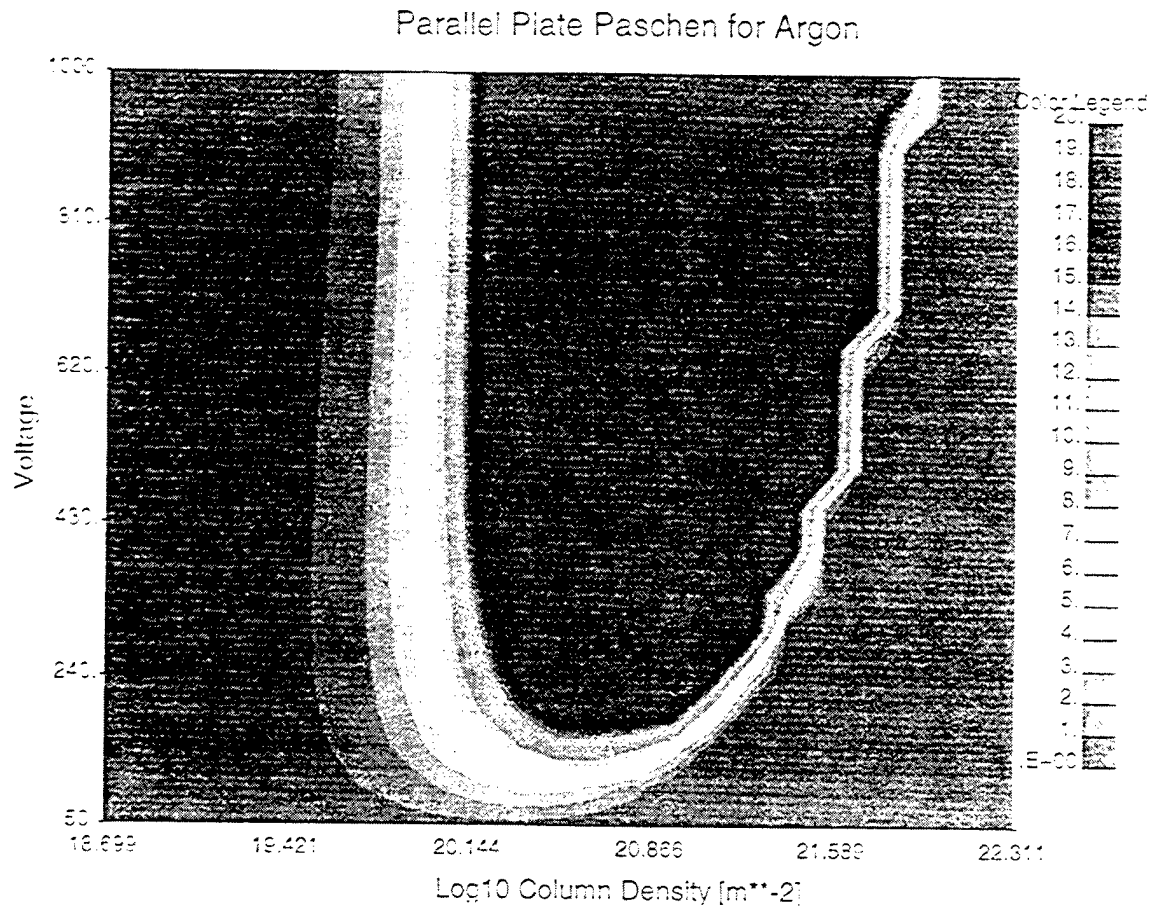
Figure 27. Argon Paschen Profile for the parallel plate geometry using the continuous slowing down approximation.

Using this approach, the second Townsend coefficient was computed for radial electron paths outward from the SPEAR 3 rocket body for various flow rates. The inverse of the second Townsend coefficient for nozzle flow rates of 0.25, 1, and 2 grams per second are shown in Figure 27 as a function of direction and potential.
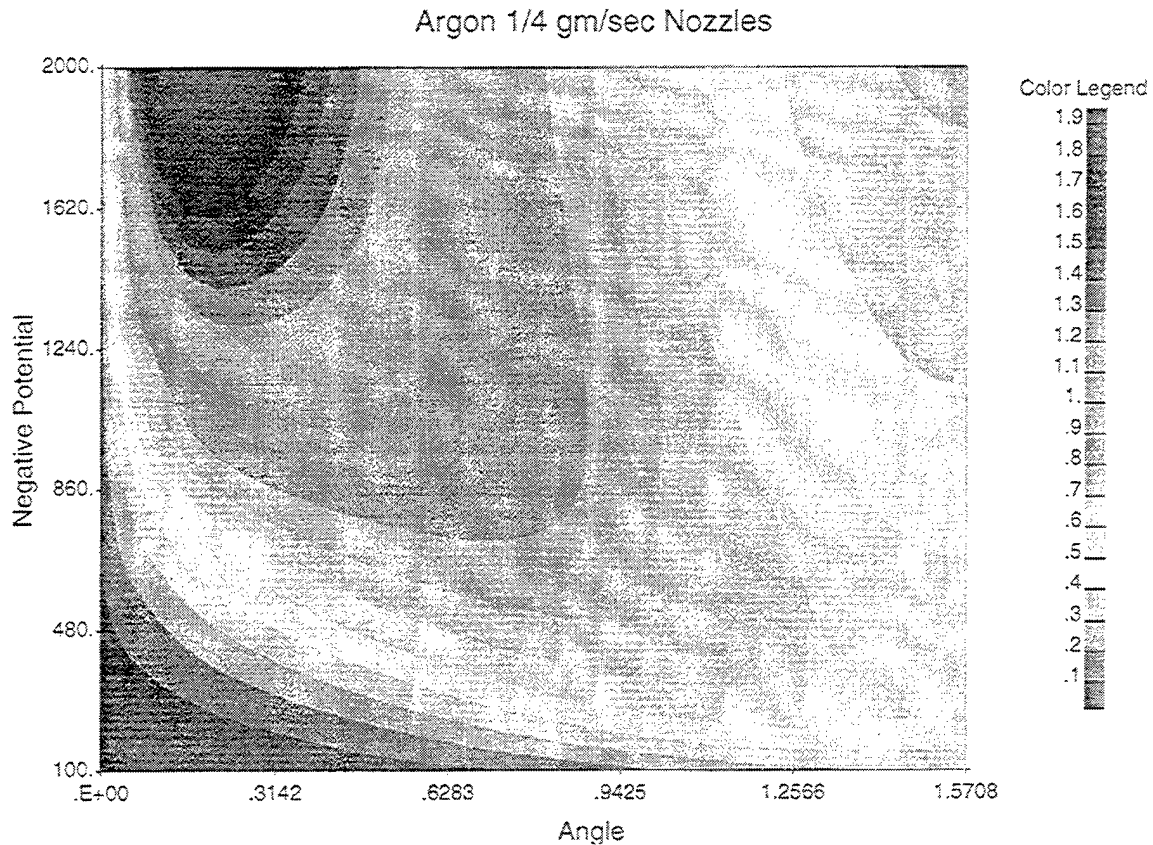
Argon 1/4 gm/sec Nozzles

Figure 28. (a) Inverse of the second Townsend coefficient for a nozzle flow rate of 0.25, 1, and 2 grams per second as a function of the angle from the nozzle location and the potential of the body with respect to the plasma.

The conclusions of these calculations were that (a) A nozzle flow of 2 grams per second per nozzle would be required to produce breakdown and ground the rocket. (b) During such grounding the rocket potential would be held to about 200 volts negative. (c) The breakdown path would occur 90 degrees from the nozzle location, in the direction of the gas flow.
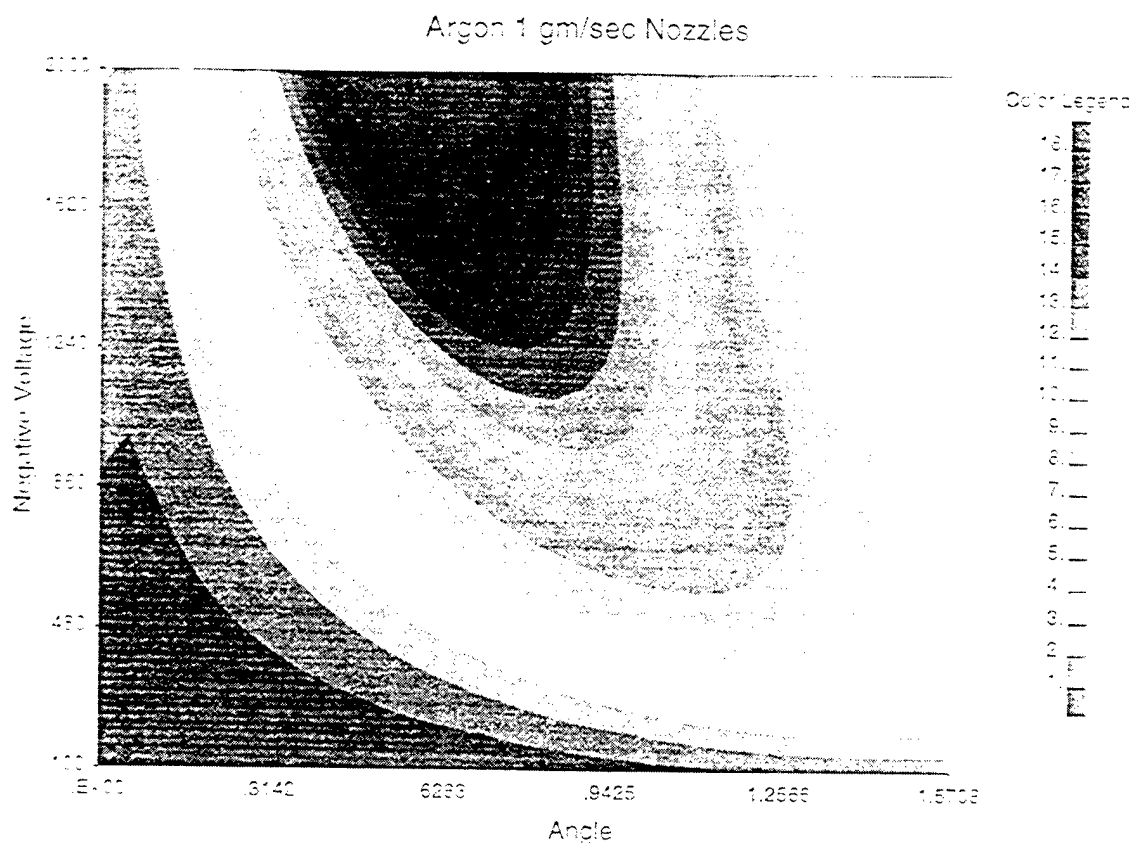
Figure 28. (b) Inverse of the second Townsend coefficient for a nozzle flow rate of 0.25, 1, and 2 grams per second as a function of the angle from the nozzle location and the potential of the body with respect to the plasma.
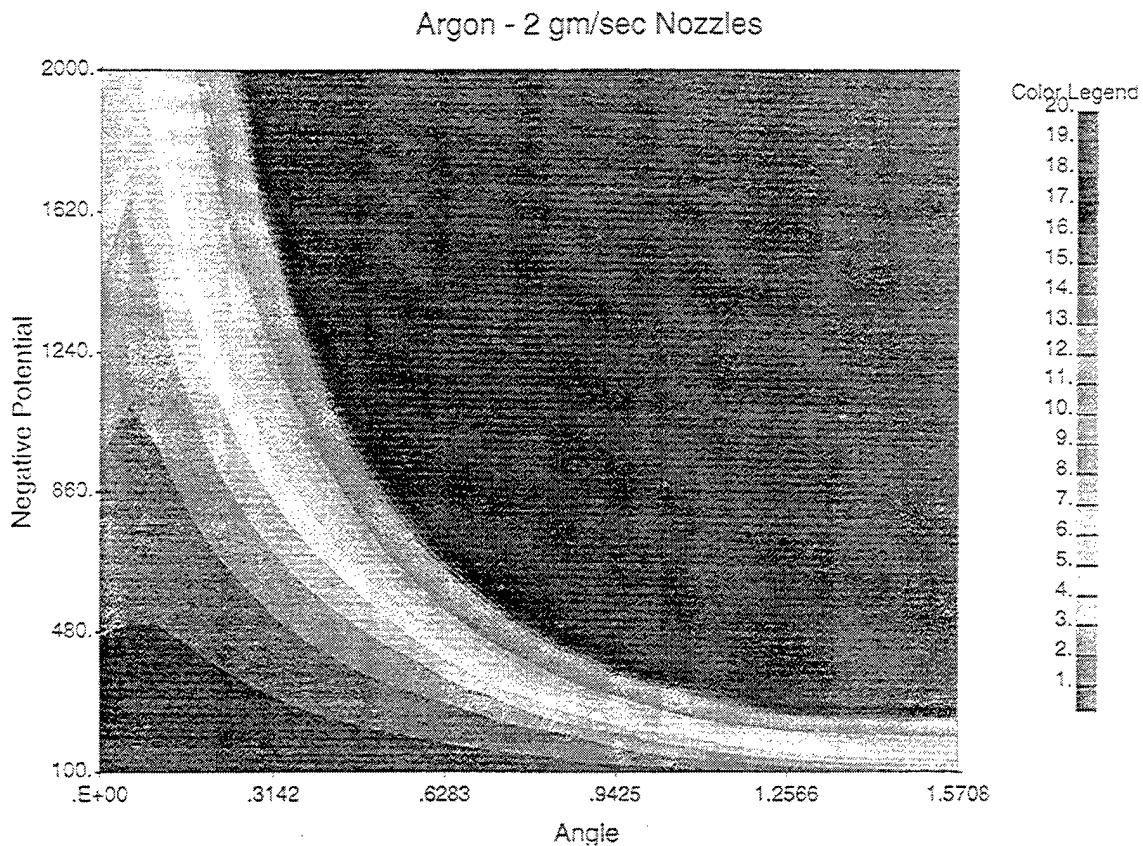
Argon - 2 gm/sec Nozzles

Figure 28 (c) Inverse of the second Townsend coefficient for a nozzle flow rate of 0.25, 1, and 2 grams per second as a function of the angle from the nozzle location and the potential of the body with respect to the plasma.

These results were presented at the SPEAR-3 Mockup Review Meeting, Arlington VA, 2 September 1992, and later at the 1992 American Geophysical Union (AGU) Fall Meeting, San Francisco CA, December 1992. It was strongly recommended that the flow rate be increased from the then baselined 0.5 grams per second per nozzle to 2 grams per second per nozzle. At the project meeting, similar recommendations on the flow rate were made by E. E. Kunhardt (on theoretical grounds), and by J. Antoniades (based on Mockup Test results). The higher flow rate was adopted by the project.

7. SPEAR-3 Mockup Analysis - Floating Potential

The SPEAR-3 Mockup tests took place at Plum Brook Station, Sandusky, Ohio during July, 1992. The material in this chapter was presented at the Mockup Data Review in Arlington, VA, 2 September 1992.

DynaPAC calculations for the SPEAR-3 floating potential in space predict that about 40 percent of the bias potential applied to the sphere will appear (in a negative sense) on the rocket body (Figure 29). We have confidence in these results because the same techniques were able to match the floating potential of SPEAR-I (Figure 30). By contrast, the floating potentials observed in the Plum Brook chamber, in the presence of plasma, were typically near 70 percent of the applied potential (Figure 31). To maintain confidence in the DynaPAC predictions for the space environment, we must identify the factors causing the Mockup test results to be considerably more negative.
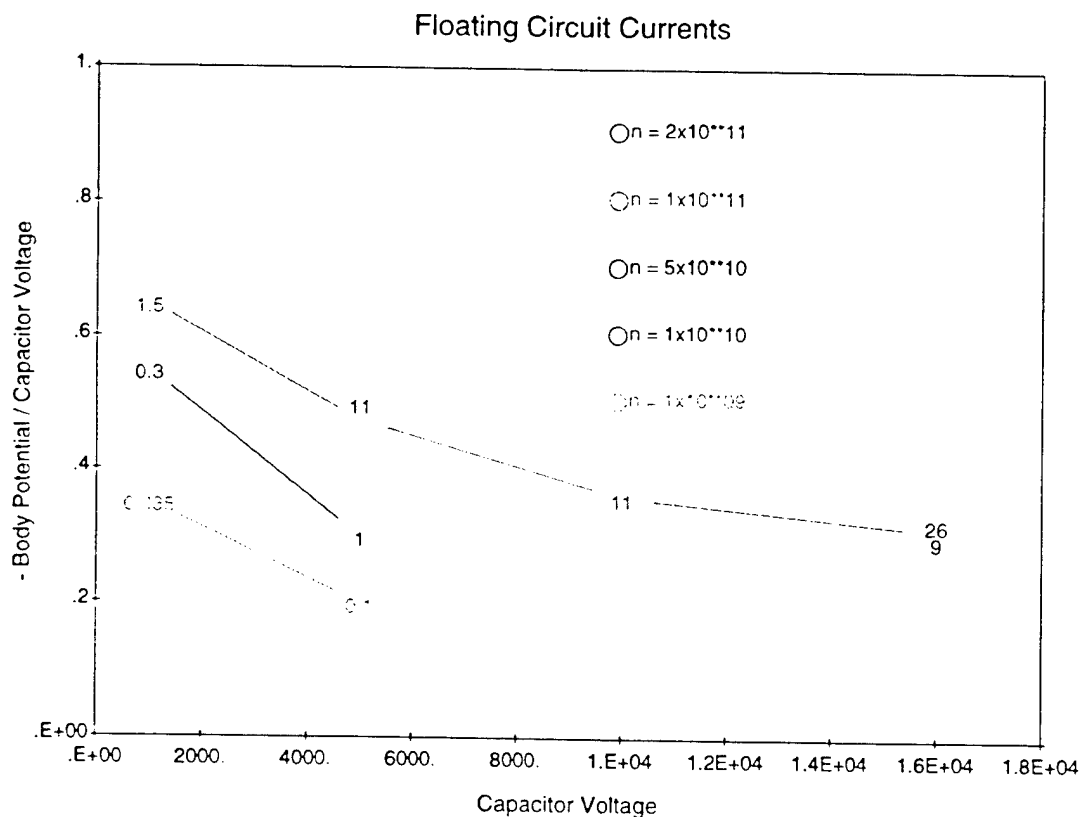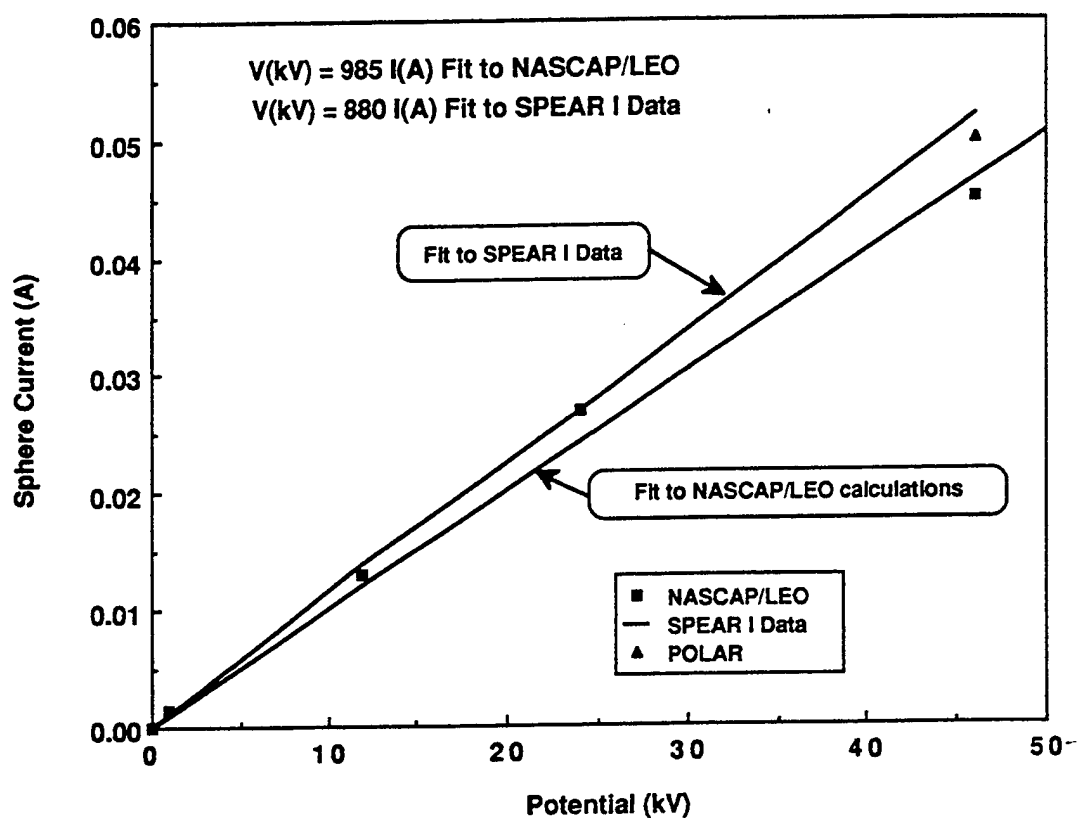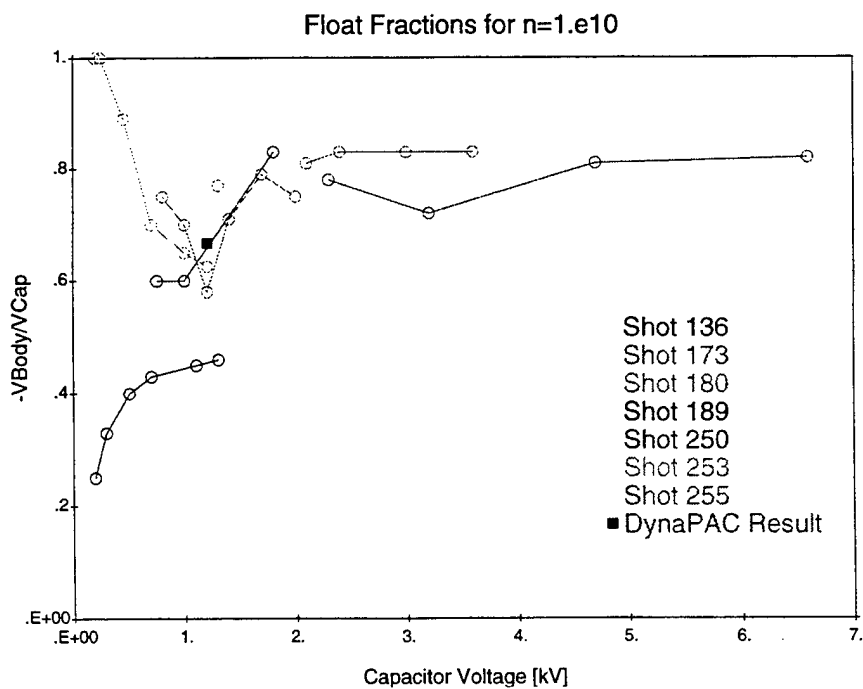

Figure 29.

Figure 30.

Figure 31.

43

7.1. Plasma Differences

The chamber plasma density was representative of space conditions, but was considerably warmer and had heavier ions (Table 6). We can identify three effects directly leading to a more negative floating potential:

Table 6

	Chamber	Space
Plasma Density [m^{-3}]	10^{10} - 10^{11}	(comparable)
Plasma Temperature	1 eV	0.1 eV
Ion Mass	40 amu	16 amu

(a)   The increased ion mass directly reduces incident ion current (by a factor of 1.6), so that the model must go more negative to increase ion current and decrease electron current to meet the floating condition.

(b)   The increased ion mass also reduces the velocity of ions striking the rocket surface, resulting in lower secondary electron emission.

(c)   The increased temperature results in higher current density. Since space charge density (at a given potential) is proportional to current density times the square root of mass, the space charge is increased (relative to space) by the square root of the temperature (a factor of 3). This reduces the size of the ion sheath. The smaller ion sheath directly reduces the ion current. Even more important, the smaller ion sheath is less effective at blocking electron flow into the sphere sheath. Both effects lead to a more negative floating potential.

Table 7 shows four DynaPAC calculations performed with only the plasma conditions changed relative to space.

Table 7.

Sphere Voltage	Body Voltage	Density	Sheath Radius	Current for **B**			Ion Current
				Body	Boom	Normal	
400	-800	1×10^{11}	0.7	6.8	1.9	6.0	0.9
2000	-4000	1×10^{11}	1.0	5.7	3.4	3.4	3.9
400	-800	1×10^{11}	0.8	0.40	0.21	0.35	0.3
1500	-4500	$1 \times 10{11}$	0.5	0.0	0.0	0.0	0.85

In the first three cases, the results indicate that an assumed floating potential of two-thirds negative is plausible, and this is reasonably close to the chamber results and considerably more negative than the space results. For the fourth case (which was experimentally nearly 80 percent negative), the calculation indicates a floating fraction considerably less than the assumed 75 percent. For this case (but not the other three), the ion sheath (Figure 32) is extremely large and totally chokes off the electron sheath.
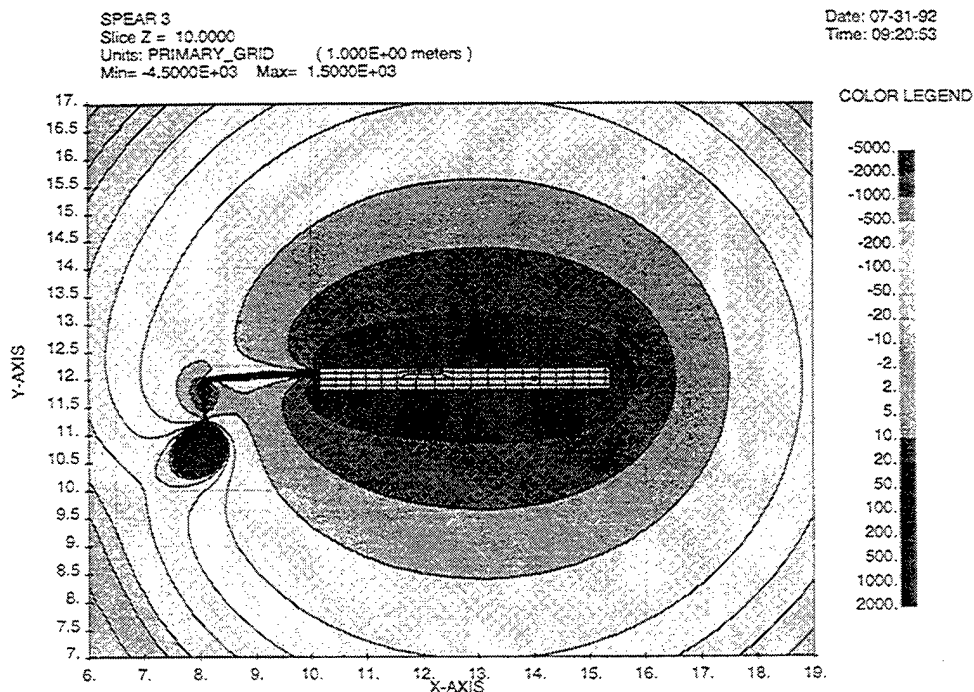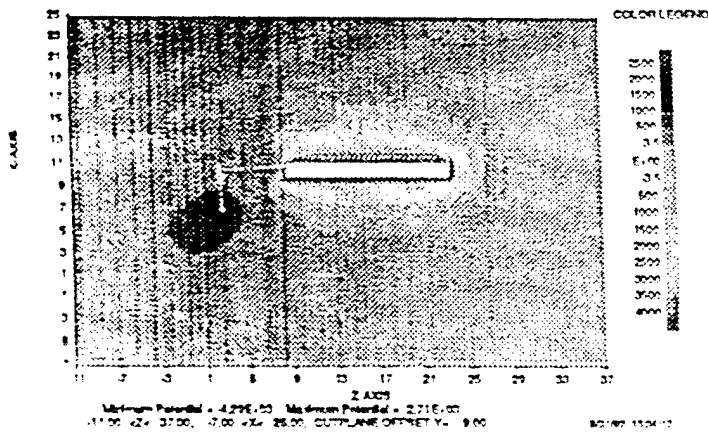

Figure 32.

45

7.2 Chamber Size Effects

The key to the fourth case listed above is that the ion sheath exceeds the size of the chamber. The metal chamber walls serve to confine the ion sheath so that it does not choke off the electron sheath. Figure 33(a and b) shows two NASCAP/LEO sheath calculations for potentials comparable to the fourth case above. With the chamber wall removed (b) the ion sheath engulfs the electron sheath. When the ion sheath is constrained by chamber walls (a) there is ample path for collection of electrons. This means that a more negative (relative to space) floating potential is needed to suppress electron collection by the sphere.

SPEAR 3 Sheath
Plumbrook Chamber B

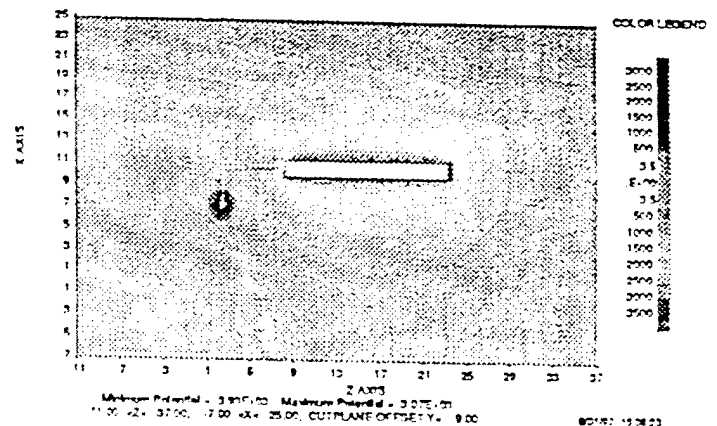## SPEAR 3 Sheath
Without Chamber Wall

Figure 33.

7.3 Ionization Effects

At the vacuum level achieved in the Mockup tests (2×10^{-5} torr) ionization in the electron sheath can cause considerable increase in the sheath size. One-dimensional (radial) calculations show that, for parameters characteristic of the tests and realistic ionization cross-sections, ionization can roughly double the sheath radius, even if the ionization-enhancing effect of a magnetic field is neglected. The calculations indicate that the effect would be negligible if the neutral density were a factor of four lower. This ionization effect provides yet another factor making the Mockup floating potential more negative.

7.4 Sheath Breakdown

Prior to installation of the "Disruptor Plate" the sphere sheath invariably broke down when high voltage was lied under plasma conditions. A DynaPAC simulation was performed to simulate the time development of the breakdown. In the simulation, a 1200 volt bias was lied to the sphere at time zero, leading to a body potential (as in vacuum) of -80 volts. The potential then developed in accordance with collection from a plasma with density 1×10^{10} m^{-3}. The body collected ions in the usual way. The sphere (and boom) collected (a) electrons tracked inward (in the presence of a 0.55 gauss magnetic field) from the sphere sheath, and (b) electrons created by ionization within the sheath (collected instantly). The space charge in the sphere sheath consisted of the tracked electrons and the slowly outward moving ions created within the sheath.

Figure 34 shows the time development of the body potential, which increased roughly linearly in time to nearly -800 volts at 80 microseconds. Figure 35 shows the time development (plotted as a function of body potential) of the components of current to the rocket. The sheath electron current decreases roughly linearly as the rocket goes negative, decreasing the sphere potential. However, the rate of ion production increases nonlinearly after an initial drop. This is because the sphere sheath, which was initially fairly compact (Figure 36a) due to screening by the circulating electrons (Figure 37), is swelled by the presence of slow ions (Figure 36b).
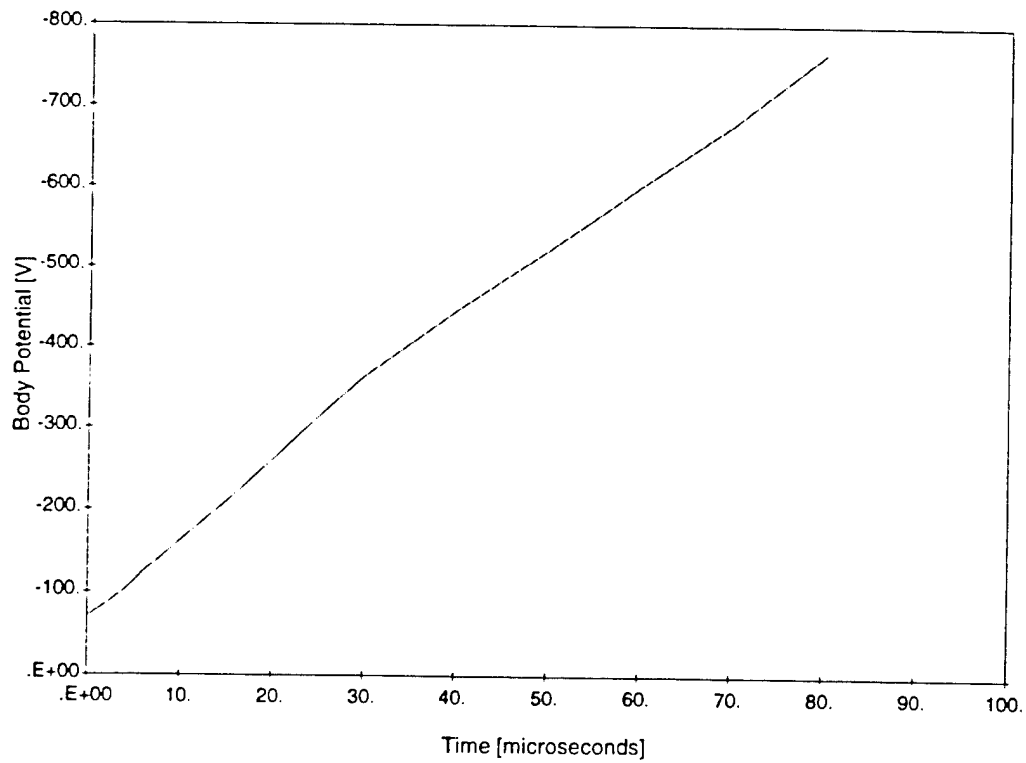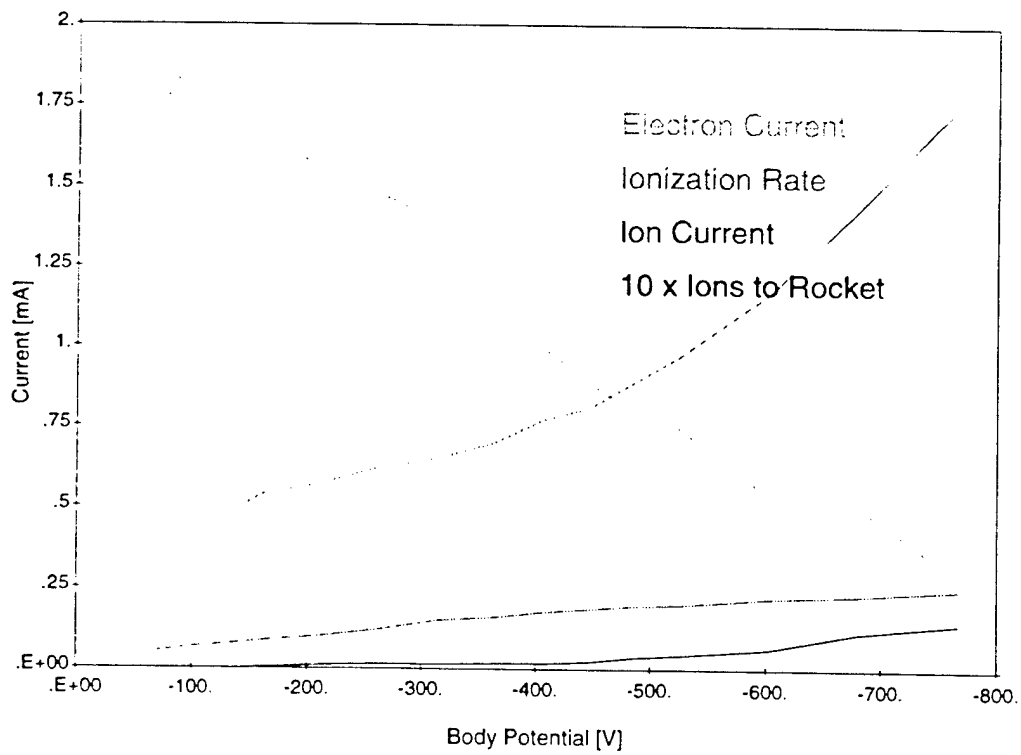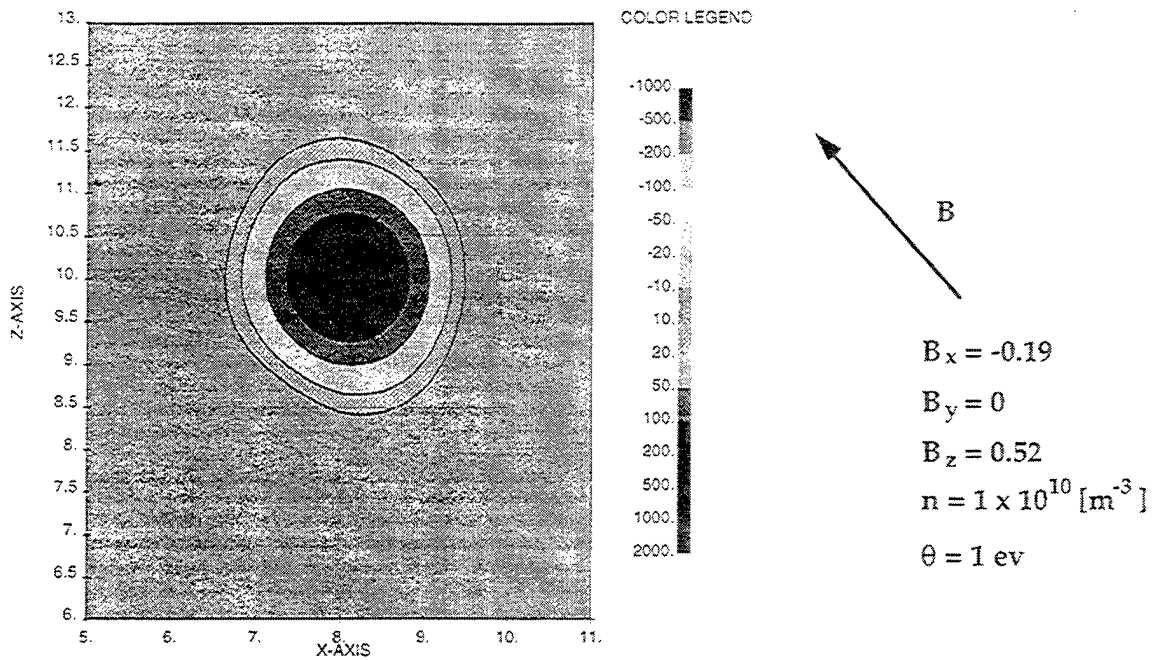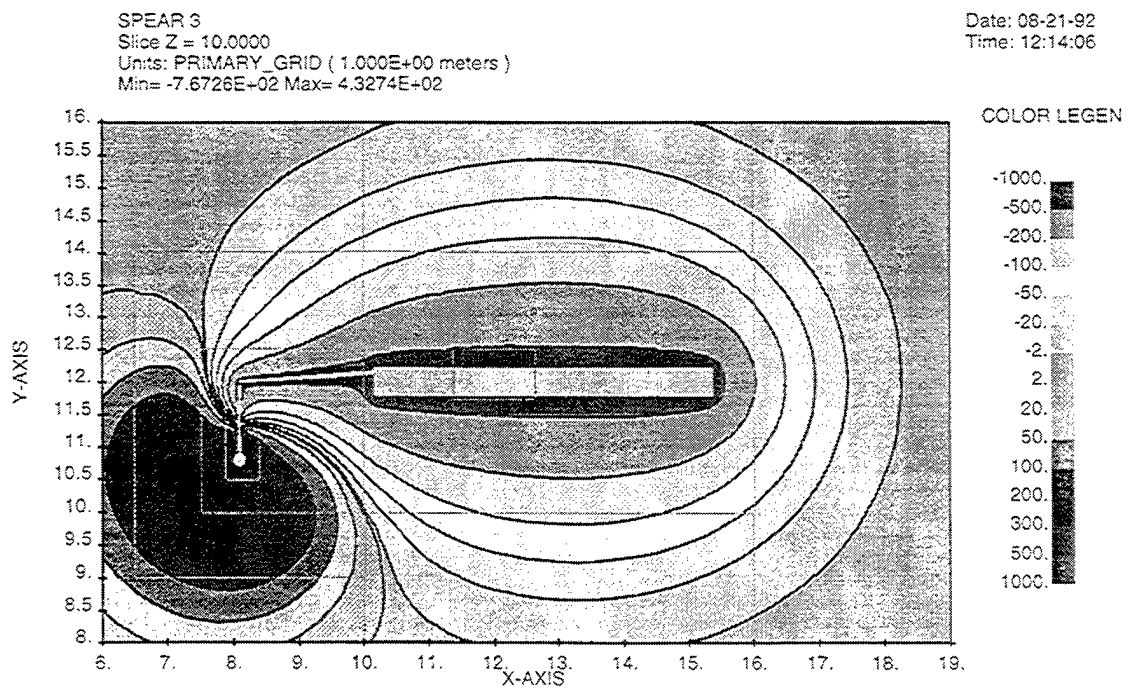
47

Figure 34.

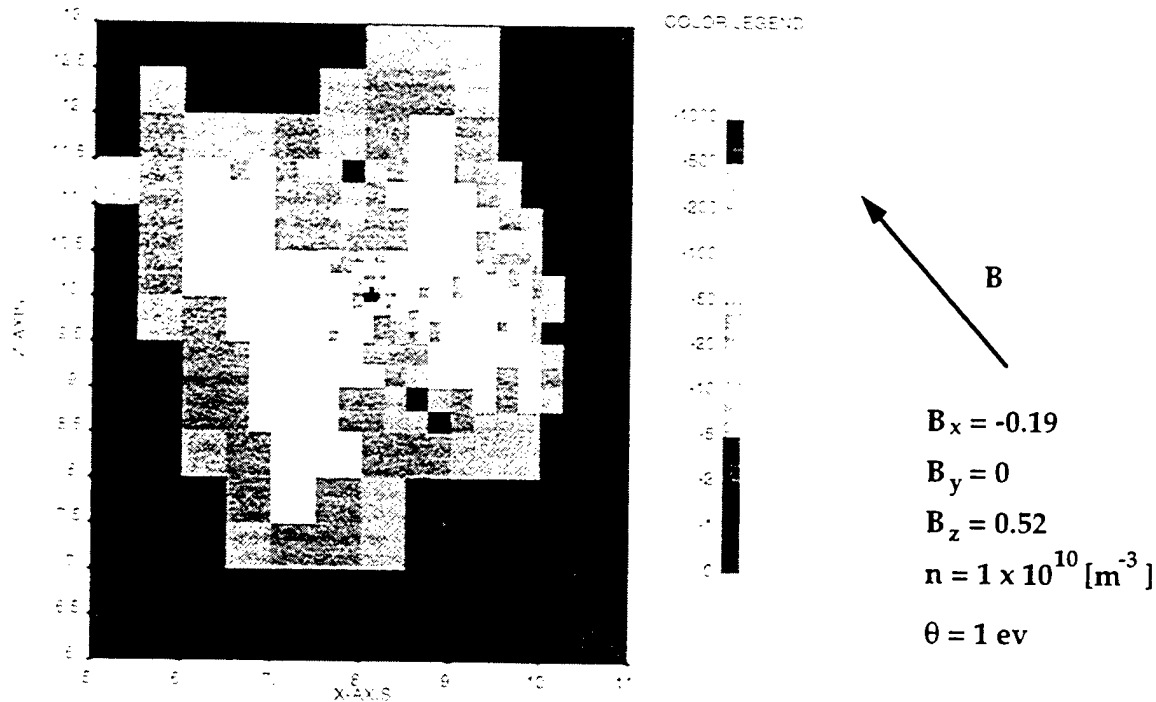**Figure 35.**

48

Figure 36a.

Figure 36b.

Figure 37.

While there is much to criticize about the way this calculation was done, we feel that it provides good insight into the breakdown invariably observed in the chamber. The breakdown mechanism is swelling of the sphere sheath due to ionization of the ambient neutrals by accelerated plasma electrons. If the chamber vacuum were an order of magnitude better, these breakdowns would not have taken place.

7.5 Breakdown Quenching by the Disruptor Plate

The artifice which brought success to the Mockup tests was placing a grounded "Disruptor Plate" in the path of the circulating electrons. The rationale was that electrons would no longer make many $E \times B$ orbits, reducing the rate of ion production.

We performed DynaPAC and NASCAP/LEO calculations, with and without the disruptor plate, to examine the mechanism of discharge suppression. We were led to the conclusion that the proposed mechanism was not valid because:

(a) Few electrons made multiple $\mathbf{E} \times \mathbf{B}$ orbits in any case;

(b) Many electron orbits missed the disruptor plate;

(c) By Gauss's law, the total sheath electron charge could not be much affected by interruption of the $\mathbf{E} \times \mathbf{B}$ orbits;

(d) Calculations showed that the initial rate of ion production was not significantly affected by the presence of the disruptor plate.

We then proposed that the primary mechanism of discharge quenching by the disruptor plate was purely electrostatic. The plate provided a ground plane near the outer edge of the sheath, which prevented the sheath from swelling, as the ions would be neutralized by image charges on the disruptor plate. Calculations indicated that the disruptor plate reduced the effective charge of ions by about two-thirds.

We also noted that vacuum conditions were apparently better during the test series with the plate, as evidenced by improvement in the vacuum breakdown behavior of the body sheath (which cannot be attributed to the plate's presence).

We concluded that the supression of sphere breakdown was due primarily to the electrostatic effect of the plate in preventing the sheath from swelling, secondarily to improvement in vacuum conditions, and only in a minor way to perturbation of electron orbits by the plate.

8. Statistical Analysis of CHAWS Flight Data

The purpose of the CHAWS experiment is to determine the current to a high potential object in the wake of another object. The collected current depends on the geometry of the two objects, the distribution of potentials on the two objects, the plasma environment, the orientation of the objects with respect to any motion of the plasma, and the presence and direction of sunlight. Our hope is that an examination of the role of each of these parameters in the WSF/CHAWS system will provide insight into the role of these parameters in other systems.

8.1 Relevant Parameters

First, we consider how many of the above parameters are directly measured and how the rest are related to directly measured quantities.

The geometry of the CHAWS system is fixed and known.

The distribution of potentials depends on the applied bias, the floating potential of WSF, and the magnitude of $\mathbf{v} \times \mathbf{B} \bullet \mathbf{L}$ at each location referenced to WSF. The applied bias is directly measured. The floating potential at the location of the CHAWS ram side detector along with the plasma environment and the WSF orientation determine the distribution of counts in energy in the ram side detectors. The energy at which half of the incoming particles are rejected can be used as an estimate of the floating potential. The floating potential is determined by $\mathbf{v} \times \mathbf{B} \bullet \mathbf{L}$ referenced to the shuttle, the plasma environment, the presence and direction of sunlight, the applied bias, and the attitude of WSF and the shuttle. The most important parameter in determining the floating potential is $\mathbf{v} \times \mathbf{B} \bullet \mathbf{L}$ referenced to the shuttle. This quantity is computed from the known shuttle velocity, the measured magnetic field, and the vector distance from WSF to the engine bells. While other surfaces may contribute to current collection, it is assumed that the one value adequately estimates the average. Variations in $\mathbf{v} \times \mathbf{B} \bullet \mathbf{L}$ across WSF are small enough that they can be ignored.

The plasma environment consists of several flowing low-temperature ionic components, low temperature electrons, possible high energy contributions at the highest magnetic latitudes, and ions created in the shuttle environment. No

obvious auroral events were observed. It would be desirable to have separate measurements of the ionospheric O+, ionospheric H+, and shuttle generated plasma components. At present, the only parameter available from the ram side detectors is the overall plasma density.

The orientation of the system components with respect to the ram direction is known. The most important quantity is the tilt of WSF with respect to the ram direction. This is the angle about the axis through the center of WSF perpendicular to the axis that passes through CHAWS. During one period, the wag (the angle about the axis through the center of WSF that passes through CHAWS) becomes significant. Note that the shuttle orientation plays a role in the determination of $v \times B \bullet L$. We ignore other orientational information as less important.

When the CHAWS probe is sunlit and negatively biased, an electron photocurrent on the order of microamperes is generated. For present purposes, we use the sun-WSF angle and eclipse times to estimate the influence of photocurrent.

8.2 Parameters Available From Models

We use the EPSAT computer code to reinforce our confidence in measured quantities and to estimate quantities that are not measured or difficult to determine from the flight data. Figure 38 compares the spacecraft location as measured and as determined by EPSAT's orbit generator. The orbit param- eters used are given in Table 8. The model orbit adequately follows the actual orbit. Figures 38 through 41 show the ionospheric plasma environment as computed by EPSAT using the IRI-90 model extended to higher altitudes. Figure 42 compares the model plasma density with the measured plasma density. Figure 42 shows the spacecraft geomagnetic attitude. Auroral charging is expected only above 65° geomagnetic latitude.
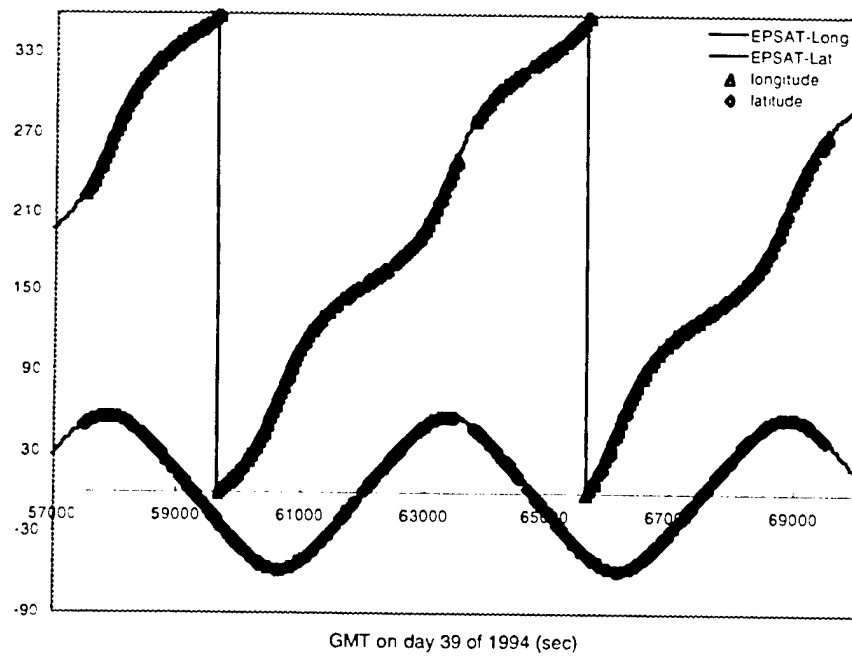
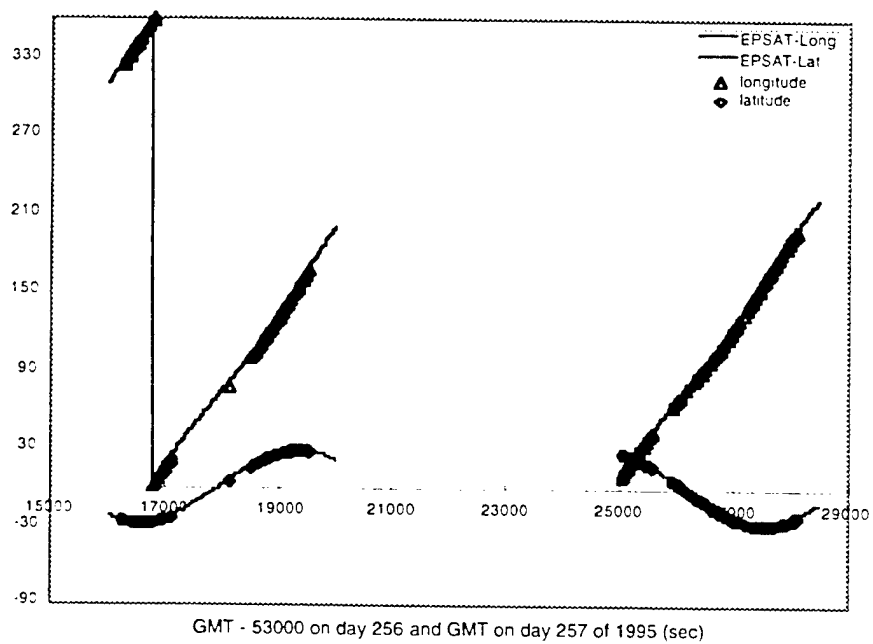**Figure 38.** (a) Spacecraft location as measured and as determined by EPSAT's orbit generator.

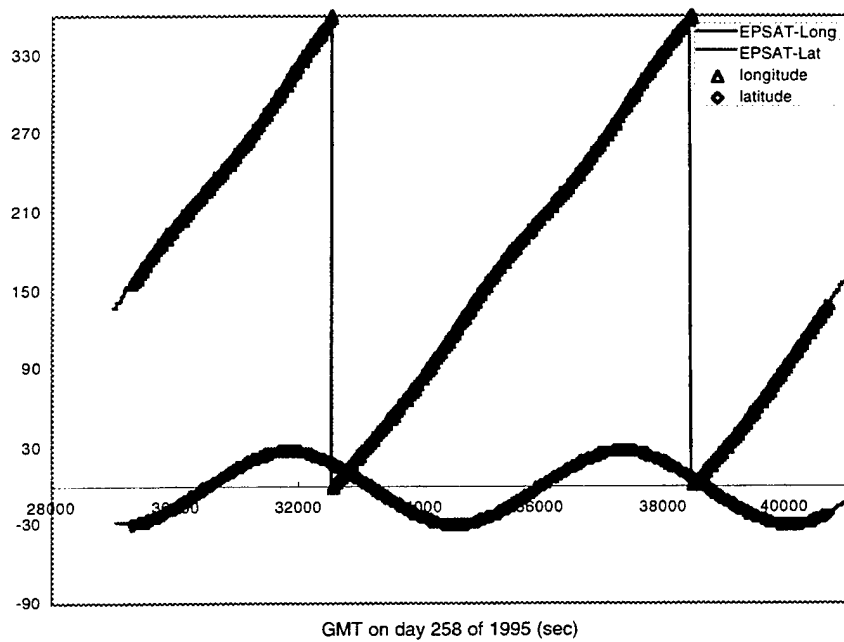**Figure 38.** (b) Spacecraft location as measured and as determined by EPSAT's orbit generator.

54

Figure 38. (c) Spacecraft location as measured and as determined by EPSAT's orbit generator.

Table 8. Model Orbit Parameters

	Flight 1	Free Flight	Flight 2
Effective Time	1994, Day 39 04:03:10	1995, Day 256 10:28:25	1995, Day 258 06:00:37
Apogee	360	409	352
Perigee	345	401	342
Inclination	56.99	28.47	28.47
Mean Anomaly	217.28	63.52	217.08
Right Ascension	195.16	2.5	349.51
Argument of Perigee	275.40	295.51	281.36

55

Figure 39. (a)Ionospheric plasma environment. Densities of the two major constituents as computed by EPSAT from the IRI-90 model.

Figure 39. (b)Ionospheric plasma environment. Densities of the two major constituents as computed by EPSAT from the IRI-90 model.
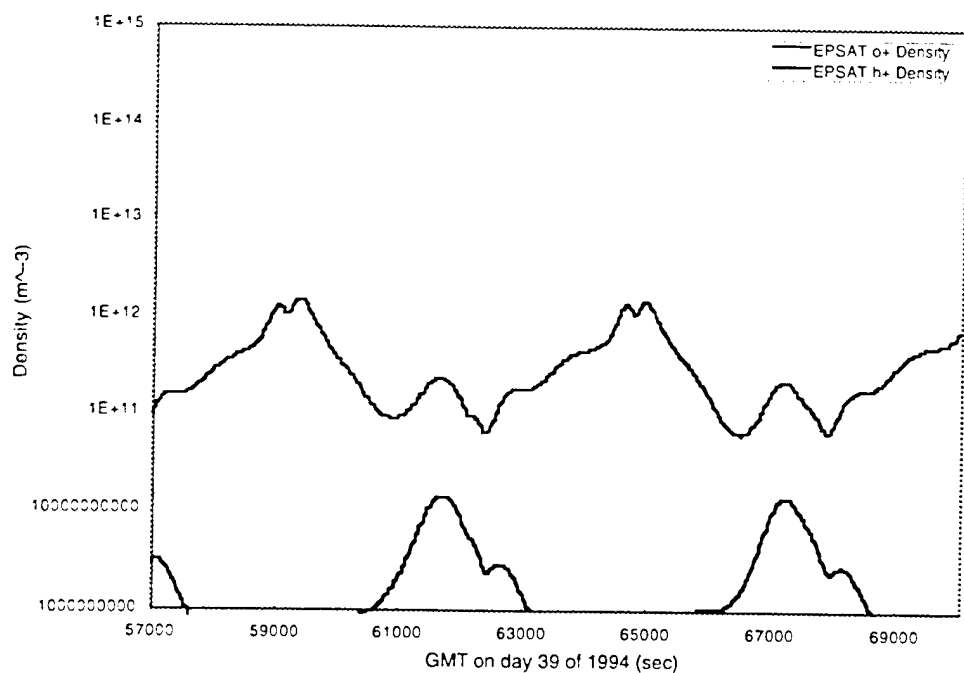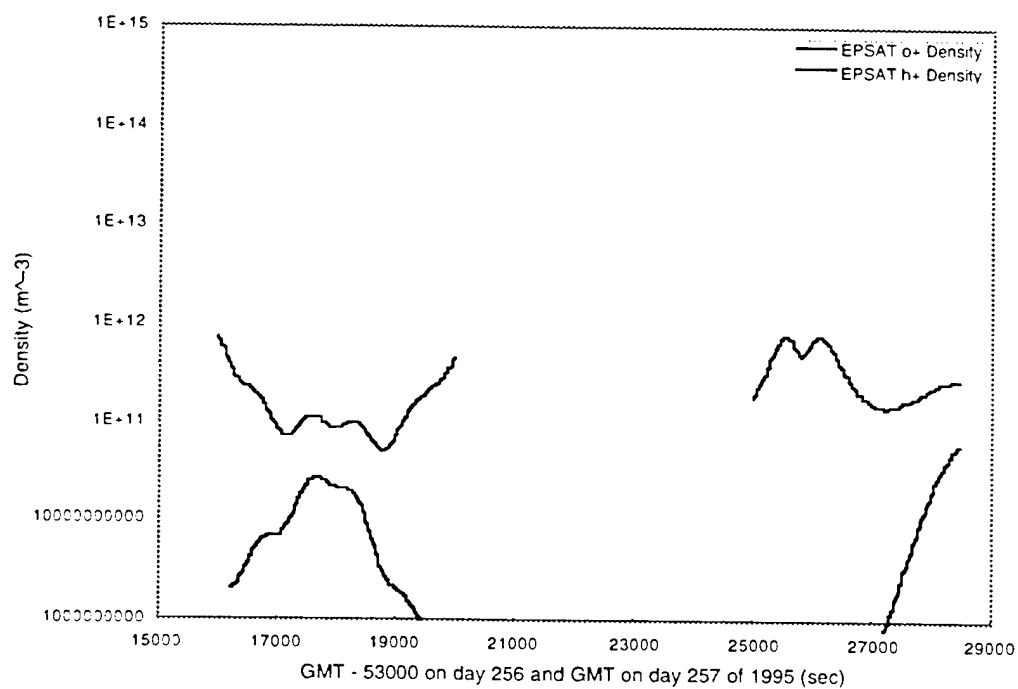
56
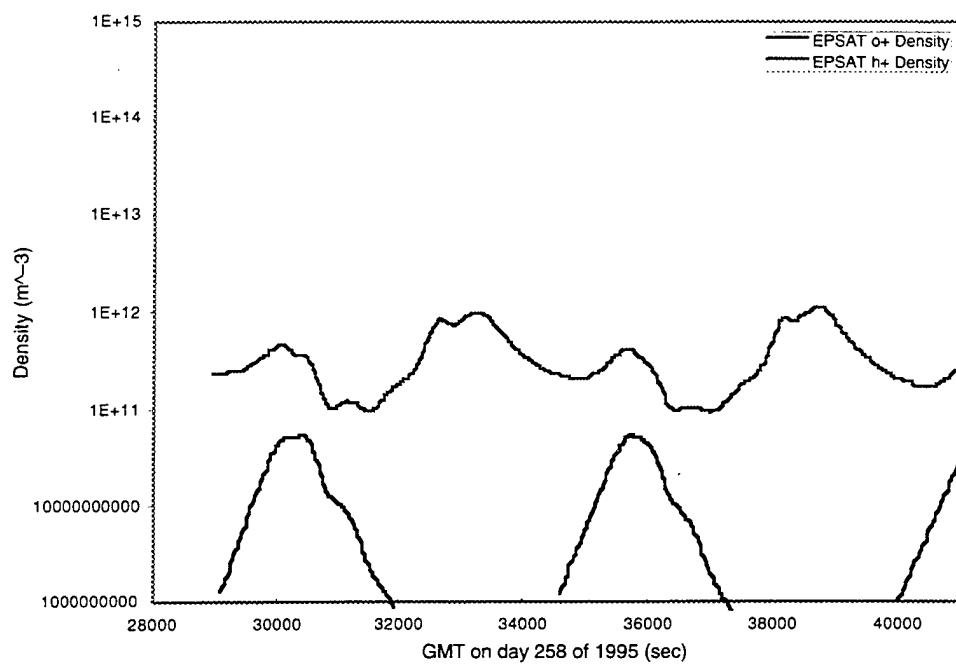
Figure 39. (c) Ionospheric plasma environment. Densities of the two major constituents as computed by EPSAT from the IRI-90 model.

57
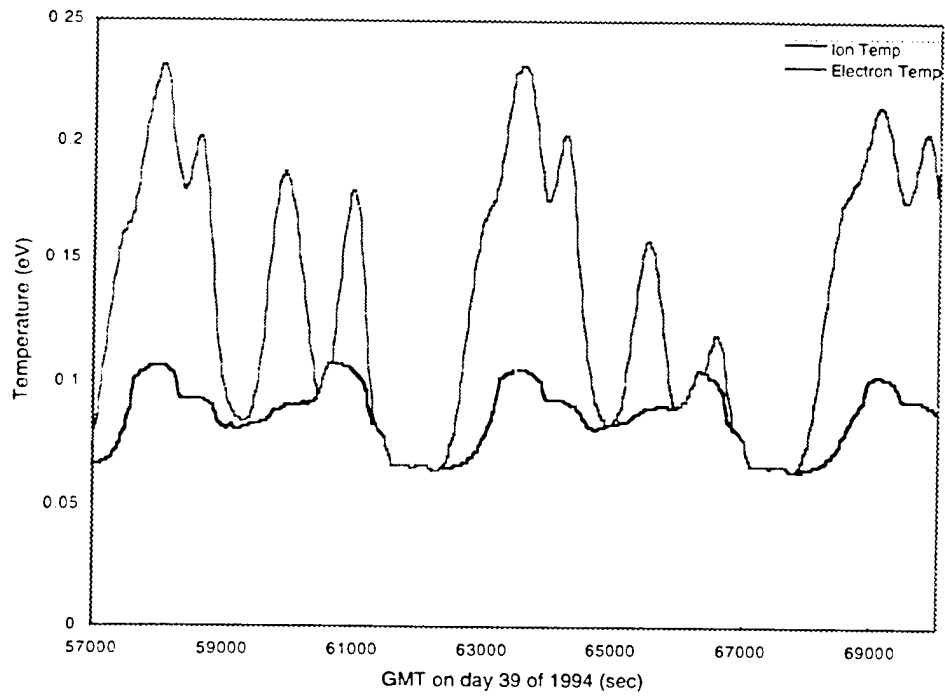
Figure 40. (a) Ionospheric plasma environment. Component temperatures as computed by EPSAT from the IRI-90 model.
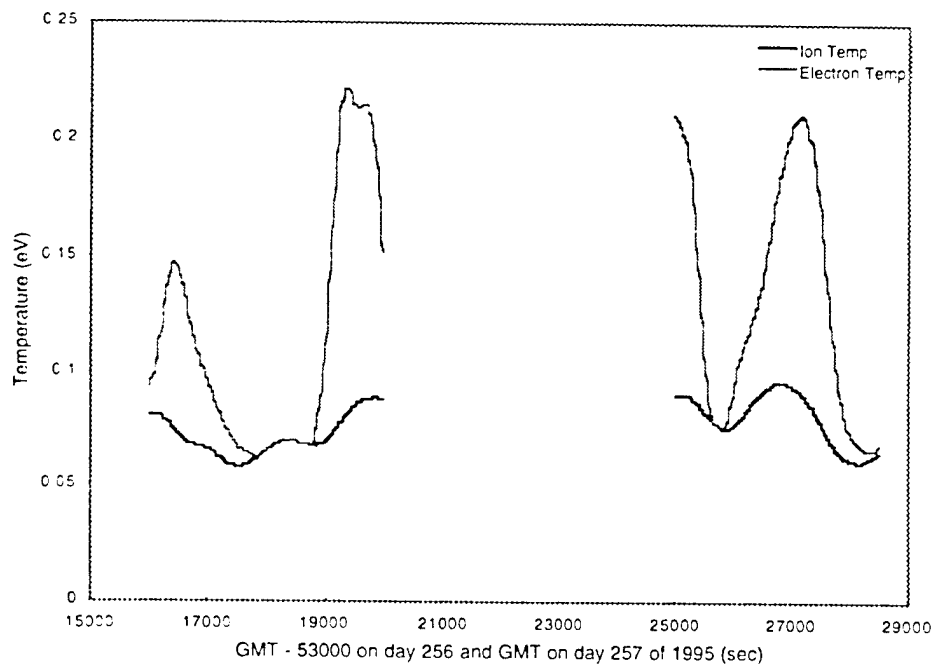
Figure 40. (b) Ionospheric plasma environment. Component temperatures as computed by EPSAT from the IRI-90 model.

58
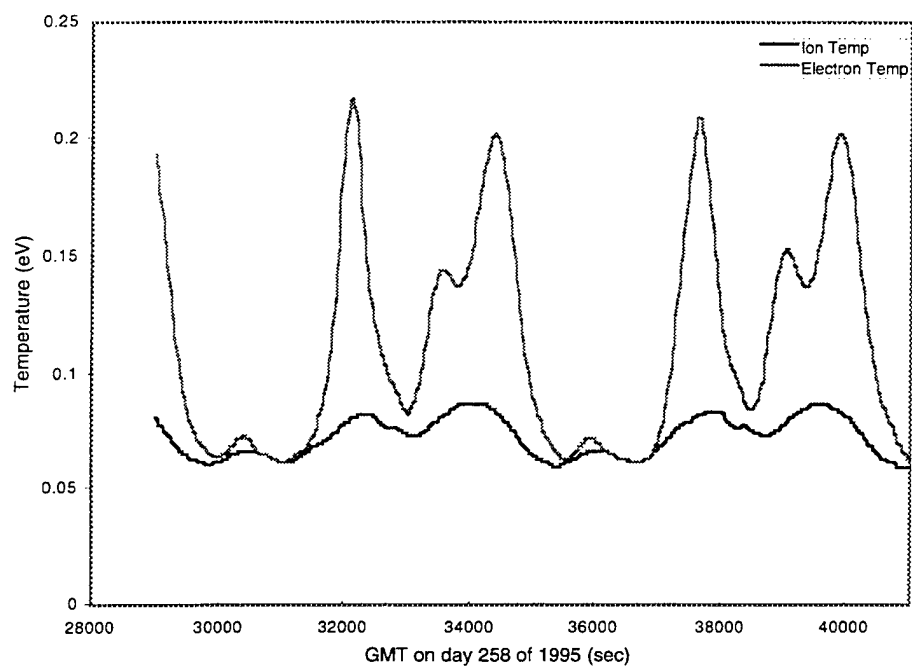
Figure 40. (c) Ionospheric plasma environment. Component temperatures as computed by EPSAT from the IRI-90 model.
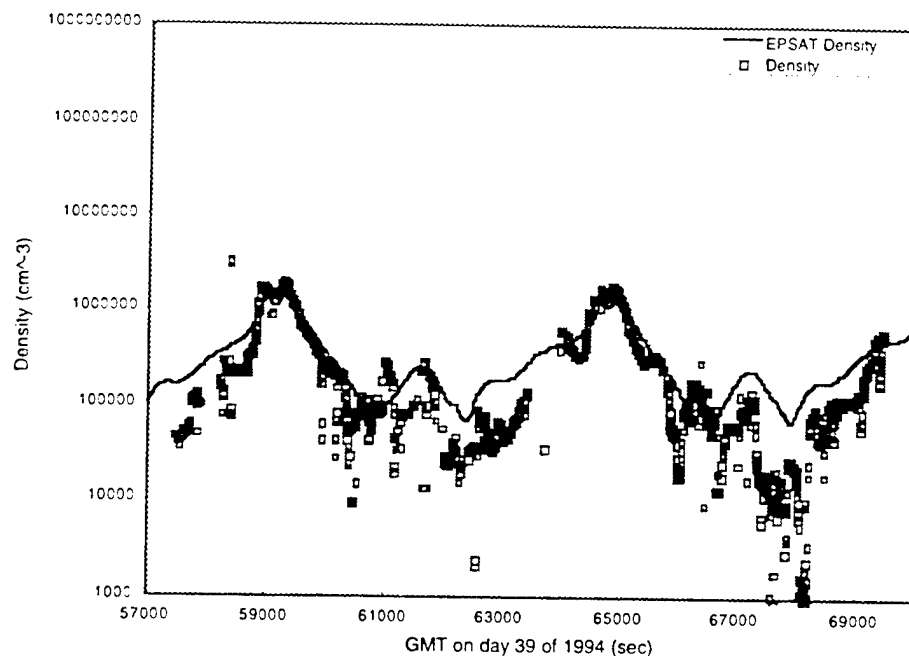
Figure 41. (a) Ionospheric plasma environment. Density as determined from the IRI model with the ram density as measured by the ram side CHAWS detectors.
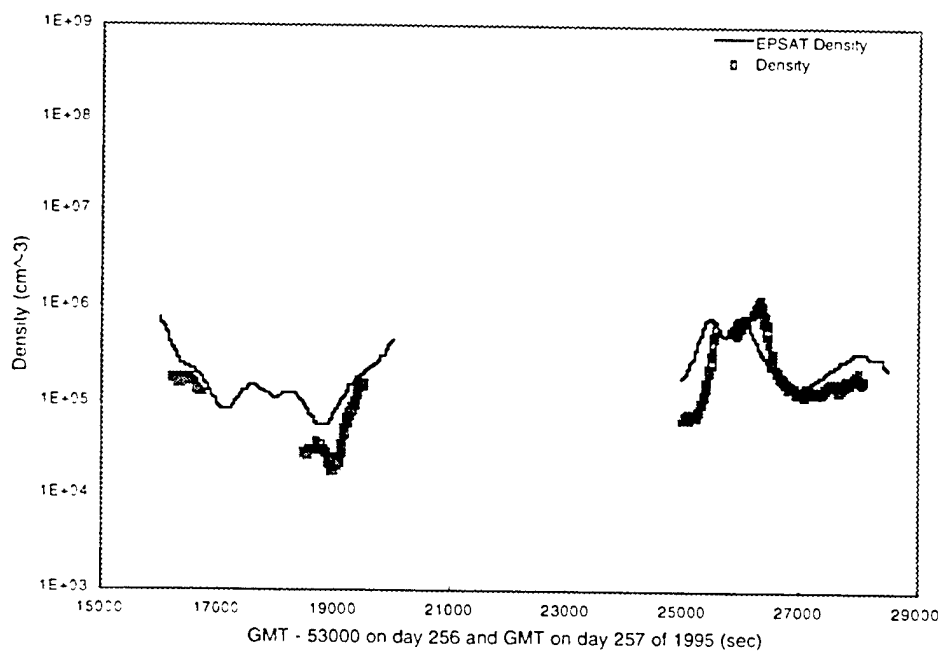
Figure 41. (b) Ionospheric plasma environment. Density as determined from the IRI model with the ram density as measured by the ram side CHAWS detectors.

60
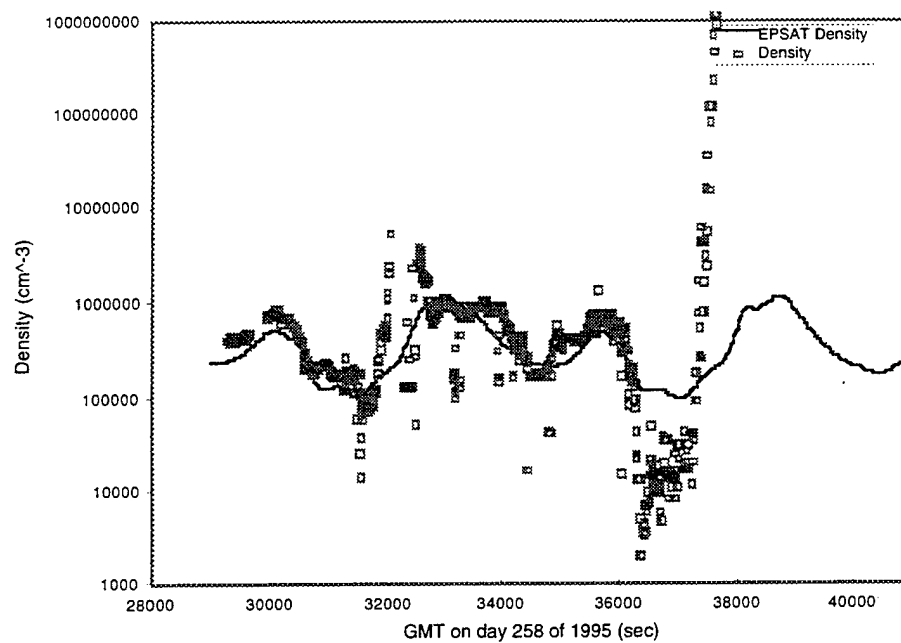
Figure 41. (c) Ionospheric plasma environment. Density as determined from the IRI model with the ram density as measured by the ram side CHAWS detectors.

GMT on day 39 of 1994 (sec)
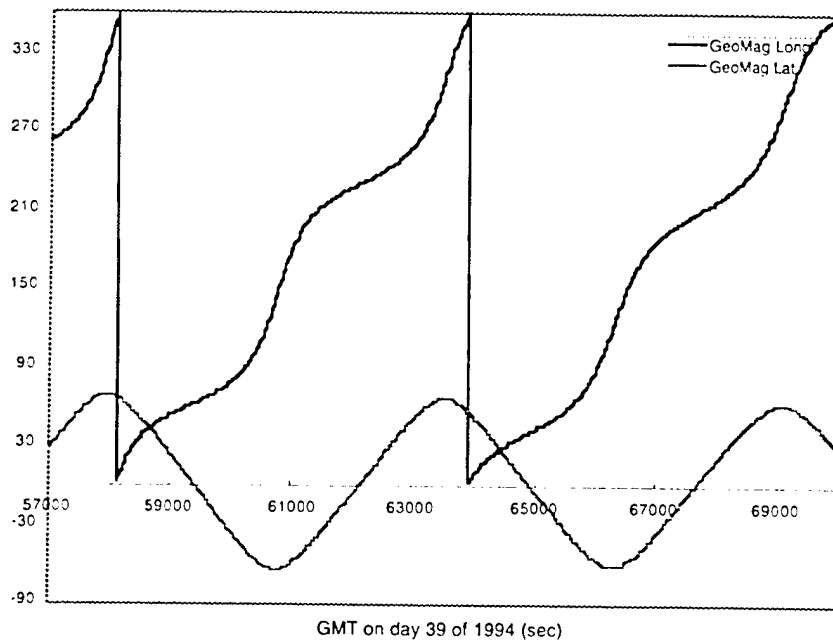
Figure 42. (a) Geomagnetic latitude and longitude of the shuttle. Auroral currents are most likely at the highest geomagnetic latitudes.

GMT - 53000 on day 256 and GMT on day 257 of 1995 (sec)
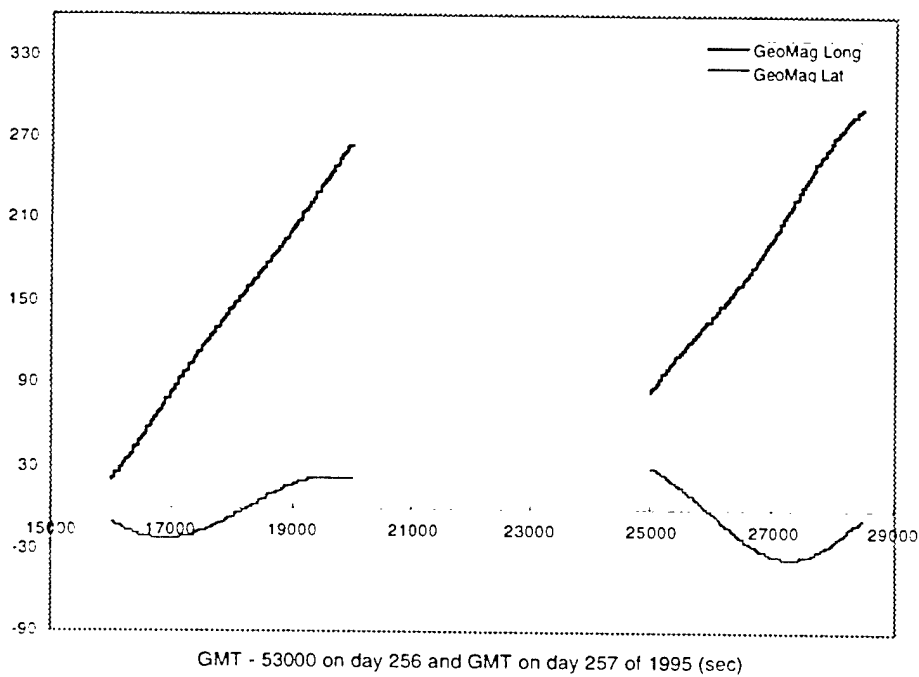
Figure 42. (b) Geomagnetic latitude and longitude of the shuttle. Auroral currents are most likely at the highest geomagnetic latitudes.

62
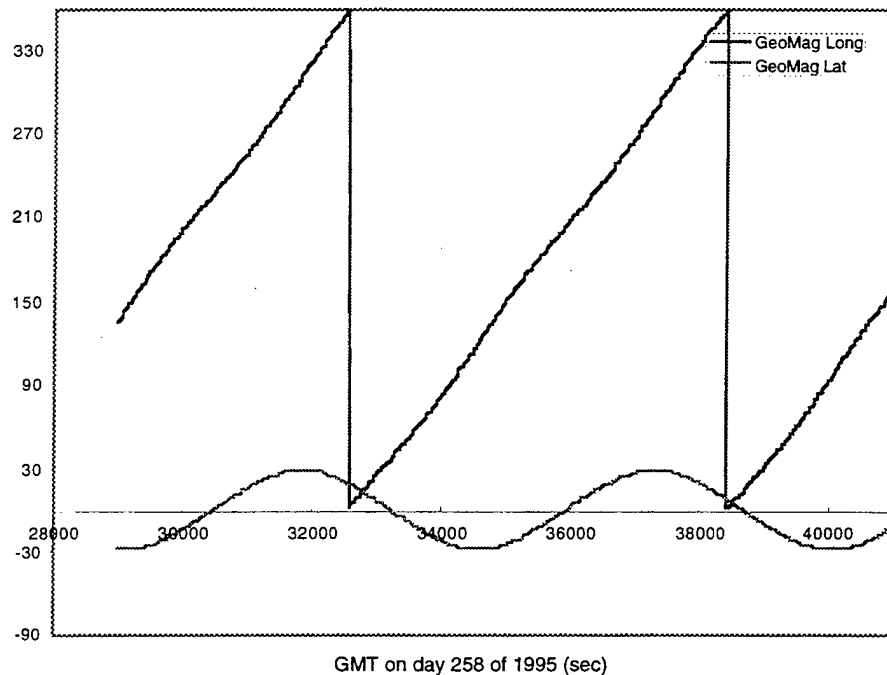
Figure 42. (c) Geomagnetic latitude and longitude of the shuttle. Auroral currents are most likely at the highest geomagnetic latitudes.

8.3. Measured Quantities

We used the chunks program to determine a number of quantities for the time period of interest. We show data for four different time periods. The first time period is Day 39 of 1994 from 57300 s to 70000 s GMT, dedicated CHAWS time during Flight 1. The second time period is Day 256 of 1995 from 69200 s to 72600 s GMT, during free flight. The third time period is Day 257 from 25000 s to 28200 s GMT, during free flight. The second and third time periods are shown together. The fourth time period is Day 258 from 29000 s to 41000 s GMT, dedicated CHAWS time during Flight 2.

The data extracted from the databases is shown in Figures 43 through 50. This includes some not used in the following analysis. The process used to extract this information is described in the Appendix.
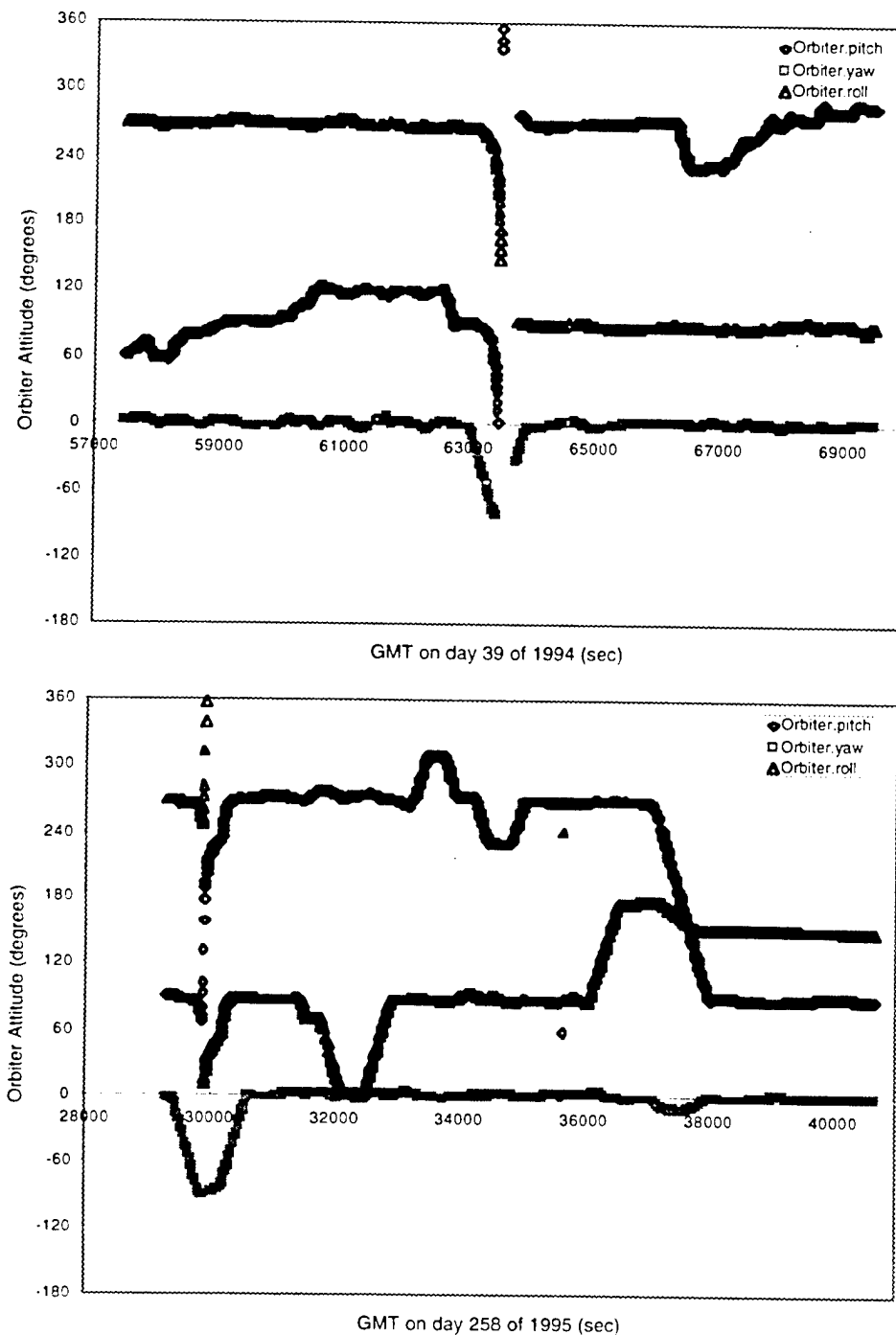
Figure 43. Orbiter attitude was used to control the attitude of WSF. Note that the pitch over maneuver from 63000 s to 63500 s during the first flight changed the WSF floating potential by about 4 V. The maneuver at 32000 s during the second flight placed the wake side probe in the ram. The maneuver at 37000 s placed the WSF in the wake of the shuttle. The RMS arm was used to move WSF into the ram flow for measurements taken after 40000 s.

64
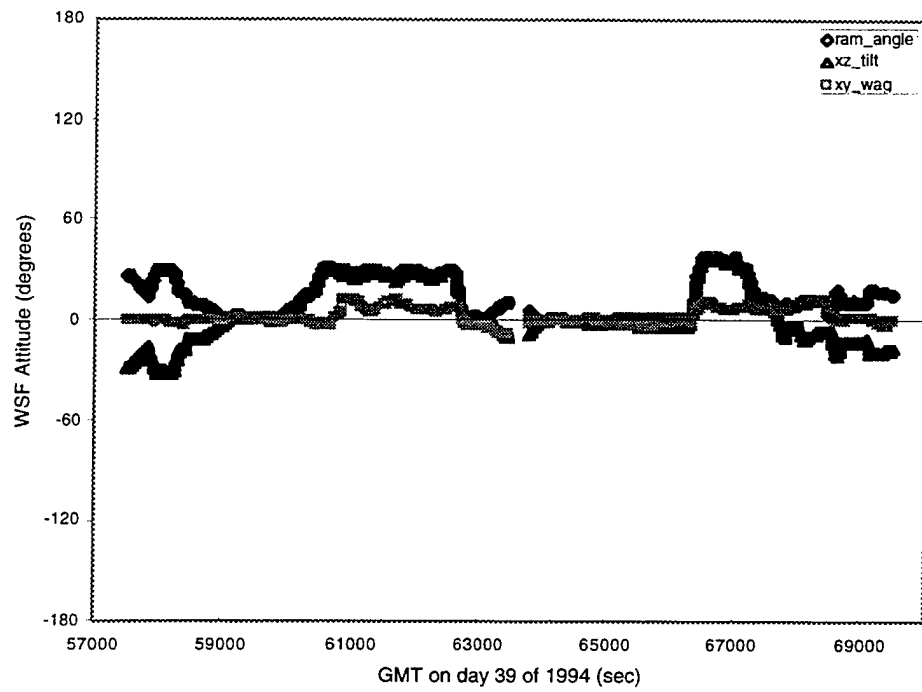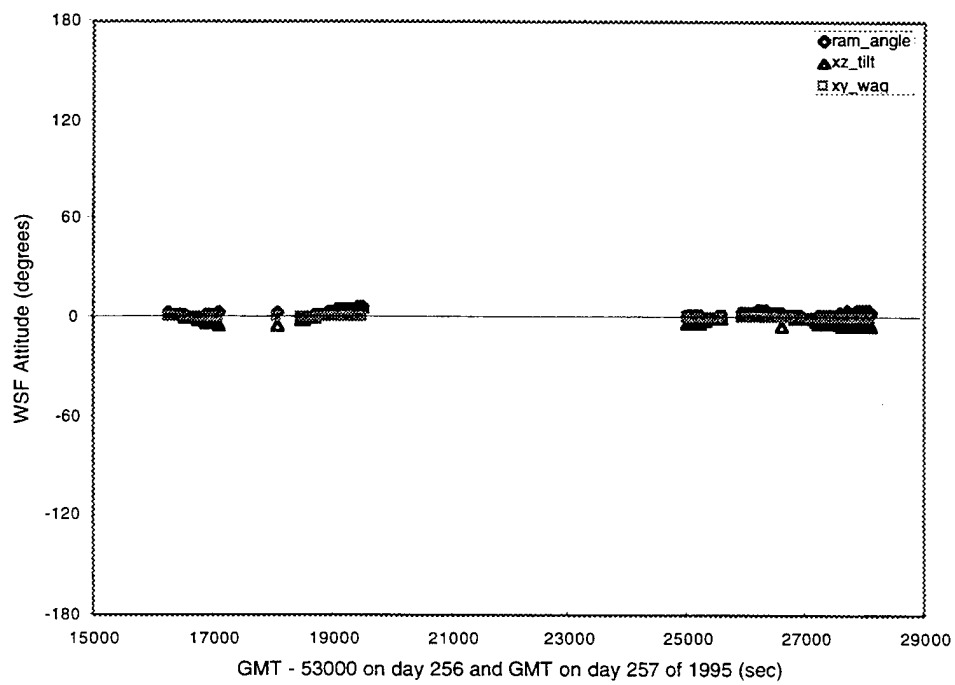
Figure 44. (a)

Figure 44. (b)
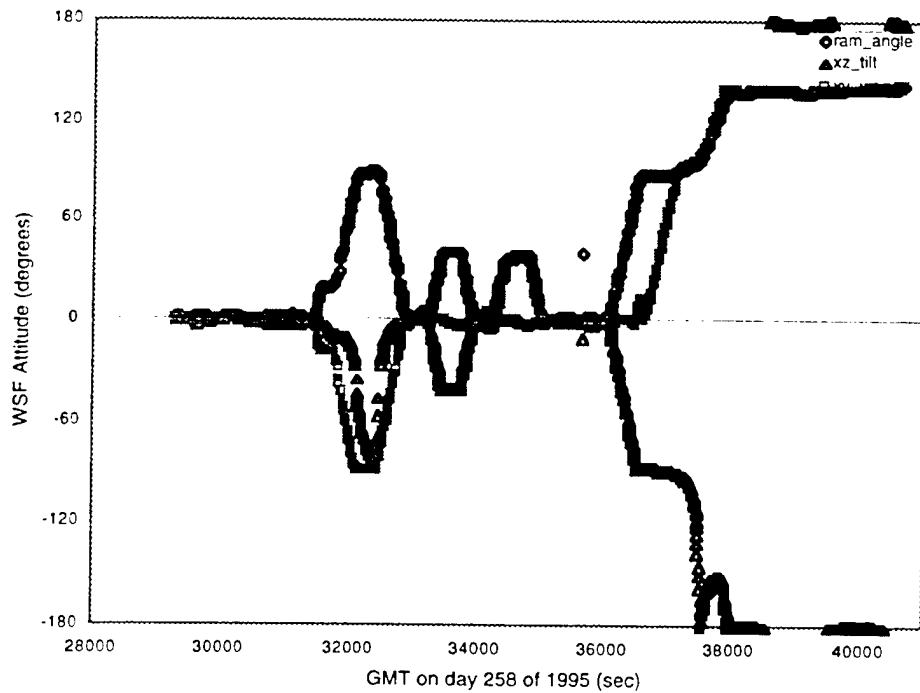
Figure 44. (c) The ram angle is the unsigned angle between the ram direction and the normal to the WSF disk. The tilt is the primary indicator of how much the probe is tilted into the ram flow. Non-zero wag values indicate an increase of exposure to the ram flow. Even at the largest excursions of 10 degrees, this is a secondary effect as indicated by the fact that the ram angle and the absolute value of the tilt closely track. During the free flight period the WSF orientation was nearly constant.

66
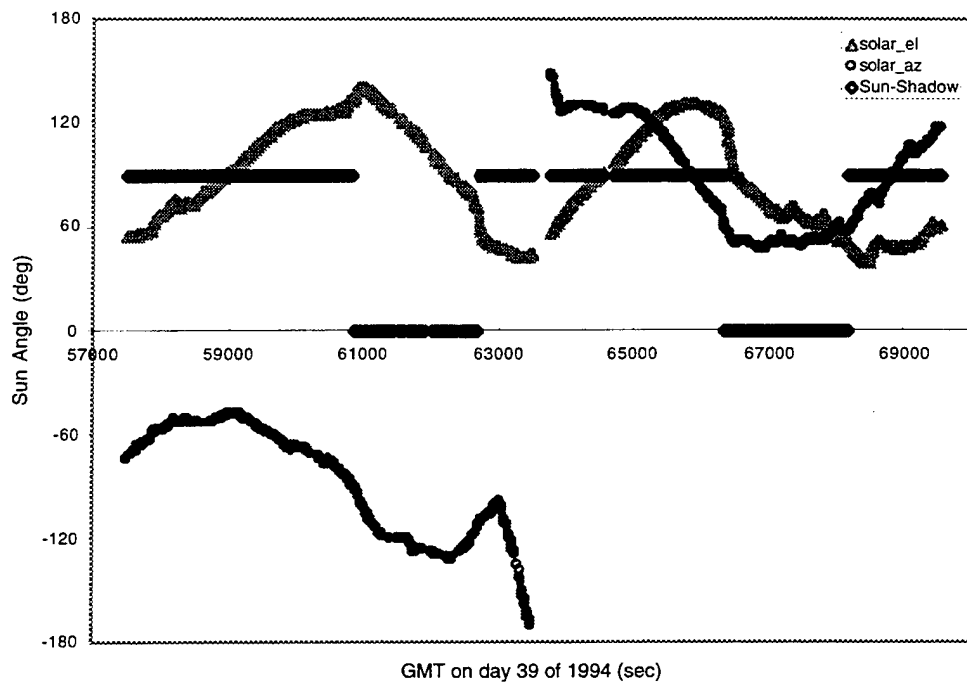
Figure 45. (a) The sun angle.
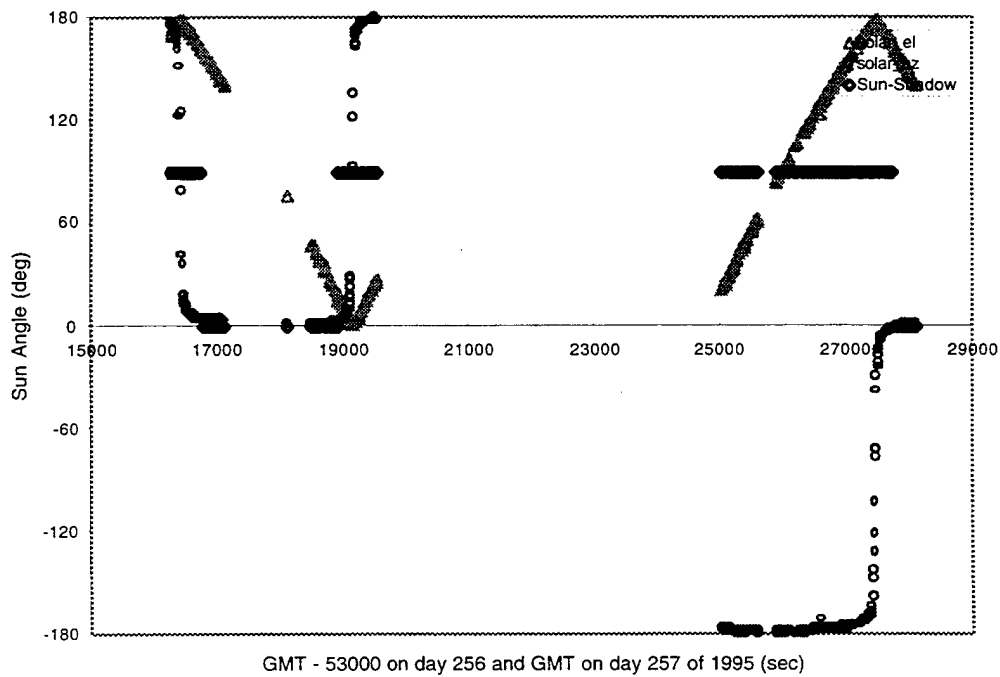
Figure 45. (b) The sun angle.

67
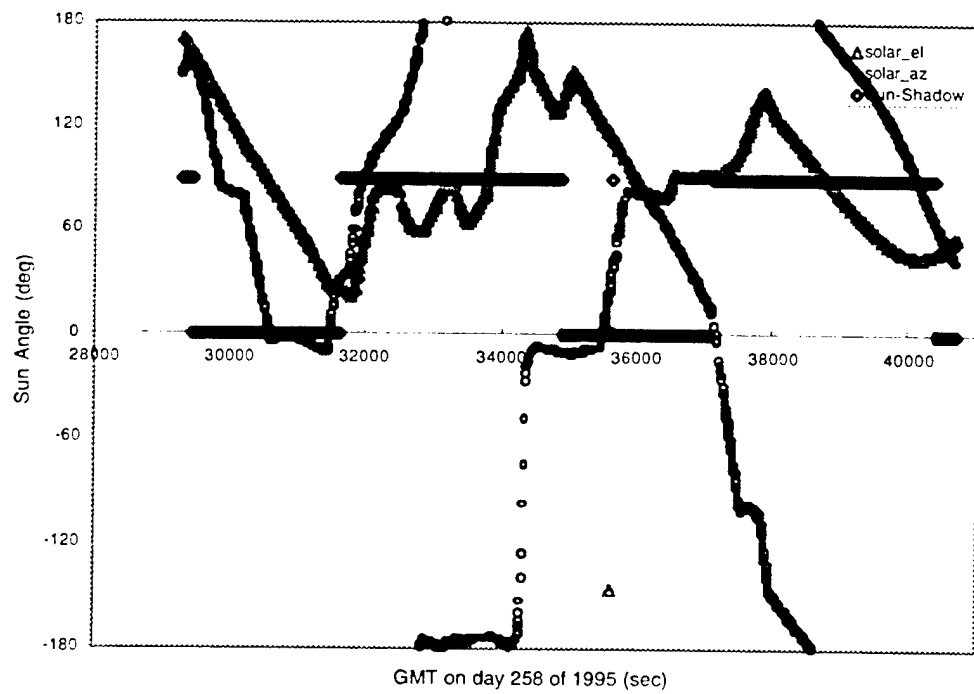
Figure 45. (c)The sun angle.

68
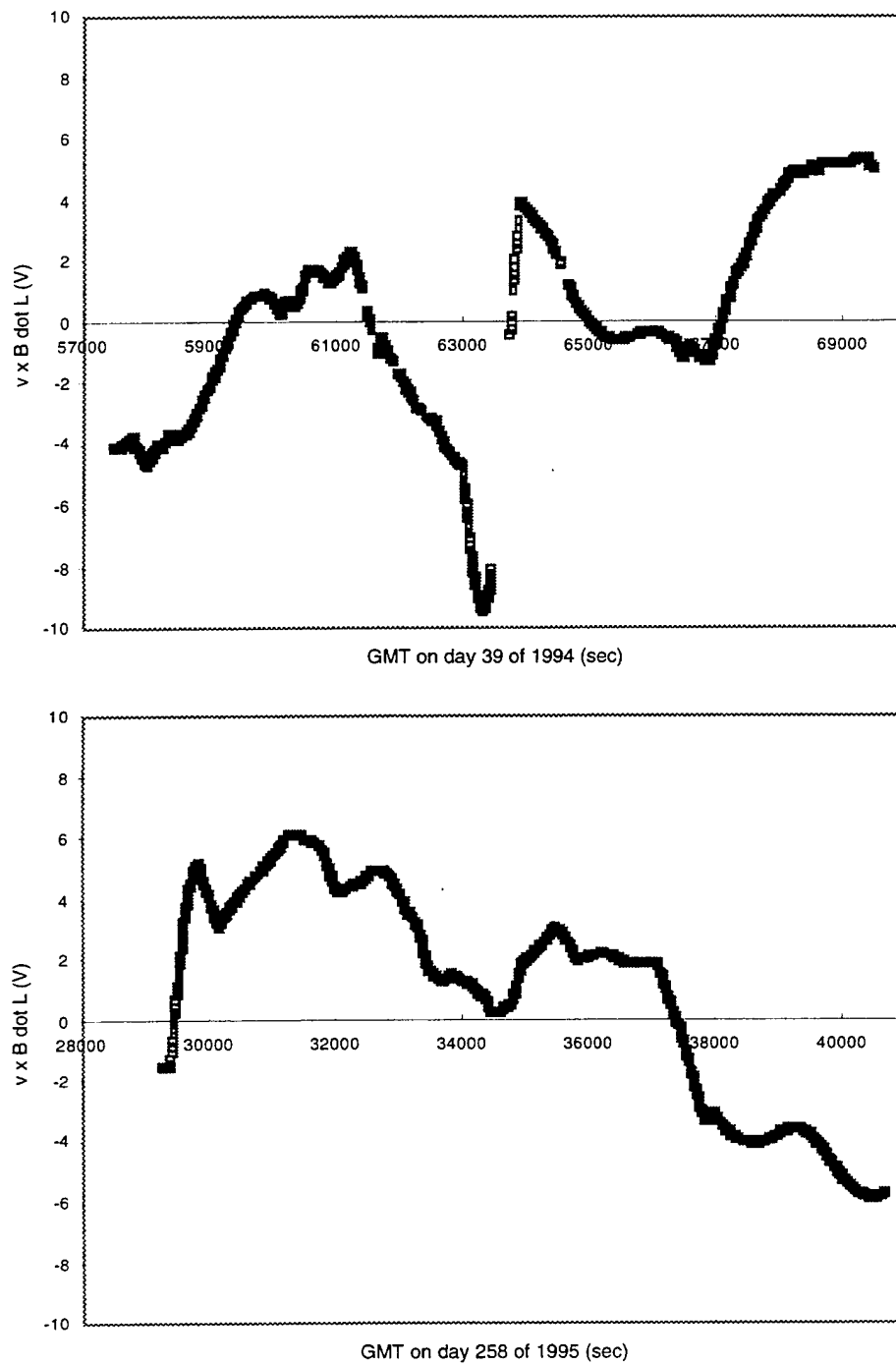
Figure 46. The value of $v \times B \bullet L$ varies by 16 V during the measurement periods. When $v \times B \bullet L$ is positive, we expect the engine bells to remain grounded and the disk to be negative with respect to the plasma. When $v \times B \bullet L$ is negative, we expect WSF to remain within a volt of plasma ground and the shuttle to be negative with respect to the plasma.
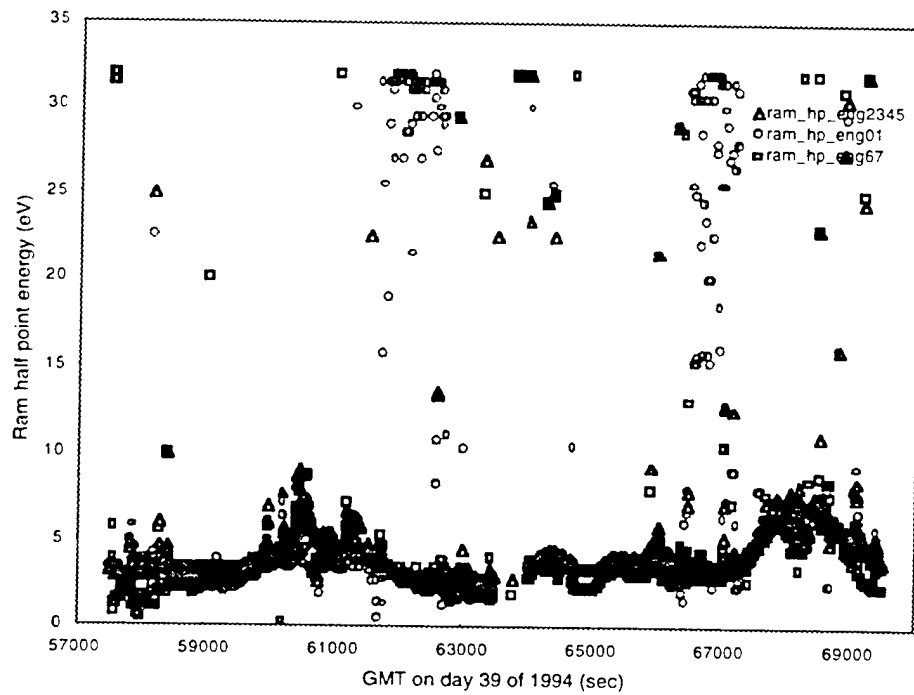
Figure 47. (a)
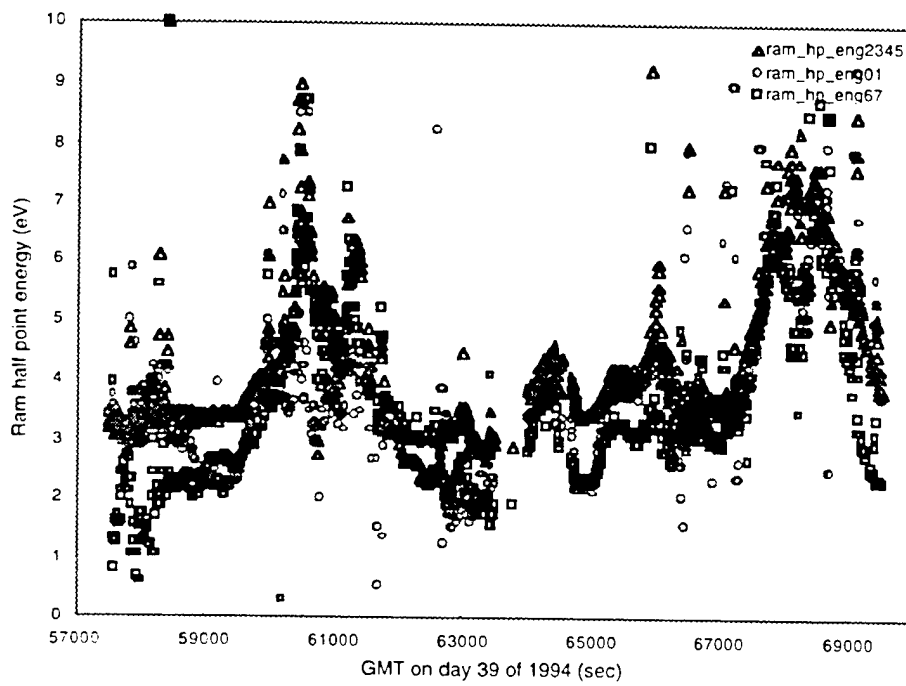
Figure 47. (b)
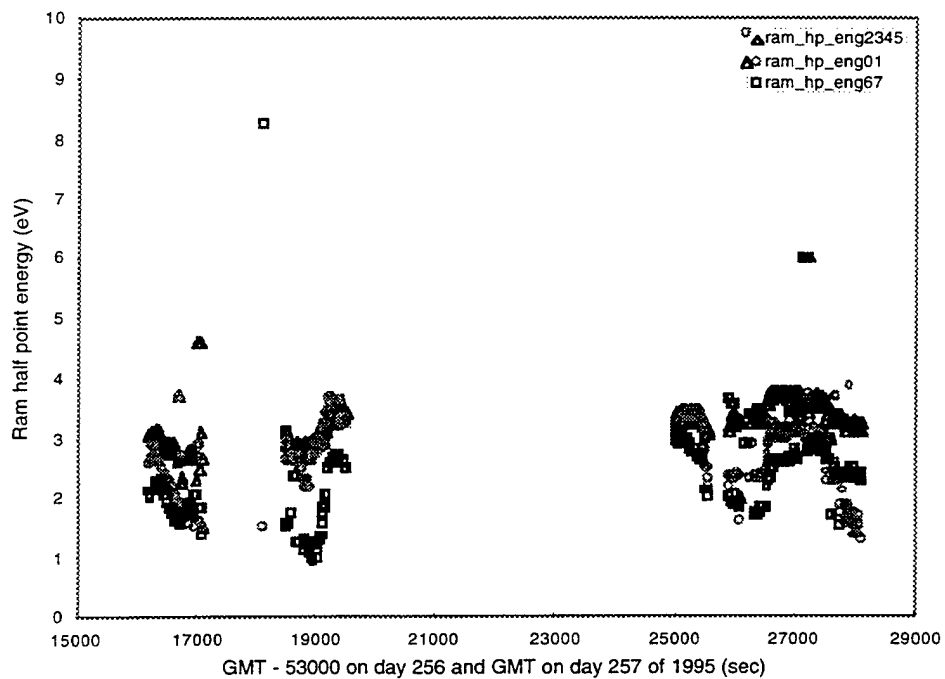
Figure 47. (c)
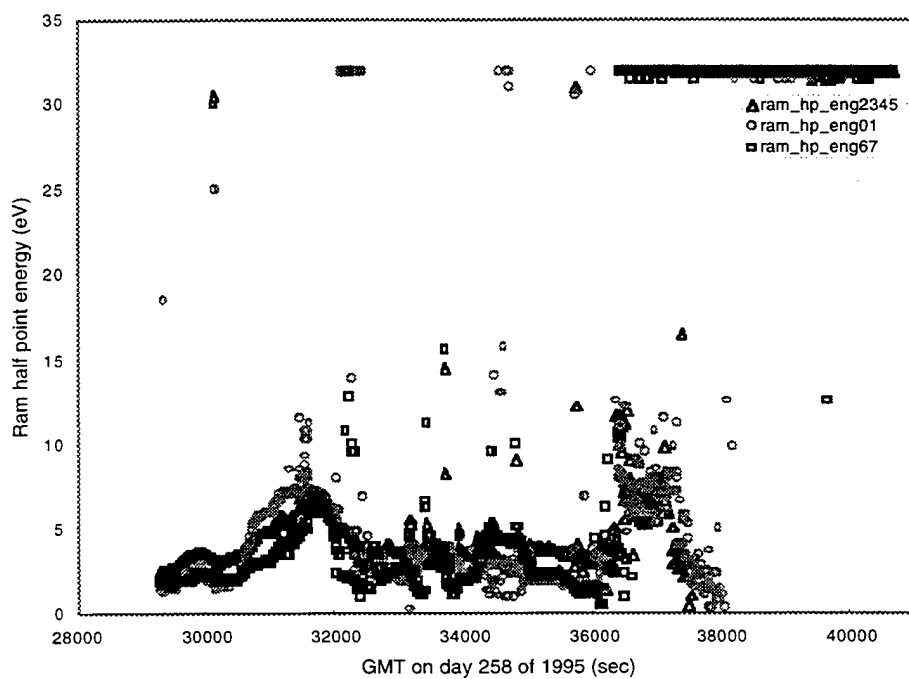
Figure 47. (d)
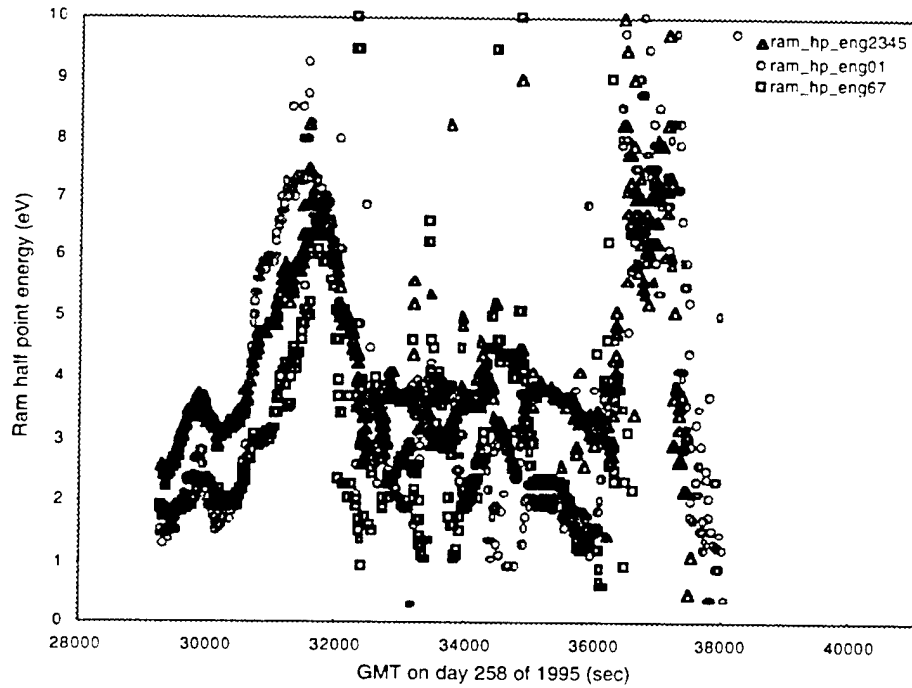
Figure 47. (e) The potential at which one-half of the incident ram ions are repelled is an indication of the disk potential at the location of the CHAWS ram side detectors. The energy determined from the inboard (ram_hp_eng67) and outboard (ram_hp_eng01) detectors is different from that determined from the center (ram_hp_eng2345) detectors, due to orientation effects. The half-point energy roughly follows $\mathbf{v} \times \mathbf{B} \cdot \mathbf{L}$. The peak in $\mathbf{v} \times \mathbf{B} \cdot \mathbf{L}$ at about 61000 s is matched by a comparable rise in the ram half-point energy, while the energy measurement is only modestly affected by the strong dip in $\mathbf{v} \times \mathbf{B} \cdot \mathbf{L}$ at 63000 s. The rise in $\mathbf{v} \times \mathbf{B} \cdot \mathbf{L}$ from 0 to 5 volts following 67000 s is well matched by a rise in ram half-point energy from about 3 to 8 volts. The variation during free flight may reflect small variations in the potential across the disk or, more likely, is related to how variation in orientation changes the measurement. The variation during the third time period does not track $\mathbf{v} \times \mathbf{B} \cdot \mathbf{L}$ as well. The two figures for each time period use different vertical axis scales. The full scale figure is included to illustrate the difficulty of interpreting this measurement.
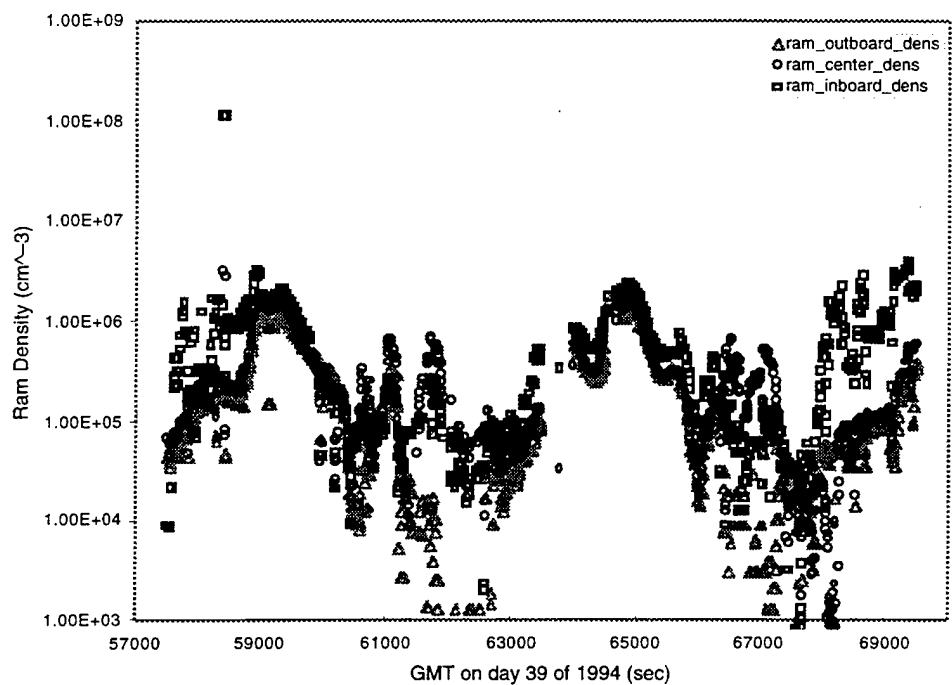
Figure 48. (a)

Figure 48. (b)

73
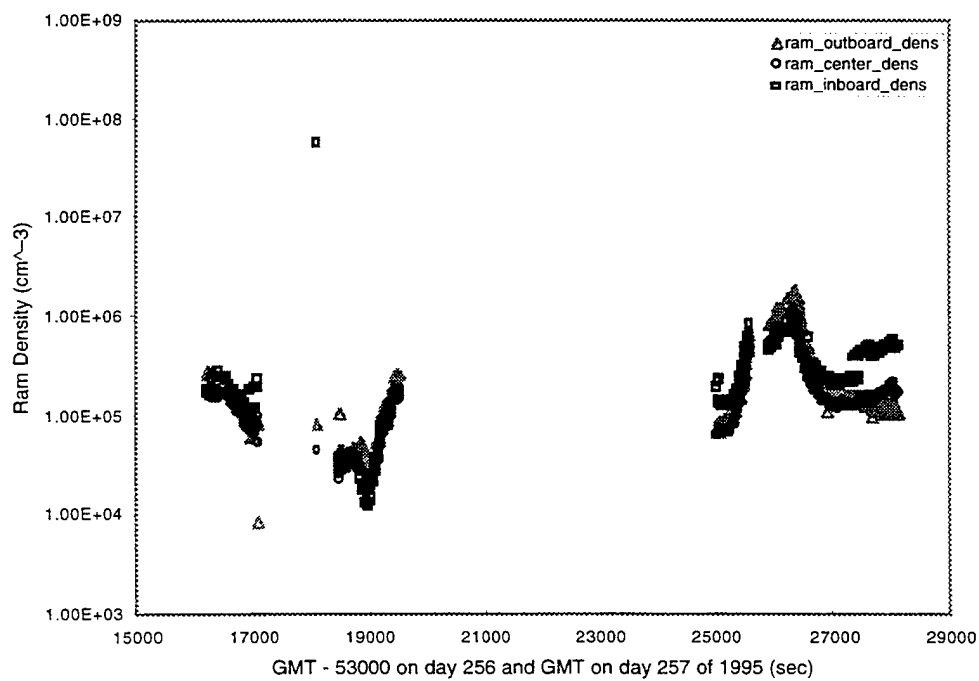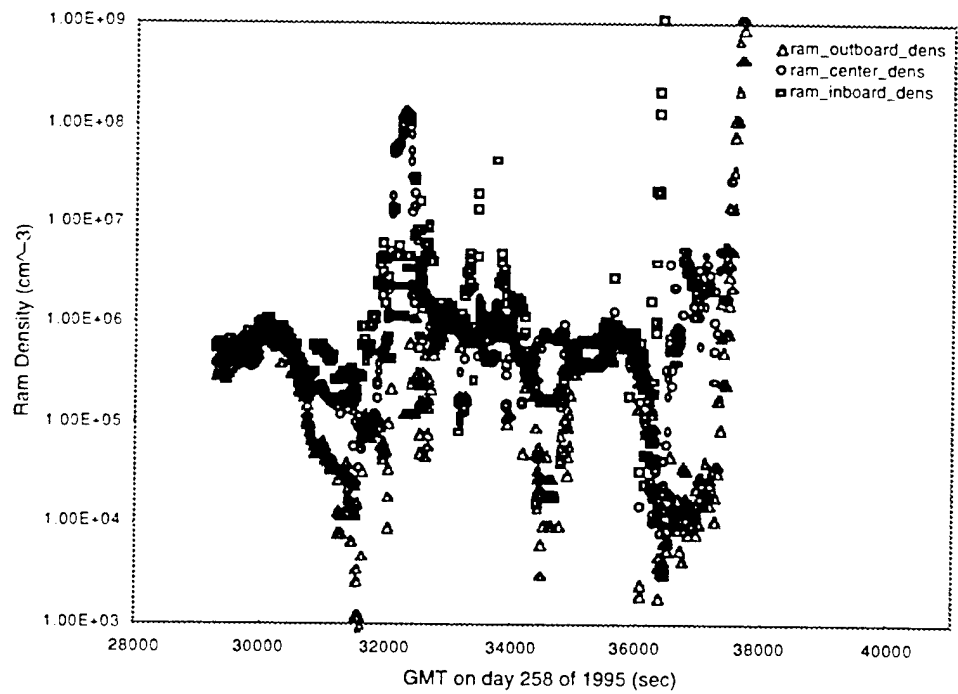
Figure 48. (c) Density as measured by the ram side detectors. For the following calculations, the density calculated from the detector most nearly aligned with the ram direction is used. (Figure 41 shows this density.)
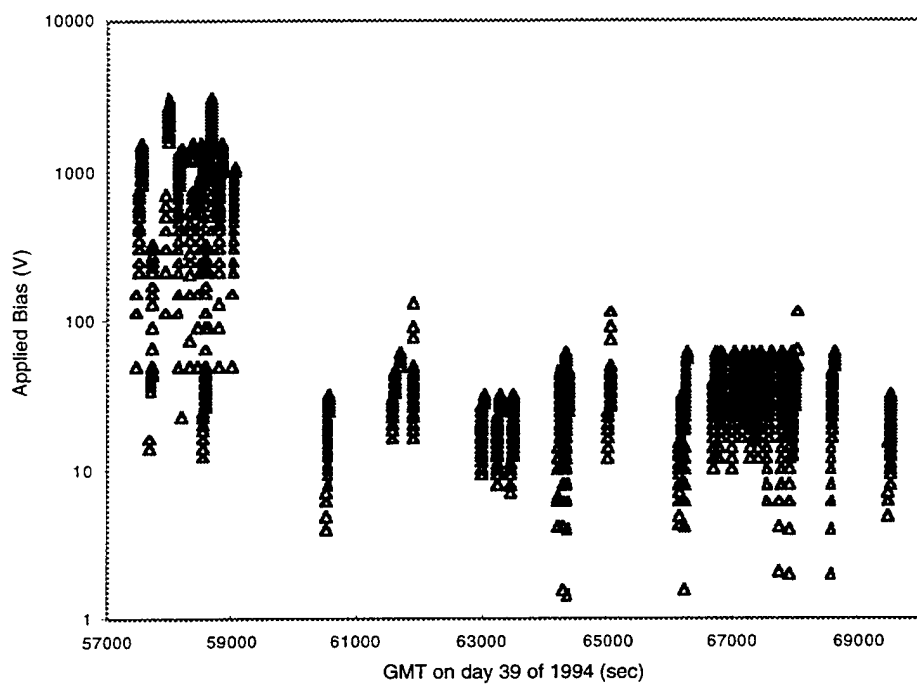
Figure 49. (a) Applied potential.
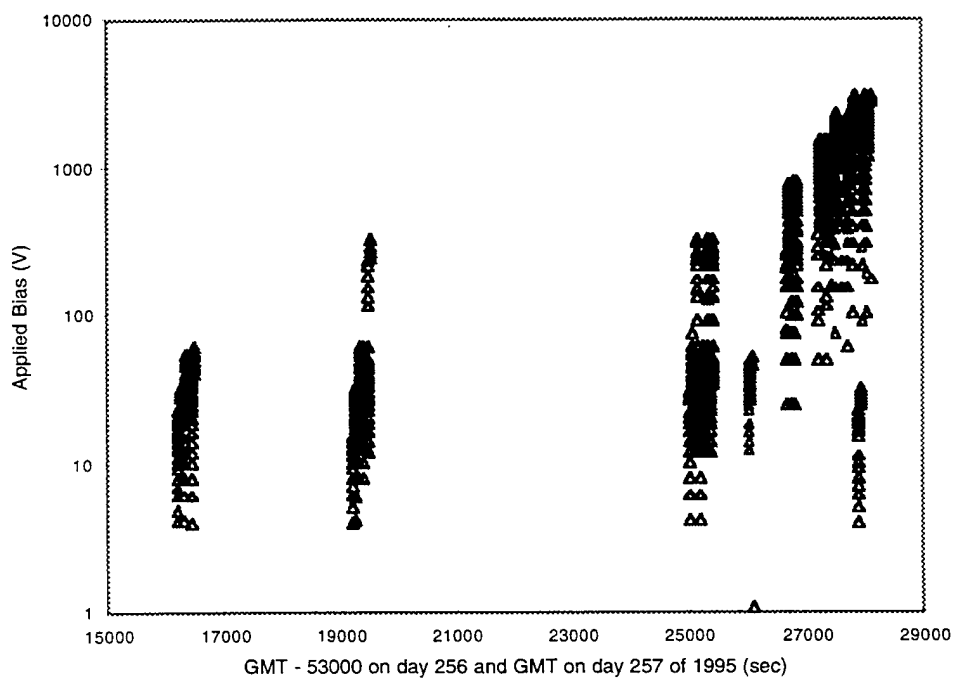
Figure 49. (b) Applied potential.

75
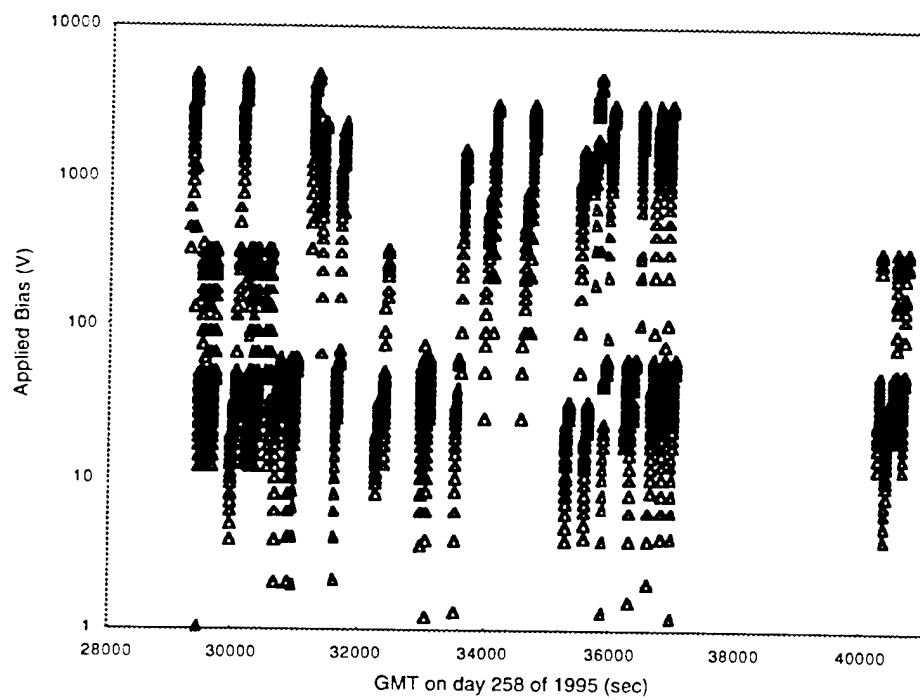
Figure 49. (c) Applied potential.
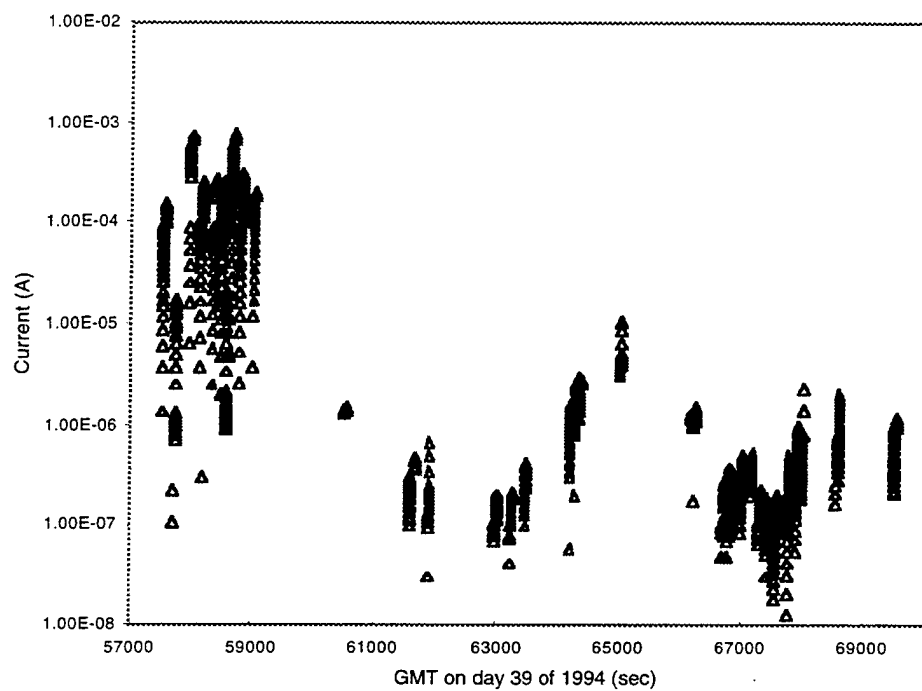
Figure 50. (a)

Figure 50. (b)

77
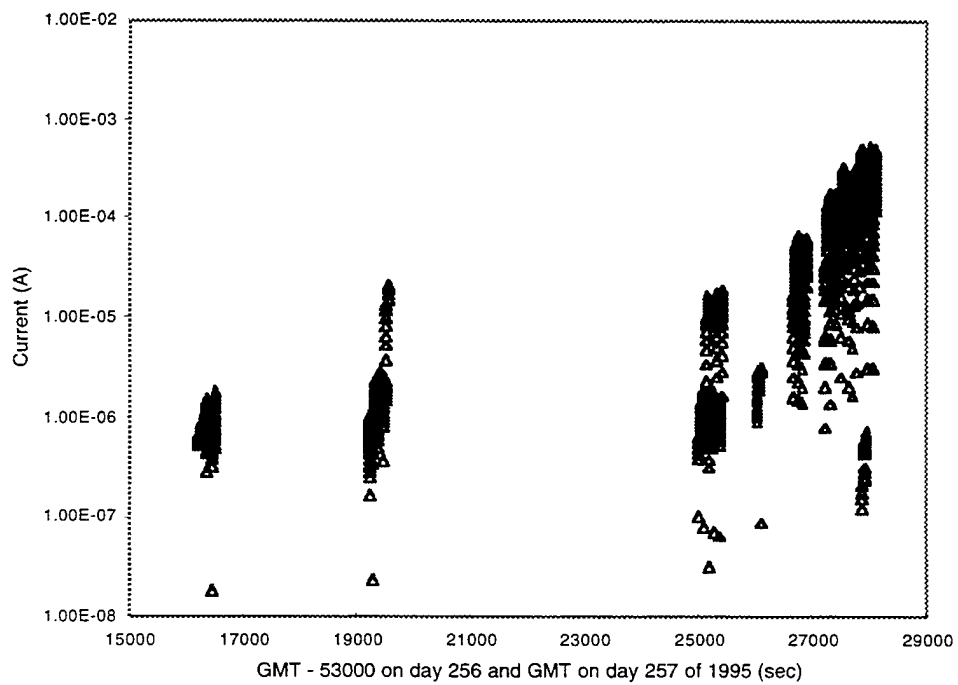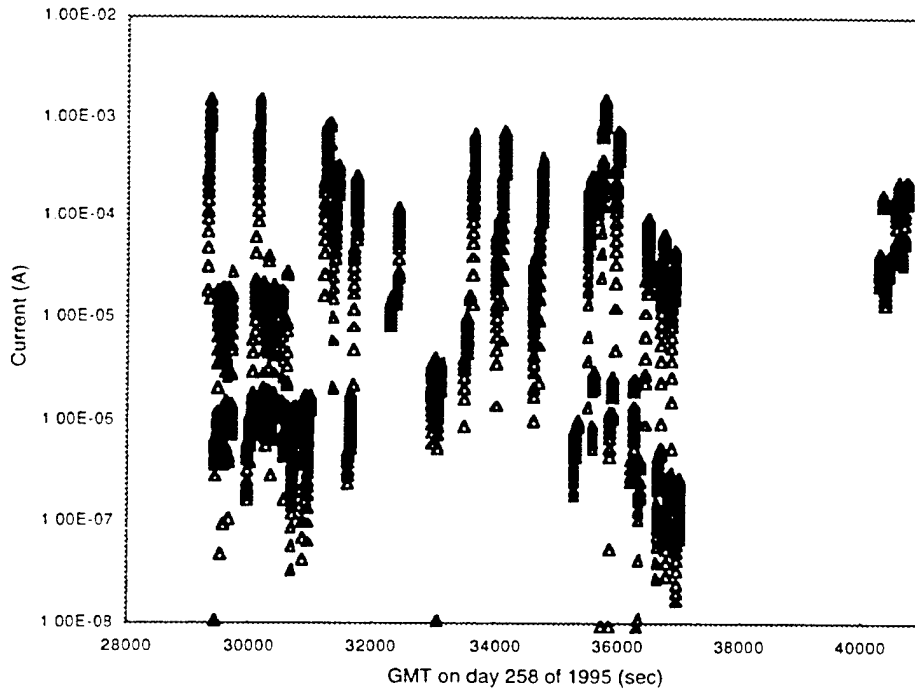
Figure 50. (c) Collected current. The currents are determined by CHUNKS using a stencil. For each step, current measurements made by the appropriate channels are averaged. Measurements are included only if there are more than six consecutive good frames where a good frame is one with two or more steps with the voltage over 2.5 V and the voltage is increasing from step to step.

8.4 Derived Parameters

While the potential at which one-half of the incident ram ions are repelled is an indication of the disk potential at the location of the CHAWS ram side detectors, this quantity shows a great deal of scatter. The value of $v \times B \bullet L$ may be a better estimate. Figure 51 shows the relationship between these quantities. Positive values of $v \times B \bullet L$ show a larger amount of scatter in half-point energy. The function

$$h = \begin{cases} 3.5 + 0.075 \, v \times B \bullet L & \text{if} \quad v \times B \bullet L \leq 1 \\ 2.575 + v \times B \bullet L & \text{if} \quad v \times B \bullet L \geq 1 \end{cases}$$

estimates the half-point energy.

78

Day 39 of 1994

Day 258 of 1995
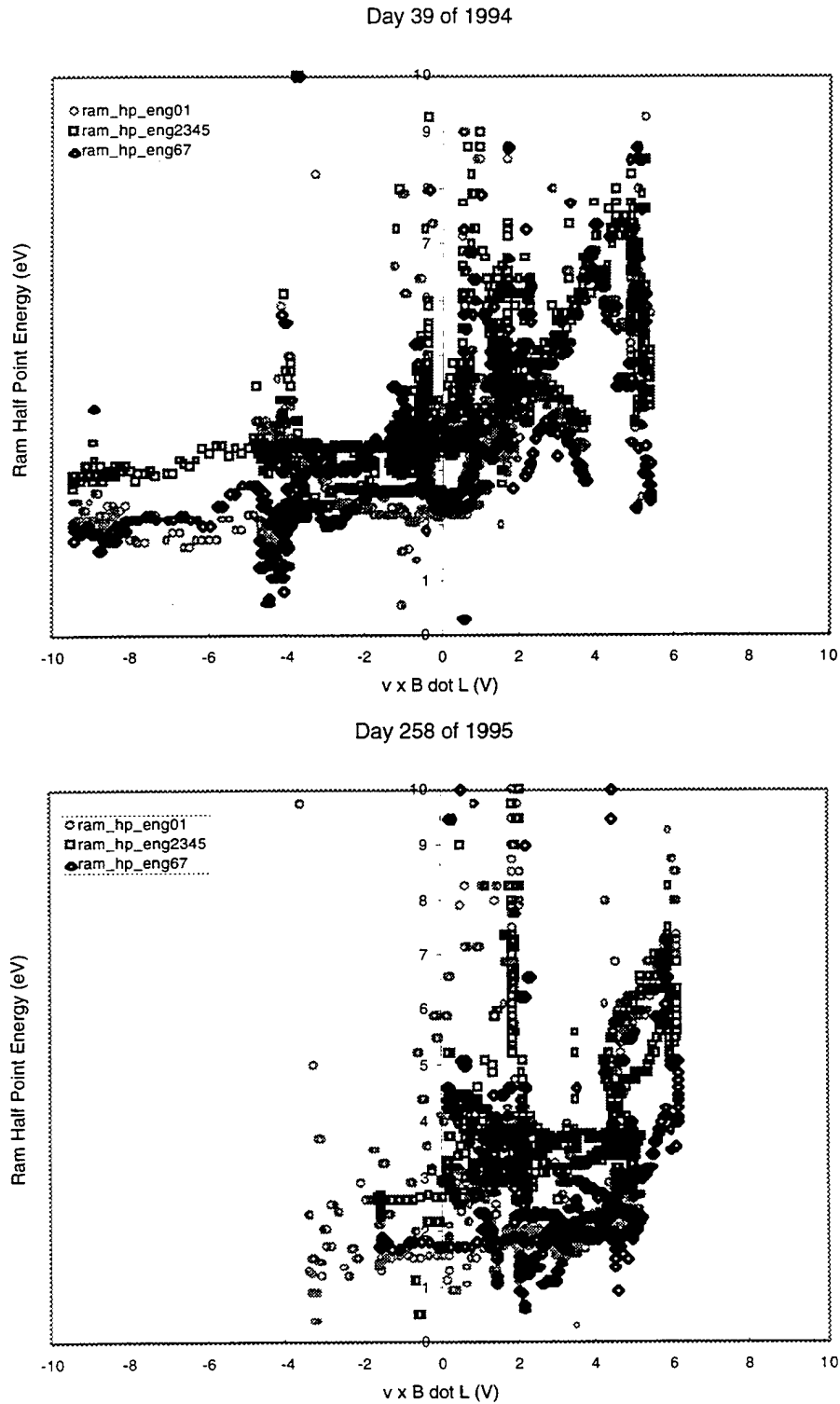
Figure 51. Potential at which one-half of the incident ram ions are repelled as a function of $v \times B \bullet L$ as determined from the inboard (ram_hp_eng67), outboard (ram_hp_eng01), and center (ram_hp_eng2345) detectors.

8.5. Current Measurements

To gain a sense of the importance of each of the parameters, Figures 52 through 55 show the collected current as a function of the applied bias, plasma density, tilt, $\mathbf{v} \times \mathbf{B} \bullet \mathbf{L}$, and for the low potential measurements, sun-disk angle. 40 V is the dividing line between high and low potential measure- ments. From these figures, it is clear that the applied bias is the most important parameter. The potential measurements show a slight increase in current with plasma density. Dependence on tilt and $\mathbf{v} \times \mathbf{B} \bullet \mathbf{L}$ are much smaller.

Day 39 of 1994

Figure 52. (a)

80
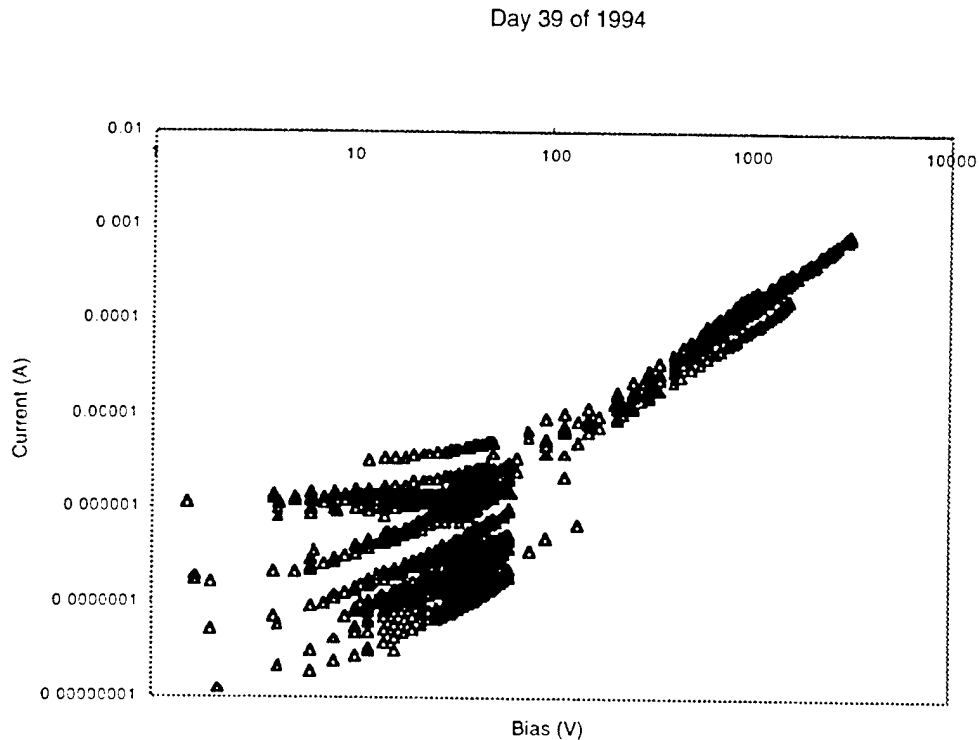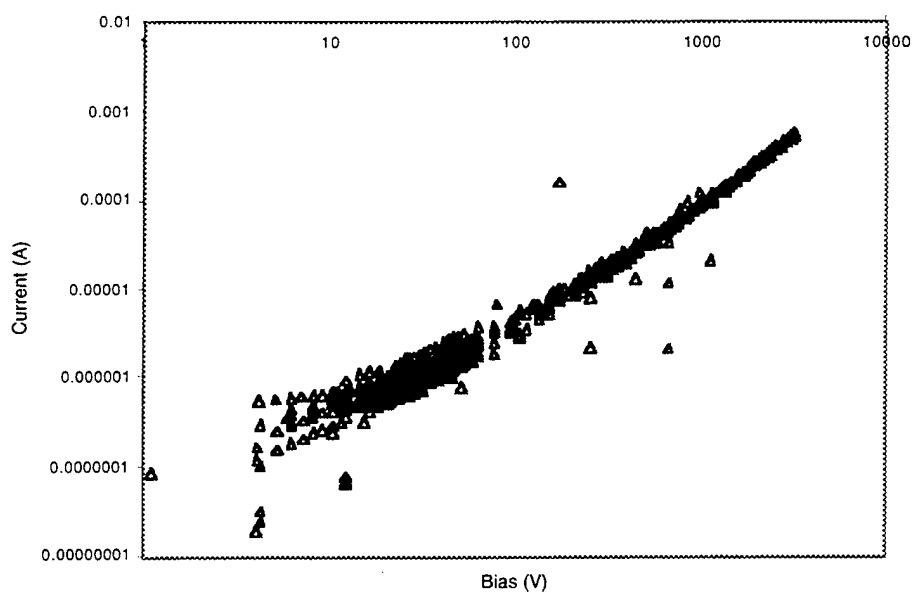
Figure 52. (b)

Day 258 of 1995
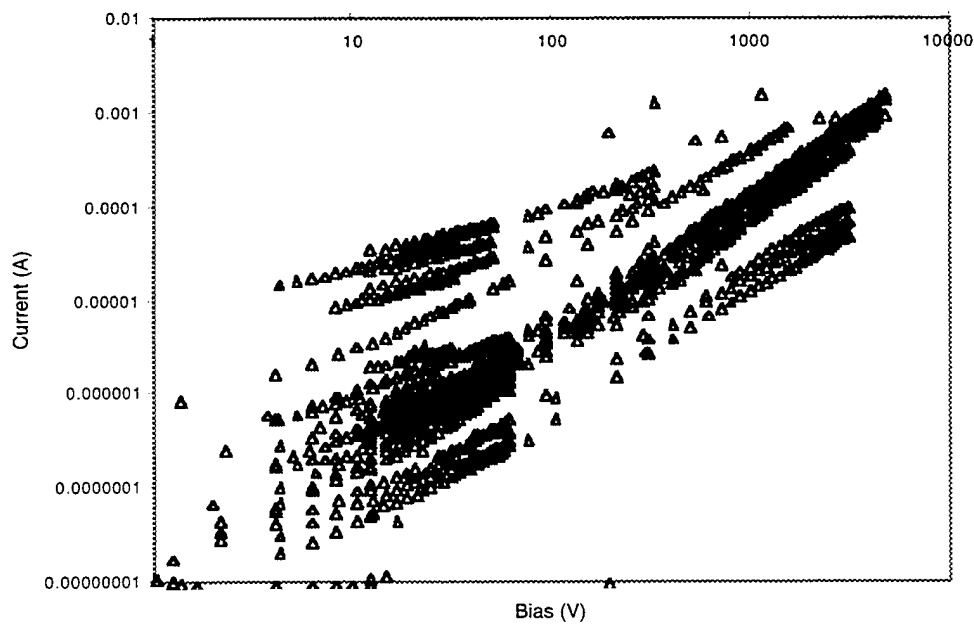
Figure 52. (c) Collected current as a function of applied bias. The measurements for day 258 fall into three groups. The top set were taken while the probe was in the ram flow. The bottom set were taken while WSF was in the wake of the shuttle.

Day 39 of 1994
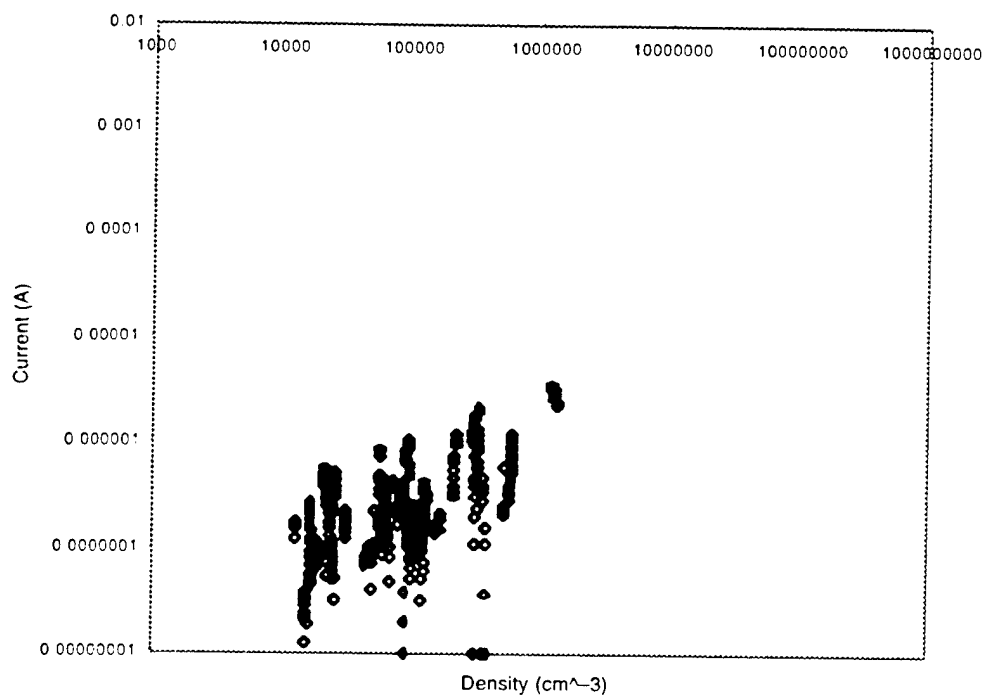
Figure 53. (a)

Days 256 and 257 of 1995

Figure 53. (b)

82
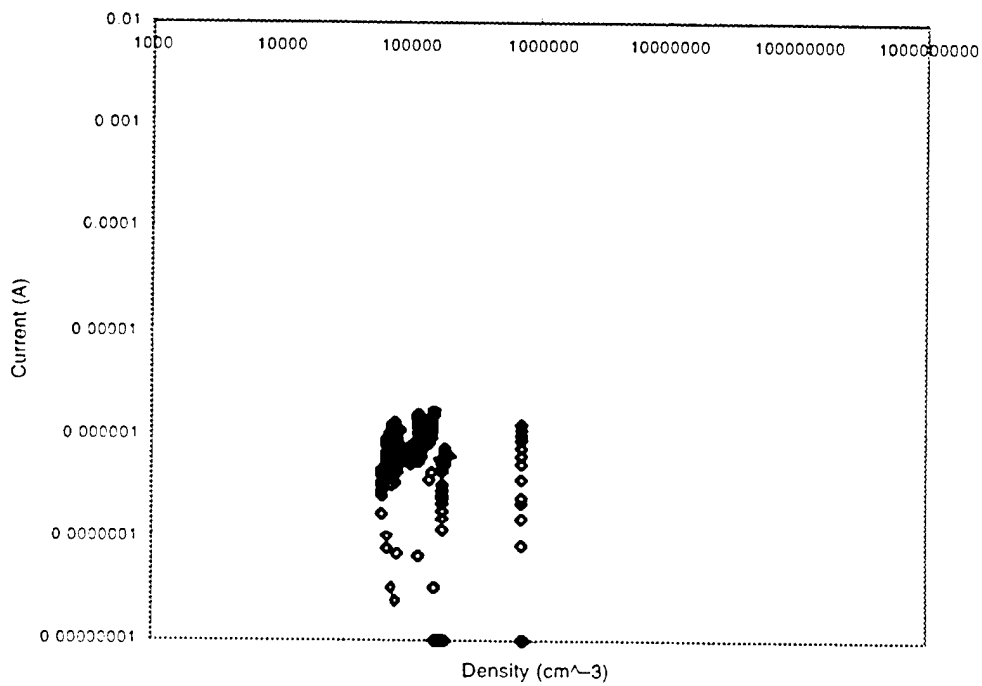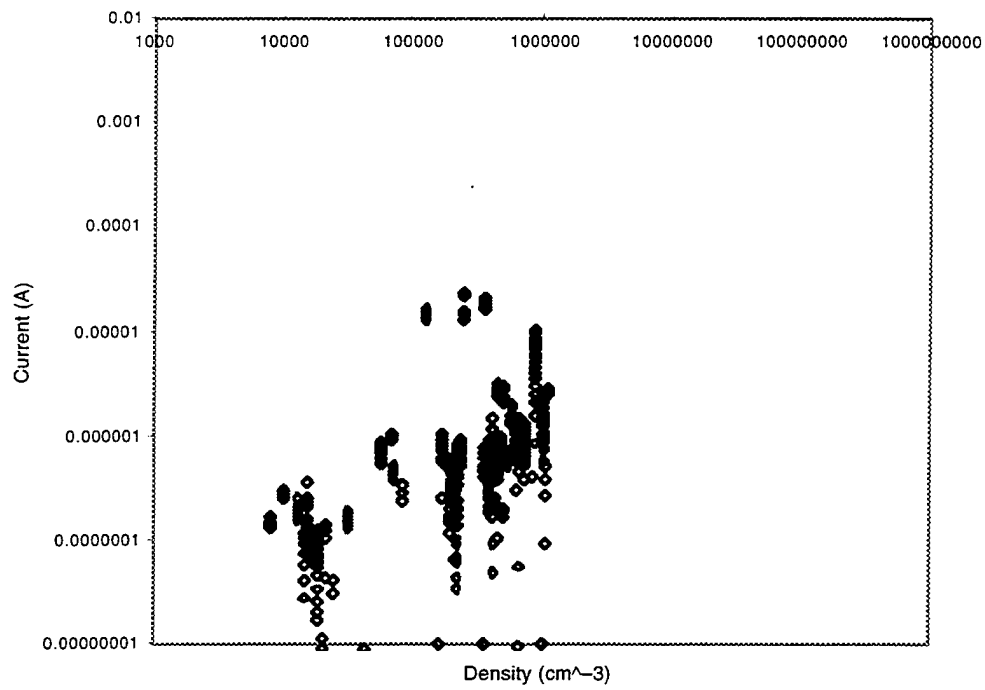
Day 258 of 1995

Figure 53. (c)

Day 39 of 1994

Figure 53. (d)

83
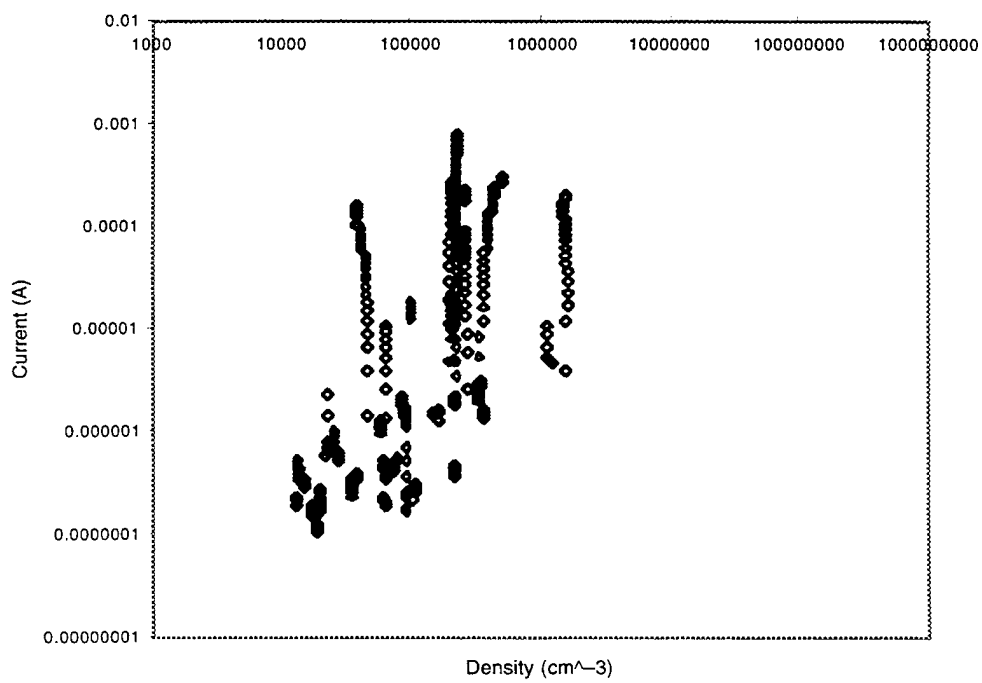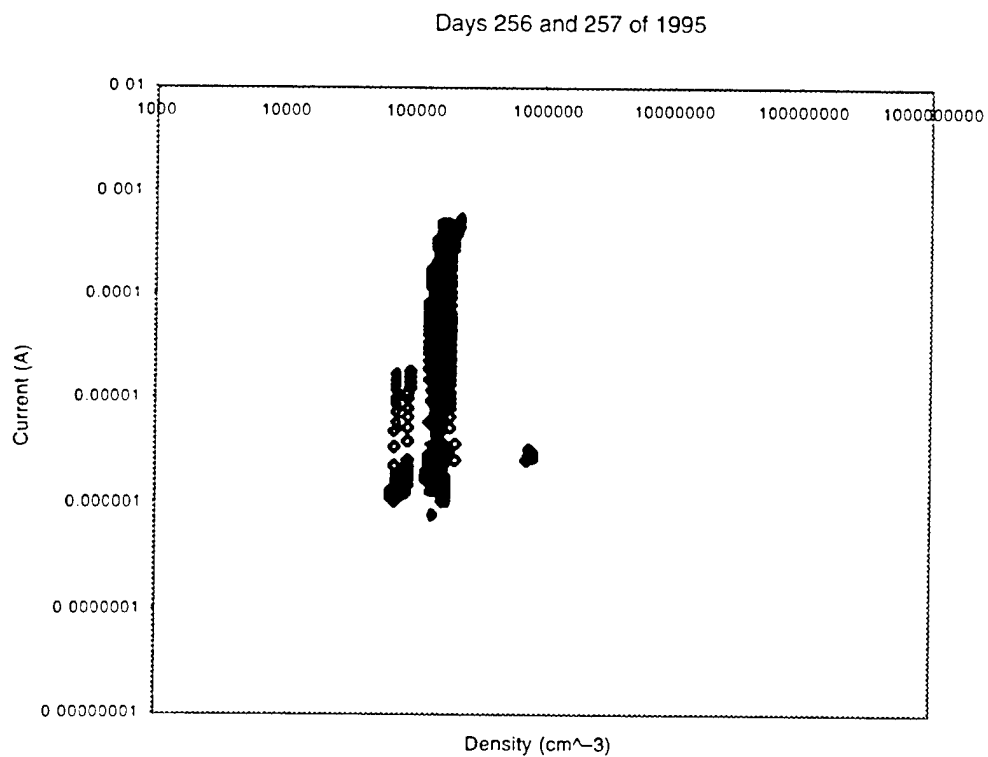
Figure 53. (e)
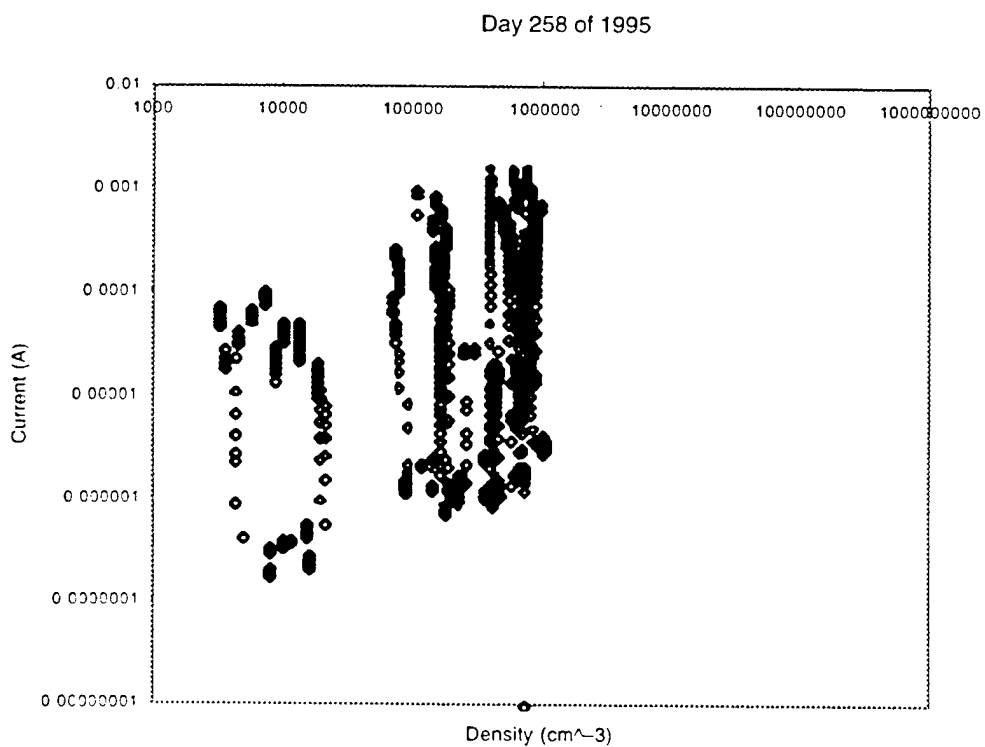
Day 258 of 1995

Figure 53. (f) Collected current as a function of plasma density for (a) low (under 40 V) and (b) high (over 40 V) potential measurements.

Day 39 of 1994

Figure 54. (a)

Days 256 and 257 of 1995

Figure 54. (b)

85
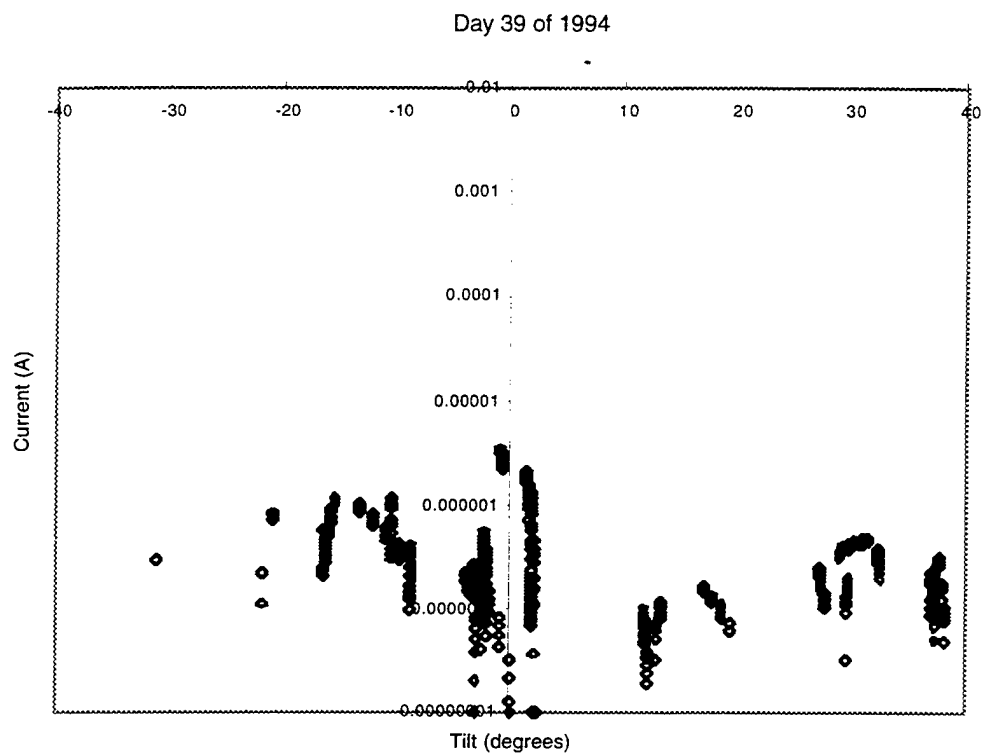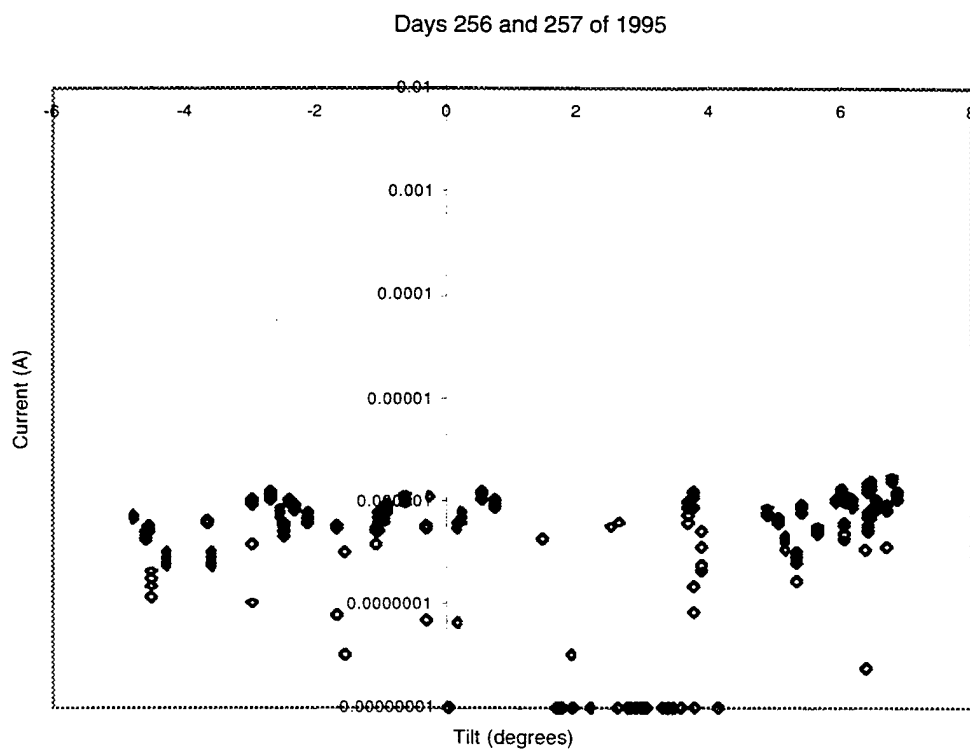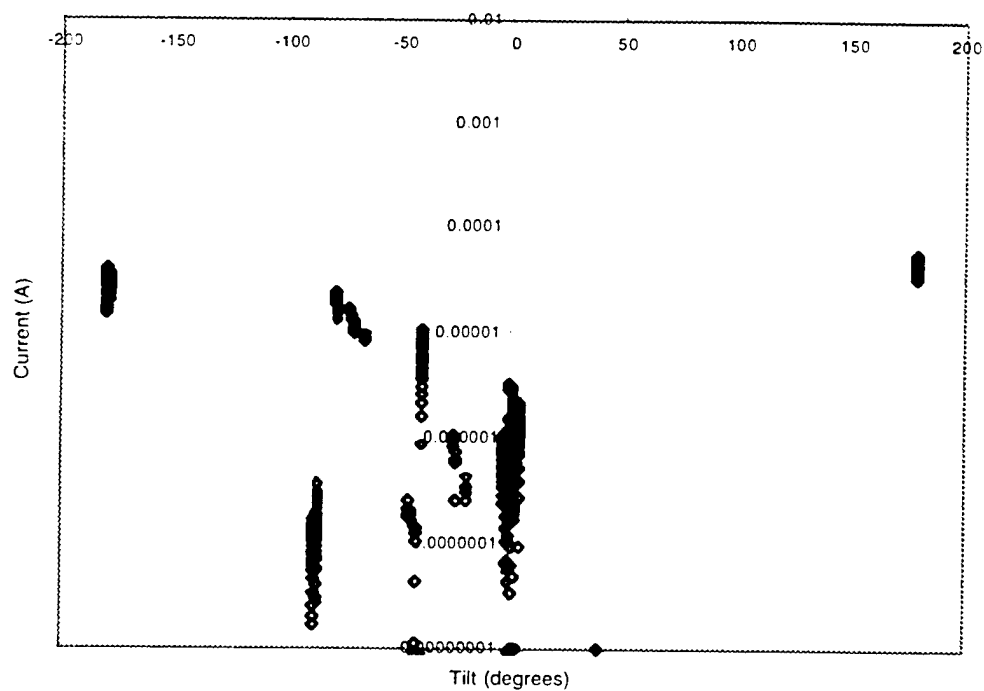
Day 258 of 1995

Figure 54. (c)

Day 39 of 1994

Figure 54. (d)

Days 256 and 257 of 1995
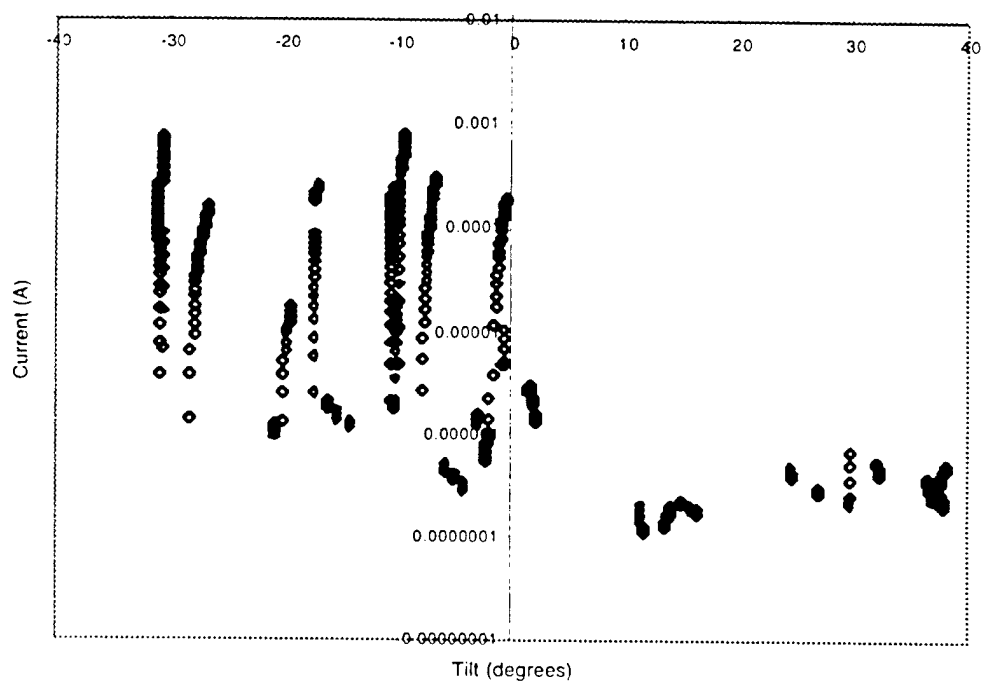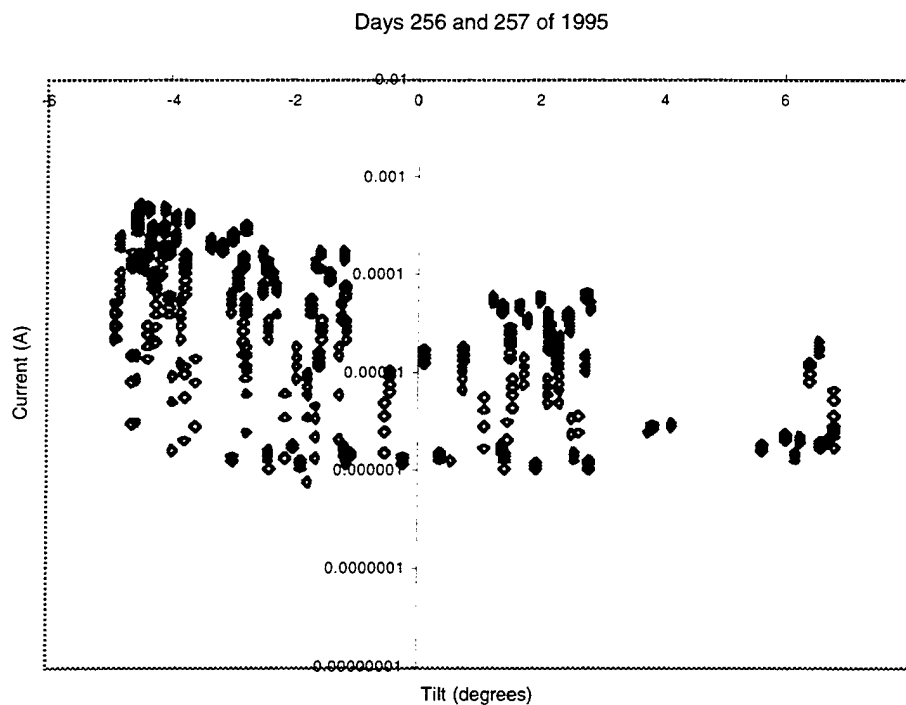
Figure 54. (e)

Day 258 of 1995
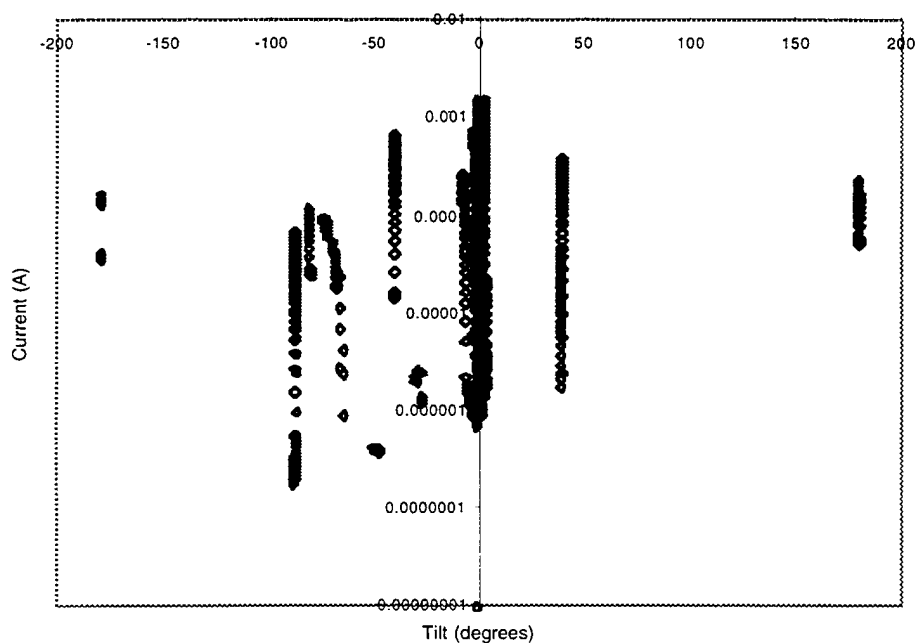
Figure 54. (f) Collected current as a function of tilt for (a) low (under 40 V) and (b) high (over 40 V) potential measurements. Measurements for free flight are not shown as the orientation does not vary significantly. Note that the range of tilt values is different for each time period.

Day 39 of 1994
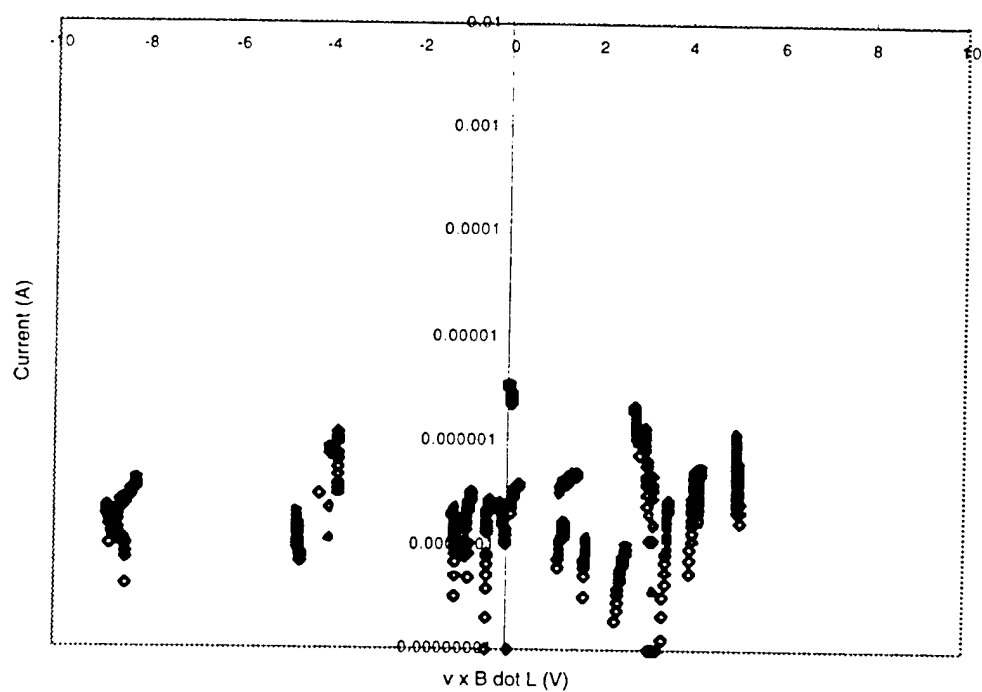
Figure 55. (a)

Day 258 of 1995

Figure 55. (b)

Day 39 of 1994

Figure 55. (c)

Day 258 of 1995
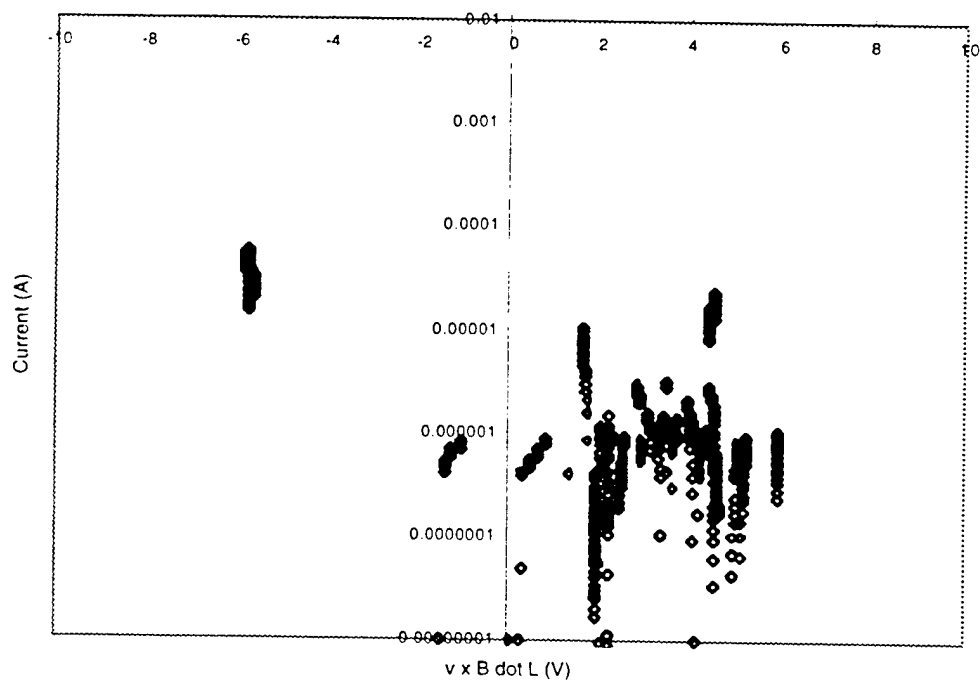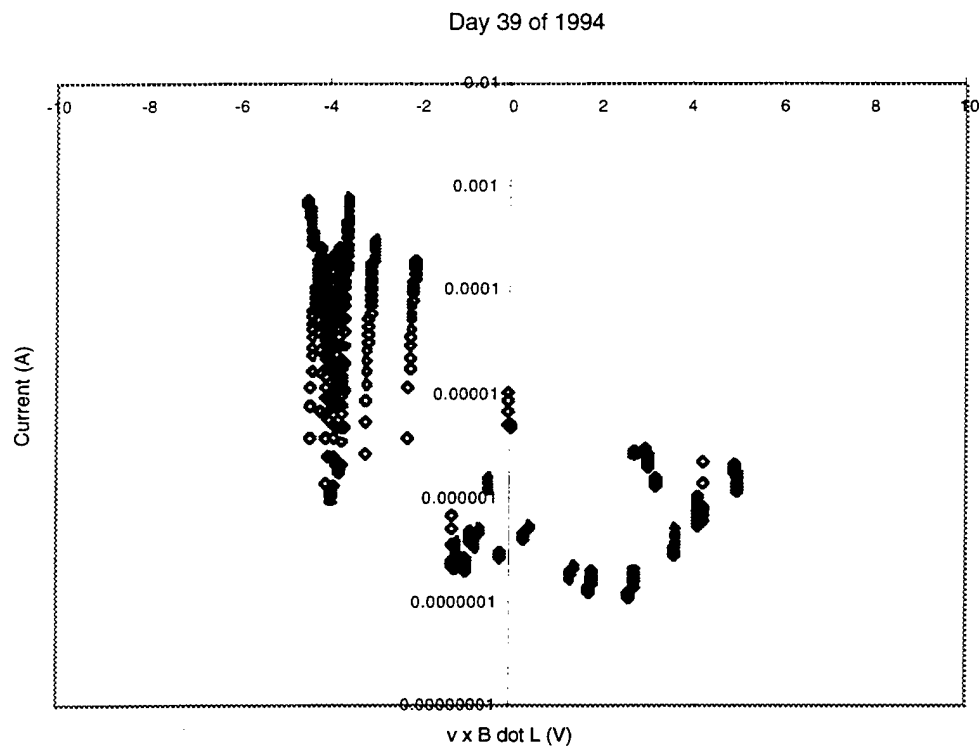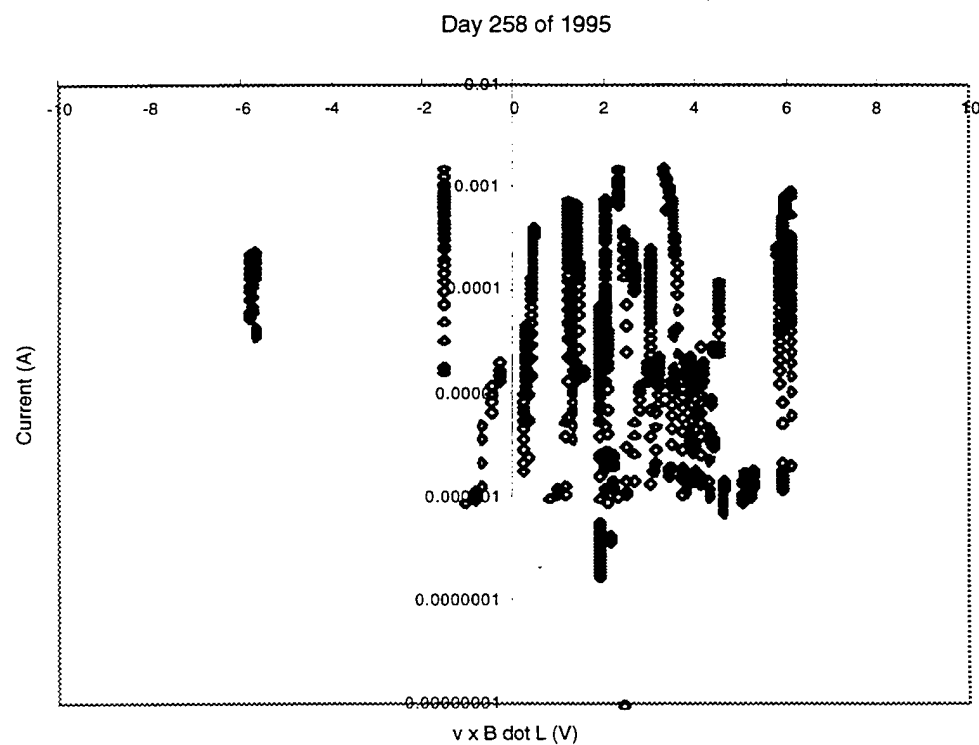
Figure 55. (d) Collected current as a function of $\mathbf{v} \times \mathbf{B} \bullet \mathbf{L}$ for (a) low (under 40 V) and (b) high (over 40 V) potential measurements. Free flight measurements are not shown because shuttle orientation is not relevant.

89

A sunlit probe has more current than a dark one due to photoemission and the fact that plasma density is higher during the day. When the sun-disk angle is 90°, the sun is incident on the edge of the disk and the probe is fully illuminated. When the sun-disk angle is greater than 90°, the sun is illuminating the back of the disk. When the probe is fully illuminated the photocurrent appears to be approximately 1 μA. Since the distance from the probe to the edge of the disk is approximately equal to the length of the probe, the probe is entirely shadowed by the disk for a sun-disk angle of under 45° for any orientation. There is some angle between 45° and 90° at which just the tip of the probe is illuminated. This angle depends on the orbit and the disk orientation. It appears to be near 77° for the first flight and does not show clearly for the second flight. Figure 57 shows a model of the shuttle from the viewpoint of the sun as the tip of the probe comes into view. Between 77° and 90°, we approximate the photocurrent by linear interpolation between 0 and 1 μA.

Day 39 of 1994
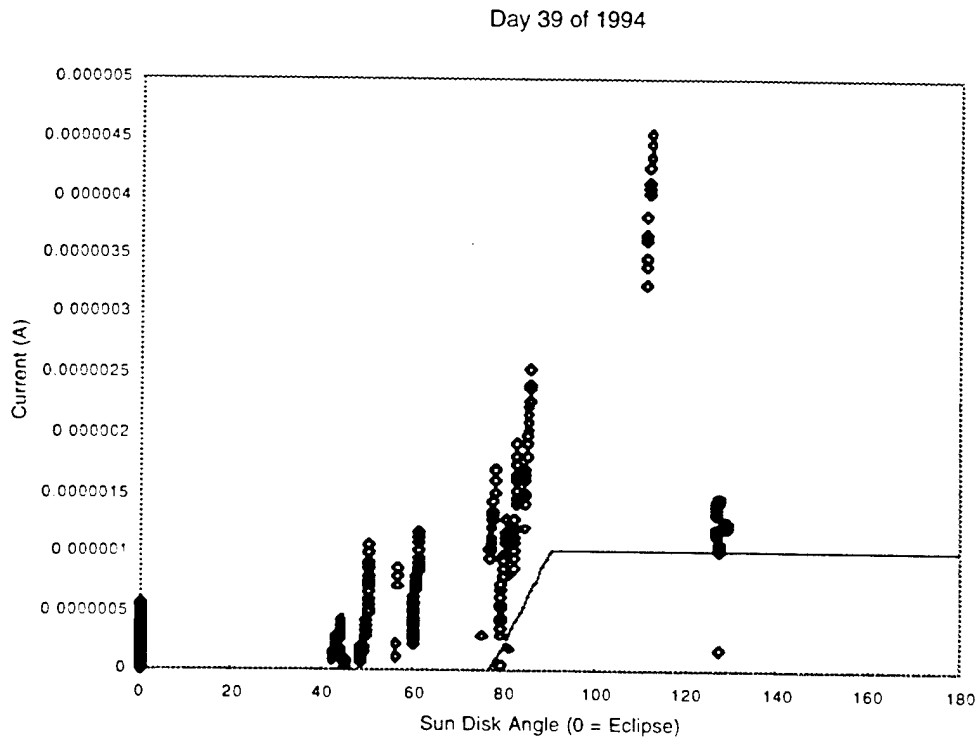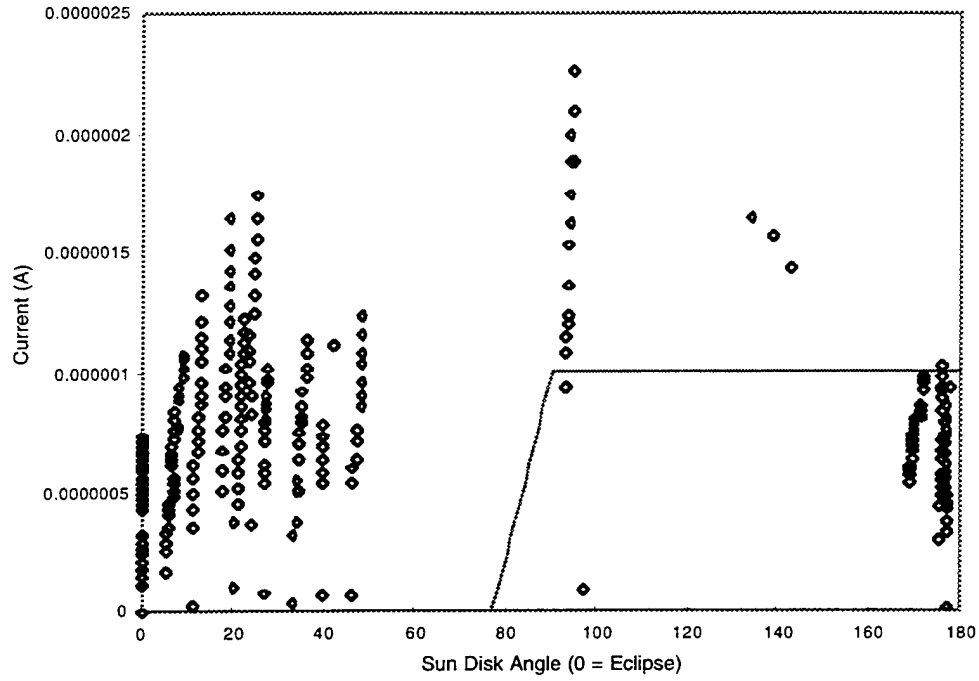
Figure 56. (a)

Figure 56. (b)

Day 258 of 1995
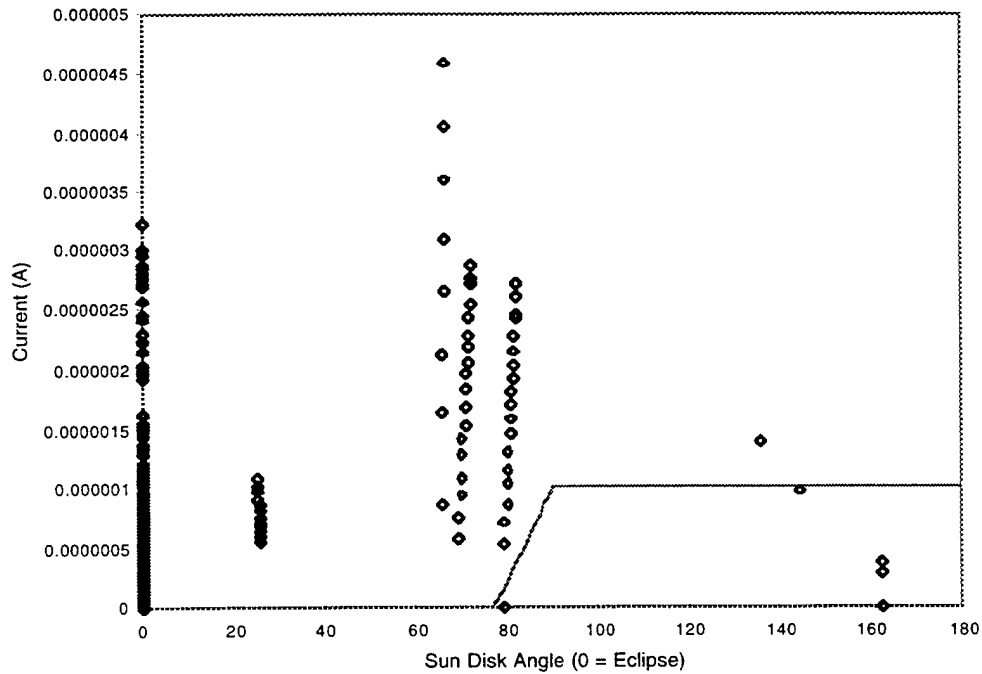
Figure 56. (c) Collected current as a function of sun-disk angle for low potential (under 40 V) measurements. An angle of zero indicates eclipse. The solid line is the photocurrent estimate. There are measurements with even higher currents than shown during day 258.
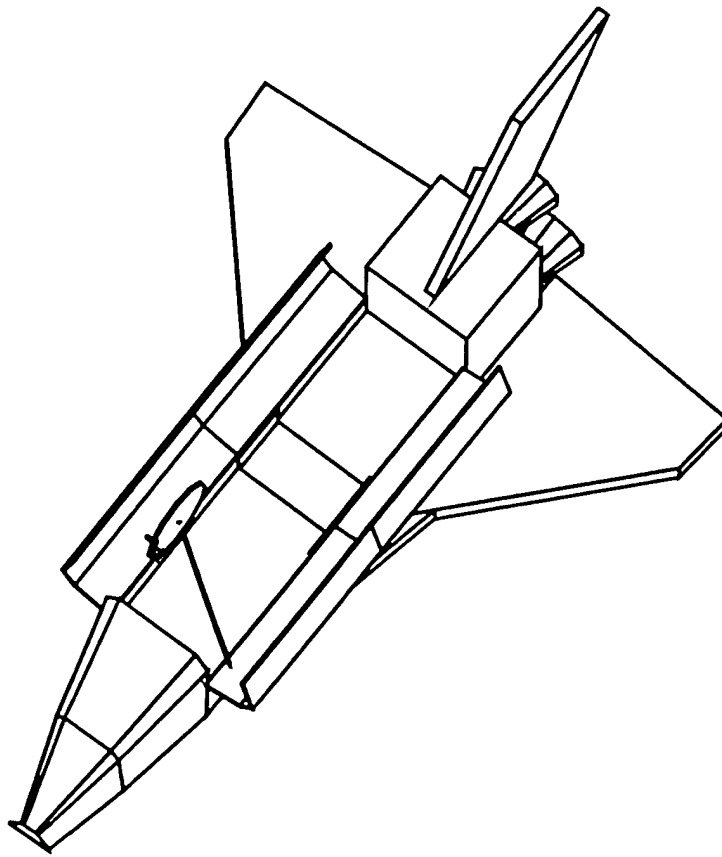
Figure 57. View of the shuttle and WSF from the point of view of the sun when the tip of the CHAWS probe comes into view.

The strong dependence on applied bias seen in Figure 52 suggests an examination of how current measurements vary for a few specific applied bias values might be useful. Figures 58 and 59 show how the current varies over times and with density for some specific bias values for the first flight. The highest current values occur with full sun. Figures 59 and 60 compare the CHAWS current with the atomic oxygen plasma thermal current to an unbiased probe for a plasma with the specified density and a 0.1 eV temperature for the first flight and during free flight. That this plasma thermal current is similar in magnitude to the measured current suggests that the density in the wake region is not significantly below the ambient plasma. That this occurs during free flight means that the shuttle environment is not entirely responsible for the wake density.
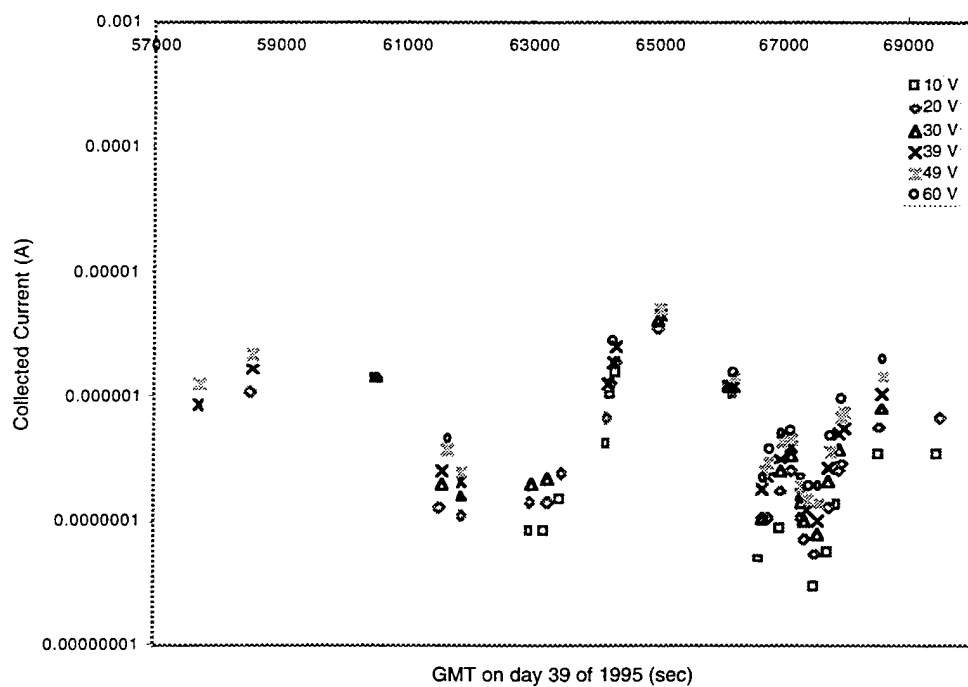
Figure 58. Collected current for specific applied bias values.
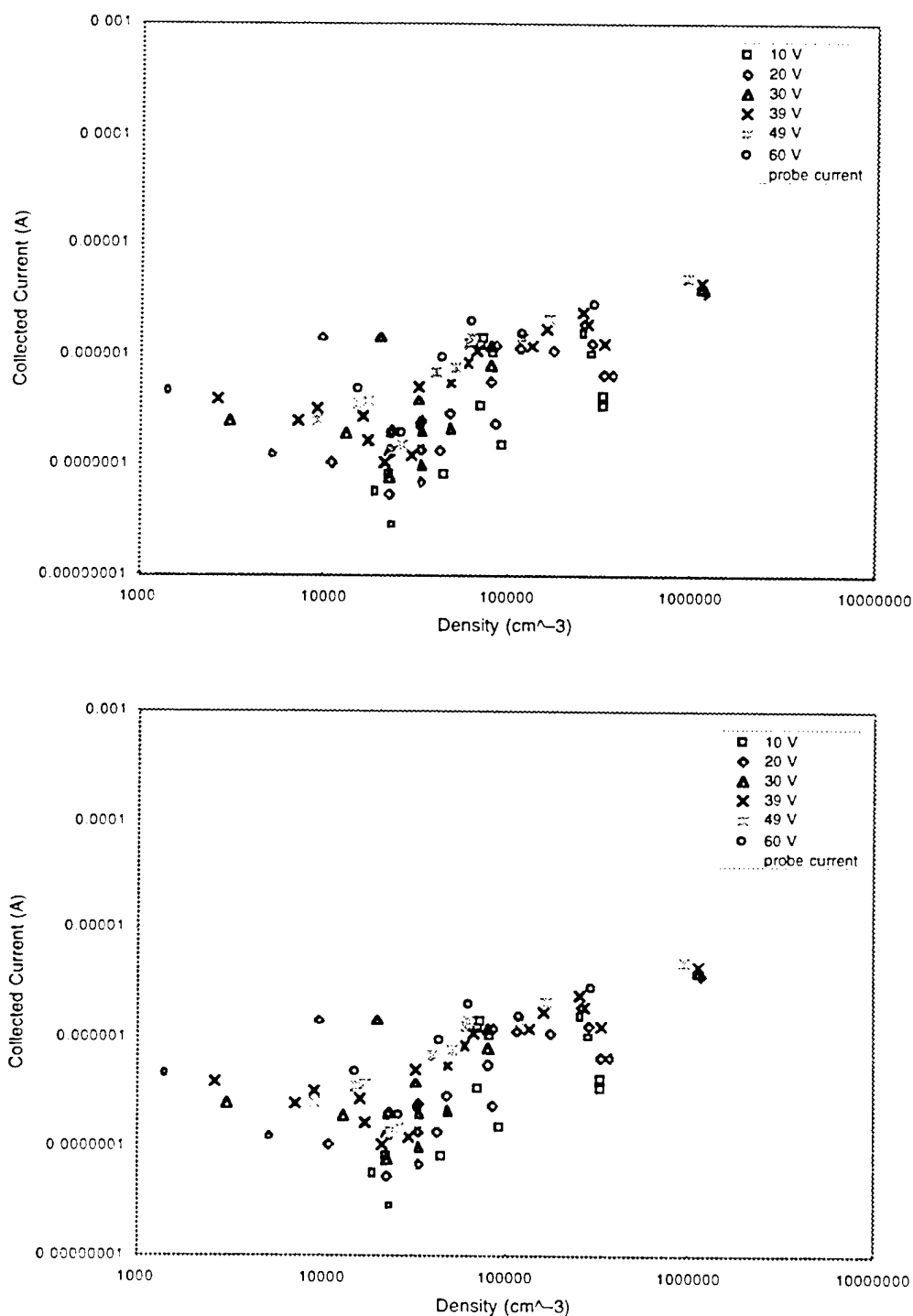
Figure 59. Collected current as a function of plasma density for a few specified bias values during the first mission. The measured current is compared with the atomic oxygen plasma thermal current to an unbiased probe for a plasma with the specified density and a 0.1 eV temperature. The bottom figure shows the same data points with the estimated photoemission subtracted.

94
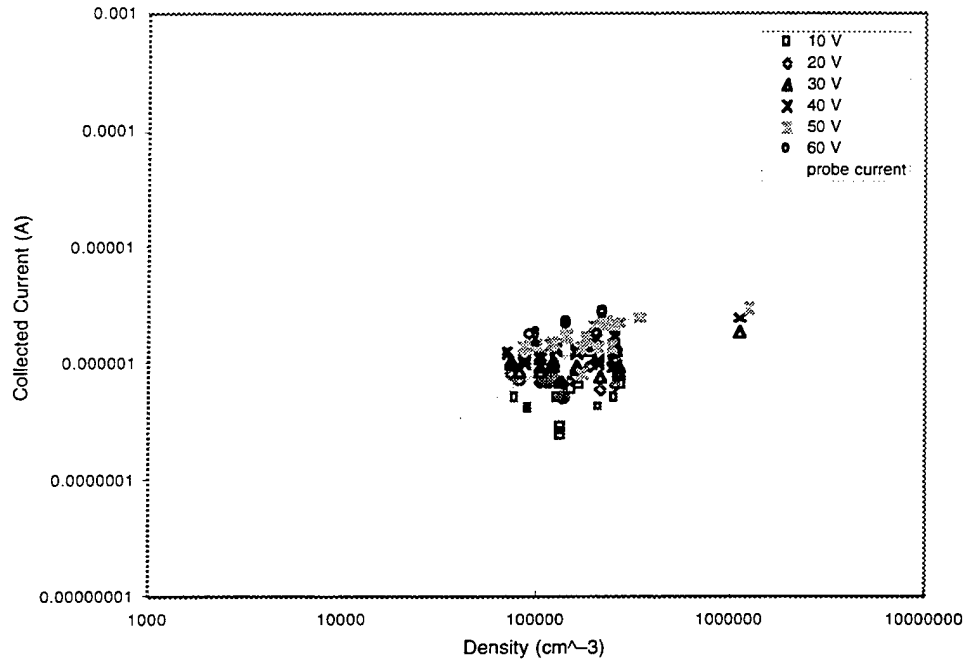
Figure 60. Collected current as a function of plasma density for a few specified bias values during free flight. The measured current is compared with the atomic oxygen plasma thermal current to an unbiased probe for a plasma with the specified density and a 0.1 eV temperature.

8.6 Fitting

The data was divided into three sets: low potential (10 V to 40 V), high potential (over 40 V), and large tilt (absolute value of tilt greater than 40°). The independent variables used are applied bias, density, tilt, $f(\mathbf{v} \times \mathbf{B} \bullet \mathbf{L})$, and $g(\text{eclipse, sun-ram angle})$ where

$$f(x) = \begin{cases} 0.075\,x & \text{if} \quad x \le 1 \\ x - 0.925 & \text{if} \quad x \ge 1 \end{cases}$$

and

$$g(\text{eclipse}, \theta_{sr}) = \begin{cases} 0, & \text{eclipse} = \text{true} \\ 0, & \theta_{sr} < 77 \\ (\theta_{sr} - 77)/13, & 77 > \theta_{sr} > 90 \\ 1, & \theta_{sr} > 90 \end{cases}$$

Values of $f(\mathbf{v} \times \mathbf{B} \bullet \mathbf{L})$ vary from –0.7 to 5.2.

For the first flight and second flight day 258 data under 40 V, we did a least square linear fit to a function of the form

$$\ln(I - g(\text{eclipse,sun ram angle}) \cdot 1\mu A) = a + b \cdot \ln(\phi) + c \cdot \ln(n) + d \cdot \text{tilt} + e \cdot f(\mathbf{v} \times \mathbf{B} \bullet \mathbf{L})$$

For the rest of the data we used

$$\ln(I) = a + b \cdot \ln(\phi) + c \cdot \ln(n) + d \cdot \text{tilt} + e \cdot f(\mathbf{v} \times \mathbf{B} \bullet \mathbf{L}) .$$

The terms can rearranged to write the current as

$$I = \exp(a) \phi^b n^c \exp(d \cdot \text{tilt}) \exp(e \cdot f(\mathbf{v} \times \mathbf{B} \bullet \mathbf{L})) + g(\text{eclipse,sun ram angle}) \cdot 1\mu A .$$

This form was chosen because it accounts for photoemission, uses power laws to fit the primary variables, and varies slightly above and below the null values for variations in tilt and $f(\mathbf{v} \times \mathbf{B} \bullet \mathbf{L})$. Also we know that

$$\exp(x) \approx 1 + x, \text{for } x < 0.5$$

Table 9 shows the values of the coefficients for the fit of the high voltage data (over 40 V) when all the variables are used and when some coefficients are set to zero. Some points to be noted are as follows:

(1) The current shows no significant dependence on the disk potential as represented by $f(\mathbf{v} \times \mathbf{B} \bullet \mathbf{L})$.

(2) The sign of the tilt dependence is consistent with an increased current when the probe is closer to the ram flow. The tilt change during free flight is so small that any dependence on this value is not physically relevant.

(3) The voltage exponent is near 1.4, suggesting orbit-limited collection of whatever plasma is in the vicinity of the probe with an enhancement due to secondary emission.

(4) The density exponent varies from 0.22 to 0.50. This could be due to accidental correlations or differences in the experiment.

(5) The coefficient of determination compares estimated and actual values and ranges from 0 to 1, where 1 indicates a perfect correlation. In these cases, the fit is good.

Table 9. Fit to Data over 40 V.

	Parameter	Fit 1	Fit 2	Fit 3
		Day 39 of 1994		
b	Potential	1.60 (0.02)	1.40 (0.02)	1.38 (0.01)
c	Density	0.50 (0.02)	0.50 (0.01)	0.49 (0.01)
d	Tilt	0	−0.025 (0.001)	−0.026 (0.001)
e	$\mathbf{v} \times \mathbf{B} \bullet \mathbf{L}$	0	0.06 (0.02)	0
η		0.961	0.985	0.985
		Days 256 and 257 of 1995		
b	Potential	1.32 (0.01)	1.35 (0.01)	1.36 (0.01)
c	Density	0.25 (0.04)	0.29 (0.04)	0.22 (0.04)
d	Tilt	0	0.018 (0.005)	0.22 (0.005)
e	$\mathbf{v} \times \mathbf{B} \bullet \mathbf{L}$	0	−2.3 (0.5)	0
η		0.976	0.978	0.977
		Day 258 of 1995		
b	Potential	1.44 (0.01)	1.45 (0.01)	1.45 (0.01)
c	Density	0.30 (0.03)	0.29 (0.03)	0.27 (0.02)
d	Tilt	0	−0.008 (0.002)	−0.009 (0.001)
e	$\mathbf{v} \times \mathbf{B} \bullet \mathbf{L}$	0	0.01 (0.01)	0
η		0.957	0.960	0.959

(η is the the coefficient of determination.)

Table 10 shows similar fits to the low voltage data (10 V to 40 V):

(1) The "coefficient of determination" is lower, indicating that other factors contribute significantly to the current.

(2) The voltage exponent is near 6/7, suggesting space-charge-limited collection of whatever plasma is in the vicinity of the probe. If the density in the wake is proportional to the ram density, this is consistent with the approximate square dependence seen on the ram density. The dependence on density is lower during the free fly period. As the density did not vary much during this period, the fitting coefficient is not accurate.

(3) The tilt dependence appears to be much weaker than in the high voltage case. The inclusion of tilt does not improve the fit. In some cases, the sign of the tilt dependence is consistent with an increased current when the probe is closer to the ram flow. Tilt is not a dominant variable, perhaps because the sheath remains entirely within the wake.

(4) The dependence on $f(\mathbf{v} \times \mathbf{B} \bullet \mathbf{L})$ is larger than for the higher potential measurements. This indicates that the disk potential is more important at lower biases. The sign of the coefficient is such that when the disk is negative, (positive f) the current increases. The value for the free flight period is indicative of an accidental correlation as the distance between the RMS arm and the shuttle engines is not relevant for free flight. Assigning the magnetically-induced potential to an increase in the effective probe potential accounts for only a quarter to a half of the observed effect. We conjecture that the bulk of the effect is due to an attraction of ions into the probe region by the negative induced potential on the disk.

Table 10. Fit to Data from 10 to 40 V.

Parameter		Fit 1	Fit 2	Fit 3	Fit 4
		Day 39 of 1994			
b	Potential	0.82 (0.08)	0.83 (0.07)	0.85 (0.08)	0.82 (0.07)
c	Density	0.63 (0.03)	0.59 (0.03)	0.59 (0.03)	0.61 (0.02)
d	Tilt	0	−0.004 (0.002)	−0.0086 (0.002)	0
e	$v \times B \bullet L$	0	0.14 (0.02)		0.15 (0.02)
η		0.627	0.69	0.646	0.682
		Days 256 and 257 of 1995			
b	Potential	0.85 (0.06)	0.83 (0.05)	0.85 (0.05)	
c	Density	0.18 (0.04)	0.22 (0.03)	0.17 (0.03)	
d	Tilt	0	0.045 (0.005)	0.045 (0.005)	
e	$v \times B \bullet L$	0	−0.11 (0.03)		
η		0.524	0.672	0.641	
		Day 258 of 1995			
b	Potential	0.89 (0.08)	0.90 (0.08)	0.89 (0.08)	0.90 (0.08)
c	Density	0.47 (0.04)	0.54 (0.06)	0.46 (0.05)	0.51 (0.05)
d	Tilt	0	−0.005 (0.007)	0.001 (0.007)	0
e	$v \times B \bullet L$	0	0.080 (0.02)	0	0.08 (0.02)
η		0.438	0.458	0.438	0.457

(η is the the coefficient of determination.)

8.7 Comparison with Calculation

For space charge limited collection and simple geometries

$$I \prec n \times \text{function}\left(\frac{\phi^{3/4}}{n^{1/2}}\right)$$

where function(x) varies from x^1 for one-dimensional systems to $x^{8/7}$ for three-dimensional systems. Orbit limited collection depends on density and potential as

$$I \prec n\,\phi$$

The signature of space charge limited collection in three dimensions is a density exponent of 3/7, which is close to the density dependence of the high voltage measurements. This is consistent with the preflight DynaPAC and POLAR calculations, which showed space charge to be important at high potentials, and that the current scaled approximately as three-dimensional space charge limited collection. The calculations showed a nearly linear voltage dependence at high potentials, above the 6/7 power expected for pure space charge limited collection. If we assume an approximate square root dependence of the secondary emission on the potential, the high potential flight measurements are consistent with the preflight calculations.

The preflight calculations with an oxygen plasma show a potential threshold. If 10 percent of the plasma is hydrogen, the threshold disappears. The size of the currents at low biases suggests that the shuttle plasma includes a large component of slow moving ions. The low potential measurements have potential and density dependencies in between space charge limited and orbit limited. Since the currents at the lowest bias values are below the theoretical plasma thermal current to the probe with no bias, the wake plasma must have a lower density than the ram plasma.

The preflight DynaPAC and POLAR calculations showed a threshold for ram oxygen collection at about 100 volts of negative bias. In the flight data, current was collected with only a few tens of volts. This might be due to either hydrogen or slow-moving spacecraft generated ions. Figure 59 shows that for the lowest (10 V) bias the collected current is consistently about one order of magnitude

100

below what would be collected by a stationary unbiased probe in the measured ambient plasma. Assuming orbit-limited collection, this implies a plasma density in the probe region about three orders of magnitude below ambient. Such a density is far higher than the theoretical values in a spacecraft wake, but may well be consistent with a plasma due to thrusters, outgassing, and other contamination sources.

8.8 Probe in Ram Measurements

Three sets of measurements were made with the wake side probe exposed to the ram flow on day 258 of 1995. We consider all measurements in which the absolute value of the tilt is above 40 degrees to be ram measurements. The measurements are shown in Figure 61. The first set were made at about 62300 s. The shuttle was rolled about its long axis with WSF above the bay and its edge toward the shuttle. During this period, the plasma density probably varied from about 10^5 to 10^6 cm^{-3}. The second set were made at about 33500 s. At this time the disk was at a tilt of 41 and 42 degrees. The plasma density was near 10^6 cm^{-3}. The third set were taken while the wake side of WSF was exposed directly to ram at the end of the measurement period. The IRI model gives a plasma density of about 2×10^5 for this period.

Day 258 of 1995
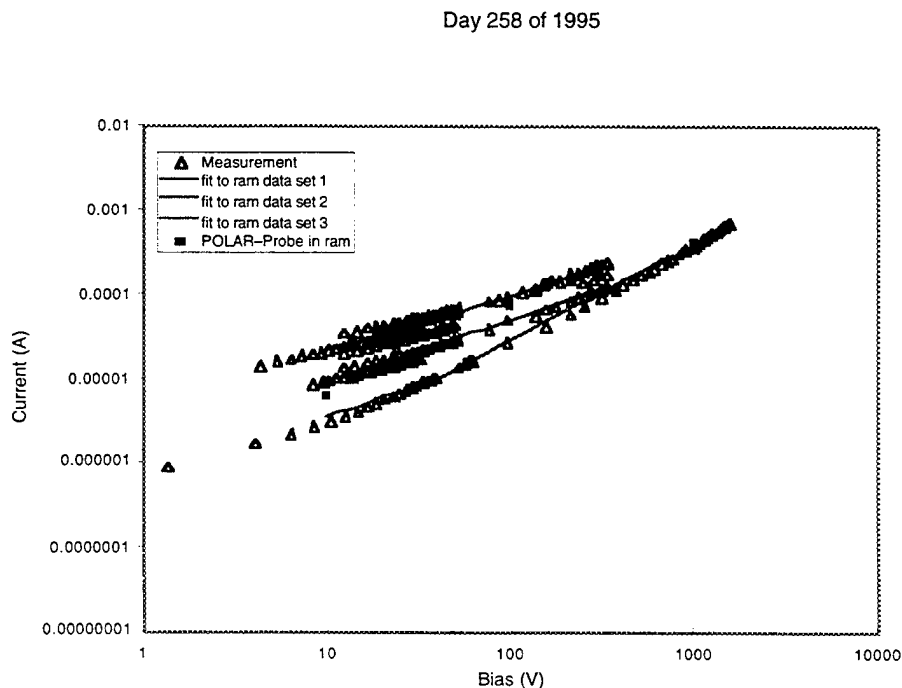
Figure 61. Current as a function of applied bias for measurements in which the absolute value of the tilt is above 40 degrees. (Probe in ram flow.)

If we fit the three sets of ram facing measurements to the function

$$I = a \, \phi^b$$

we get the coefficients shown in Table 11. The resulting curves are plotted in Figure 61.

Table 11. Fits to Ram Facing Data

	32300 s	33500 s	40500 s
a for $\phi < 40$ V	2.1335E-06	5.6646E-07	6.9142E-06
b for $\phi < 40$ V	0.62680257	0.76995794	0.50244858
a for $\phi > 40$ V	1.4772E-06	1.3479E-07	3.8995E-06
b for $\phi > 40$ V	0.75482842	1.14960772	0.68816357

Prior to the first flight of CHAWS, Dr. David Cooke of Phillips Laboratory used the POLAR code to compute the current collected by an isolated probe of the size and shape of the CHAWS probe in a 10^{11} m^{-3}, 0.1 eV, mach 7.1 atomic oxygen plasma. The results of these calculations are shown in Figure 61 for comparison. The calculations show a current of approximately the same magnitude, but a different slope than the flight results.

8.9. WSF in Shuttle Wake

A set of measurements were made while WSF was in the wake of the shuttle. For this time period IRI gives the plasma density as near 10^5 m^{-2}. These measurements are shown in Figure 62. The currents are lower than in any other measurements. Table 12 shows coefficients for a fit to these measurements using the same functional form as for the ram facing measurements. This fit is also plotted in Figure 62. We also did a single calculation at 2000 V using DynaPAC for a plasma density of 10^{10} m^{-3} and this geometry. The result of this calculation is also shown in Figure 62. The measured current is much higher than the calculated current indicating that the actual density in the shuttle wake is much higher than the calculated density. As both hydrogen and species originating at the shuttle are present this is not surprising.
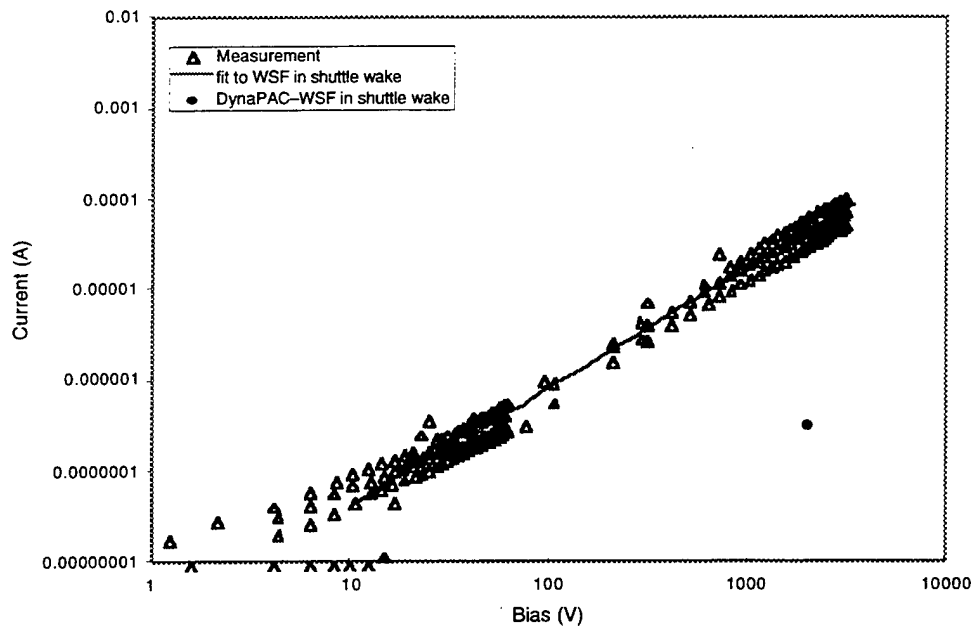
Figure 62. Current versus applied bias for WSF in shuttle wake.

Table 12. Fits to WSF in Shuttle Wake Data

a for $\phi < 40$ V	1.7249E-09
b for $\phi < 40$ V	1.36100094
a for $\phi > 40$ V	1.6984E-09
b for $\phi > 40$ V	1.32637772

8.10 Additional Material

The following describes how chunks, a couple of short specialized FORTRAN programs and EXCEL 5.0 can be used to create this report. It is assumed that the reader is fortran and unix literate.

Step 1 – Run Chunks

103

Documentation for chunks is available with the "official" version of this software. The following script and input files were used.

```
rm inputs
ln inputs.39early inputs
chunks > output.39early
mv output_CHA_current current.39early
rm inputs
ln inputs.39 inputs
chunks > output.39
mv output_CHA_current current.39
rm inputs
ln inputs.256 inputs
chunks > output.256
mv output_CHA_current current.256
rm inputs
ln inputs.257 inputs
chunks > output.257
mv output_CHA_current current.257
rm inputs
ln inputs.258 inputs
chunks > output.258
mv output_CHA_current current.258
```

Figure 63. Script used to run chunks.

104

```
start_date      39:03:30:00        day:hr:min:sec
 stop_date      39:04:25:00        day:hr:min:sec

stdio_cas               1       stdio_switch
stdio_wsf               1       stdio_switch
stdio_chaws             1       stdio_switch
stdio_merge             1       stdio_switch
logical                 0       on/off

output_CAS              0       on/off
output_CAS              1       GMT_ut
output_CAS              2       Orbiter.pitch
output_CAS              3       Orbiter.yaw
output_CAS              4       Orbiter.roll
output_CAS              5       latitude
output_CAS              6       longitude
output_CAS              7       sun_angle

output_WSF              0       on/off
output_WSF              1       ram_angle
output_WSF              2       xz_tilt
output_WSF              3       xy_wag
output_WSF              4       vxb_dot_L
output_WSF              5       solar_el
output_WSF              6       solar_az

output_CHA_frame        0       on/off
output_CHA_frame        1       ram_hp_eng01
output_CHA_frame        2       ram_hp_eng2345
output_CHA_frame        3       ram_hp_eng67
output_CHA_frame        4       ram_inboard_dens
output_CHA_frame        5       ram_center_dens
output_CHA_frame        6       ram_outboard_dens

output_CHA_channel      0       on/off

output_CHA_current      1       on/off
```

Figure 64. Standard input for chunks execution.

start_date	39:15:55:00	day:hr:min:sec
stop_date	39:19:50:00	day:hr:min:sec
start_date	256:19:13:00	day:hr:min:sec
stop_date	256:20:10:00	day:hr:min:sec
start_date	257:06:27:00	day:hr:min:sec
stop_date	257:07:50:00	day:hr:min:sec
start_date	258:08:07:00	day:hr:min:sec
stop_date	258:11:20:00	day:hr:min:sec

Figure 65. Modified dates used for other chunks executions.

The stdio params control the print to standard output. The logical switch controls the column order of merged output. The output_CAS, output_WSF, and output_frame, output_CHA_channel commands control the generation of separate files of CAS, WSF, and single frame, and single channel data. The variables are GMT_ut, universal time in seconds constructed from the CAS data structure, Orbiter.pitch, Orbiter.yaw, Orbiter.roll (directly from the CAS data structure), latitude, longitude, (as computed by CHAPS), sun_angle, (negative value means eclipse) ram_angle, xz_tilt, xy_wag, vxb_dot_L, solar_el, solar_az, ram_hp_eng01, ram_hp_eng2345, ram_hp_eng67, (the last energy at which the ram mcp distribution falls to 0.5 times the count for 0 V based on the summed contributions from the indicated detectors) ram_inboard_dens, ram_center_dens, ram_outboard_dens (calibrated density for the ram side detectors using a mach value of 5).

The output_CHA_current controls the printing of the additional file output_CHA_current. It contains currents extracted from within a CHAWS 7.5 sec frame according to a fixed pattern. The pattern used is as follows. For step 1: volts is average of voltages 1 to 4; current is average of channels 60 to 68, for step 2: volts is average of voltages 5 to 6; current is average of channels 108 to 116, for step 3: voltage 7; current is average of channels 132 to 140, for step 4: voltage 8; current is average of channels 148 to 156. The contents are CHAWS time = day and total seconds (2 integers), langmuir voltage = lv or hv from stencil, depending on saturation (float), langmuir current = from stencil (float), langmuir sweep profile and status flag (2 integers), delta between stencil voltages (float), goodness flag: =1 if voltage > 2.5, =2 if also delta > 0.0 (integer), event and sweep counters (2 integers). The event counter tries to flag "interesting" events. the

event counter is incremented if there was a transition from goodness flag 0 to 2. It is printed until there is a departure from goodness = 2, then it shows 0. The sweep counter tries to flag good sweeps. Note that there are 4 steps per frame, and thus 4 goodness flags per frame. The sweep counter is incremented if there are more than 6 consecutive good ,where a good frame is one with 2 or more steps having goodness flags that are = 2

Step 2 – Filter Chunks Output

The standard output files from Chunks include lines indicating that WSF data is missing. As these lines are of no use to us (at least here and now) we use grep to eliminate them. We use a short fortran program called process to pick out the clean measurements (event counter has a nonzero value) from the i-v curves. The script used to do this and the program process follow. Then by hand we removed lines in the out* files at the beginning and end that correspond to times not represented in the ave* files. This is not necessary.

```
grep -v WSF output.39early > out.39early
process < current.39early > averaged.39early
grep -v WSF output.39 > out.39
process < current.39 > averaged.39
grep -v WSF output.256 > out.256
process < current.256 > averaged.256
grep -v WSF output.257 > out.257
process < current.257 > averaged.257
grep -v WSF output.258 > out.258
process < current.258 > averaged.258
```

Figure 66. Script used to prepare chunks output files for EXCEL.

```
      print 1100
1100        format (' Time        Potl        Current')
            do 20 i=1,400000
               read *, day,time,pot,cur,t1,t2,t3,t4,t5,t6
               if (pot.gt.1..and.cur.gt.5.87e-9.and.t6.gt.0)
     &                              print 1200, time,pot,cur
1200            format (1x,g15.7,g13.5,1g12.4)
20          continue
999         continue
            stop
            end
```

Figure 67. Source code for program process.

Step 3 – Transfer files to EXCEL.

107

APPENDIX A

A copy of the SPEAR-2 Products Report follows:

CHAPTER 9

THEORETICAL AND COMPUTER MODELING SUPPORT FOR SPEAR II

M. J. Mandell, I. Katz, G. A. Jongeward,
V. A. Davis, D. E. Parks
S-CUBED Division, Maxwell Laboratories Inc.,
and D. L. Cooke, Phillips Laboratory

9.1 DEVELOPMENT AND APPLICATION OF PLASMA INTERACTION MODELS FOR REALISTIC HIGH-POWER SPACECRAFT

9.1.1 Introduction

Recognizing that an understanding of the ambient plasma interactions with high-voltage, pulsed power systems was essential for the development, testing and flight of SPEAR II, and for extending the SPEAR II technology to other systems and environments, two existing S-Cubed plasma simulation codes, NASCAP/LEO and Gilbert, were extensively utilized during the SPEAR II program. In addition, since there were requirements for simulations which were both dynamic and fully three-dimensional, which could not be done with these codes, the SPEAR II program contributed to the development of the DynaPAC (Dynamic Plasma Analysis Code) code [1].

NASCAP/LEO is a three-dimensional computer code developed by the NASA/Lewis Research Center [2] for the study of high-voltage plasma interactions and the design of high-voltage systems in LEO. It has been successfully applied to numerous laboratory and spaceflight experiments [3-9]. NASCAP/LEO was successfully used to predict plasma currents and floating potentials for SPEAR I, whose geometry, while truly three-dimensional, was relatively simple. The SPEAR II mock-up and chamber tests showed, for the first time, that NASCAP/LEO could predict sheath plasma currents for a complicated geometry.

Gilbert is a general-purpose, two-dimensional, plasma and electrostatic analysis code developed internally by S-Cubed. The Gilbert calculations performed for the SPEAR II program provided important quantitative assessments of the validity of space plasma simulations using laboratory chambers. Experiments showed that the computational techniques used in Gilbert were accurate enough to be used in the design of independent components for space-based power systems. Pending development of a 3-D dynamic code, transient-to-equilibrium current scaling relations developed using Gilbert were coupled with NASCAP/LEO sheath calculations in the "equilibrium" and "frozen-ion" approximations to make successful pretest estimates of enhanced transient currents to the SPEAR II payload.

DynaPAC is a fully three-dimensional, dynamic plasma interaction code which includes, through models developed and validated as a part of the SPEAR program, much of the knowledge of plasma physics and system/plasma interactions gained during the SPEAR program. The code allows the SPEAR II laboratory data to be extended to orbital plasma conditions for systems using different geometries.

9.1.2 Prior State-of-the-Art

The SPEAR I laboratory and flight experiments, along with three-dimensional computer modeling, demonstrated the capability to predict steady state interactions between geometrically simple high-voltage spacecraft and the space plasma. However, the ability to make calculations for spacecraft which are truly geometrically complex had not been demonstrated. In addition, neither the time-dependent response of the space plasma to the high fields and voltages associated with pulsed power systems like SPEAR II nor the associated dynamic spacecraft charging had been fully investigated. Processes not adequately modeled include: formation of the space charge sheath, current flow in the quasi-neutral pre-sheath, breakdown phenomena, plasma kinetics, ionization processes, and the effect of dynamic processes on spacecraft charging.

These inadequacies became apparent in trying to make plasma interaction predictions for the SPEAR II high-voltage system. Equilibrium sheath calculations (e.g., using NASCAP/LEO) gave very different results from sheath calculations using short time approximations. Therefore the plasma currents to the high-voltage components could not be calculated with confidence. Existing Particle In Cell (PIC) codes had neither the generalized geometry necessary for realistic systems nor the sophisticated algorithms required to make simulations of the SPEAR II payload possible in a reasonable amount of computer time. Two dimensional dynamic codes, such as Gilbert, could give only a hint of the detailed information needed for the design of complex three-dimensional systems.

9.1.3 Innovative Concepts

NASCAP/LEO was the first code to combine plasma sheath physics with fully CAD/CAM compatible, three-dimensional geometry. Thus, it was the first code with the ability to model a payload with the geometrical complexity of SPEAR II.

A "frozen ion" capability was developed and incorporated into NASCAP/LEO in order to provide estimates of very early time plasma sheath currents. In the frozen ion approximation, the time scales are assumed to be short enough that inertia prevents the ions from moving under the influence of the fields. This was a stop-gap method for calculating time-dependent currents to the SPEAR II payload prior to the development of the DynaPAC code.

The Gilbert code uses grids created with commercial finite element programs (such as PATRAN [10]). This enables the use of grids with variable resolution in order to model processes in detail, where needed, while still modeling extended range interactions. Higher-order finite elements with continuous electric fields and a third-order particle tracking algorithm are used in order to obtain the accuracy needed for time-dependent calculations. The code allows the appropriate plasma description to be chosen for the problem under consideration. Models based on particle tracking, analytic formulas and hybrid methods are available. The code is written with advanced programming and numerical techniques to take advantage of modern computational capabilities and to promote ease of use, ease of modification and data interchange with other codes.

In order to model SPEAR laboratory experiments (described later in this chapter), an internal boundary condition to mimic the presence of a grid (made of ordinary window screen) was developed and incorporated into Gilbert. It was shown that the mean potential of the screen was related to the electric field discontinuity across the screen.

The data from space simulation chamber tests of the SPEAR II payload revealed the importance of transient plasma phenomena to high-voltage power systems. A screen-

handler utility provides for interactive input file generation. DynaPAC's DataBase Manager is a programmer-friendly way of allocating, storing and retrieving large blocks of gridded or otherwise structured data. DynaPAC pioneers the use of higher order elements that produce strictly continuous electric fields and potentials. Arbitrarily nested grids accommodate simulations of complex systems with extended-range plasma interactions. Graphical display is available using a variety of graphics interfaces, including the X-Windows protocol, which allows display from a remote host.

9.1.4 Description of Code

9.1.4.1 Description of the NASCAP/LEO Steady State Plasma Sheath Code.
NASCAP/LEO [2,4] is a three-dimensional, finite-element code based on a cubic grid structure. For NASCAP/LEO, a spacecraft is defined as a boundary surface element representation using any standard finite element preprocessor. NASCAP/LEO places the spacecraft within a cubical grid structure, and geometrical descriptions and coupling matrices are constructed for cubic zones containing the object surfaces. Local subdivision of the basic grid is used to resolve critical regions, and nested outer grids are used to include a large volume of space.

NASCAP/LEO was used to calculate the plasma current distributions to the SPEAR II payload. Such calculations are based on the concept that a high-voltage object in a dense plasma forms a sheath within which the plasma is highly disturbed, and outside of which the plasma is quiescent. All of the computer codes described in this chapter solve Poisson's Equation in various ways. In order to achieve short computational times, NASCAP/LEO does not use particle trajectory information to calculate the spacecharge density appearing in Equation (9-1). Poisson's equation is given as

$$-\varepsilon_o \nabla^2 \phi = \rho. \tag{9-1}$$

Instead, a nonlinear analytic expression for the charge density as a function of the local potential and electric field, based upon a spherical sheath, is used

where:

ρ = space charge (coul-m^{-1}),

ε_0 = 8.854x10^{-12} (farad-m^{-1}),

λ_D = plasma Debye length (m),

θ = plasma temperature (eV),

ϕ = local space potential (volts),

E = local space electric field (volts-m^{-1}),

$$\rho / \varepsilon_0 = -(\phi / \lambda_D^2)(1 + |\phi / \theta| C(\phi, E)) / (1 + (4\pi)^{1/2} |\phi / \theta|^{3/2}),$$

$$C(\phi, E) = |\theta / \phi| \left[(R_{sh} / r)^2 - 1 \right], \text{ and} \tag{9-2}$$

$$(R_{sh} / r)^2 = 2.29 |E\lambda_D / \theta|^{1.262} |\theta / \phi|^{0.509}.$$

111

The sheath structure is usually spherical where the charge density most greatly influences the potential, so Equation (9-2) is a good approximation for the LEO environment.

Using Equation (9-2) for the space charge within the sheath region, together with the appropriate boundary conditions at surfaces, NASCAP/LEO solves Equation (9-1) to determine the electrostatic potential about a spacecraft with a highly complex geometry. Once the potential field is known, the sheath boundary can be identified, and plasma ions and electrons crossing the sheath boundary can be tracked to determine the current distribution on the spacecraft.

9.1.4.2 Gilbert 2-D Dynamic Plasma Code. Gilbert is a two-dimensional (R-Z or X-Y), finite element computer code. It solves Poisson's Equation [Equation (9-1)] and performs particle generation, tracking and deposition on a grid whose elements may be linear triangles, bilinear quadrilaterals and/or biquadratic quadrilaterals. A commercial finite-element preprocessor (such as PATRAN [10]) is used to generate the grid. Sequences of nodes can be specified for use in assigning electrostatic boundary conditions or as current sources. Elements can be specified as empty-space or dielectric-filled (with optional conductivity).

Gilbert is highly modular and flexible. Preprocessors are used to interpret the finite element grid input and to generate initial particle distributions. The main analysis routine solves problems either by time-stepping or by iteration on a nonlinear problem. Postprocessors display potential contour plots, particle scatter plots and time history plots, and generate and display particle trajectories.

9.1.4.3 DynaPAC Three-Dimensional Dynamic Plasma Code. DynaPAC was designed to perform static or dynamic plasma calculations for geometrically complex problems. It was written to take advantage of modern techniques for input generation, problem solution and visualization. The core modules of DynaPAC allow the user to:

(1)   define the spacecraft geometry and the structure of the computational space,

(2)   solve the electrostatic potential about the spacecraft, with flexible boundary conditions on the spacecraft surfaces and a space charge computed either fully by particles, fully analytically, or in a hybrid manner, and

(3)   generate, track, and otherwise process representative macroparticles of various species in the computational space.

The core modules were designed to have the maximum practical user control and to facilitate the incorporation of new or modified algorithms. Preprocessors are provided to set boundary conditions and generate input files in a modern, screen-oriented way. Similarly, screen-oriented postprocessors are provided for graphical and textual data display.

Spacecraft geometrical definitions are done using standard finite element preprocessors, such as PATRAN [10]. Advantages of this approach are that the geometry can be realistically represented, and that finite element models of a spacecraft, constructed for other purposes, can be adapted for plasma calculations. The computational space around the spacecraft is constructed interactively using the GridTool module. Arbitrarily nested subdivision allows resolution of important object features while including a large amount of space around the spacecraft. A high-order, finite element representation for the electrostatic potential ensures that electric fields are strictly continuous throughout space.

112

The electrostatic potential solver uses a conjugate gradient technique to solve for the potentials and fields on the spacecraft surfaces and throughout the surrounding space. Five space charge options presently incorporated include: Laplacian (appropriate in the absence of plasma), equilibrium sheath (appropriate to timescales of milliseconds or longer), "frozen ions" (appropriate to the submicrosecond stage of a negative transient pulse), "mobile ions - barometric electrons" (appropriate to the SPEAR II case of several microsecond time scale response to a negative pulse), and "full PIC" (appropriate to nanosecond timescales).

Particle tracking is used to study sheath currents and particle trajectories, or to generate space charge evolution for dynamic calculations. Macroparticles can be generated at either a "sheath boundary" or throughout all space. Particles are tracked for a specified amount of time, with the time step automatically subdivided at each step of each particle to maintain accuracy. The current to each surface cell of the spacecraft is recorded for further processing.

The strength of DynaPAC lies in the wide range of length scales, time scales and physical phenomena it can handle. Arbitrarily nested subdivision allows the modeling of small geometrical features within large scale problems (e.g., features a few centimeters in size in sheaths several meters in dimension). By suitable choice of algorithms, a user can model equilibrium problems, problems dynamic on an ion timescale (microseconds), or problems dynamic on an electron timescale (nanoseconds). Trajectories are calculated taking account of user-specified magnetic fields, and it is planned to introduce a procedure to obtain potential and space charge fields consistent with magnetic effects.

9.1.5 Gilbert Application to High-Voltage Breakdown Experiments

The SPEAR program supported a series of experiments at Maxwell Laboratories, Inc., to systematically study the influence of a background plasma in promoting the breakdown of representative high-voltage fixtures [11]. Figure 9-1 shows a typical test fixture, consisting of a 1 cm diameter electrode protruding from a 3 cm diameter insulator, which was embedded in a 7 cm diameter ground plate. In vacuum, this fixture would hold off a few kilovolts indefinitely with the center electrode at a negative potential; however, in a plasma, the insulator surface would flash over in a short time.

If the plasma-induced discharge resulted from electric field modification by plasma charge collected on the dielectric surface, we would expect the hold-off time to be inversely proportional to the plasma current. Supposing this to be the case, a hemisphere of ordinary aluminum window screen was mounted on the fixture in order to reduce the total ion current collected. Calculations showed that the screen would reduce the ion current by approximately a factor of five. Experimentally, the screen was found to increase the holdoff time from 30 ms to 30 s at -2.5 kV, and from 15 ms to 5 s at -5.0 kV in a background plasma density of 4×10^5 cm^{-3}. This increase in the holdoff time was too great to be explained solely in terms of the total plasma current to the fixture.
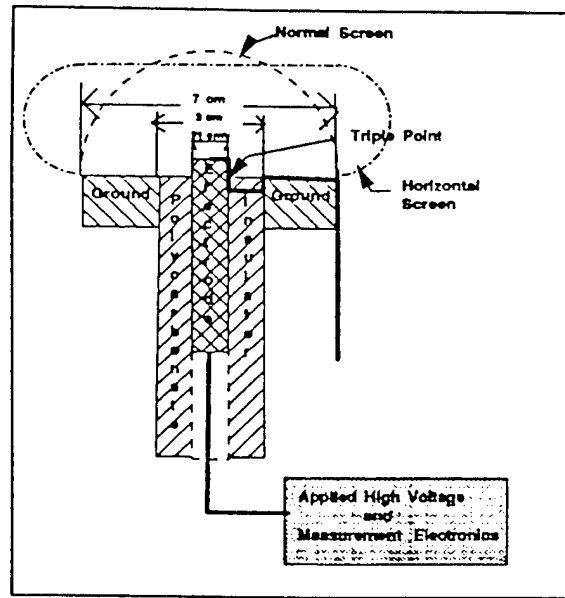
Figure 9-1. Typical axisymmetric test fixture for high voltage breakdown experiments. Two alternative discharge-mitigation screens are shown. The heavy solid line indicates the fixture outline as seen in Figures 9-2 through 9-4.

Calculations of the plasma ion trajectories, performed with the Gilbert code, were used to attempt to understand this phenomenon. Figure 9-2 shows the trajectories of ions impinging on the original fixture (without the screen). It is apparent that ions impacted the entire surface of the fixture, including the sensitive "triple point" area where the insulator contacts the high-voltage electrode.

In order to study the ion trajectories in the presence of the screen, it was necessary to develop an internal boundary condition that would mimic the presence of the screen. It was found that the mean potential of the screen was related to the electric field discontinuity across the screen. Figure 9-3 shows the ion trajectories with the "normal" screen present. The ion current is focused on the top of the center electrode, with no calculable ion current to the triple point. Thus, the effect of the screen was to steer plasma ions away from the triple point, in addition to reducing the total ion current to the fixture.

In order to confirm this finding, a further calculation was performed which showed that if the screen was configured horizontally at its attachment point, then there would be calculable current to the triple point (Figure 9-4). The fixture with the horizontal screen broke down in 40 ms with an applied voltage of -15 kV and a plasma density of 8×10^5 cm^{-3}, compared with 750 ms for the normal screen. Additional calculations and experiments, involving larger fixtures and various screen shapes, showed good correlation between rapid breakdown and the calculated ion current to the triple point (see Table 9-I). These studies also illustrated that trying to improve breakdown characteristics by the obvious step of enlarging the insulator may, in fact, promote breakdown by reducing the electrostatic-inertial insulation of the triple point. These results show the utility of accurate two-dimensional potential and trajectory calculations in designing axisymmetric high-voltage fixtures for maximum holdoff time.

114
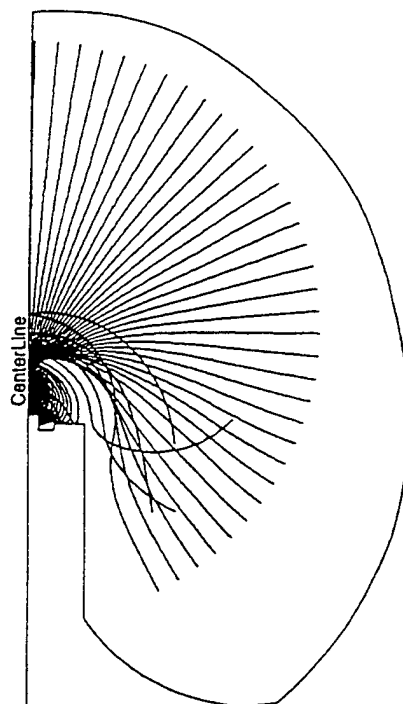
Figure 9-2. Ion trajectories to the test fixture without the screen, indicating substantial current to the triple point. (Refer to Figure 9-1 to relate the fixture outline to the actual fixture).
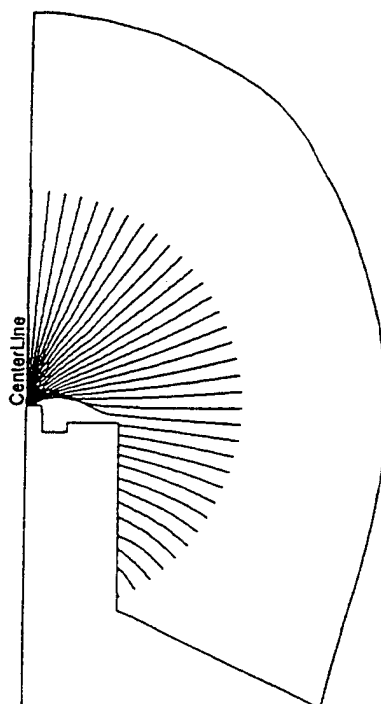
Figure 9-3. Ion trajectories to the test fixture with the normal screen, indicated no calculable current to the triple point. (Refer to Figure 9-1 to relate the fixture outline to the actual fixture).
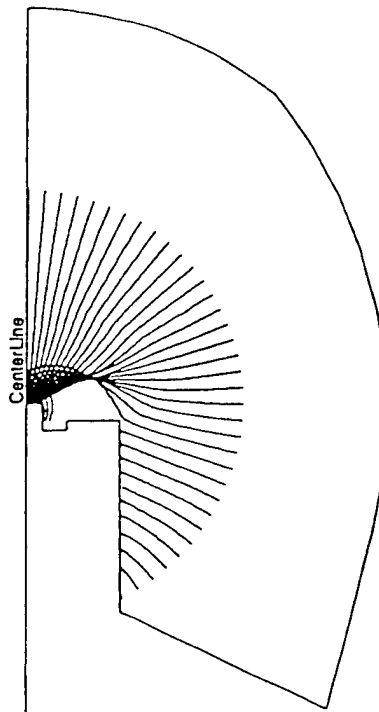
Figure 9-4. Ion trajectories to the test fixture with the horizontally configured screen, showing ions incident on the insulator near the triple point. (Refer to figure 9-1 to relate the fixture outline to the actual fixture).

Table 9-I. Holdoff Time for Various Insulator Widths and Screen Shapes

Insulator Width	Applied Voltage	Time to Breakdown	Trajectories to Triple Point
1.0 cm (n)	-15 kV	750 ms	No
1.0 cm (h)	-15 kV	40 ms	Yes
1.0 cm (n)	-50 kV	20 ms	No
2.0 cm (n)	-50 kV	70 ms	No
4.5 cm (l)	-50 kV	7 ms	Yes
4.5 cm (s)	-50 kV	3 ms	Yes

Time to breakdown for fixtures with differing insulator widths is shown. The plasma density was 8×10^5 cm^{-3}. The screen shapes are (n) normal screen (Figure 9-1), (h) horizontal screen (Figure 9-1), (l) "long" screen (not shown) and (s) "short" screen (not shown).

9.1.6 Code Calculations for SPEAR II

9.1.6.1 Gilbert Small Chamber Model for SPEAR II. The SPEAR II payload was first tested with a background plasma in a small vacuum chamber at Maxwell Laboratories, Inc. It was observed that the high-voltage system 10 μs pulses were more likely to cause breakdown than the 3 or 50 μs pulses. This finding motivated a computer simulation using Gilbert of the plasma interactions in the small chamber to determine if plasma dynamic effects might be responsible for this phenomena.

Figure 9-5 shows an artist's concept of the two-dimensional axisymmetric representation of the payload used in the calculation. A grid was constructed to represent the space between the model and chamber walls, and ion macroparticles were placed in the grid to represent an initial uniform Ar plasma with a density of 1×10^5 cm^{-3}. The applied voltage on the model was increased with a risetime appropriate to the pulse width under study, and the ions were allowed to move in the resulting fields.
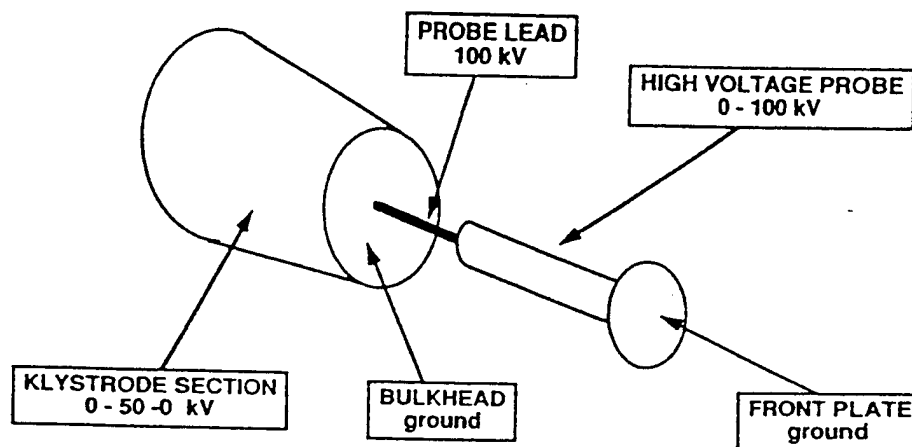
Figure 9-5. **Artist's representation of the axisymmetric model of SPEAR II used in the two dimensional plasma dynamic studies. The labels indicate the peak potentials applied to each component: -100 kV on the probe lead, a linear gradient on the high voltage probe from -100 kV on the probe lead, a linear gradient on the high voltage probe from -100 kV at the probe lead to 0 at the front plate, and on the Klystrode section (representing a cavity partially enclosed by several struts) linear gradients from 0 at either end to -50 kV at the center.**

Figure 9-6 shows the ion macroparticle positions 4 µs into the pulse. The ions are focused on the high-voltage end of the voltage divider, precursive to the results later obtained in three dimensions with DynaPAC. By this time, about half the plasma ions (which initially filled the chamber with a nearly uniform dot pattern) are gone. The chamber will be almost completely drained of plasma ions within about 10 µs. (The plasma source is not able to replenish the plasma on such a short timescale).

117

KLYSTRODE
SECTION →

PLASMA
SOURCE ←

↑
VOLTAGE DIVIDER
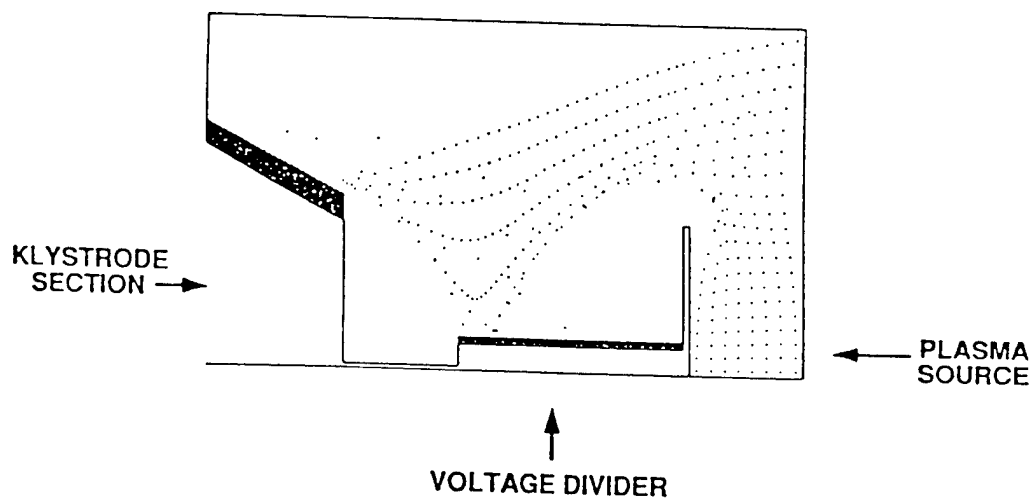
Figure 9-6. Gilbert-calculated ion macroparticle positions 4 µs into a SPEAR II high voltage pulse.

Figure 9-7 shows the calculated current to the payload for two cases: (1) a risetime of 1.5 µs (characterizing the 3 µs and 10 µs SPEAR II high-voltage pulses), and (2) a risetime of 3 µs (characterizing the 50 µs high-voltage pulse). The peak current occurred at about 3 µs into the pulse for both cases, but it is noticeably higher for the 1.5 µs risetime pulse. There is no current beyond 10 µs, as the chamber is drained of plasma. The suggested interpretation is that:

(1) The 3 µs pulse does not lead to breakdown because the pulse is over when the current peak occurs.

(2) The 10 µs pulse is more likely to cause breakdown than the 50 µs pulse due to the higher peak incident ion current.

(3) Extending the pulse beyond 10 µs does not lead to breakdown because there is no further ion current to the payload.

118
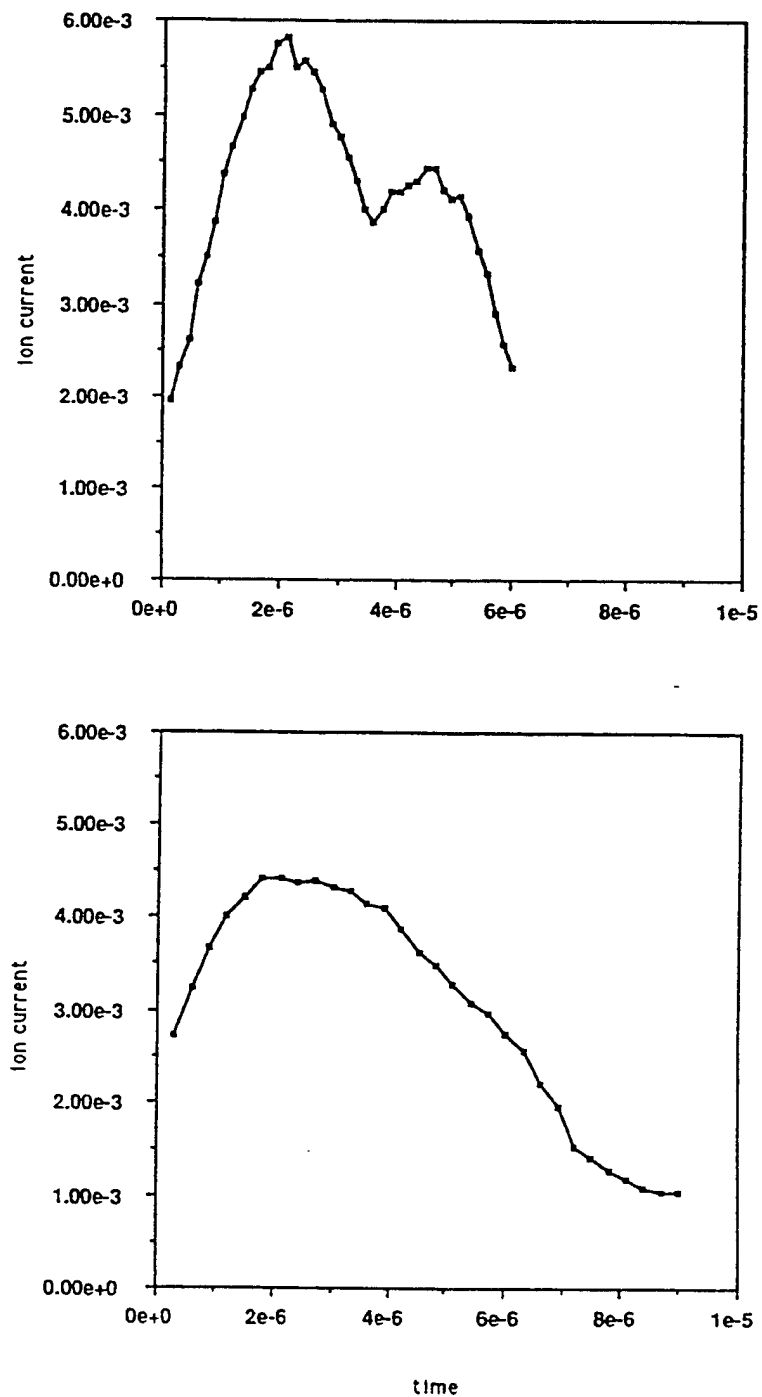
Figure 9-7. The calculated ion currents to the axisymmetric model for 1.5 and 3 μs rise time pulses (see text for explanation).

The overall conclusion from these calculations is that a small chamber may produce results unrepresentative of the behavior of a system in a very large chamber or in the ionosphere.

119

9.1.6.2 SPEAR II Geometrical Model for NASCAP/LEO and DynaPAC.
Figure 9-8 shows the geometrical model of the SPEAR II payload used for the NASCAP/LEO and DynaPAC calculations. (The identical model was used for the SPEAR II mock-up.) This geometry was based on the EUCLID (an engineering drafting and modeling product [12]) model constructed by Westinghouse, and it was converted to a PATRAN (a finite element modeling code [10]) model using IGES (Initial Graphics Exchange Specification protocol [13]) files as an intermediate transfer mechanism. The PATRAN "Neutral File" (specifying node locations and surface element connectivities, material numbers and conductor numbers) is read by the object definition interface module of either code, which places the object in the grid system and performs other appropriate preprocessing.
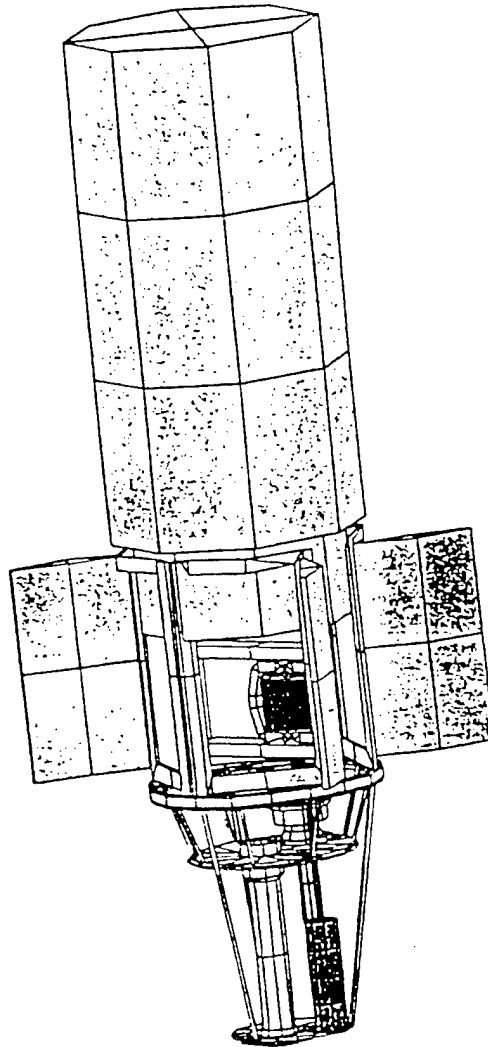
Figure 9-8. Geometrical model of the SPEAR II payload used in the NASCAP/LEO and DynaPAC calculations.

Figure 9-9 shows the DynaPAC grid for SPEAR II, illustrating the arbitrarily nested subdivision capability. The grid spacing ranges from one meter (outermost grid, not shown) to 3 cm in the payload interior. The NASCAP/LEO grid had a basic mesh size of 16 cm, with subdivided regions down to 4 cm, and surrounding outer grids up to 64 cm.

120

Mesh Size = 5.0000E-01 meters
Date: 02-14-91
Time: 16:15:43
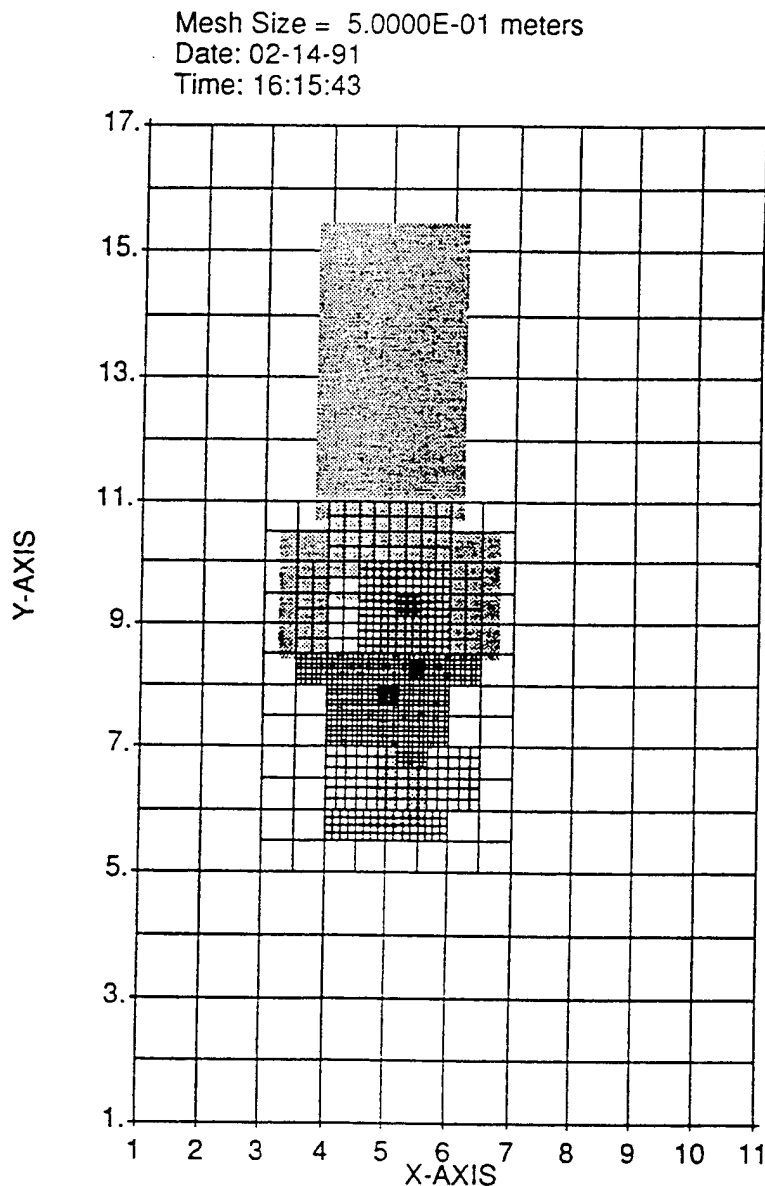
Figure 9-9. **DynaPAC grid for SPEAR II. (The outmost grid, with 1 meter mesh spacing, is omitted).**

9.1.6.3 NASCAP/LEO Calculations for SPEAR II. Prior to the development of DynaPAC, NASCAP/LEO was the only plasma interaction code capable of predicting sheath currents and potentials for a payload with the geometrical complexity of SPEAR II. It was recognized that the "equilibrium" plasma treatment used in NASCAP/LEO was not appropriate to the SPEAR II high-voltage pulse lengths. Nonetheless, predictions made using an equilibrium code were better than no predictions at all. Figure 9-10 shows the NASCAP/LEO calculated equilibrium sheath contours for SPEAR II.

121
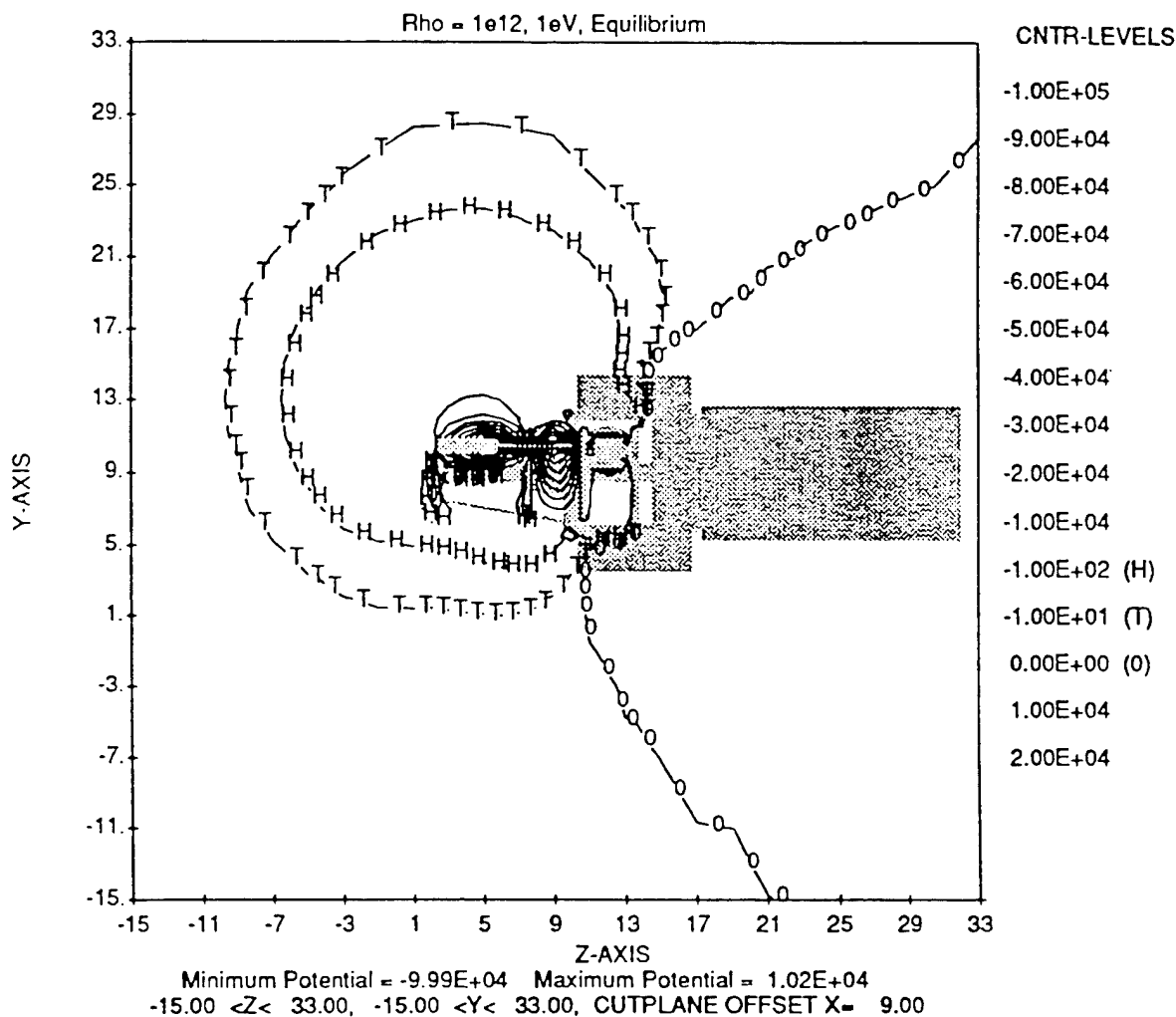
Figure 9-10. NASCAP/LEO calculated equilibrium sheath ("H" contour) about SPEAR II under laboratory conditions (1×10^6 cm^{-3}; 1 eV). Space charge densities are calculated using formulas appropriate to a steady-state plasma sheath (e.g., Langmuir-Blodgett). The shaded area represents the projection of the payload on the contour plans, and the equipotential lines with 10 kV spacings appear near the payload. The contour at -100 volts (marked "H") is considered the sheath contour because the potential should drop to zero within 0.3 meters of the -100 volt equipotential surface. Also shown are contour lines at -10 volts (marked "T") and at zero volts (marked "0"). The payload ground surface is at +100 volts. The horizontal and vertical axes are marked in units of 16.3 cm.

As part of the SPEAR program, a "frozen ion" approximation was added to NASCAP/LEO. In the "frozen ion" approximation, it is assumed that electrons instantaneously attain an equilibrium distribution, but ions do not move. The space charge function, Equation (9-2), is thus replaced by

$$\rho / \varepsilon_0 = 0 \qquad ; \qquad \phi \geq 0,$$

$$\rho / \varepsilon_0 = (\theta / \lambda_D^2)\left[1 - e^{\phi/\theta}\right] \qquad ; \qquad \phi \leq 0. \qquad (9\text{-}3)$$

This approximation (appropriate up to about 1 μs for SPEAR II parameters) provided a means for calculating sheath sizes during the short SPEAR II high-voltage pulses (Figure 9-11). However, it did not provide any straightforward means of · calculating the transient currents to the payload or the time dependence of the currents and sheath structure.
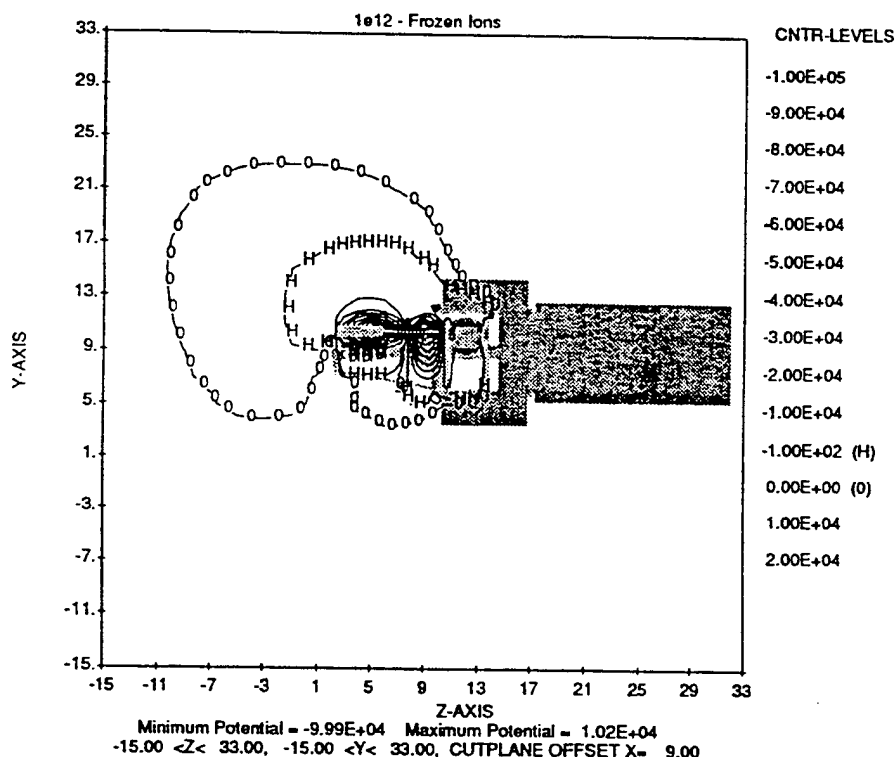
Figure 9-11. NASCAP/LEO calculated "frozen ion" sheath ("H" contour) about SPEAR II under laboratory conditions. Space charge densities are calculated assuming that ion motion is negligible (appropriate to times up to a few microseconds). Otherwise, the description of Figure 9-10 applies. Note that the transient sheath is far smaller than the equilibrium sheath, leading to considerably elevated currents in the transient regime.

The first question to be addressed using NASCAP/LEO was the floating potential of the payload during high-voltage operation. It was not sufficient simply to assume that the floating potential would be a small fraction of the 100 kV operating potential, since a floating potential exceeding 1 kV would cause unacceptable levels of electron bombardment and volume ionization. By calculating the electron and ion currents to the payload for several assumed values of floating potential, NASCAP/LEO predicted that the equilibrium floating potential would be less than 150 V. This prediction was confirmed insofar as the

123

SPEAR II mock-up instrumentation was unable to show any evidence of a positive, steady-state floating potential.

The code was next used to study the current distribution to the various components of the SPEAR II payload. For the mock-up test under positive bias, NASCAP/LEO predicted a total current of -1.2 amperes for a plasma of density 1×10^6 cm^{-3} and temperature 1 eV. The distribution of this current to the SPEAR II components is shown in Table 9-II.

Table 9-II. Currents to SPEAR II Components

SPEAR II Component	Calculated Current
100 kV portion of probe	500 mA
75 kV portion of probe	410 mA
Klystrode battery canister	87 mA
50 kV portion of probe	75 mA
Various grounded surfaces	59 mA
High voltage lead	49 mA
Transformer secondary	34 mA
25 kV portion of probe	5 mA
Klystrode bushing	0.2 mA

The NASCAP/LEO calculations predicted that nearly all of the current would be incident to the high potential end of the high-voltage probe. This prediction was qualitatively confirmed by visual observations during the mock-up test of a strong optical glow from the electron-bombarded region. However, the question of how dynamic effects would modify this current distribution in the negative bias case remained unanswered.

9.1.6.4 Transient Current Estimates Using Gilbert and NASCAP/LEO. It was recognized that equilibrium current calculations for the SPEAR II payload could not be trusted for the short pulse durations. Without a three-dimensional modeling capability, it was not known to what degree the transient current would differ from the equilibrium current, or how much time was required to achieve the equilibrium configuration. To shed some light on these topics, a two-step strategy was used. First, the Gilbert code was used to calculate the time-dependent current to a sphere with parameters similar to the SPEAR II system. From the results, scaling relations were developed relating the "frozen ion" sheath size to the peak transient current. Second, NASCAP/LEO was run to calculate the size of the "frozen ion" and equilibrium sheaths about the high-voltage probe, and the scaling relations were applied to determine the peak transient current.

The sample problem consisted of a 0.3 m radius sphere in an O$^+$ plasma with a density of 10^5 cm^{-3}. The potential was raised to -100 kV with a 1.5 μs risetime. Using spherical probe theory, the equilibrium sheath around the sphere was calculated to have a radius of 15 m, and the steady-state ion current to the sphere was 14 mA.

The Gilbert calculation was run for 30 μs. It was found that the transient sheath expands rapidly to a radius of 4.0 m as the voltage is applied, and thereafter it expands by plasma erosion at the slow rate of 3 cm/μs, reaching a radius of 4.7 m at the end of the calculation. The current to the sphere (Figure 9-12) reached a peak of 140 mA at 15 μs into the pulse, and decreased slowly thereafter. (These calculations gave the first indication that the SPEAR II incident ion currents might be an order of magnitude above the values obtained from the equilibrium treatment.) It was estimated that 10 ms would be required for the current to relax to the Langmuir-Blodgett [14] equilibrium current of 14 mA. (Note

that the collected current correlates inversely with the sheath size. This is analogous to the space-charge-limited current collected by an inner sphere from a concentric outer sphere.)
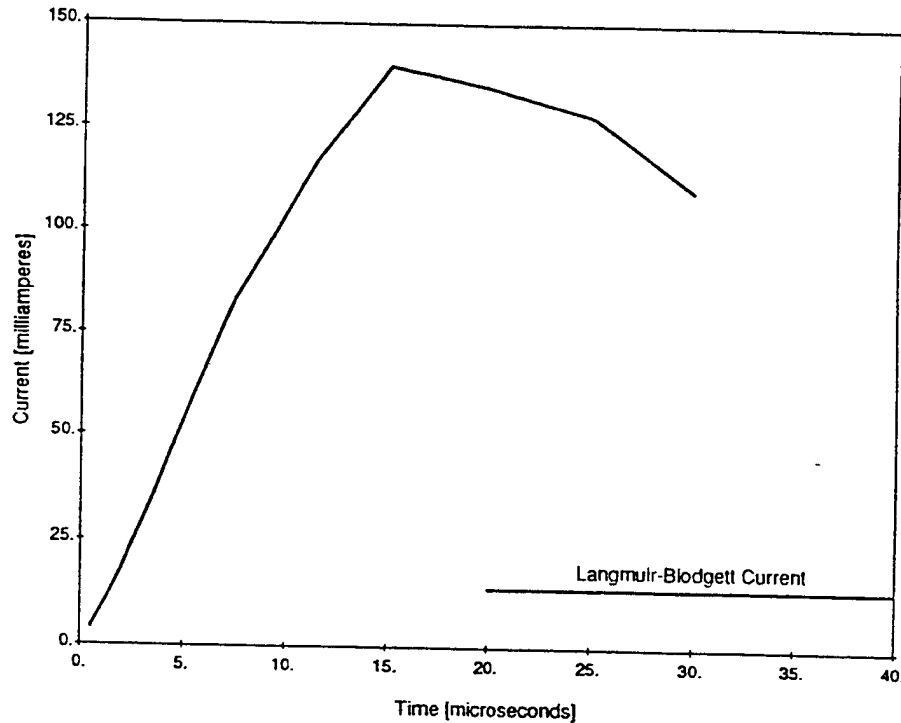
Figure 9-12. Time-dependent ion current to the sphere model of the SPEAR II payload. The Langmuir-Blodgett [14] steady state current is shown for reference.

To develop scaling a relation, we postulate that the peak current is given by

$$I_{peak} = \alpha\, Q\, /\, \tau, \tag{9-4}$$

where Q is a characteristic charge, and τ a characteristic time. The characteristic charge is logically taken as the space charge in the sheath (which must balance the surface charge on the probe):

$$Q = (4\pi\, /\, 3)ne\, R_s^3, \tag{9-5}$$

where we have neglected the probe volume relative to the sheath volume. The characteristic time may be taken as the time for an ion to travel the sheath radius in a uniform field given by the applied voltage over the sheath radius:

$$\tau = (2mR_s^2\, /\, eV)^{1/2}. \tag{9-6}$$

125

For the Gilbert calculation, we have $Q = 4.3 \times 10^{-6}$ coulombs, and $\tau = 7.3 \times 10^{-6}$ seconds, so that the scaling constant takes the value

$$\alpha = I_{peak} \tau / Q \approx 1/4, \qquad (9\text{-}7)$$

and the scaling relation is

$$I_{peak} = Q / 4\tau. \qquad (9\text{-}8)$$

Table 9-III shows "frozen ion" estimates of the sheath size (calculated by NASCAP/LEO for the three-dimensional representation of the SPEAR II payload under space and laboratory conditions) and the peak transient currents to the high-voltage probe (predicted by scaling the Gilbert results). To obtain the actual parasitic current in the circuit, the incident ion current must be enhanced by a large factor to take into account the secondary electron yield of the incident ions. While there is a great deal of uncertainty in the secondary yield value, a yield of 25 would be a reasonable estimate [15]. This gives a parasitic current exceeding two amperes under laboratory conditions. In comparison, the fully dynamic results (obtained from DynaPAC, as described below) predicted a total peak incident ion current of 50 mA, with 35 mA on the probe, for a parasitic current of 0.9 amperes.

Table 9-III. Transient Current Estimates

	Gilbert	Space	Laboratory
Density [cm^{-3}]	1×10^5	1×10^5	1×10^6
Equilibrium Sheath Radius [m]	15	2.3	1.8
Equilibrium Current [mA]	14	1.6	10
Transient Sheath Radius, R_s [m]	4.0	1.3 m	1.0 m
Transit Time, τ [μs]	7.3	2.4	1.6
Sheath Charge [μcoul]	4.3	0.15	0.7
$Q/4\tau$ [mA]	140	15	11
Secondary Electron Yield	25	25	25
Peak Parasitic Current [A]	3.6	0.39	2.6

Estimates of peak parasitic current; (1) calculated by Gilbert for a 0.3 meter radius sphere; (2) estimated for space conditions (plasma density 10^5 cm^{-3}) using the NASCAP/LEO "frozen ion" approximation; and (3) similarly estimated for laboratory conditions (plasma density 10^6 cm^{-3}).

The predicted current levels would not impair the high-voltage system operation, but they would seriously impact the ability of the high-voltage probe to measure the transformer secondary voltage. Figure 9-13 shows a circuit model of the probe, in which parasitic plasma current is injected one-tenth of the way from the high-voltage end, and the voltage measurement is taken one-tenth of the way from the ground end. For the case of -100 kV applied to the probe, this circuit model predicts that a parasitic current of 0.5 amperes will result in the measurement being low by a factor of two.
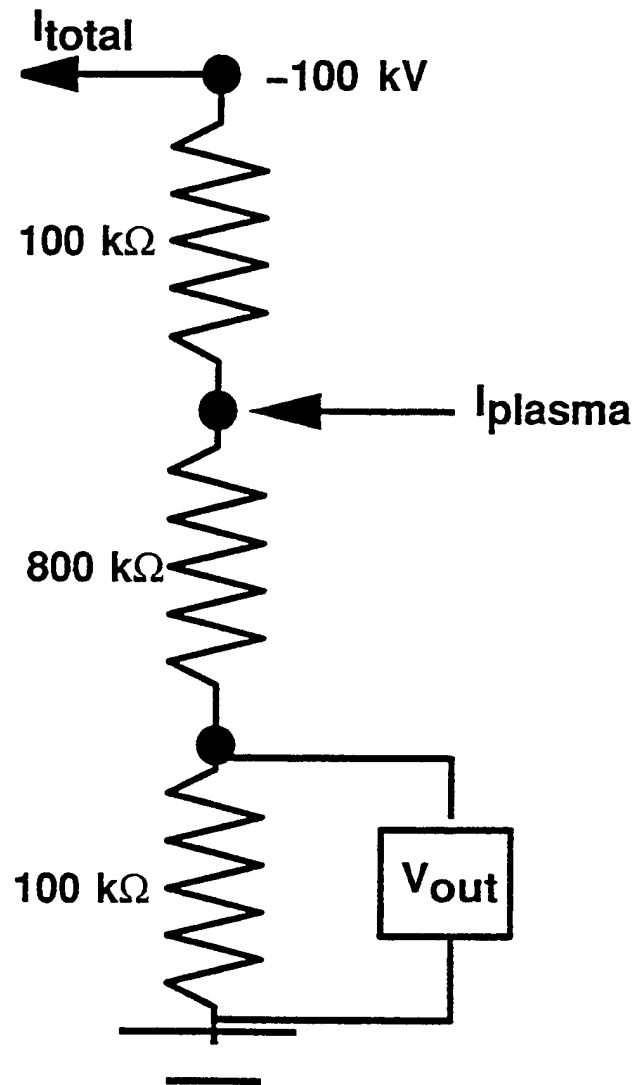
Figure 9-13. Circuit model of high voltage probe, used to estimate the effect of parasitic plasma current. The transformer secondary voltage is measured as $10 \times V_{out} = (I_{Total} - I_{plasma}) \times 100$ kV.

A comparison of the probe traces obtained from the space simulation chamber tests under vacuum and plasma conditions dramatically illustrates this effect. Figure 9-14 shows diagnostic signal traces for a 50 μs, 80 kV pulse in vacuum. The high-voltage probe trace is the dark, upper trace; the other traces are diagnostics taken at other components of the high-voltage circuit. In Figure 9-15, the trace is shown for the same pulse parameters in the presence of a 10^6 cm^{-3} Ar plasma. The high-voltage probe reading is diminished by about a factor of two, but all of the other diagnostic signals are indistinguishable from the vacuum shot. The conclusion is that the high-voltage circuit is operating properly in the presence of plasma, but the high-voltage probe read incorrectly.

127
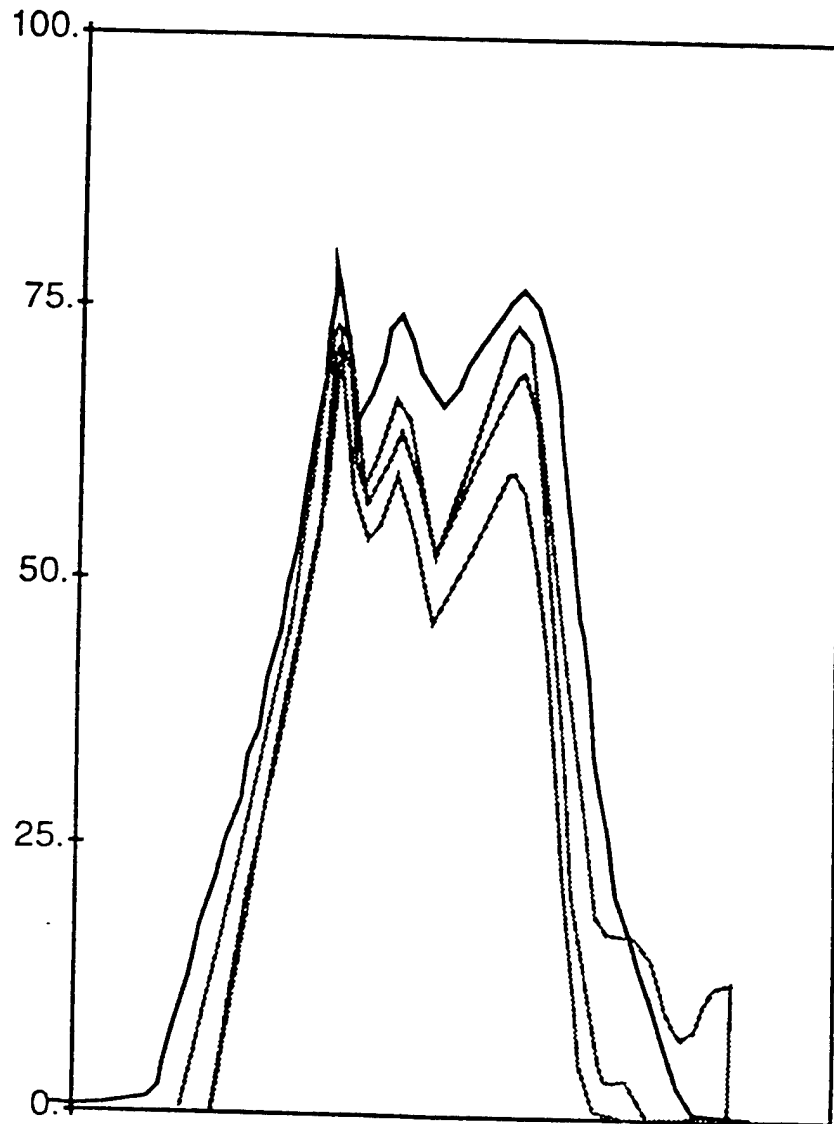
Figure 9-14. Circuit diagnostics for an 80 kV, 50 microsecond SPEAR II pulse with no plasma sources operating. The upper trace represents the transformer secondary voltage as measured by the voltage divider probe. The remaining traces are diagnostics for other components of the high voltage circuit.

128
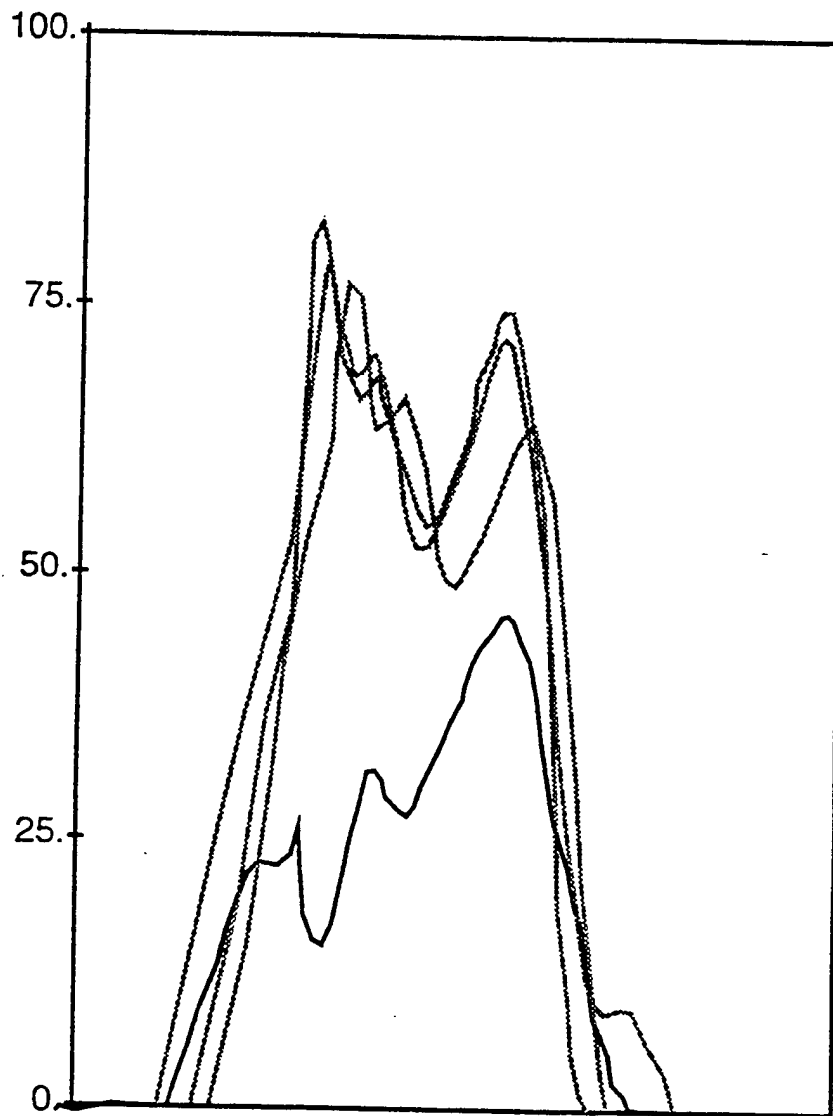
Figure 9-15. Circuit diagnostics for an 80 kV, 50 microsecond SPEAR II pulse with plasma sources operating. The transformer secondary voltage measurement is about half the value measured in vacuum, and now appears as the lower curve. Remaining circuit diagnostics are unchanged. DynaPAC calculations, anticipated by NASCAP/LEO and Gilbert results, showed that the voltage divider probe measurement was incorrect in the presence of plasma due to high incident ion currents to the probe.

9.1.6.5 DynaPAC Calculation of Transient Currents to SPEAR II High-Voltage Components.

All the calculations described above use either an equilibrium or "frozen ion" space charge representation, neither of which adequately models the dynamics of the SPEAR II pulse, or else models the geometry as axisymmetric, which is not an adequate approximation to the partially enclosed structure of SPEAR II. Estimates of the peak incident ion current, the division of this current among the SPEAR II high-voltage components, and the timescale of the current obtained by scaling the results of equilibrium codes based on results for poorly representative geometry required confirmation by a fully three-dimensional dynamic code. For this reason, the DynaPAC code, already under development for Geophysics Laboratory (now Phillips Laboratory) was supported by the SPEAR program.

With the development of DynaPAC for the SPEAR II program, it was possible to calculate the time dependent ion currents to the various SPEAR II high-voltage components. The geometrical model of the SPEAR II payload was the same as the one used for the NASCAP/LEO calculations described above. Initially, each DynaPAC grid was filled with a regular array of ion macroparticles, representing an Ar plasma with a density of 1×10^6 cm^{-3}. At each timestep, a time-dependent voltage, representing a 100 kV, 50 μs pulse with 3 μs risetime, was applied to the high-voltage components. The electrostatic potential field was calculated using the known ion distribution and an analytic expression for the electron charge density, and the ion macroparticles were tracked in the new field for the specified timestep length. After 3 μs, the ion macroparticles assumed the configuration represented in Figure 9-16. The figure shows ion voids near the Klystrode battery pack and the transformer. This indicates that substantial ion motion took place in these regions, regions which had high fields due to the close proximity of grounded struts and bulkheads. By contrast, ions at large distances were just beginning to be accelerated toward the high-voltage probe, as indicated by the curvature of the originally straight lines of macroparticles.
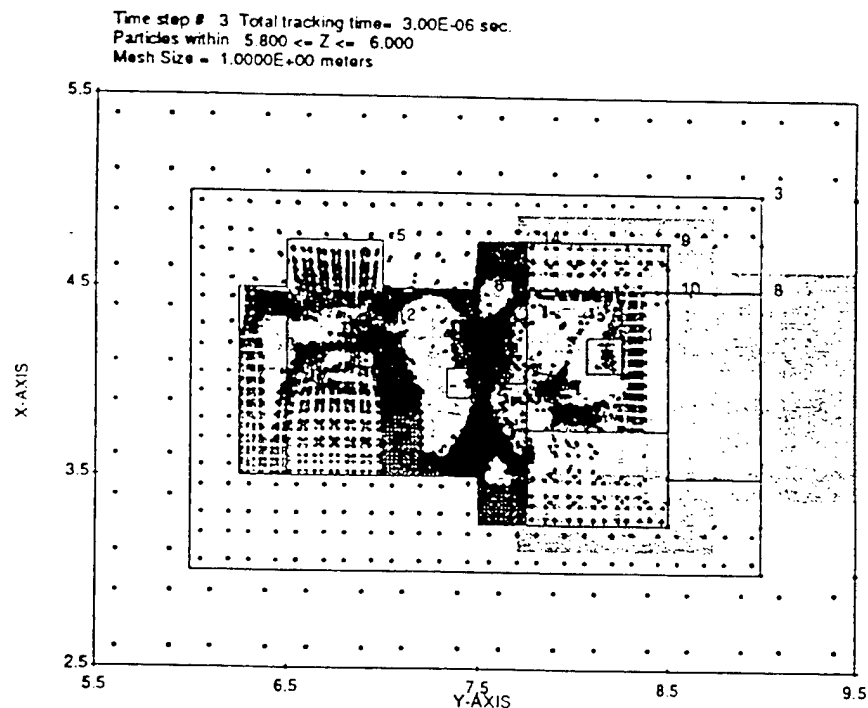
Figure 9-16. Calculated ion macroparticle positions 3 μs into a SPEAR II high voltage pulse (scale marked in units of meters).

130

Figure 9-17 shows the calculated ion currents incident on various SPEAR II payload components. The Klystrode battery pack and transformer (which are well shielded electrostatically by struts and bulkhead) had peak currents of about 12 mA each, which occurred approximately 6 μs into the pulse. The current to the high-voltage probe (which influences a larger volume of plasma) rose to a peak exceeding 30 mA at about 12 μs. The total incident ion current (which includes currents to the high-voltage leads) peaked at around 55 mA approximately 8 μs into the pulse. All of the currents decreased slowly after reaching their peak values. (For comparison, NASCAP/LEO equilibrium calculations for these conditions gave a total payload current of 6 mA. (See Table 9-IV.)
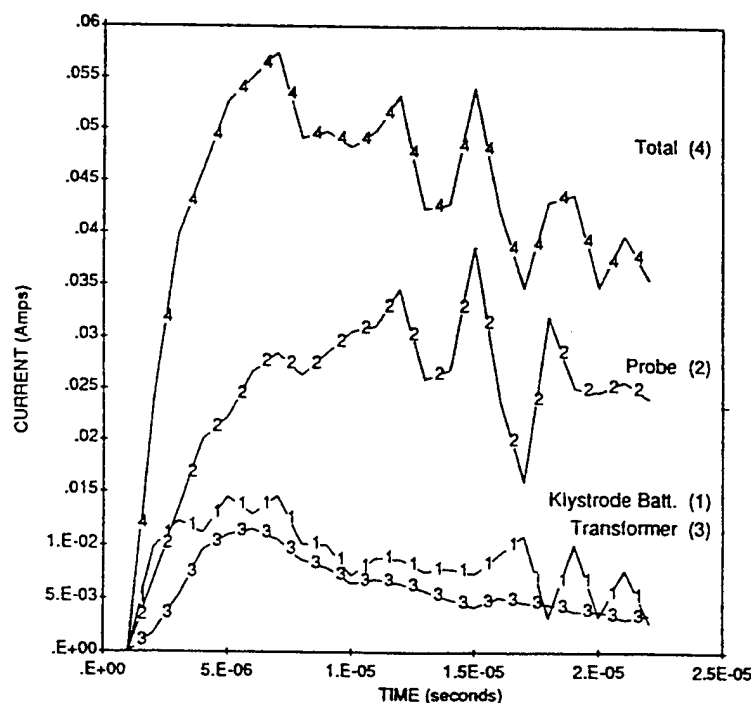
Figure 9-17. Calculated incident ion currents to the SPEAR II high voltage probe, Klystrode battery canister, and pulse transformers.

Table 9-IV
Predicted Incident Ion Currents to SPEAR II

Equilibrium Calculation	6 mA
Pre-Test Prediction	100 mA
DynaPAC Calculation	55 mA

Taking into account the secondary electron yield, the predicted parasitic current through the upper part of the probe was nearly one ampere. As discussed in the previous section, this is easily enough current to cause the observed erroneous measurements by the high-voltage probe.

A rough estimate of the time needed to approach an equilibrium sheath may be obtained as the time required to drain the equilibrium sheath volume (approximately a 2.1 meter radius sphere) of charge at a mean current of about 40 mA. This approach yielded a sheath formation time of 150 μs, which is three times the longest SPEAR II high-

voltage pulse. Therefore, the equilibrium formulation was never appropriate for the SPEAR II operating conditions.

9.1.7 Summary of Technical Achievements and Capabilities

This chapter has discussed the development of three plasma interaction model computer codes and their applications to the SPEAR program. The two existing codes, NASCAP/LEO and Gilbert, were both enhanced under the SPEAR program, and their ability to make useful and non-obvious predictions was demonstrated. The new code, DynaPAC, demonstrated its ability to perform dynamic plasma interactions calculations for complex systems.

Achievements in the area of code development, enhancement, and validation include:

(1)   For NASCAP/LEO:

    (a)   Demonstrating the ability to calculate equilibrium sheaths and current distributions for systems with high geometrical complexity;

    (b)   Adding a "frozen ion" approximation to aid the analysis of transient sheath phenomena.

(2)   For Gilbert:

    (a)   Developing an internal boundary condition to mimic the electrostatic effects of a screen;

    (b)   Demonstrating the ability to predict spatial and temporal current distributions with sufficient accuracy to make meaningful physical predictions.

(3)   For DynaPAC:

    (a)   Developing a computer code capable of performing dynamic plasma calculations for systems with high geometrical complexity;

    (b)   Developing a programmer-friendly DataBase Manager for the allocation, storage and retrieval of large arrays of data;

    (c)   Developing high-order, finite element techniques to guarantee accurate potential solutions with strictly continuous electric fields;

    (d)   Developing pre- and post-processors for ease of problem setup, input generation and data visualization.

Applications of these codes to the SPEAR program include:

(1)   Prediction (using Gilbert) of the (rapid or slow) breakdown of a negatively biased, high-voltage fixture by the presence (or absence) of calculable ion current to the "triple point";

(2)   Calculation (using Gilbert) of dynamic ion currents for the small chamber test of SPEAR II, showing that the intermediate-length pulse was most likely to break down;

(3) Calculation (using NASCAP/LEO) of the equilibrium current distribution and estimate of the equilibrium floating potential for SPEAR II;

(4) Development (using Gilbert) of a theory for dynamic sheath development and transient current for a negative probe, showing that transient currents can exceed equilibrium currents by an order of magnitude;

(5) Pre-test prediction (using Gilbert and NASCAP/LEO) of high parasitic currents to the SPEAR II high-voltage probe in the presence of plasma;

(6) Calculation (using DynaPAC) of the time-dependent plasma currents to the SPEAR II high-voltage components.

9.2 SURFACE FLASHOVER THEORY WITH APPLICATIONS TO HIGH-VOLTAGE CONDITIONING

9.2.1 Introduction

Conditioning consists of repeatedly applying high voltages to a component allowing it to arc until it is capable of withstanding the high voltage. The SPEAR program recognized the need to condition high-voltage components for the space environment, especially during a sounding rocket flight. Both the high-voltage transformer and the Klystrode bushing required a conditioning sequence before high-voltage standoff could be achieved. The art of conditioning is unpredictable, and techniques that work for one design or environment can fail in a different situation. In practice, it is not possible to guarantee that a conditioning technique will work, or to know how long the conditioning will last. To gain insight into the conditioning process, a surface flashover theory was developed that describes, quantitatively, the initiation of flashover. The theory reveals the role that surface desorption plays in the arc initiation process, and may be an important step in understanding quantitatively the process of conditioning.

9.2.2 Application

High-voltage insulation in space emerges as a critical issue because of the advantages inherent in operating high-voltage SDI systems in configurations where bushings, components and distribution networks are exposed to the ambient environment. Recognizing this, the SPEAR program initiated a number of space simulation experiments, conducted in laboratory plasma chambers, that demonstrated two important concepts:

(1) The plasma induced arcing could be diminished through changes in the geometry of high-voltage components. Computer simulations substantiated by laboratory experiments showed that the use of electrostatic screens and electrode shaping redirected ions away from the triple points and increased high-voltage standoff.

(2) High-voltage standoff capability of insulators improved with conditioning. The conditioning process is understood qualitatively as resulting from changes in the surface properties, such as removal of surface contaminants and gas desorption. The theory developed for the SPEAR program relates high-voltage standoff to surface desorption coefficients, and conditioning leakage currents to quantity of desorbed gas. The theory can predict pressure increases during the conditioning process which can be used as an independent measurement to verify that conditioning is occurring and to estimate the conditioning time required.

133

9.2.3 Innovative Concepts

The SPEAR model of surface flashover initiation quantitatively predicts breakdown thresholds and gas release, given surface electron impact desorption properties. The theory combines the effects of surface charging, surface secondary electron emission, neutral desorption, and ionization within the desorbed gas. Because the theory relates the quantity of desorbed neutrals to the flashover current and applied voltage, it can be tested in laboratory experiments. With additional data on surface desorption over periods of electron impact, the theory can be used to predict the conditioning needed to reduce the desorption rate below flashover thresholds. This also could be tested and, if confirmed, used in the design of high-voltage components and conditioning strategies.

9.2.4 A Theory of Surface Flashover

In SPEAR chamber tests, the neutral pressure was observed to increase during conditioning of the high-voltage components. This revealed the role of surface neutral desorption in the arc initiation process. Impact by impinging electrons has been proposed as the mechanism for this desorption[17]. We utilize the hypothesis of desorption of gas and its subsequent ionization by electron bombardment to construct a model of surface flashover. The idealized configuration in Figure 9-18 shows two electrodes separated by an insulator of length, l, and charged to a potential difference ϕ. The inter-electrode space may be filled by a plasma of density n_p.

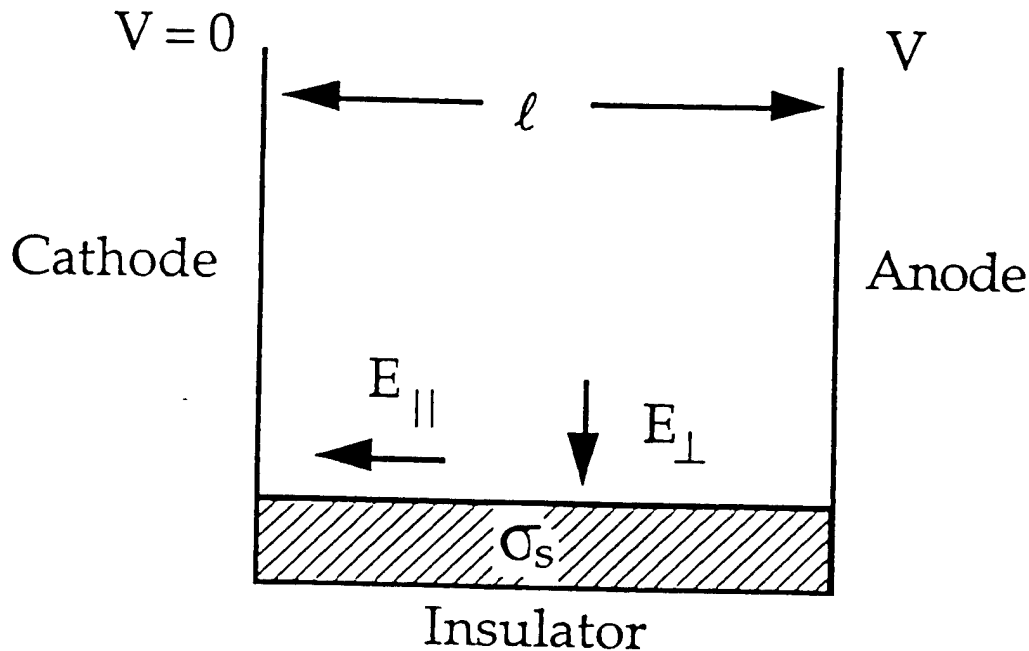Figure 9-18. Idealized configuration for surface flashover problem shows insulator of length ℓ with surface charge density σ_e.

The surface of the insulator becomes positively charged, so that any electrons emitted from the cathode near the triple point strike the insulator and produce secondary electrons which also remain close to that surface. Electrons bombarding the surface release

adsorbed gases that become ionized by collisions with sufficiently energetic electrons, increasing the flux of electrons bombarding the insulator.

The model equations for this system are as follows:

The time rate of change of charge on the surface of the insulator is

$$\frac{1}{e}\frac{d\Sigma}{dt} = -j_{out} + j_{in},$$ (9-9)

where Σ is the charge per unit area on the insulator, and j_{in} and j_{out} are the ingoing and outgoing fluxes of electrons. The fluxes j_{in} and j_{out} are related by the secondary emission yield $Y(\varepsilon)$ at the energy of the incident electrons, ε.

$$j_{out} = Y(\varepsilon)\, j_{in}.$$ (9-10)

It is useful to define the surface charge density, σ_e, to be the charge in a layer above the surface

$$\sigma_e = \int_0^\delta n_e\, dy,$$ (9-11)

where n_e is the electron density in the space above the layer, whose thickness is δ. The charge density, σ_e, is determined by continuity as shown in Equation (9-12).

$$\frac{\partial \sigma_e}{\partial t} + \frac{\partial K}{\partial x} = j_{out} - j_{in} + S.$$ (9-12)

The three terms on the right hand side of Equation (9-12) are the sources and sinks of charge due to charge leaving the layer and entering the layer from the surface, and from the creation of charge in the layer due to ionization. In Equation (9-12), K is the flux $\sigma_e v$ (cm^{-1} sec^{-1}) corresponding to movement of the layer charge σ_e. The ionization rate per unit area of the current layer is denoted by S. Recombination and attachment are neglected.

For simplicity, we have assumed that all electrons in the layer are born on the surface of the insulator (y=0) with a single energy $\varepsilon_0 = {}^1\!/_2 m v^2_0$ and a velocity v_0 in the y direction.

The preceding equation must be complemented by an equations that determine the density N of gas in the layer:

$$N v_0 = \gamma\, j_{in},$$ (9-13)

where γ is the number of gas molecules desorbed per incident electron, and v_0 is the mean velocity of desorbed molecules normal to the insulator surface. It is assumed that gas molecules move through δ in times δ/v_0 that are negligible in comparison with the time scales of the phenomena of interest.

We now consider steady state solutions of the foregoing equations and seek conditions indicative of breakdown. From Equations (9-9) and (9-10), to keep the surface charge constant we must have that $j_{out} = j_{in}$ and this requires [17]

$$\varepsilon = \varepsilon_1, \qquad (9\text{-}14)$$

where ε_1 is the first crossover energy defined by

$$Y(\varepsilon_1) = 1, \qquad (9\text{-}15)$$

$$\left.\frac{\partial Y(\varepsilon)}{\partial \varepsilon}\right|_{\varepsilon_1} \geq 0. \qquad (9\text{-}16)$$

We can relate the parallel and perpendicular electric fields as follows. The secondary electrons leave the surface with energy ε_0 and return to the surface with energy ε_1 in a time $t = \dfrac{2mv_0}{eE_\perp}$. The distance traveled under the influence of the parallel electric field is $d_{hop} = \dfrac{eE_1}{2m}t^2$. This, along with energy conservation, $\varepsilon_1 - \varepsilon_0 = E_1 d_{hop}$, can be used to produce[17]

$$E_\perp = 2\left(\frac{\varepsilon_0}{\varepsilon_1 - \varepsilon_0}\right)^{\frac{1}{2}} E_\parallel. \qquad (9\text{-}17)$$

In obtaining this relation, electron energy lost by ionization and by inelastic processes is neglected. The effect of this neglect should be examined.

The ionization rate, S, due to collisions by the surface current of electrons, K, with the desorbed gas, of density N, is

$$S \approx NK\sigma = \frac{\gamma j_{in}}{v_0} K\sigma. \qquad (9\text{-}18)$$

where σ is the ionization cross section.

The surface flux, K, can be expressed in terms of the incident electron flux, j_{in} by noting that K is just the flux generated by the secondary electrons hopping.

$$K = \left(j_{in}\tau\right)\left(\frac{d_{hop}}{\tau}\right) = j_{in}\frac{4\varepsilon_0 E_\parallel}{eE_\perp^2}. \qquad (9\text{-}19)$$

Solving for j_{in} and substituting into Equation (9-18) gives an equation for S in terms of K.

$$S = \frac{\gamma\sigma}{v_0}\left(\frac{eE_\parallel}{\varepsilon_1 - \varepsilon_0}\right)K^2 \equiv \alpha K^2, \qquad (9\text{-}20)$$

136

where we have gathered the constants into the coefficient, α. Substituting this expression for S into Equation 9-12 and invoking the steady state conditions of Equations 9-15, 9-16 and $\dot{\sigma}_e = 0$

$$\frac{\partial K}{\partial x} = \alpha K^2.$$ (9-21)

Integrating Equation (9-21) gives

$$K = \frac{K_0}{1 - K_0 \alpha x},$$ (9-22)

where eK_0 is the current at the cathode end of the insulator. Electrons may be liberated at the cathode by field emission or as a result of ion bombardment of the cathode. In general, the magnitude of K_0 depends on the parameters of the discharge and the surrounding ambient plasma including, in particular, the electric field and ion current distribution near the cathode triple point. We denote these dependencies by the expression $K_0 = K_0(\{E_c\}\{j_i\})$, that is, K_0 is taken to be some function of the electric field E_c and ion current density j_i at the cathode. The latter includes ions generated by collisions with electrons in the layer d that move to the cathode under the influence of the fields.

Although the mechanisms associated with cathode emission are not well understood, we can nevertheless define a critical emission current corresponding to breakdown conditions.

$$K_{0_c} = (\alpha \ell)^{-1}.$$ (9-23)

9.2.5 Application to SPEAR II and Other Systems

We seek to determine if the critical current given in Equation (9-23) is in accord with the current $I = 1.3 \times 10^{-4}$ amp observed by Gray [16] in a simple flashover channel with a gap $= 1.3 \times 10^{-2}$ cm, and a channel width $w \sim 10^{-3}$ cm. This gives

$$eK \approx \frac{I}{w} \approx 0.1.$$ (9-24)

From Equations (9-15)-(9-23)

$$\alpha \ell = \frac{\gamma \sigma}{v_0} \left(\frac{eE_{\shortparallel}}{\varepsilon_1 - \varepsilon_0} \right) \ell.$$ (9-25)

From Pillai and Hackam[17], the vacuum surface flashover for plexiglass at $\ell = 0.4$ cm is 120 kV/cm. Taking $<\sigma> = 10^{-16}$ cm^2, $v_0 = 10^5$ cm/sec, $\varepsilon_1 - \varepsilon_0 \approx 30$ eV, we find $\alpha \ell = 1.5 \times 10^{-18}$ cms. The surface current eK is then

$$eK = \frac{1.6 \times 10^{-19}}{1.5 \times 10^{-18}} = \frac{0.1}{\gamma}$$ (9-26)

This value is in reasonable accord with experimental results for $\gamma \sim 1$. A desorption probability of a few molecules per electron is consistent with results reported by Hackam [17], and it is a reasonable value if the surface is heated by electrons.

The theory relates the surface current, eK, to the rate of desorption of gas from the insulator surface. As will be shown below, the rates predicted are in qualitative agreement with the pressure increases observed in SPEAR II during conditioning sequences on the pad at White Sands.

Using Equation (9-13), we can integrate the flux of desorbed neutrals over the surface contributing to the flashover to get the total current of neutrals, R.

$$R = \oiint_{surface} N V_0 dA. \tag{9-27}$$

With Equations (9-19) and (9-22) this can be expressed in terms of the flashover current, I_C, as

$$R = \gamma w K_{oc} \frac{\ell}{d_{hop}} \ell n (1 - K_{oc} \alpha \ell)^{-1}. \tag{9-28}$$

where w is the width of the flashover surface.

During flashover described by Equations (9-22) and (9-23), a large but obviously finite current flows. Power supplies have current limits and will control K_0 to give a large but finite current. With this in mind we can approximate Equation (9-28) by assuming $K_0 \alpha \ell$ is near one, say 0.9 to 0.99, corresponding to an amplification of 10-100. In this case we have

$$R \approx \gamma \frac{I_c}{e} \frac{\ell}{d_{hop}} (\ell n \text{ factor}) \tag{9-29}$$

where the logarithm factor is a number between 1 and 5.

Ignoring the log factor, this equation states that the rate of desorbed neutrals equals

$$R = \frac{I_c}{e} \frac{\ell}{d_{hop}} \gamma.$$

The total amount of neutrals produced during conditioning flashover is the rate of neutral production times the flashover time. For the SPEAR II conditions, the number of electrons involved in a typical flashover of length $\tau = 10^{-5}$s and $I_c = 10$A is

$$\frac{I_c \tau}{e} \approx 10^{15} \tag{9-30}$$

138

For SPEAR II the ratio, $\dfrac{\ell}{d_{hop}}$, is the number of hops of the electrons along the flashover surface. This is just the number of intervals with energy $\varepsilon_I \approx 50$ eV that makes up the standoff voltage of 100,000V.

$$\frac{\ell}{d_{hop}} = 2000. \qquad (9\text{-}31)$$

For each electron impact onto the surface, γ neutrals are released into the chamber. The precise value of γ is uncertain, but is between 1 and 10 for impact energies of $\varepsilon_I = 50$ eV. The number of gas molecules released during a discharge is $n \approx 10^{18} - 10^{19}$.

Assuming that during the SPEAR II conditioning sequences this amount of neutrals was emitted into a volume of about a cubic meter, it would produce a pressure of between 10^{-4} and 10^{-3} Torr. This is consistent with the observations from White Sands that the pressure increased a measurable amount during each conditioning sequence.

Equations (9-20), (9-22) and (9-29) are important steps in understanding conditioning. Equations (9-20) and (9-22) reveal the drivers in the surface flashover process. In general, it is not possible to control the flashover path length, ℓ, so conditioning must modify the surface desorption properties described by α, namely γ. Decreasing the surface desorption coefficient will increase the flashover threshold. Conditioning does exactly this by driving neutrals from the surface of the insulator. Moreover, Equation (9-29) relates the amount of surface desorption to the conditioning current. With further development and experimental confirmation, this could be used to diagnose conditioning of high-voltage components by giving a measure to the conditioning process. For example, measuring the flashover current and the pressure of the desorbed neutrals could be used with Equation (9-29) to give γ, which could be used as a measure of the condition of the surface.

9.2.6 New Technical Achievements and Capabilities

A surface flashover theory based on electron impact induced surface desorption has been developed for use by the SPEAR program and other high-voltage operations in space. The theory provides a closed form expression of the surface flashover thresholds and pre-breakdown currents, extending the work of Pillai and Hackam[17]. The theory relates surface flashover current to the electron impact induced surface desorption. The pressure increases predicted by the theory are consistent with the pressure observations during the SPEAR II conditioning sequences on the pad at White Sands.

The theory provides an important first step in understanding the process of high-voltage conditioning. Further development could result in a predictive model of conditioning.

9.3 QUICK MODEL OF SPACECRAFT OUTGASSING PLUMES

9.3.1 Introduction

A new, quick-running model of the bulk neutral density from outgassing was developed after the SPEAR I flight for the SPEAR II program. The model includes the effects of reflection from surfaces as well as scattering by the ambient ram neutrals. The model is quick-running and can be integrated into engineering design codes such as EPSAT [18] Calculations performed for SPEAR II showed that sheath ionizations would have no effect on the power system performance. This was consistent with the results of the Plum Brook chamber tests where no sheath breakdowns were observed.

9.3.2 Application

Typical space systems must operate in a wide range of neutral contaminant environments. The ambient neutral density changes with season, time of day, and orbit. Attitude control thrusters periodically fire. Outgassing rates from surfaces change with time, and accommodation rates depend on incident fluxes, which in turn depend on all of the above variables. The neutral environment can cause deleterious effects to exposed high-voltage components. Paschen breakdown can occur if the neutral density falls near the Paschen minimum. Neutrals in electron collecting sheaths can have bulk breakdown (sheath ionization) to the background plasma and other components, as was observed in the SPEAR I Plum Brook chamber tests. When designing for these changing environments, it is necessary to have quick estimates for the neutral density at select positions (such as near a high-voltage component) throughout the time period. The SPEAR outgassing model allows the rapid calculation of the bulk neutral densities around complex spacecraft such as SPEAR II. The model is complementary to the Auburn outgassing model; the S-Cubed model uses the Auburn surface and complex object outgassing rates as input (see Chapter 8) and calculates the external expansion including scattering off surfaces and the ambient ram.

9.3.3 Innovative Concepts

The SPEAR contamination model includes the return flux scattered from the ambient ram. The model makes use of the scale in variance of the physics to enable a quick look-up scheme that replaces the volume integral used in standard contamination codes to be employed.

The surface-to-surface view factors, which determine the reflection contributions are computed by breaking the surfaces into triangles and then using the analytic result for the solid angle subtended by a triangle. This approach replaces a surface integral that is used in many contamination models.

9.3.4 The Quick Outgassing Model

The neutral effluent due to outgassing and accommodation is generally of low enough density that collisional mean free paths are large compared with object dimensions. In this case, neutrals leaving a surface travel in straight lines and either leave the region of interest or hit another surface. Neutrals that hit another surface either stick or are accommodated. This process is shown in Figure 9-19.
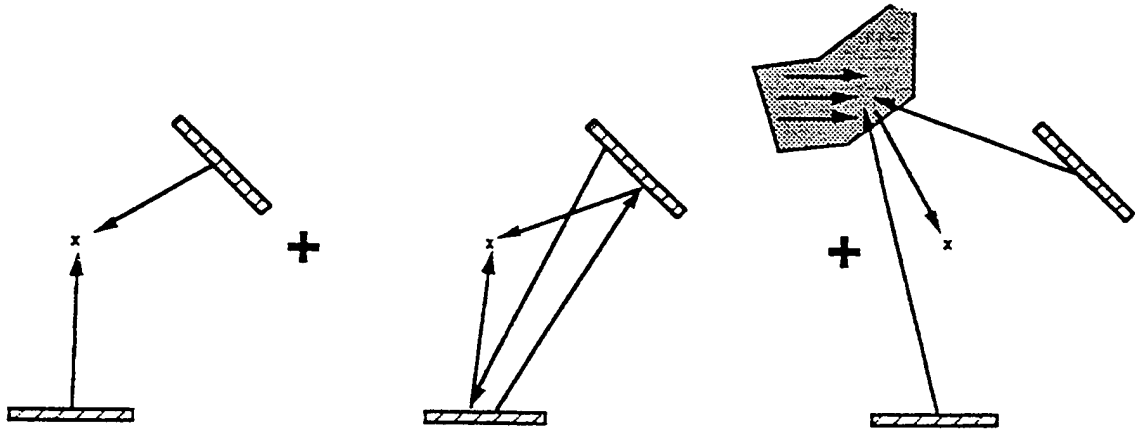
140

Figure 9-19. The neutral density at a point arises from a) direct surface outgassing, and b) reflections (accommodation) from surfaces, and c) scattering off of the ambient ram neutrals.

The neutral density at x is the sum of the outgassing density from each surface plus contributions due to accommodation of neutrals incident from other surfaces and the ram scattering. Each surface contributes a density given by

$$\rho = \iint dS \cdot \hat{r} \frac{C}{r^2},$$
(9-32)

where C determines the outgassing rate. The above expression is proportional to the view factor of the surface S at r. It is convenient to evaluate r directly above the surface, S

$$\rho(0) = 2\pi C.$$
(9-33)

Hence we can express the density at r from S in terms of the outgassing density at the surface and the solid angle Ω, subtended by S at r.

$$\rho = \rho(0) \frac{\Omega}{2\pi}.$$
(9-34)

The total density from all surfaces is then

$$\rho = \sum \sum_{surfaces\,i} p_i(0) \frac{\Omega_i}{2\pi}.$$
(9-35)

141

In the above expression, $\rho_i(0)$ is not the bare density due to outgassing by surface i, but must include accommodated neutrals from other surfaces. Designating ρ^0 to be the bare outgassing density column vector for all surfaces, and (0) to be a vector containing the total neutral densities for all surfaces, including multiple accommodations, we have the following matrix equation

$$\rho(0) = \rho^0 + M \cdot \rho(0), \qquad (9\text{-}36)$$

where M is a matrix of surface-to-surface view factors, including an accommodation factor (which conserves flux at the surface and depends on the incoming flux and the surface temperature). Although this can be directly solved for $\rho(0)$ in terms of ρ^0 as

$$\rho(0) = (1 - M)^{-1}\rho^0, \qquad (9\text{-}37)$$

it is more convenient to iteratively estimate $\rho(0)$ using,

$$\rho(0) = \rho^0 + M \cdot \rho^0 + M \cdot M \cdot \rho^0 + \dots . \qquad (9\text{-}38)$$

Each iteration corresponds to a reflection. Typically one iteration (corresponding to single reflection) is sufficient. The calculations presented below use the single reflection approximation. In practice, M is computed once for a system configuration and then used for any ambient ram environments and outgassing rates.

Finally, the total neutral density at a point is given by the sum of the contributions from each surface plus the ram scattering contribution. This latter component can be expressed as a volume integral over the scattering sources throughout space with

$$\rho_{return} = \rho_{outgassing} \frac{A_s}{\lambda x_s} \iiint \frac{\bar{r}_s \cdot \bar{v}_s}{r_s^3} \frac{\bar{r} \cdot \bar{v}_r}{r^3} \, d^3 r, \qquad (9\text{-}39)$$

where $r_s = r - x_s$, A_s is the area of the surface, $\rho_{outgassing}$ is the outgassing density at the surface, λ^{-1} is $\sigma \rho_{ambient}$, and $\bar{v}_s$, $\bar{v}_r$ are unit vectors in the direction of the outgassing surface and the ram, respectively. All distances are expressed in terms of x_s, the distance between the surface and observation point. In the above equation, if the dot products are less than zero, the dot product is taken to be zero. This occurs when the integration volume is behind the outgassing surface and when the scattering by the ram cannot get to the observer.

As seen in Equation (9-39), the dimensional variables have been entirely scaled out, leaving only the orientational (angular) dependences α, β, and ϕ. (see Figure 9-20) Therefore, the integral can be done numerically for several values of these angles and can be tabulated for subsequent use. This reduction of a three-dimensional integral to a simple table look-up is the key to the speed of the backscatter return flux calculations in the SPEAR outgassing model.
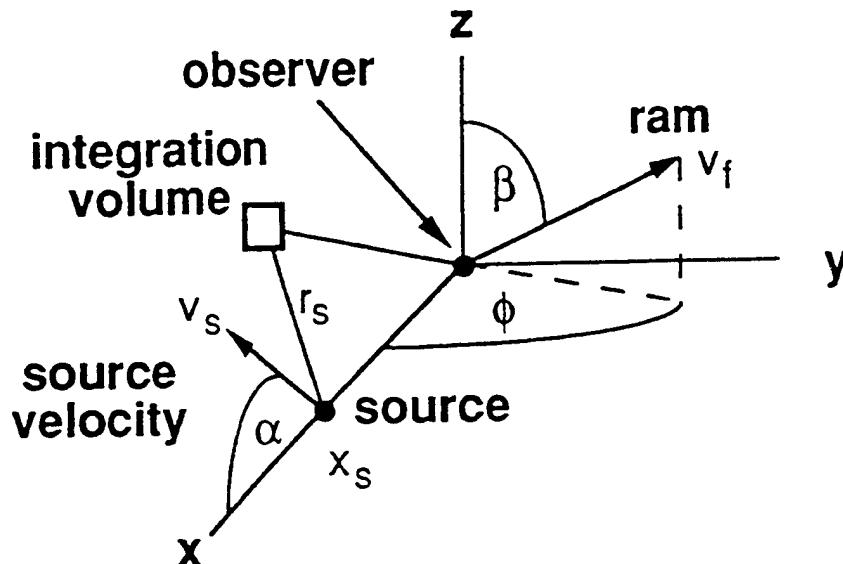
142

Figure 9-20. The ram scattering contribution to the neutral density can be expressed as a volume integral over the scattering sources throughout space.

Equation (9-39) also shows that the return flux from outgassing scattering is negligible unless the size of the source is comparable to the mean free path of the ambient neutral. For SPEAR above 200 km where the neutral density is $<10^{16}/m^3$, this is less than 1% effective.

9.3.5 Application To SPEAR

The SPEAR experiments were designed to investigate the space environment interactions with high-voltage components. In SPEAR I, high-voltage plasma current collection in the presence of the earth's magnetic field was investigated. At issue were the extent that non-classical mechanisms, such as anomalous scattering, turbulence and ionization, affect current collection. The methodology of this investigation was to compare the SPEAR I experimental results for current collection with the results of the NASCAP/LEO [22] and POLAR [23] codes which assume classical current collection mechanisms (plasma particles move under the influence of non-oscillating fields). This, however, would be conclusive only if the effects of neutral ionization could be ignored. The neutral density calculations using the outgassing model discussed showed just that. Preflight calculations performed for SPEAR II showed that external outgassing would not cause sheath ionization breakdown.

Calculations of SPEAR II external outgassing densities were performed assuming the same outgassing rate for all materials. The value chosen was 0.01 W/m^2, the maximum ambient rate for hot aluminum (Chapter 8). The resultant gas cloud was orders of magnitude less dense than necessary for ionization enhanced sheath currents of for

sheath breakdown. The calculated gas cloud surrounding SPEAR II is shown in Figure 9-21. The SPEAR II Plum Brook chamber tests showed no bulk ionization breakdown in the sheath, consistent with the low outgassing densities predicted by the model.
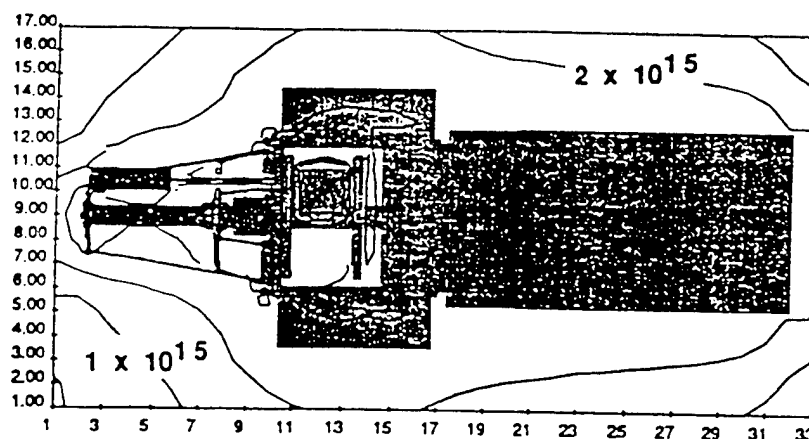

Figure 9-21. Outgassing densities about SPEAR II using outgassing rates of 0.01 W/m^2 for all surfaces.

9.3.6 Summary

The new SPEAR model enables the neutral density due to outgassing, including scattering from the ambient, to be computed quickly, making system trade studies practical. The model has been incorporated into the NASCAP/LEO and EPSAT codes for use in engineering design analysis. Calculations using the model show that normal outgassing has little impact on collecting sheaths for the power systems, and that ambient neutral-outgassing scattering is negligible for few meter size systems above 200 km. For SPEAR I, the neutral density in the electron collecting sheath due to outgassing was shown to be below breakdown thresholds. This result is consistent with the lack of sheath ionization breakdown during the SPEAR I flight. For SPEAR II, the neutral density in the ion collecting sheaths was shown to be insufficient to cause significant ionization enhancements to the collected current. This is consistent with the Plum Brook chamber tests. In Plum Brook tests, the observed current collection was in agreement with DynaPAC calculations, implying that only classical phenomena, not ionization, controlled the plasma interaction physics.

144

REFERENCES

1. M.J. Mandell, T.T. Luu and J.R. Lilley, Analysis of Dynamical Plasma Interactions with High-Voltage Spacecraft, Interim Report. Maxwell Laboratories/S-Cubed Division, La Jolla, CA, SSS-DPR-90-11973, 1990.

2. M.J. Mandell and V.A. Davis, User's Guide to NASCAP/LEO, Maxwell Laboratories/S-Cubed Division, La Jolla, CA, 1990.

3. I. Katz, M. J. Mandell, G. W. Schnuelle, D. E. Parks and P. G. Steen, "Plasma Collection by High-Voltage Spacecraft in Low Earth Orbit", *Journal of Spacecraft and Rockets*, 18, p. 79, 1981.

4. M. J. Mandell, I. Katz and D. L. Cooke, "Potentials on large spacecraft in LEO", *IEEE Trans. Nucl. Sci.*, NS-29, p. 1584-1588, 1982.

5. T. Neubert, M.J. Mandell, S. Sasaki, B.F. Gilchrist, P.M. Banks, P.R. Williamson, W.J. Raitt, N.B. Meyers, K.D. Oyama and I. Katz, "The sheath structure around a negatively charged rocket payload," *J. Geophys. Res.*, 95, p. 6155, 1990.

6. M. J. Mandell, J. R. Lilley and I. Katz, "Computer Modeling of Current Collection by the CHARGE-2 Mother Payload," *Geophys. Res. Lett.*, 17, p. 35, 1990.

7. I. Katz, G. A. Jongeward, V. A. Davis, M. J. Mandell, R. A. Kuharski, J. R. Lilley, Jr., W. J. Raitt, D. L. Cooke, R. B. Torbert, G. Larson and D. Rau, "Structure of the Bipolar Plasma Sheath Generated by SPEAR I," *Journal of Geophys. Res.*, 94, p. 1450, 1989.

8. M. J. Mandell and I. Katz, "Potentials in a Plasma over a Biased Pinhole," *IEEE Trans. Nucl. Sci.*, NS-30, p. 4307, 1983.

9. M. J. Mandell, I. Katz, G. A. Jongeward and J. C. Roche, "Computer Simulation of Plasma Electron Collection by PIX-II," *Journal of Spacecraft and Rockets*, 23, p. 512, 1986.

10. PDA Engineering, Inc., Costa Mesa, CA.

11. K.C. Maffei, I. Katz, J.R. Cooper, R.S. Ingermanson, M.J. Mandell and D.E. Parks, A Program for Enhancing the Surface Breakdown Strength of Components and Systems in the Space Environment, Maxwell Laboratories/S-Cubed Division, SSS-DFR-90-11204, La Jolla, CA, 1990.

12. S.A. Matra, Paris, France.

13. American National Standards Institute (ANSI).

14. I. Langmuir and K.B. Blodgett, *Phys. Rev.*, 24, p. 49, 1924.

15. L.A. Dietz and J.C. Sheffield, *J. Appl. Phys.*, 46, p. 4361, 1975.

16. Eoin W. Gray, "Vacuum Surface Flashover: A High-Pressure Phenomenon," *J. Appl. Phys.*, 58(1), p. 132, July 1985.

17.   R. Pillai, A. Sivathanu and Reuben Hackam, "Surface Flashover of Solid Dielectric in Vacuum," *J. Appl. Phys.*, 53, 4, p. 2983, 1982.

18.   G.A. Jongeward, R. A. Kuharski, E. M. Kennedy, K. G. Wilcox, N. J. Stevens, R. M. Putnam and J. C. Roche, "The Environment-Power System Analysis Tool Development Program," *Proceedings of the 24th Intersociety Energy Conversion Engineering Conference*, p. 371, Washington, DC, August 6-11, 1989.

19.   R.J. Hoffman, and M. A. Hetrick Jr., "Plume Contamination Effects Prediction: CONTAM III Computer Program," Tech. Rep. AFRPL TR82-033, Air Force Rocket Propul. Lab., Edwards Air Force Base, CA, 1982.

20.   R.O. Rantanen and T. D. Gordon, "Contaminant Buildup on Ram Facing Spacecraft Surfaces," SPIE Paper, 777-04, May 1987.

21.   L.T. Melfi, J. E. Hueser, and F. J. Brock, "Direct Simulation Monte Carlo Technique for Modeling of the Environment in the Vicinity of the Space Shuttle Orbiter," SPIE Paper, 286, 1981.

22.   M.J. Mandell and I. Katz, "High Voltage Plasma Interactions Calculations Using NASCAP/LEO," AIAA Paper, No. 90-0725.

23.   D.L. Cooke, I. Katz, M. J. Mandell, D. E. Parks, J. R. Lilley, Jr., J. H. Alexander and A. G. Rubin, "POLAR Code Development," AFGL-TR-83-0046, Proceedings of Air Force Geophysics Laboratory Workshop on Natural Charging of Large Space Structures in Near Earth Polar Orbit: 14-15 September 1982, p. 321, 1983.

24.   D.L. Cooke and I. Katz, "Ionization Induced Instability in an Electron Collecting Sheath," *Journal of Spacecraft and Rockets*, 25, p. 132, 1988.

APPENDIX B

A copy of the paper presented at the DNA Numerical Methods Symposium follows:

DynaPAC - A 3-D finite Element Plasma Analysis Code*

M. J. Mandell,[†] T. T. Luu and J. R. Lilley

S-Cubed, Division of Maxwell Laboratories, Inc.

D. L. Cooke

Phillips Laboratory

Presented to:

DNA Numerical Methods Symposium

Menlo Park, CA

April 28-30, 1992

1. Introduction

DynaPAC (Dynamic Plasma Analysis Code) is a three-dimensional finite element code for the study of the interaction between a high voltage or pulsed power spacecraft and the low-Earth orbit plasma environment. It is being developed for Phillips Laboratory with support from the SPEAR (Space Power Experiments Aboard Rockets) program.

Figure 1 indicates some of the interactions of a high voltage payload with the ionospheric environment. Because mobile plasma electrons conspire against high positive potentials, applied voltages will balance out predominantly negative relative to the ambient plasma potential. A plasma sheath will form, through which plasma ions will be accelerated toward the negative surfaces. The current associated with these ions is amplified severalfold by secondary electron emission. Neutral species (whether ambient, the result of outgassing, or effluents from active operations) may be ionized by the high energy electrons and ions, leading to optical contamination, surface contamination, or even to short circuits which prevent proper operation of the high voltage system.

DynaPAC is written for operation on UNIX workstations. Current versions are maintained for SUN Microsystems SPARCStation and for Silicon Graphics, Inc. IRIS Indigo.

2. DynaPAC Functionality

2.1. Object Definition and Gridding

DynaPAC is designed to faithfully model objects of high geometrical complexity (such as shown in Figure 2) within a cubic grid structure. Spacecraft are defined as boundary surface element representations using standard finite element preprocessor programs (such as PATRAN). A cubic grid structure of arbitrarily nested grids is created using DynaPAC's interactive GridTool module. Object definition interface modules enter the object and grid information into DynaPAC's DataBase, and calculate the finite element information for those elements neighboring the spacecraft.

Figure 3 shows the DynaPAC model of the SPEAR-3 rocket payload, with several experiments and sensors visible on the next-to-top section of the rocket body. Figure 4 shows the DynaPAC grid structure around the payload. The grid structure extends many meters away from the payload to accommodate the expected very large plasma sheath, while achieving resolution as small as 4 cm near the experiments on the rocket body, and 1 cm around the floating probe.

2.2. Poisson's Equation

DynaPAC solves a nonlinear Poisson equation, in which space charge is a function of the local potential and electric field, as well as the results of particle tracking. A menu of such functions is available within the code, and it is easy to add additional functions as

applications demand.

Boundary conditions at the object allow fixed potential or fixed electric field at each surface cell. Additionally, the object may be allowed to "float" as it dynamically accumulates charge.

Unlike more common trilinear Poisson solvers, DynaPAC potential solutions have strictly continuous electric fields. This is achieved by allowing four degrees of freedom (corresponding to potential plus three electric field components) at each node. As illustrated for the one-dimensional case in figure 5, this is achieved by using potential interpolation functions (blue curve) with unit value and zero slope, and gradient interpolation functions (red curve) with zero value and unit slope. All interpolation functions have zero value and slope at the three opposite faces. The DynaPAC scheme can represent exactly, among other functions, constant potential, constant field, and a potential which is any linear combination of x^2, y^2, and z^2.

2.3. Particle Generation and Tracking

DynaPAC's PartGen module generates arrays of macroparticles which can then be tracked in electric and magnetic fields by the Tracker module. Particles can be generated either volumetrically (e.g., for dynamic space charge simulations), on contour surfaces (e.g., for equilibrium space charge and surface current calculations), or on contour lines or via user input (e.g., for trajectory visualization).

The Tracker module advances all particles for a specified timestep. The timestep is automatically subdivided for each macroparticle, as appropriate to the conditions of that particle. Surface currents and charges are accumulated as macroparticles strike object surfaces, and volume charge density is accumulated as particles pass through the sheath region.

2.4. Usability

DynaPAC is designed for ease of use (through the provision of interactive modules for input generation and output display), for ease of algorithm insertion and modification (through modular coding practices), and for ease of dealing with new arrays of data (through the DataBase Manager).

Interactive modules include:

(1) GridTool, for defining DynaPAC's arbitrarily nested cubic grid structure.

(2) DynaPre, for defining surface potential boundary conditions, and for creating input files to the Potent, PartGen, and Tracker modules. (Figure 6 shows the interactive menu for creating a fully commented Potential Solver input deck.)

(3) Scanner, for plotting spatial potentials and other spatial data, and for printing spatial and surface data.

150

(4) DynaPost, for running the ObjPotl module to plot surface potentials, materials, electric fields, and current densities, and for retrieving, printing, and plotting time histories for dynamic problems.

DynaPAC's DataBase Manager is a programmer-friendly utility for defining data and data structures, allocating disk storage and dynamically allocated memory, and reading and writing spatial,surface, or list structured data.

3. Example: Potentials Around an Octahedron

An octahedron is a regular solid with eight triangular sides. Calculation of the potential field around such an object provides a non-trivial exercise for a cubic code. When such an object is input to DynaPAC through the object definition interface module, the procedure for each non-empty zone is to first generate bounding polygons for the empty portion of the zone, then, with the help of assumed interpolation functions, generate the finite element matrices needed to solve Laplace's or Poisson's equation.

Figure 7 shows potentials (in a plane through the center of the octahedron) calculated using a trilinear potential solver (NASCAP/LEO). The potentials remain aspherical quite far from the object, and the field enhancement at the corners is not apparent. DynaPAC potentials (figure 8) rapidly become spherical and show the enhanced corner fields. Note also the illustration of bounding polygons for the non-empty zones.

4. Example: Particle Trajectories over a Slab

Accuracy of particle trajectories is a primary motivation for DynaPAC's continuous field algorithms. Accurate particle trajectories are needed for such problems as wake structure, current distribution over a surface, and simulation of particle detectors.

Figures 9 and 10 show trajectories for a set of particles passing near an attractively charged slab. Trajectories calculated with the trilinear code (NASCAP/LEO) (figure 9) show anomalous division into three groups. The division occurs as the particles pass to the left or right of a grid point in the high field region. By contrast DynaPAC calculated trajectories (figure 10) show a continuous distribution of particle destination as a function of particle origin.

Note that, in both cases, the maximum deflection occurs for a particle passing one-half zone away from the slab. This is characteristic of the short range potential used. Particles passing closer to the slab are strongly accelerated in their direction of travel, and thus receive a smaller deflection impulse.

5. Summary

DynaPAC is an advanced electrostatic and quasi-static plasma simulation code. Advanced features of DynaPAC include

(1) The ability to handle a high level of geometrical complexity;

(2) A cubic grid structure with arbitrarily nested gridding;

(3) Non-Linear solution for Poisson-like equations with strictly continuous electric fields;

(4) A selection of options for particle generation and tracking;

(5) User-Friendly pre- and post-processors;

(6) A programmer-friendly DataBase Manager for ease of modifying and extending the code.

All modules of DynaPAC are currently operational and have been applied to the SPEAR program as well as to other applications. We are expanding the algorithm set within DynaPAC to meet the needs of applications as such needs occur. We also use DynaPAC as a workbench to develop and test new algorithms for three-dimensional plasma simulation.

Figure Captions

Figure 1. Interactions of a high-voltage spacecraft with the environment include plasma sheaths, plasma ion and electron bombardment, secondary electron emission, and ambient and spacecraft-produced neutral species.

Figure 2. DynaPAC is able to faithfully model the geometric complexity of realistic spacecraft.

Figure 3. DynaPAC model of the SPEAR-3 payload. Note the instruments and experiments in the next-to-top section.

Figure 4. DynaPAC gridding for the SPEAR-3 model. With 1 meter basic resolution, 4 centimeter resolution is achieved near the experiments and instruments to be modeled.

Figure 5. One-dimensional interpolation functions, showing the independent definition of potential and electric field at node points.

Figure 6. Interactive screen for creating a Potential Solver input file.

Figure 7. Laplacian potentials about an octahedron, calculated using a trilinear code (NASCAP/LEO).
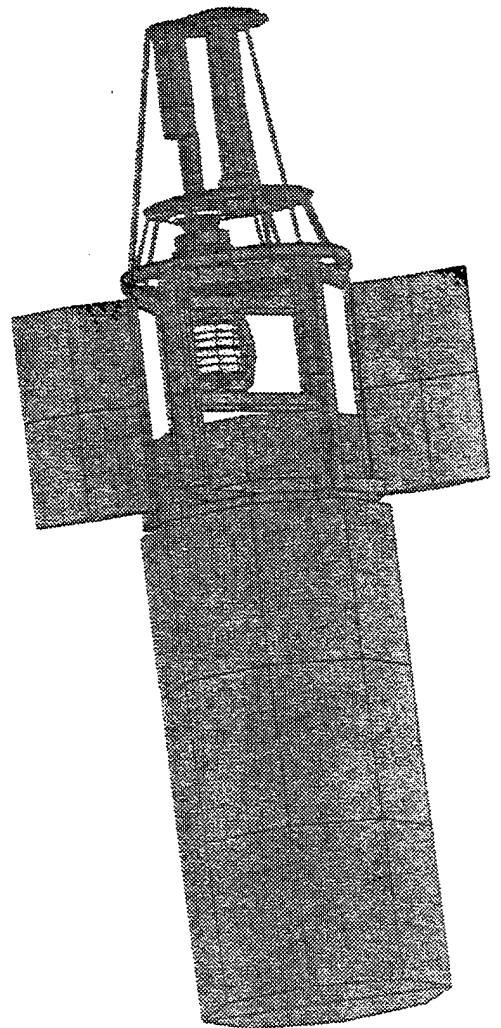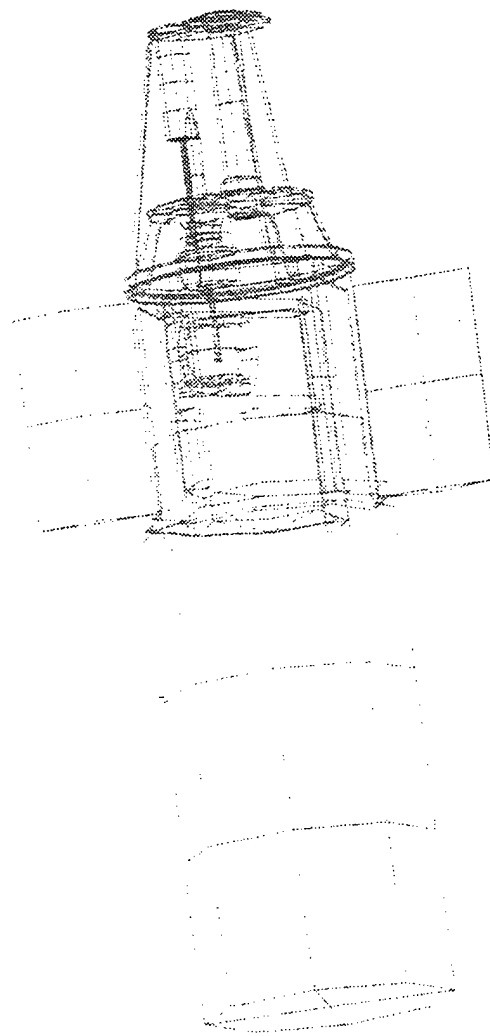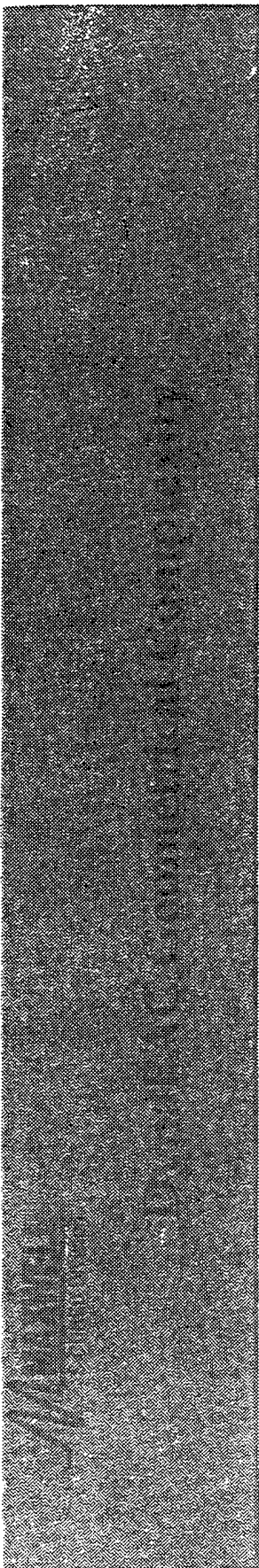
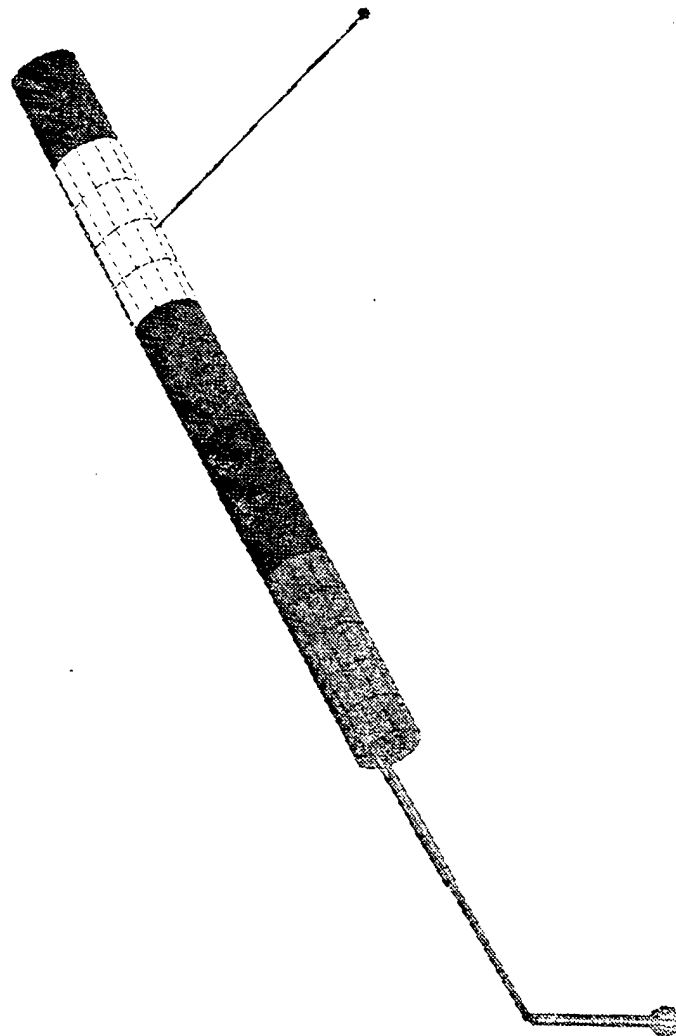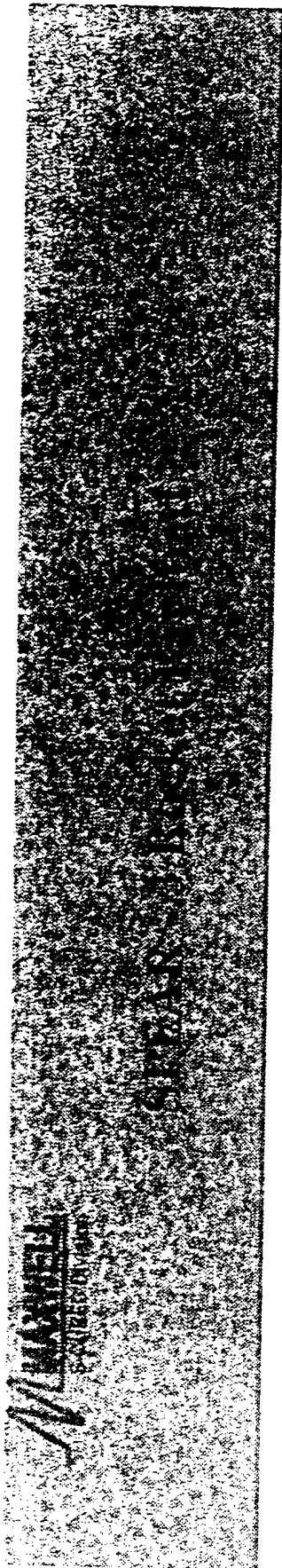Figure 8. Laplacian potentials about an octahedron, calculated using DynaPAC.

Figure 9. Particle trajectories over a slab, calculated using a trilinear code (NASCAP/LEO).

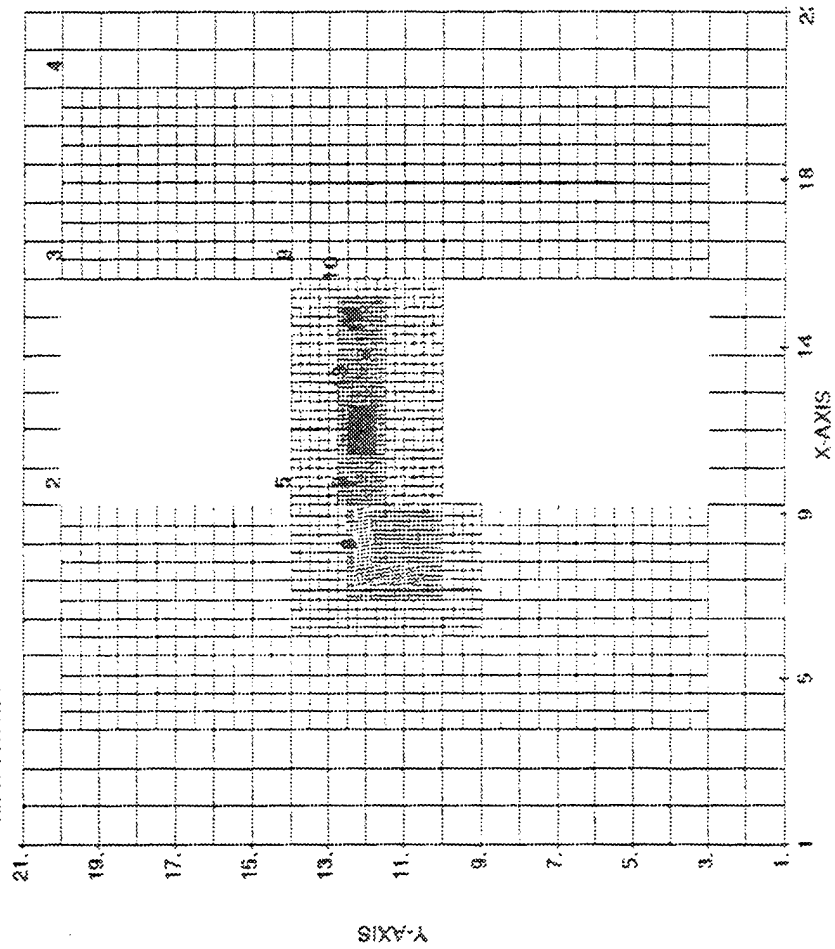Figure 10. Particle trajectories over a slab, calculated using DynaPAC.

MAXWELL
S-CUBED Division

High Voltage Ionospheric Interactions

Plasma Electrons

Secondary Electrons

Plasma Ions

Plasma Sheath

High Voltage Components

Neutral Particles

Effluent

MAXWELL
S-CUBED Division
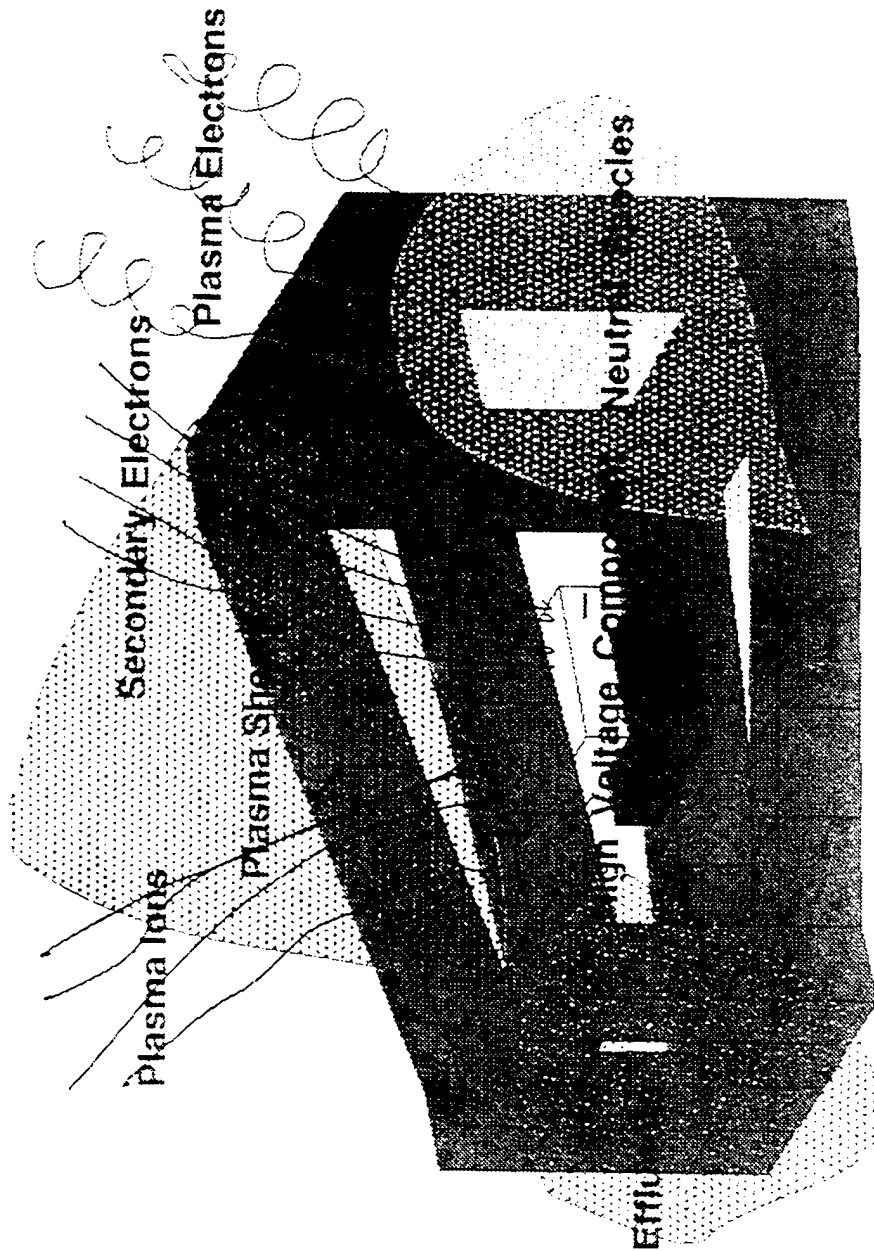
DynaPAC Features — Gridding

Mesh Size = 1.0000E+00 meters
Date: 04-20-82
Time: 18:39:56

X-AXIS

Y-AXIS

Interpolation Functions

Dist. from Node

High - Order Interpolants

Potential and electric field are well-defined at all space nodes to give strictly continuous electric fields for accurate particle tracking.
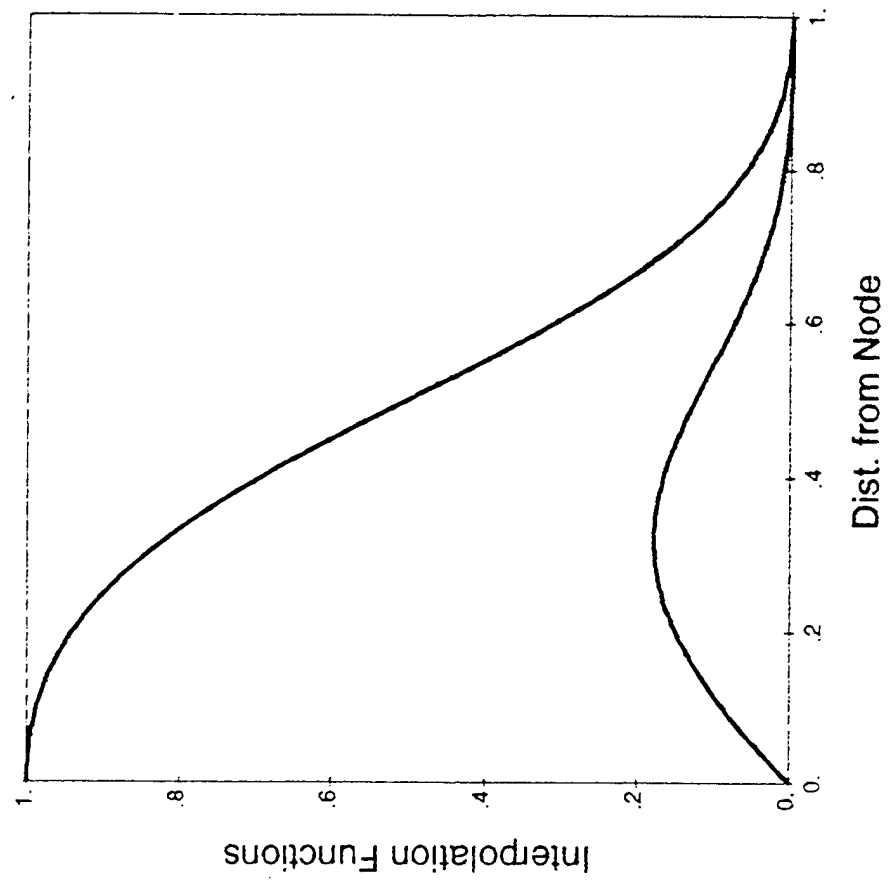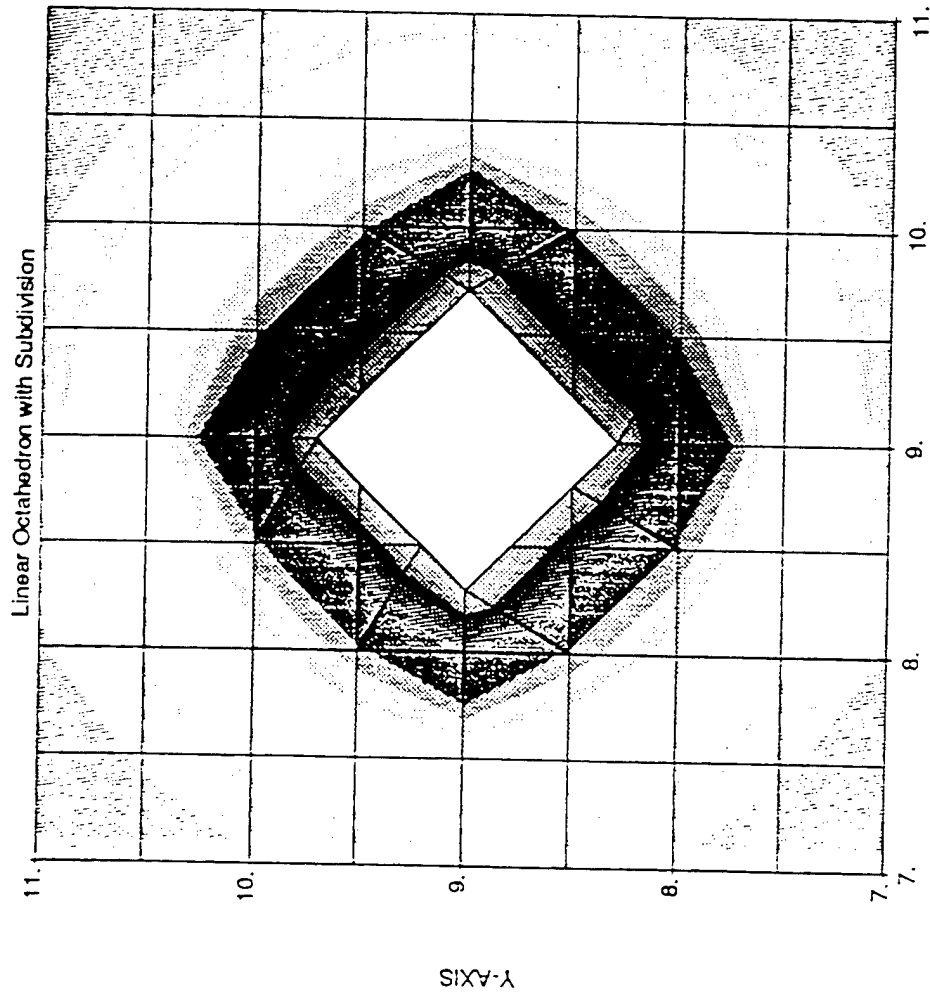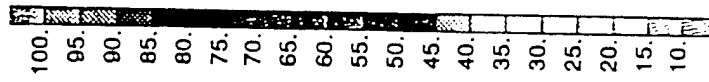
Potential Solver Input Menu

Exit CadDyn IPS DPP Potent PartGen Tracker Help

READY ....

Comment: Run script for Dynapac Potential Solver module.

Potential Solver Parameters

Run option: NEW   Debye Scaling: LOCAL   Timer: 1
Algorithm :   32_NODE   Cond. potential: OLD   Diagnostics:
Problem type: LAPLACE   Solution Mix: 0.000E+00   Initial: 1
Wake Effect: OFF   Final : 1
                                                            SCG   : 1
Convergence criteria: Environment: Screen : 0
  Maxits = 10   Temp = 1.000E-01   Special: 0
  RdRmin = 1.000E-03   Dens = 1.000E+11   Interf : 1
  RMSmin = 1.000E-02   Debye = 0.000E+00   Wake : 1
  Maxitc = 40   IO files :
  PotCon = 2.000E+00   PS_input : ps_in
  DebLim = 2.000E+00   PS_output: ps_out
  Conv. Effect: ON   Time parameters:
                              Start = 0.000E+00
Selected Grids: Rise = 1.000E-06
  From # 0 to #   0   Fall = 1.000E+30

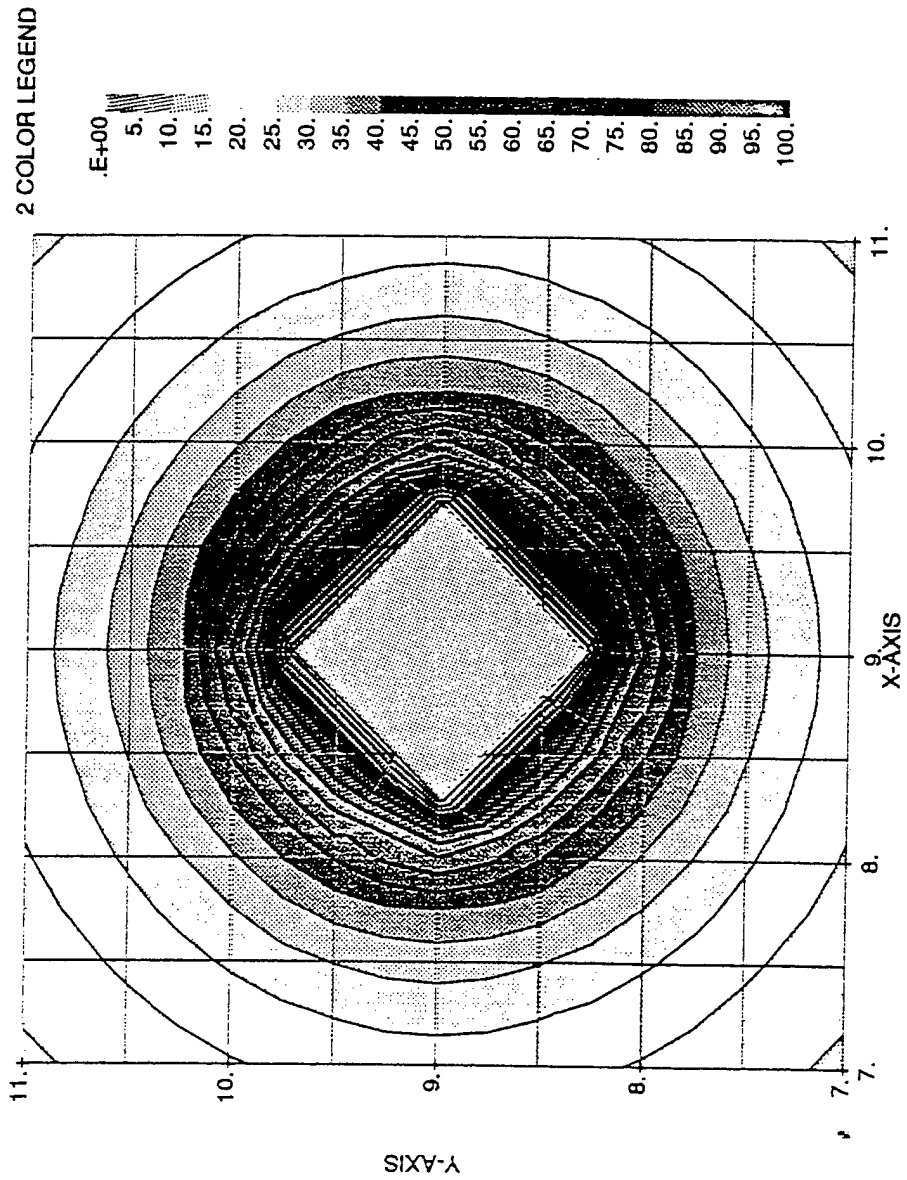159

COLOR LEGEND

Linear Octahedron with Subdivision

Y-AXIS

Z-AXIS

Minimum Potential = 8.42E+00   Maximum Potential = 1.00E+02
7.00 <Z< 11.00,   7.00 <Y< 11.00, CUTPLANE OFFSET X= 9.00
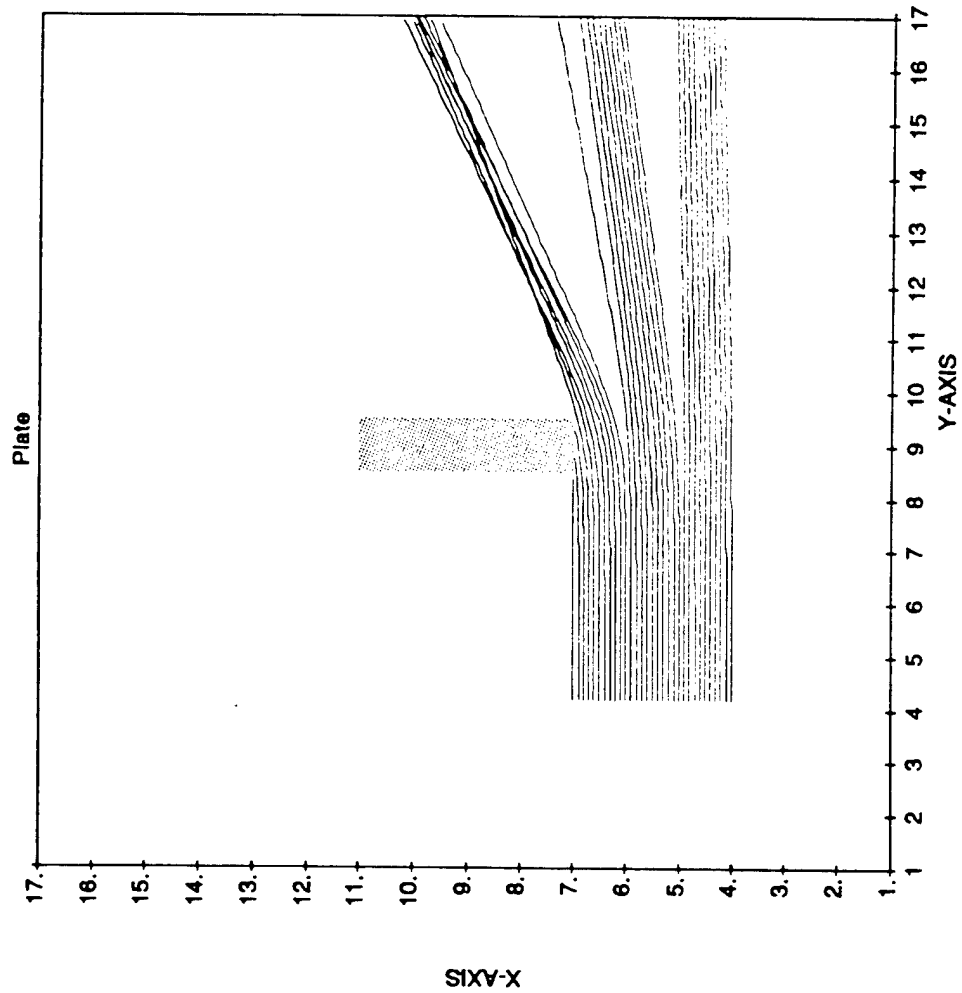
Octahedron Potentials - Trilinear

4/09/91 14:10:01

Octahedron with Cont. Fields and Subd.
Slice Z = 9.0000
Mesh Size = 1.4142E+00 meters
Min= 1.4101E+01   Max= 1.0000E+02

Date: 04-09-91
Time: 14:12:27

2 COLOR LEGEND

E+00
5.
10.
15.
20.
25.
30.
35.
40.
45.
50.
55.
60.
65.
70.
75.
80.
85.
90.
95.
100.

X-AXIS

Y-AXIS

Octahedron Potentials - DynaPAC

TriLinear Particle Trajectories

MAXWELL
S-CUBED Division

Plate

Y-AXIS

X-AXIS

4/09/91 14:17:24

162

DynaPAC Particle Trajectories

MAXWELL
S-CUBED Division

Slice Z = 9.0000
Mesh Size = 1.0000E+00 meters

Date: (
Time:

163
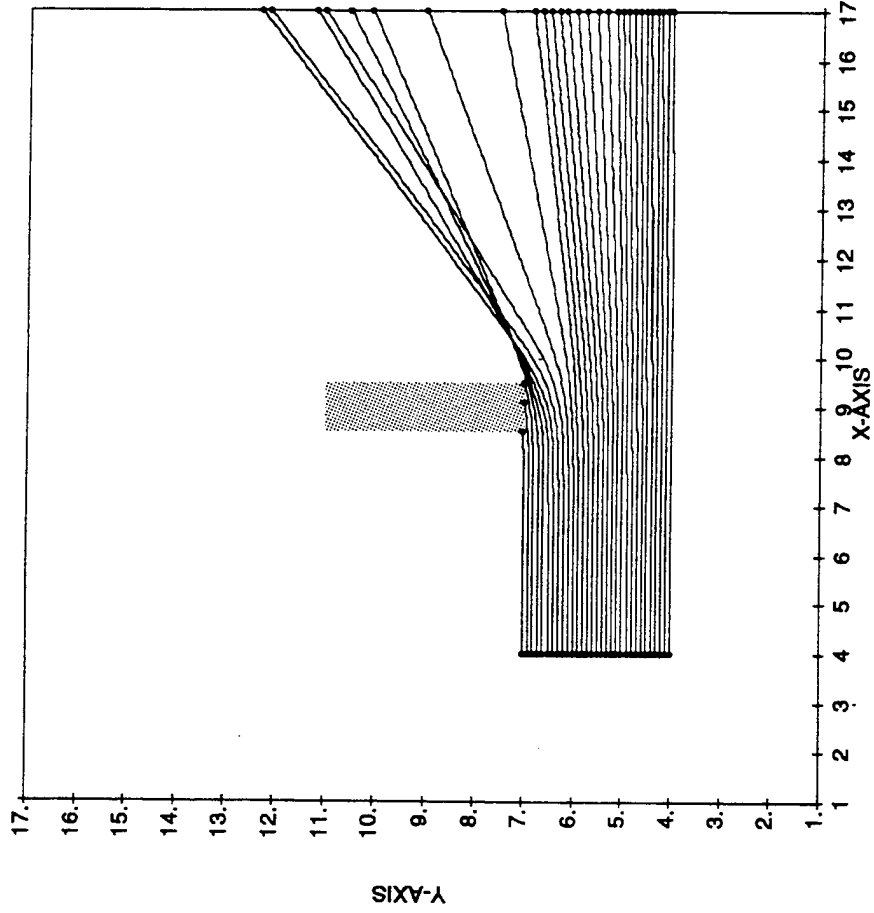
APPENDIX C

A copy of the paper presented at the AIAA Aerospace Meeting in Reno, NV follows:

AIAA-94-0327
Sheath Physics and Potential Mitigation
on the SPEAR-III Rocket Experiment

M. J. Mandell and G. Jongeward
Maxwell Laboratories, Inc., S-Cubed Division
La Jolla, CA

D. L. Cooke
Phillips Laboratory

W. J. Raitt
CASS, Utah State University

32nd Aerospace Sciences
Meeting & Exhibit
January 10-13, 1994 / Reno, NV

SHEATH PHYSICS AND POTENTIAL MITIGATION ON THE SPEAR-III ROCKET EXPERIMENT

M. J. Mandell and G. Jongeward
Maxwell Laboratories, Inc., S-Cubed Division,
P. O. Box 1620, La Jolla, California 92038-1620

D. L. Cooke
Phillips Laboratory
Hanscom AFB, MA 01731-5000

W. J. Raitt
CASS, Utah State University
Logan, Utah 84322-4405

Abstract

The SPEAR-III rocket experiment was launched on 15 March 1993 to test grounding devices for negative payloads. In this paper we review some of the high altitude flight data, and compare it with preflight predictions made using the DynaPAC computer code.

The plasma density during the high altitude portion of the flight was about 10^{11} m^{-3}. The predicted floating potential of the rocket varied from about 35% of an applied voltage of 10 kV to about 65% of an applied voltage of 1 kV, in excellent agreement with flight data. Plasma currents were also in agreement with preflight predictions.

Preflight predictions, using Paschen Law physics generalized to three dimensions, were that the high rate gas release would reduce the rocket potential to within 200 to 300 volts of plasma ground. The flight data is well-fit by a value of 225 volts. The thermionic emission device also reduced the spacecraft potential at high altitude.

Orientation relative to Earth's magnetic field had no effect on the floating potential or grounding operations, but had a large effect on the current collected by the boom.

Introduction

The SPEAR-III rocket experiment is third in a series of experiments to develop technology for the prediction and control of interactions between a spacecraft with high voltage components and the ionospheric environment. While previous experiments focused on prediction and understanding, the emphasis of SPEAR-III was on control. The objective was to test and compare four candidate devices for maintaining the main part of the payload as close as possible to plasma ground.

The need for spacecraft potential control goes beyond "Star Wars" applications. It is no longer unusual to design spacecraft power systems with primary voltages in excess of the conventional 28-32 volts. Space Station Freedom, with a 140 volt power system and a 30 year lifetime requirement, provides a major example of the need for potential control. Any spacecraft which has an ion engine or emits charged particle beams might benefit from potential control.

The three-dimensional calculations presented in this paper were performed prior to the flight using the DynaPAC computer code. (M. J. Mandell et al., 1992) DynaPAC is a general spacecraft-plasma analysis code developed by S-Cubed for Phillips Laboratory. DynaPAC is a finite element electrostatic code featuring CAD/CAM compatible spacecraft geometry, arbitrarily nested cubic grids, and strictly continuous electric fields.

SPEAR-III Description

An accompanying paper later in this session (W. J. Raitt et al., 1994) will describe the objectives, instrumentation, and basic results of the SPEAR-III rocket flight. In this section we give a thumbnail sketch sufficient for a reader to follow the subsequent discussion.

SPEAR-III was launched the evening of 15 March 1993 from Wallops Island, VA. A maximum altitude of approximately 290 km was achieved. The rocket was charged to negative potentials of 2-4 kV by applying a 10 kV positive bias to an 8-inch diameter sphere. The sphere was mounted on a 1 meter resistively graded boom oriented normal to the rocket axis. The bias decayed through an RC network with a time constant of about 1 second. Rocket potential was monitored by two devices: (1) a high impedance floating probe (measuring the potential difference between the rocket and a 2.5-inch diameter sphere on 3 meter boom). (P. L. Rodriguez et al.) and (2) a set of electrostatic analyzers measuring the energy of incident ions (H. R. Anderson et al., 1993).

166

In this paper we focus on the high altitude portion of the flight (roughly MET 220 to MET 350) during which the plasma density was ~10^{11}m^{-3}.

The four potential control devices were: (1) a thermionic electron emitter; (2) a hollow cathode "plasma contactor"; (3) a field effect electron emitter; and (4) an array of four gas jets. Of these, the gas jets (intended to systematically study a grounding effect seen accidentally during ACS firings on beam-emitting rockets) were most successful, holding the spacecraft potential to within 200- 500 volts of plasma ground. The thermionic electron emitter caused a definite reduction in spacecraft potential, though it failed to "ground" the vehicle. The other two devices were largely ineffective at high altitudes, due in part to malfunction of the devices themselves.

Current Balance with No Grounding Device

In the absence of plasma, floating potential of a biased payload such as SPEAR-III is determined by the condition that the total charge on the payload remain zero. That is, the payload acts as a capacitive divider. Since the SPEAR- III rocket has a much larger capacitance than the biased sphere, the negative potential achieved is less than ten percent of the bias voltage. Figure 1 shows a Laplace equation solution for the approximate vacuum floating condition. This configuration was observed during testing of a mockup payload in a large vacuum tank.
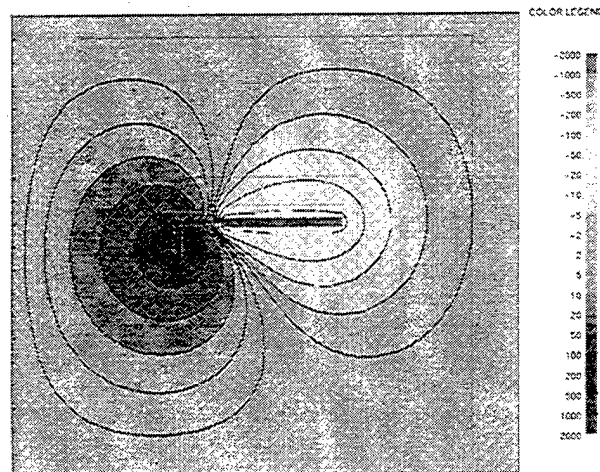

Fig. 1   Potentials around the SPEAR-III payload in approximate vacuum floating condition. Sphere is biased 1 kV relative to rocket body at -70 V.

When the payload is in the ionospheric plasma, the floating condition changes from zero net charge to zero net current. That is, the secondary-electron-enhanced ion current to the rocket body must balance the electron current collected by the sphere and boom. Since electrons have far higher mobility than ions, this means the negative, ion-collecting sheath about the rocket body must nearly choke off the positive, electron-collecting sphere sheath. Figure 2 shows a typical sheath configuration for the SPEAR-III payload in the ionospheric plasma.

Using the DynaPAC code we are able to calculate (as a function of applied potential, plasma density, plasma temperature, and magnetic field) the fraction of the applied potential that appears on the rocket body.

Figure 3 shows preflight calculations of this division of potential. The trends with potential and plasma density result from the effectiveness of the plasma in screening the body potential; this screening is most effective at low potential and high plasma density. At the expected plasma density of about 10^{11} m^{-3}, the fraction of potential appearing on the body varies from less than 36% at 10 kV bias to 65% at 1 kV bias. If the plasma density is decreased to 10^9 m^{-3}, the fraction of potential appearing on the body drops below 40% at 1 kV. Figure 4 shows the flight results (from the ESA potential measurements) for several shots with no effective grounding mechanism in operation. Agreement with the DynaPAC prediction is excellent.
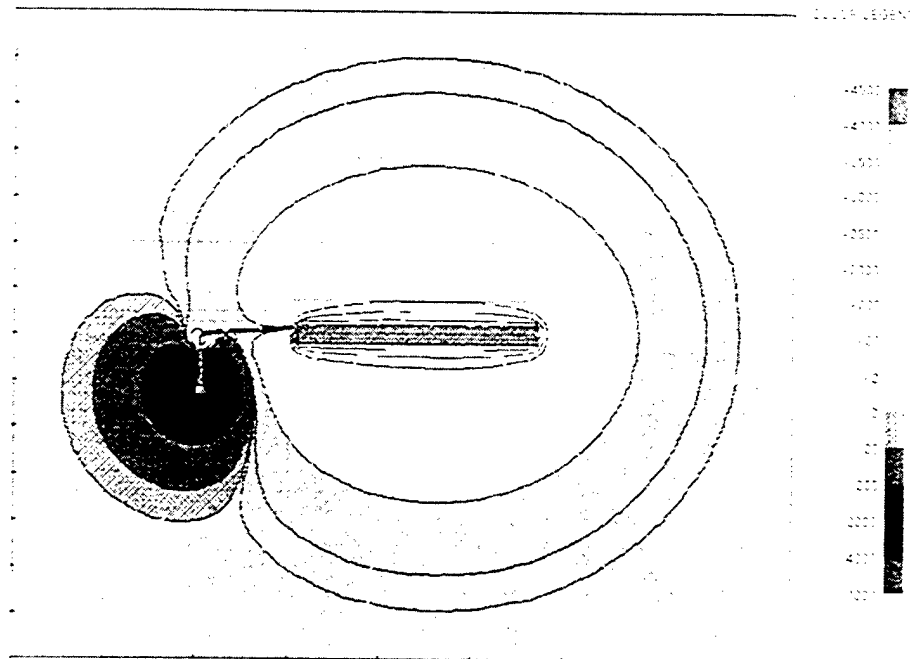
167

Fig. 2   Potentials around the SPEAR-III payload in ionospheric floating condition for plasma density 1×10^{11} m^{-3}. Sphere is biased 10 kV relative to rocket body at -3.5 kV.

The calculations also yield the plasma current through the high voltage circuit. Figure 5 shows the measured plasma currents for several shots together with DynaPAC preflight predictions. Again, agreement is excellent. Note that there is an apparent drop (by about a factor of two) in plasma density near the flight apogee.
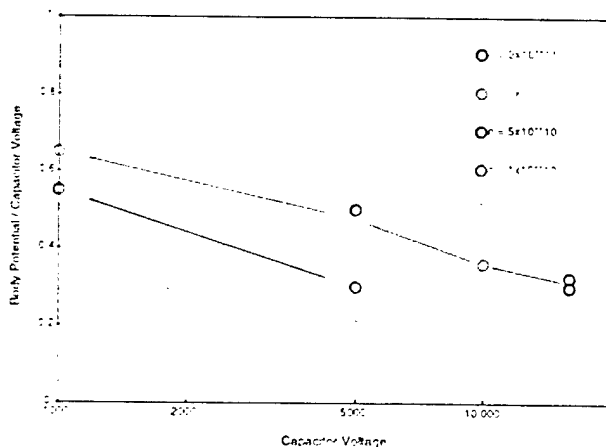

Fig. 3   DynaPAC preflight calculations of SPEAR-III floating potential, showing the fraction of applied potential on the negative body vs. the bias voltage. The upper set of lines represents the high altitude flight condition of plasma density $\sim 1 \times 10^{11}$ m^{-3}. The lower lines represent plasma densities of 1×10^{10} and 1×10^{9} m^{-3}.
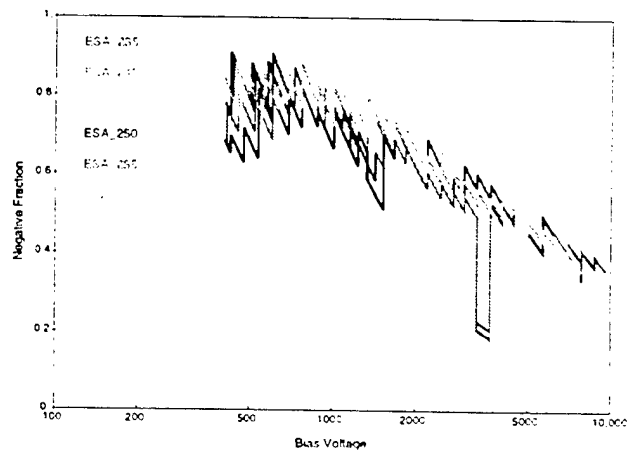

Fig. 4   ESA measured floating potential, showing the fraction of applied potential on the negative body vs. the bias voltage. The shots included have no grounding device (MET 235), Field Emission Device (MET 240, 245, 250, 255), or Hollow Cathode (MET 260), both of which were ineffective.
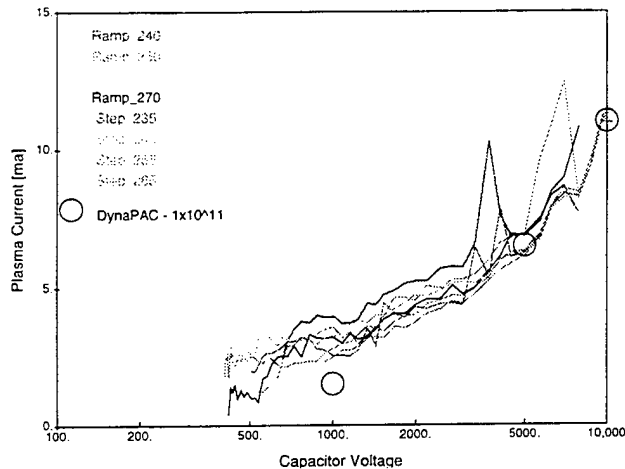
168

Fig. 5   Measured plasma currents compared with Dy-
naPAC preflight predictions. The shots included
have no grounding device (MET 235), Field
Emission Device (MET 240, 245, 250, 255), or
Hollow Cathode (MET 260, 265, 270), both of
which were ineffective. The spikes correspond
to ACS firings, which grounded the payload.

Grounding by Neutral Gas Release

The Neutral Gas Release experiment consisted of
two pairs of nozzles directed tangentially along the
rocket surface. In the high flux mode, each nozzle re-
leased two grams of argon per second for approximately
0.1 seconds. High flux releases alternated with low- and
zero-flux emissions. Both the high and low emission
levels (as well as ACS firings) are confirmed by the
Neutral Pressure Gauge data.

Figure 6 shows the gas density pattern expected to
be produced by the four nozzles. Grounding would be

accomplished by establishing a breakdown path through
this non-axisymmetric gas cloud. However, we would
expect a breakdown path to follow an electric field line
which is, at least initially, radial. We calculate the
voltage needed to sustain breakdown in the same manner
as for Paschen breakdown between parallel plates, ex-
cept that here we must account for the three-dimensional
geometry. Thus, to determine the conditions under
which breakdown would occur, we must calculate the
number of ions produced (one less than the electron mul-
tiplication factor) by an electron traveling along a path
through the gas cloud, as a function of the angular posi-
tion of the path and the negative potential on the rocket.
When this is equal to the inverse of the secondary elec-
tron emission coefficient for ion impact, the ions impact-
ing the rocket reproduce the single electron which pro-
duced them, satisfying conditions for breakdown.

Figure 7 shows the number of ions produced along a ra-
dial trajectory, as a function of the trajectory direction
and the body potential. For body potentials of a few
hundred volts or less we anticipate a secondary electron
emission coefficient of about 0.05 to 0.1. The figure in-
dicates that the breakdown threshold is fairly insensitive
to the precise value of the secondary emission coeffi-
cient, and should occur at 200 to 300 volts along a path
90 degrees from the nozzle location and parallel to the
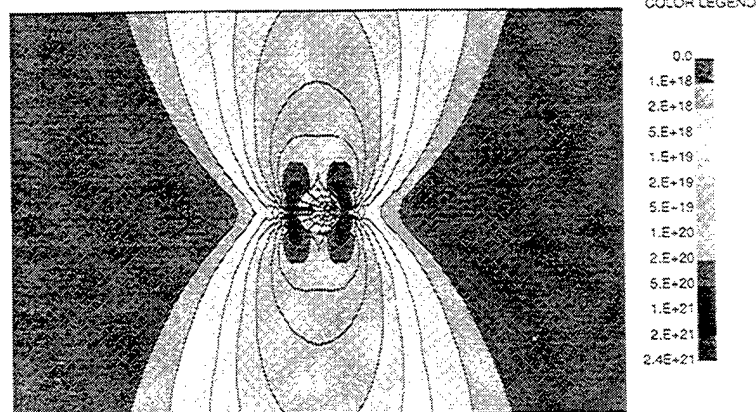nozzle flow direction.

Fig. 6   Neutral gas density contours for the SPEAR-III gas release system. The rocket axis is normal to
the page. Two pairs of nozzles are located on the left and right of the cross-section, and are
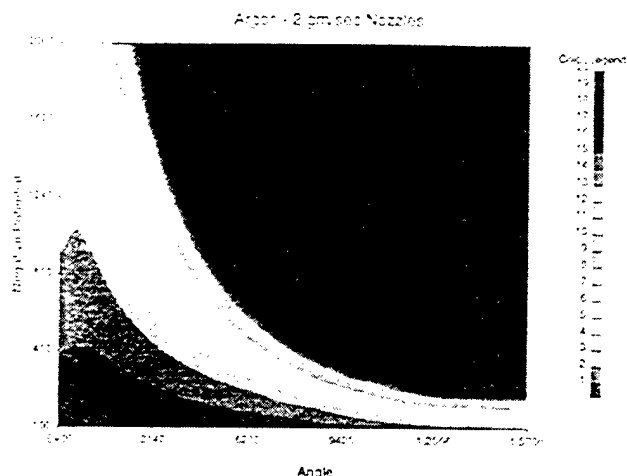aimed up and down the page.

169

Fig. 7   Number of ions produced along a radial trajec-
tory in the plane of Figure 6, as a function of
rocket potential and trajectory angle. The left
side of the figure corresponds to a trajectory be-
ginning at the nozzle and normal to the flow di-
rection. The right side of the figure corresponds
to a trajectory beginning 90 degrees from the
nozzle and parallel to the flow direction. The
calculation is for emission of 2 grams of Argon
per nozzle per second. Breakdown threshold
lies in the graded bands, at the inverse second
Townsend coefficient.

Figures 8a and 8b show the ESA-measured rocket poten-
tial fraction (as a function of applied potential) during
gas puff shots. The rocket potential is bimodal, alternat-
ing between the no-grounding-device value and a less
negative value well-fit by -225 volts. This pattern holds
down to applied potential as low as 400 volts. The high-
time- resolution Floating Probe potential measurements
show clearly that the low potential state is achieved
immediately on the commencement of the high-rate neu-
tral gas release.

and relaxes to the higher state as the gas density de-
cays. (The apparent long decay time for the gas density,
clearly observed by the Neutral Pressure Gauge, remains
unexplained.) The low-rate gas release generally fails to
reduce the rocket potential.

Potential Reduction by Thermionic Emission

Thermionic emission of electrons seems like the
obvious device to maintain a negative payload at low
potential in a nearly passive way. However, experience
(e.g., PIX-II, M. J. Mandell et al., 1986) has shown the
failure of such devices to maintain vehicle ground.
SPEAR-III is the first flight experiment in which we are
able to assess quantitatively the degree of potential re-
duction produced by a thermionic device.

Figures 9a and 9b each show the (ESA measured)
fraction of applied potential on the negative body for
three shots during thermionic emitter operation, com-
pared with a comparable no-grounding shot. The ther-
mionic emitter produces a potential reduction by about
twenty percent at the highest bias voltages, improving to
better than fifty percent at bias voltages below 1 kV.
(Indeed, at the lower bias voltages the thermionic emit-
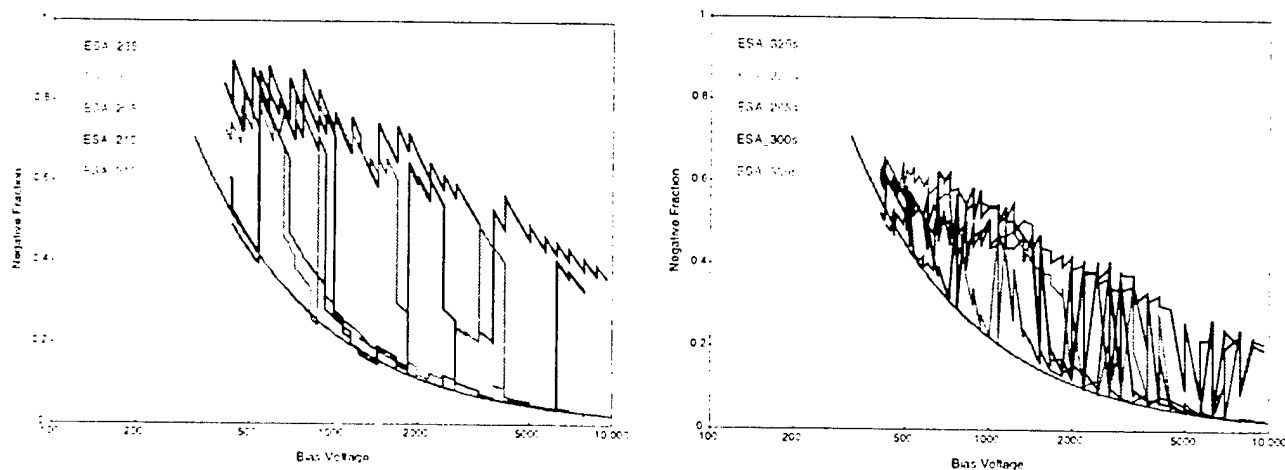ter provides better grounding than the gas jets!!)

Fig. 8   ESA measurements of grounding by neutral gas release during Science Attitude 1 (a) and Science Attitude 2
(b). Each figure contains one shot with no active grounding (MET 235 and MET 325) and four shots with in-
termittent gas puffs. The gray line on each figure corresponds to a rocket potential of -225 volts.
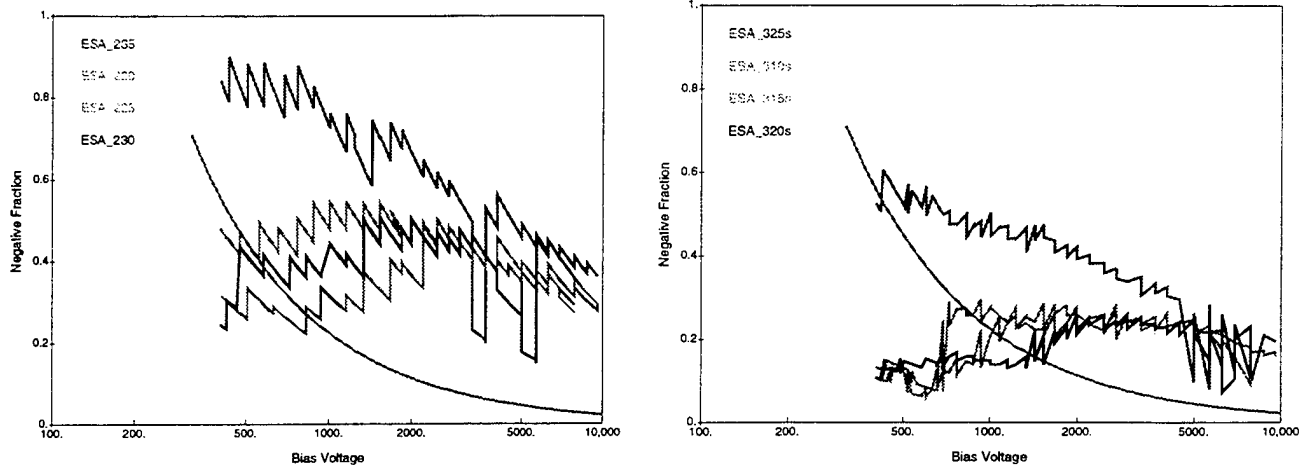
170

Fig. 9   ESA measurements of potential reduction by the Thermionic Emission Device during Science Attitude 1 (a)
and Science Attitude 2 (b). Each figure contains one shot with no active grounding (MET 235 and MET 325)
and three shots with the Thermionic Emission Device active. The gray line on each figure corresponds to the
potential level of -225 volts achieved by neutral gas release.

Figures 10a and 10b show the plasma current
through the system for the same two sequences. In both
cases there is a 2-3 milliampere increase in current due
to thermionic emitter operation. Presumably, this current
consists of an increase in electron collection by the
sphere

(due to its increased potential and reduced screening),
balanced by emission from the thermionic device. Why
the effective thermionic emitter current is held to such
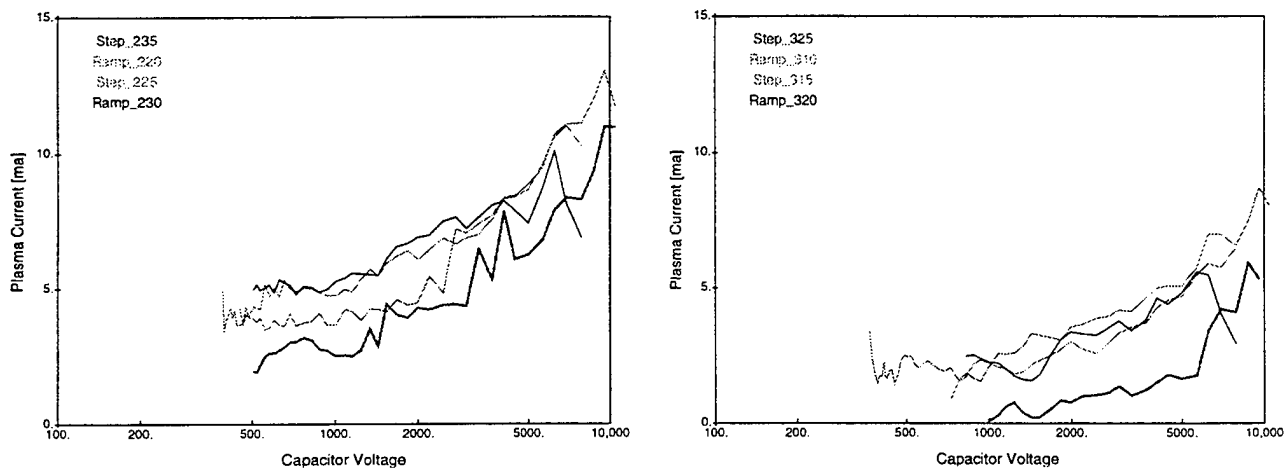low values requires further study.

Fig. 10   Increase in plasma current during Thermionic Emission Device operation during Science Attitude 1 (a) and
Science Attitude 2 (b). Each figure contains one shot with no active grounding (MET 235 and MET 325) and
three shots with the Thermionic Emission Device active.

Figures 10a and 10b show the plasma current
through the system for the same two sequences. In both
cases there is a 2-3 milliampere increase in current due
to thermionic emitter operation. Presumably, this current
consists of an increase in electron collection by the
sphere (due to its increased potential and reduced
screening), balanced by emission from the thermionic
device. Why the effective thermionic emitter current is

held to such low values requires further study.

Magnetic Field Effect

During the high altitude portion of the flight the
payload assumed two distinct attitudes relative to Earth's
magnetic field. During the early portion of the flight
(Science Attitude 1) the payload was oriented with the
magnetic field normal to the plane formed by the boom

171

and the rocket axis. In this attitude, the boom lies in the path of electrons E x B drifting in the sphere sheath, and collects a substantial fraction of the total plasma electron current. Near apogee (which occurred at about MET 290), a roll maneuver was executed to achieve Science Attitude 2, in which the boom was parallel to the magnetic field. In this second orientation, the boom is weakly magnetically insulated by the Earth's field, and collects less current, with the current concentrated slightly more toward the high voltage end of the boom.

Available from the flight data is the current measured at the low-voltage end of the 1 MΩ boom. It is convenient to cast this data in terms of the apparent impedance of the boom. When injection of plasma current at a single point of the boom is accounted for, figure 11 shows that the apparent boom impedance increases.
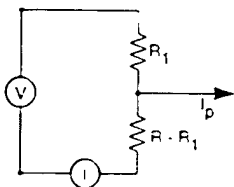
$$V = \left(I + I_p\right)R_1 + I\left(R - R_1\right)$$

$$\frac{V}{I} = R + \frac{R_1 I_p}{I}$$

$$\frac{V}{I} = \frac{RV}{V - R_1 I_p}$$

Fig. 11   Injection of plasma electron current into the graded boom causes an increase in its apparent impedance, depending upon the amount of current and its mean point of injection.

Table 1 DynaPAC preflight results, showing increase in apparent impedance of the 1 MΩ graded boom due to plasma current.

Plasma Density	1×10^{11} m^{-3}	
Plasma Temperature	0.1 eV	
Magnetic Field	0.4 gauss	
Bias Voltage	10 kV	
Negative Fraction	0.35	
Science Attitude	1	2
Total Current	11.1 ma	11.4 ma
Boom Current	5.9 ma	3.6 ma
Point of Injection	0.22 MΩ	0.19 MΩ
Apparent Impedance	1.15 MΩ	1.07 MΩ

Table 1 shows DynaPAC preflight results for the boom current in these two attitudes. We expect the apparent boom impedance to be highest in Science Attitude 1, lower in Science Attitude 2, and lowest at low altitudes when plasma current is negligible. Figure 12 shows the apparent boom impedance for five no-grounding shots, two in each orientation and the last at relatively low altitude. It is clear that the expected pattern is followed and that the effect is of the magnitude predicted.
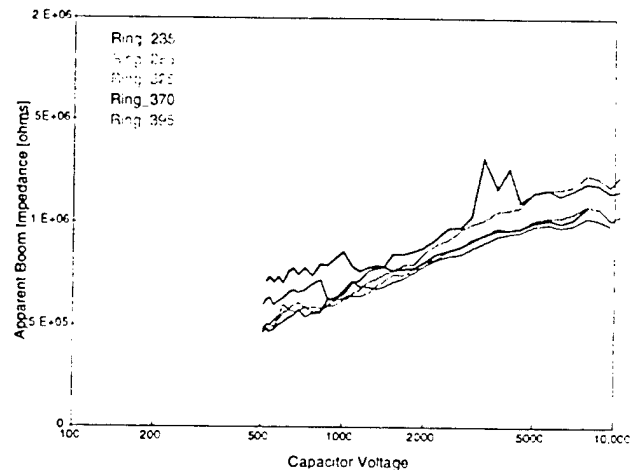
Fig. 12   Apparent boom impedance during shots with no active grounding. The apparent impedance during Science Attitude 1 exceeds the low altitude measurement by about the factor predicted by DynaPAC.

The magnetic field effect should be higher during grounding operations, because (a) the total current is higher, and (b) the sphere sheath is more nearly spherically symmetric. Figure 13 shows that this is indeed the case. During thermionic emitter operation, which, we have seen, caused a modest reduction in spacecraft potential, the apparent boom impedance increases an additional ten percent in Science Attitude 1, but not at all in Science Attitude 2. During neutral gas release the effect is a factor of two in Science Attitude 1, but no effect is apparent in Science Attitude 2.
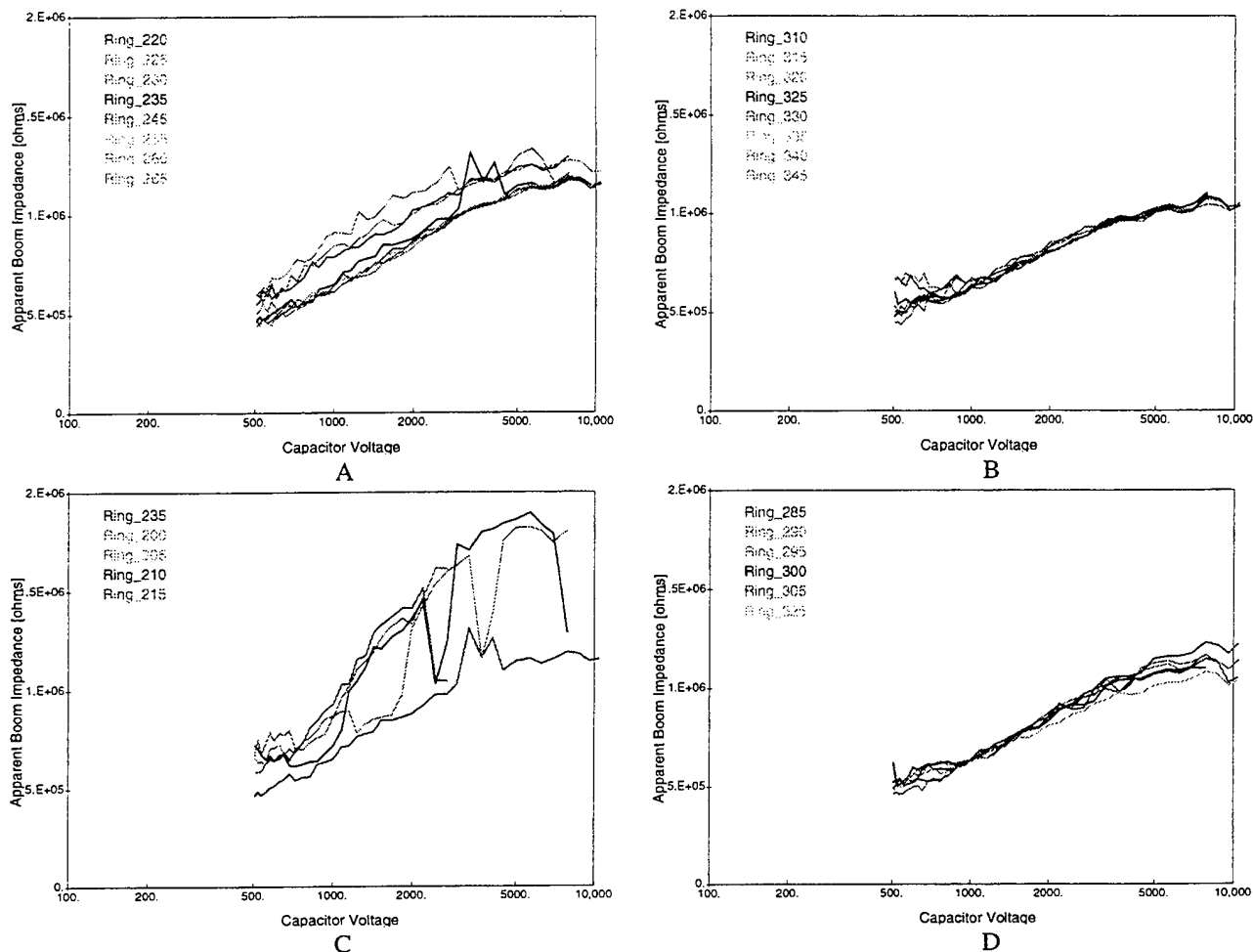
172

Fig. 13 The apparent boom impedance during Science Attitude 1 increases further during Thermionic Emitter operation (a) at MET 220, 225, and 230, and even more dramatically during neutral gas release (c) at MET 200, 205, 210, and 215. In Science Attitude 2 no effect is seen either during Thermionic Emitter operation (b) at MET 310, 315, and 320, or neutral gas release (d) at MET 290, 295, 300, and 305. (Remaining shots have no effective grounding device.)

Conclusions

SPEAR-III demonstrated our ability to create, predict and (to a limited degree) control negative spacecraft potential.

(1) The DynaPAC preflight calculations successfully predicted the points of current balance (floating potential) for a complex, three-dimensional configuration.

(2) Grounding of a negative payload by neutral gas release was demonstrated. Four jets of 2 g/s of argon held the payload to approximately -225 volts. A flow rate one order of magnitude lower had little or no effect. Both the potential value and the flow rate are in good agreement with preflight calculations using Paschen Law physics generalized to a three-

dimensional configuration.

(3) The thermionic emission device was able to reduce the payload potential. However, the effective emission current from the device seemed to be limited to 2-3 ma.

(4) As predicted by the preflight calculations, the orientation relative to Earth's magnetic field had no noticeable effect on the floating potential, the total plasma current, or the effectiveness of the grounding devices. However, the effect of the magnetic field is seen clearly in the division of current between the sphere and the boom, in agreement with preflight calculations. This effect is most pronounced when the payload is grounded by neutral gas release.

Regrettably, much potential data was lost due to mal-

173

function of the Hollow Cathode Plasma Contactor and of the Field Emission Device. Other unresolved issues include:

(a) The long decay time for the neutral gas plume.

(b) The nature of the breakdown in the neutral gas plume during grounding operations. Failure of the on-board video deprived us of much potentially useful data on this subject.

(c) An explanation for the low effective current from the Thermionic Emission Device.

(d) The ion energy distributions seen by the ESA. While clear, unambiguous "charging peaks" were observed, the current in the charging peak was well below preflight predictions, and a great deal of ion current was distributed at lower energies.

References

1. Anderson, H. R., D. W. Potter, and J. L. Johnson, "Potential of SPEAR-III Rocket Deduced from Energy Distributions of Attracted Ions," AGU 1993 Fall Meeting, San Francisco, CA, December 6-9, 1993.

2. Mandell, M. J., I. Katz, G. A. Jongeward, and J. C. Roche, "Computer Simulation of Plasma Electron Collection by PIX- II," Journal of Spacecraft and Rockets 23, 512-518, 1986.

3. Mandell, M. J., T. Luu, J. Lilley, G. Jongeward and I. Katz, Analysis of Dynamical Plasma Interactions with High-Voltage Spacecraft, Phillips Laboratory report Pl-TR-92-2248 (two volumes), June, 1992, Vol. I ADA262784, Vol II ADA262783.

4. Raitt, W. J., G. Berg, D. Thompson, and B. White, "SPEAR-3: A Sounding Rocket Experiment to Study Methods of Electrically Discharging a Negatively Charged Space Platform at LEO Altitudes," AIAA-94-0331, AIAA 32nd Aerospace Sciences Meeting, Reno, NV, January 10-13, 1994.

5. Rodriguez, P. L., C. Seifring, and J. Antoniades, Naval Research Laboratory.

APPENDIX D

A copy of the paper presented at the SPRAT XIV Conference follows:

PARASITIC CURRENT COLLECTION BY PASP PLUS SOLAR ARRAYS *

V. A. Davis and B. M. Gardner
S-Cubed Division of Maxwell Laboratories
San Diego, California 92121

D. A. Guidice and P. S. Severance
Phillips Lab, Hanscom AFB, MA 01731

SUMMARY

Solar cells at potentials positive with respect to a surrounding plasma collect electrons. Current is collected by the exposed high voltage surfaces: the interconnects and the sides of the solar cells. This current is a drain on the array power that can be significant for high-power arrays. In addition, this current influences the current balance that determines the floating potential of the spacecraft. One of the objectives of the Air Force (PL/GPS) PASP Plus (Photovoltaic Array Space Power Plus Diagnostics) experiment is an improved understanding of parasitic current collection. We have done computer modeling of parasitic current collection and have examined current collection flight data from the first year of operations.

BACKGROUND

Solar arrays provide power for nearly all space systems. Traditionally, solar arrays have operated in the 30 V range to avoid complex interactions with the plasma environment. As space systems become more ambitious, more power, therefore higher voltages, is needed.

The exposed metal and semiconductor surfaces of spacecraft collect ions and electrons from the space plasma. The potential of the spacecraft adjusts until the net current is zero. As each solar cell is at a different potential, some cells collect ions and some collect electrons. For a conventional spacecraft design, the negative side of each array is grounded to the spacecraft chassis. Therefore, the spacecraft body floats negative with respect to the plasma. Figure 1 shows the various currents that contribute to the net current to a spacecraft.

As electrons are faster than ions at the same temperature, spacecraft ground is usually slightly negative. However, it may be necessary to keep the spacecraft body near zero potential with respect to the plasma. For example, an instrument to measure the low energy plasma environment may need to be near plasma ground. Anodization arcing and negative potential arcing are potentially disruptive at potentials greater than 50 to 100 V negative with respect to the plasma (refs. 1 and 2). In these cases active control is used.

At high positive potentials, typically over 200 V, the current rapidly rises due to a phenomena called snapover. Snapover was first observed at NASA/LeRC (refs. 3, 4 and 5). Snapover can occur whenever there is a biased surface adjoining an insulating surface and the bias is above the first crossover of the secondary yield curve of the insulating surface. (refs. 6 and 7) This occurs when the cell potential is above the first crossover for the coverglass or the array support structure.

PASP Plus is the principal experiment integrated onto the Advanced Photovoltaic and Electronics Experiments (APEX) satellite bus (ref. 8). The experiment tested twelve different solar array designs. Parasitic current collection was measured for eight of the designs under various operational and environment conditions. Here we focus on the six flat designs, as the concentrators have minimal current collection as the high potential surfaces are not exposed to the plasma. The arrays considered are listed in Table 1.

Table I

Array Number	Array Type	Number of Cells	Cell Size
1	Standard Silicon Module with mesh interconnects	20	2 cm x 4 cm
2	Standard Silicon Module with mesh interconnects	60	2 cm x 4 cm
3	Space Station with wrap through interconnects	4	8 cm x 8 cm
4	Thin GaAs/Ge with wire interconnects	20	4 cm x 4 cm
5	APSA with germanium coating	12	2.6 cm x 5.1 cm
6	Thin GaAs/Ge with wire interconnects	12	4 cm x 4 cm
8	Thick GaAs/Ge with wrap through interconnects	4	4 cm x 4 cm
11	Thick GaAs/Ge with wire interconnects	8	4 cm x 4 cm

CALCULATIONS

The computation of the current collected by a specific solar array can become intractable. The gap size is of the order of tens of mils while the solar cells are a few centimeters and the entire array can be meters. Each solar cell is at a slightly different potential. The current depends on the geometry of the gap, the geometry of the entire array, the spacecraft, and the plasma conditions.

We are interested in improving our understanding of which aspects of the problem are most important and developing a tool or at least an algorithm to assist spacecraft designers. Our approach was to look in detail at current collection at a single cell gap. Using the computer we can vary each parameter independently. We then developed a formula that estimates the current collected by a single gap. We then incorporated the formula into a tool that adds up the current from all the gaps to give the current collected by an array. Information on the array geometry and how it influences the current are included in the tool.

We did two-dimensional calculations for the various geometries flown. The calculations span the space of plasma conditions, applied potential, and material parameters. We used the calculations and early flight data to develop an analytic formula for the dependence of the current on the primary problem variables. The calculational technique is discussed in a paper presented at the previous SPRAT conference (ref. 9).

The form chosen for the analytic fit appears odd at first glance.

$$\text{Sheath Area} = a\, A(\text{geom.})\, \frac{\phi^{0.35}}{\eta^{0.65}}\, (\phi\, \eta)^b\, \exp\left(\frac{c}{\eta} - \frac{d}{\eta\lambda}\right)$$

The parameters are

$$\phi = \frac{\text{potential with respect to the plasma}}{\text{plasma temperature}}$$

177

$$\eta = \frac{\text{first cross over}}{\text{potential with respect to the plasma}}$$

$$\lambda = \frac{\text{debye length}}{\text{cell thickness}}$$

The $\phi \eta$ factor is proportional to the potential. The $\phi \eta$ factor modifies the dependence on the temperature and first cross over. The exponential growth with the potential is accounted for by the exponent. The form of the exponent allows for the increase of sheath area with debye length and a decrease in sensitivity to debye length at larger sheath distances. The a, b, c, and d values were adjusted to fit the calculations. A is a function of the array geometry.

The analytic formula was incorporated into the EPSAT computer code (refs. 10 and 11).

FLIGHT DATA

We examined the measured collected current as a function of the applied bias and plasma density for the first nine months of PASP Plus data collection. We focused on measurements made in the ram and with the emitter off. We expect that the wake measurements depend on the attitude of APEX. Generally, when the emitter is on, the APEX floating potential is positive and an algorithm for the determination of the plasma density is needed. To avoid these complications, we confined our early examinations to ram, emitter off measurements.

Leakage current is measured as part of a 30 second sequence of measurements. During each 30 second sequence there are two Langmuir probe sweeps (one up and one down) with the applied bias at zero, and then 23 measurements of the leakage current with the applied bias at a constant. For each 30 second sequence, we used the 22nd current measurement and the plasma density and temperature from the following Langmuir probe sweep. We divided current by the plasma thermal current to compute a collecting area for each measurement.

$$\text{Collecting Area } \left(\text{m}^{-2}\right) = \frac{\text{Leakage Current (A)}}{2.68 \times 10^{-14} \, \text{Density} \left(\text{m}^{-3}\right) \sqrt{\text{Temperature (eV)}}}$$

In order to plot the leakage current, we binned and then averaged the data obtained over the nine months. Lower density measurements are excluded because photoemission may play a role. As the plasma conditions and applied bias are correlated with the time on orbit, attitude, and location within the orbit, unknown and unaccounted for systematic factors may influence these measurements.

Several features of interest are clear on inspection of Figure 2.

Overall, the collecting area rises about two orders of magnitude as the applied bias rises one order of magnitude. This is typical of leakage current when snapover plays a role in the current collection process (refs. 12-14). Arrays #1 and #2, the conventional interconnect design, do not rise as quickly, particularly at the high bias end. Also, the current collection curve for array #5, APSA, is different from all of the other arrays.

In general the collected current is several times the array area. Table 2 gives the array and panel areas for the various test solar arrays.

Table II Array and Panel Areas.

Array	Array Area (m^{-3})	Panel Area (m^{-3})
# 1	0.016	0.129
# 2	0.048	0.129
# 3	0.026	0.078
# 4	0.032	0.129
# 5	0.015	0.059
# 6	0.019	0.129
# 8	0.0064	0.029
# 11	0.013	0.029

There is a minimum collecting area for each plasma density that is the same for all of the arrays. The smallest measured PASP Plus leakage current value is 0.2 μA. This means that the collecting area levels off at 5×10^{-3} m^{-2} for a plasma density of 3×10^{9} and at 5×10^{-4} m^{-2} for a plasma density of 3×10^{10}. Collecting areas near and below this value are not physically meaningful.

The collecting area does not depend strongly on the plasma density. The collecting area is larger for lower densities (longer debye lengths). The dependence on density is stronger for lower densities.

And finally, there is a large amount of scatter in the graphs. When the several measurements in the same bin are compared, variations of a factor of ten are common.

DISCUSSION AND COMPARISON WITH CALCULATION

In order to compare the measurements with the model described above, it is first necessary to account for the APEX floating potential. The arrays are biased with respect to the APEX chassis. The amount of current they collect depends on the potential with respect to the ambient plasma. Like any spacecraft, there are several sources of current to APEX that must balance. We used the EPSAT (refs. 10 and 11) computer program to model the various components of the current and compute the floating potential.

The electron current collected by solar cells of the power solar arrays that are at positive potential with respect to the plasma is computed using the above model. The ion current collected by the solar cells is assumed to be negligible. The Z-93 paint on the surfaces of the panels is taken to have a conductivity divided by thickness of 10^{-6} mho m^{-2}. The body of APEX is taken to collect ions from a sheath in the same manner as a 0.45 m radius sphere in a flowing plasma. The photoelectron current emitted is taken to be constant at 2×10^{-5} A m^{-2} when APEX is not in eclipse. And the electron current collected by the test array is modeled as above.

The floating potential of APEX is near zero when the current collected by the test array is less than the ram ion current collected by the spacecraft body. A 0.45 m radius sphere moving at 7700 m s^{-1} in a 10^{10} m^{-3} plasma collects about 0.13 mA. This is the same as the electron thermal current for a 10^{10} m^{-3}, 0.1 eV plasma to a 1.5 m^{2} object. The floating potential of APEX shifts when the collecting area exceeds 1.5 m^{2}. Therefore the collecting area versus applied bias curve flattens out at 1.5 m^{2}.

The flight measurements were taken over a period of months under a variety of conditions. Plasma constituents, plasma temperature, and sunlight/eclipse condition all influence the current to the test arrays. All of these effects are included in the EPSAT computer code. In addition, EPSAT has an orbit propagator (ORB) and a plasma density and temperature model (IRI-86 with an extension to higher altitudes).

For each array, except #5, for each applied bias value, we computed the collected current, plasma density, and plasma temperature at 287 times during the 9 months covered by the flight data. Keeping only the points for which the arrays face the ram direction and APEX is below 1500 km, we computed the collecting area in the same manner as for the flight data, binned the results by density, and averaged. Figure 3 shows the results.

A few general observations can be made regarding the comparison of the calculational results and the flight results. At present the model has less density dependence than observed during flight. The computed current at the higher potentials grows faster than observed. The parameters used for arrays #4 and #6 give current values that are too low and the parameters used for arrays #8 and #11 give current values that are too high.

The current collection characteristic of array #5, APSA, is different from all of the other arrays. We believe that this is because it is coated with a layer of Germanium, which is a semi-conductor. Current is conducted through the Germanium coating even in the absence of plasma. This parasitic current is linear with the applied bias with a resistance of approximately 3 MΩ. Current is also collected from the plasma. This current is comparable to the current collected by an array with a low first cross over potential. Figure 4 shows the effective circuit. Current is collected across the entire surface of the array.

The measured current I_0 is given by the following:

$$I_0 = f\,I_p + \frac{\phi_{bias}}{R}$$

The fraction f is used to account for the fact that electrons are collected by the entire surface and not just at the array potential. When we subtract the parasitic current collected from the measured current, we get the collecting area curves shown in Figure 5. The figure compares the experimental results with the results of calculations that treat the array as a constant potential surface on a grounded spacecraft. The calculations were done using the NASCAP/LEO code (ref. 15).

The adjusted flight data values are higher than the calculations. A lower resistance value might provide a better match. Otherwise the calculations substantiate the conclusion that the measured current is the sum of the collected current and the conducted current.

CONCLUSIONS

We examined the current collected as a function of the various parameters for the six non-concentrator designs. The results are similar to those obtained in previous experiments and predicted by the calculations.

We are using the flight data to improve and validate the analytic formula developed. The formula can be used to quantify the parasitic current collected. Anticipating the parasitic current value allows the spacecraft designer to include this interaction when developing the design.

REFERENCES

1. Vaughn, J.A., et al.: Extrapolation of Electrical Breakdown Currents from the Laboratory to Space Station. AIAA 92-0822. AIAA 30th Aerospace Sciences Meeting, Reno, Nevada, 1992.

2. Ferguson, D.C.: The Voltage Threshold for Arcing for Solar Cells in LEO - Flight and Ground Test Results. NASA TM 87259, 1986.

3. Purvis, C.K.; Stevens, N.J.; and Berkopec, F.D.: Interaction of Large High Power Systems with Operational Orbit Charged-Particle Environments. NASA TM X-73867, 1977.

4. Stevens, J.N.: Interactions Between Spacecraft and the Charged-Particle Environment. Spacecraft Charging Technology - 1978, NASA Conference Publication 2071, AFGL-TR-79-0082, 1978, pp. 268-294, ADA084626.

5. Kennerud, K.L.: High Voltage Solar Array Experiments, NASA Rep. CR-121280, 1974.

6. Chaky, R.C.; Nonnast, J.H.; and Enoch J.: Numerical Simulation of Sheath Structure and Current-Voltage Characteristics of a Conductor-dielectric Disk in a Plasma. J. Appl. Phys., vol. 52, 1981, pp. 7092-7098.

7. Katz, I.; and Mandell, M.J.: Differential Charging of High-Voltage Spacecraft: The Equilibrium Potential of Insulated Surfaces. J. Geophys. Res., vol. 87, 1982, pp. 4533-4541.

8. Guidice, D.A.: High Voltage Space-Plasma Interactions Measured on the PASP Plus Test Arrays, this proceedings, 1995.

9. Davis, V.A.; and Gardner, B.M.: Parasitic Current Collection by Solar Arrays in LEO, NASA Conference Publication 3278, 1994, pp. 227-235

10. Kuharski, R.A.; Jongeward, G.A.; Wilcox, K.G.; and Rankin, T.V.: High Voltage Interactions of a Sounding Rocket with the Ambient and System-Generated Environments. IEEE Transactions on Nuclear Science, vol. 37, 1990, pp.2128-2133.

11. Gardner, B.M.; Jongeward, G.A.; Kuharski, R.A.; Wilcox, K.G.; and Rankin, T.V.: The Environmental Workbench: A Design Tool for the International Space Station. AIAA 95-0599, AIAA 33rd Areospace Sciences Meeting, Reno, Nevada, 1995.

12. Grier, N.T.; and Stevens, N.J.: Plasma Interaction Experiment (PIX) Flight Results. Spacecraft Charging Technology - 1978, NASA Conference Publication 2071, AFGL-TR-79-0082, 1979, ADA084626 pp. 295-314.

13. Grier, N.T.: Plasma Interaction Experiment II (PIX II): Laboratory and Flight Results. Spacecraft Environmental Interactions Technology, 1983 , NASA Conference Publication 2359, AFGL-TR-85-0018, 1985, pp. 333-347, ADA202020.

14. Ferguson, D.C.: RAM/WAKE Effects on Plasma Current Collection of the PIX II Langmuir Probe. Spacecraft Environmental Interactions Technology, 1983, NASA Conference Publication 2359, AFGL-TR-85-0018, 1985, pp. 349-357, ADA202020.

15. Mandell, M.J.; and Davis, V.A.: User's Guide to NASCAP/LEO. LEW-15641, SSS-R-85-7300-R2, 1990. (Available as LEW-15641 from COSMIC, U of Georgia.)
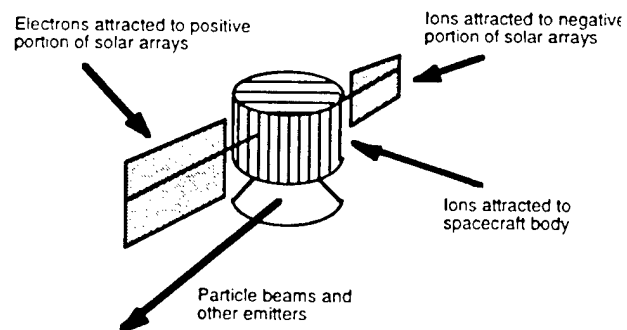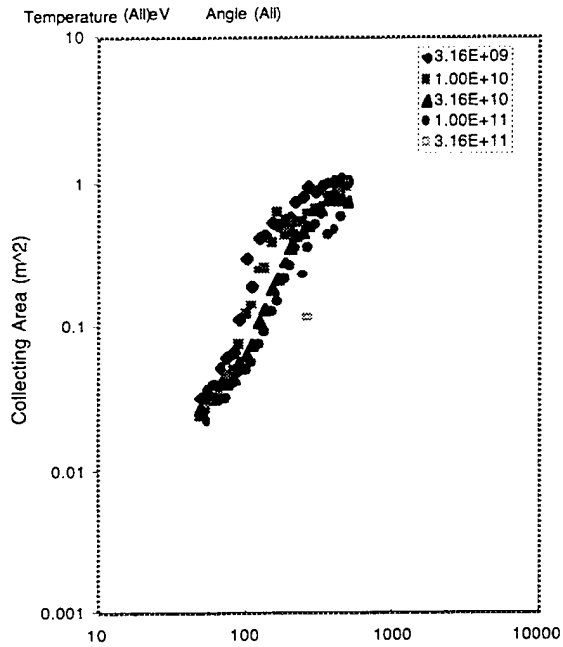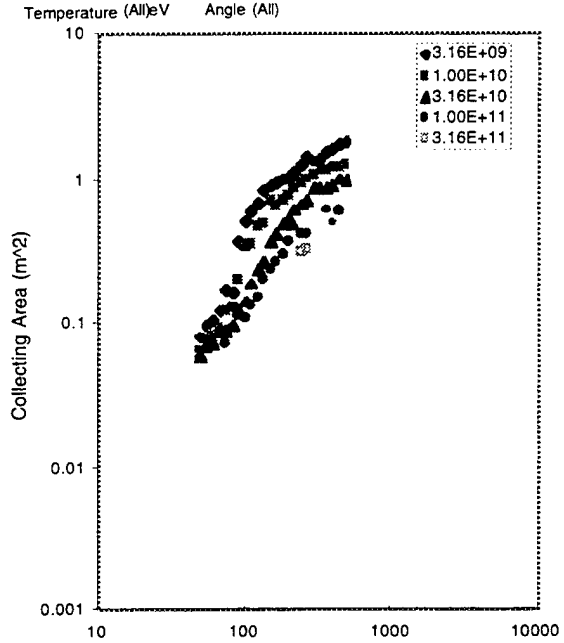
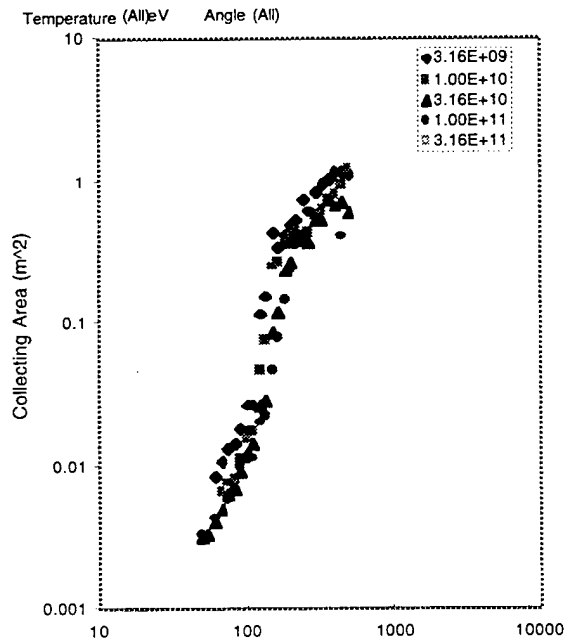Figure 1.—At the spacecraft floating potential the net current is zero. This current has several components.

PASP Plus Array #1, Ram, Emitter Off, Day 94215 to 95134

Temperature (All)eV   Angle (All)

PASP Plus Array #2, Ram, Emitter Off, Day 94215 to 95134

Temperature (All)eV   Angle (All)

PASP Plus Array #4, Ram, Emitter Off, Day 94215 to 95134

Temperature (All)eV   Angle (All)

PASP Plus Array #6, Ram, Emitter Off, Day 94215 to 95134

Temperature (All)eV   Angle (All)
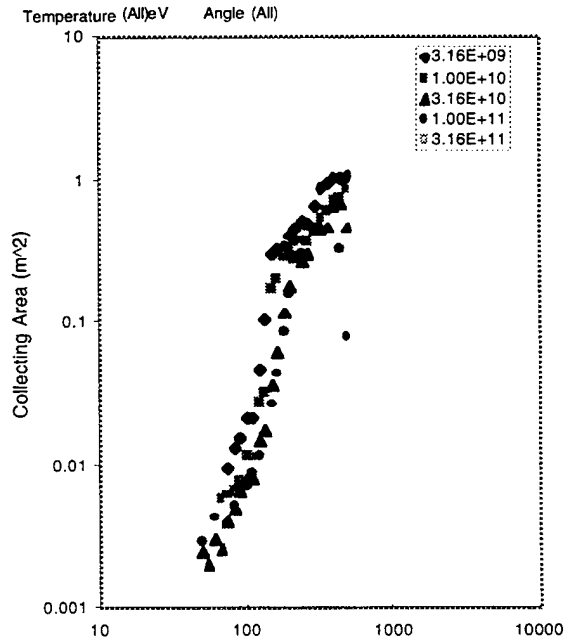
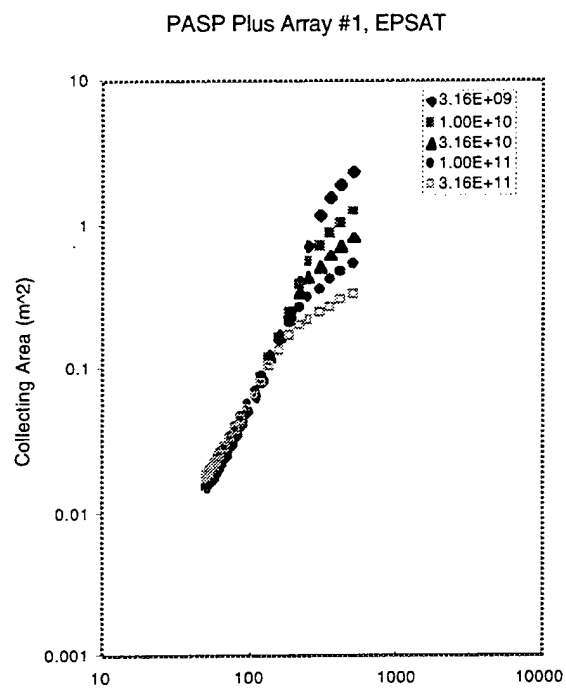Figure 2.—Experimental collecting area versus applied bias curves.

PASP Plus Array #3, Ram, Emitter Off, Day 94215 to 95134
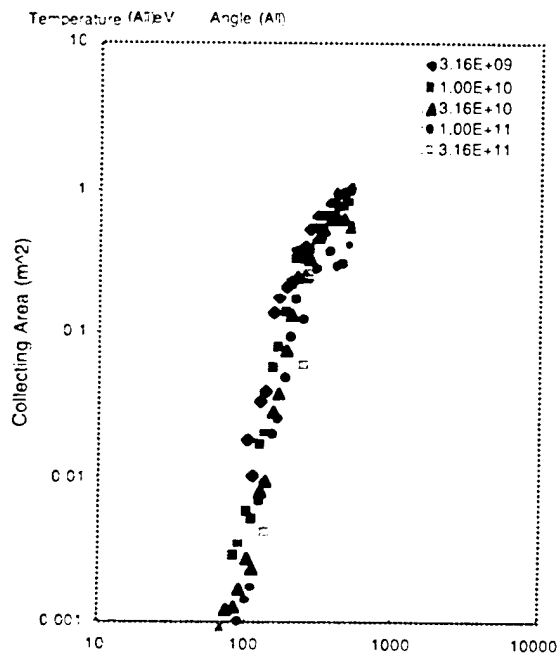
PASP Plus Array #5, Ram, Emitter Off, Day 94215 to 95134
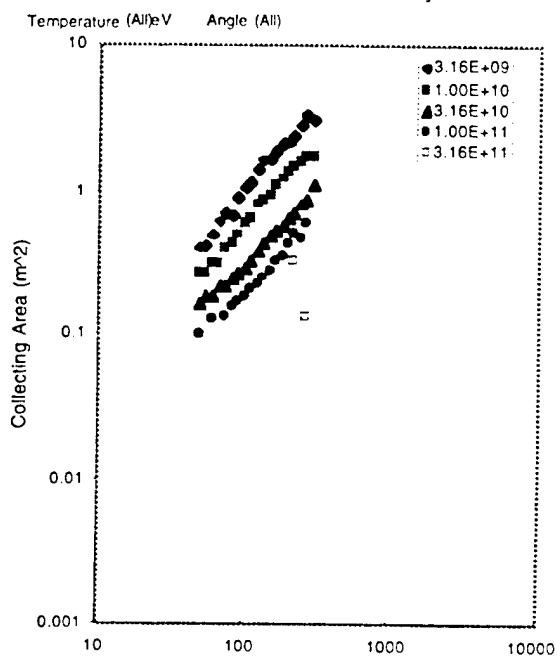
PASP Plus Array #8, Ram, Emitter Off, Day 94215 to 95136
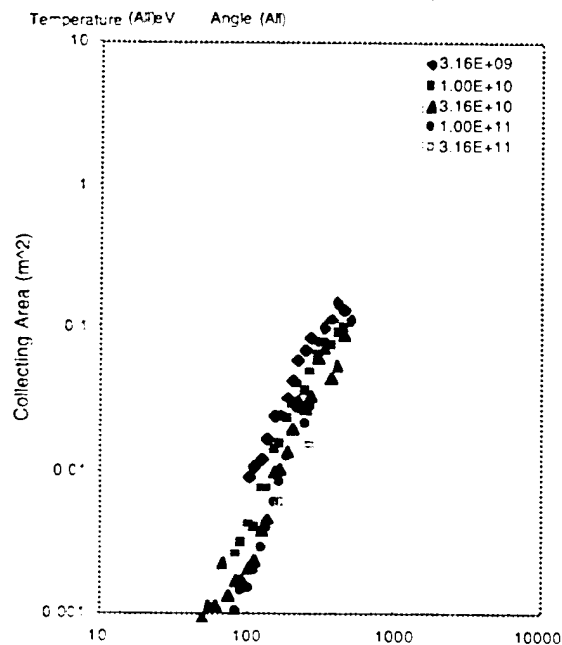
PASP Plus Array #11, Ram, Emitter Off, Day 94215 to 95134
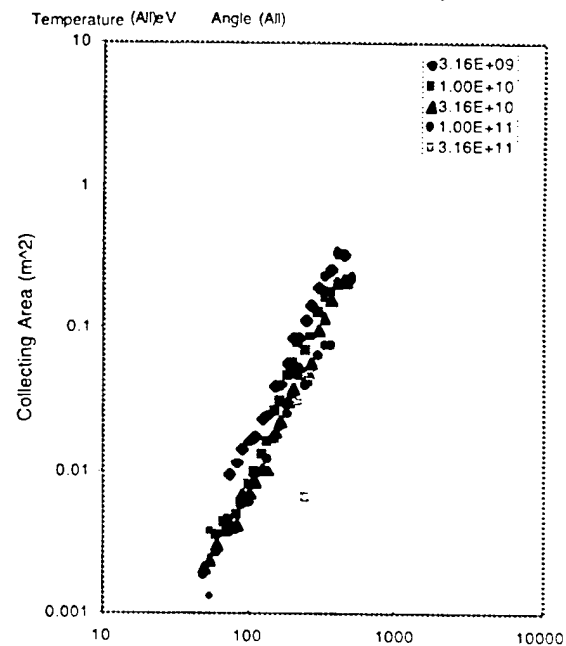
Figure 2.—Experimental collecting area versus applied bias curves.
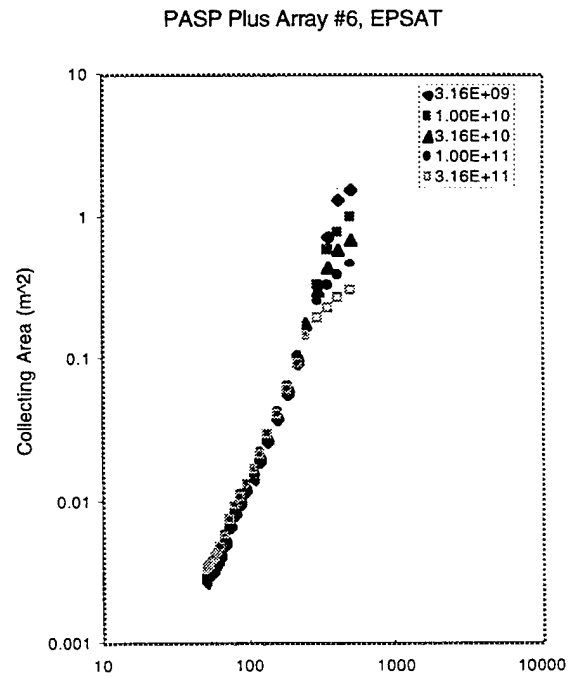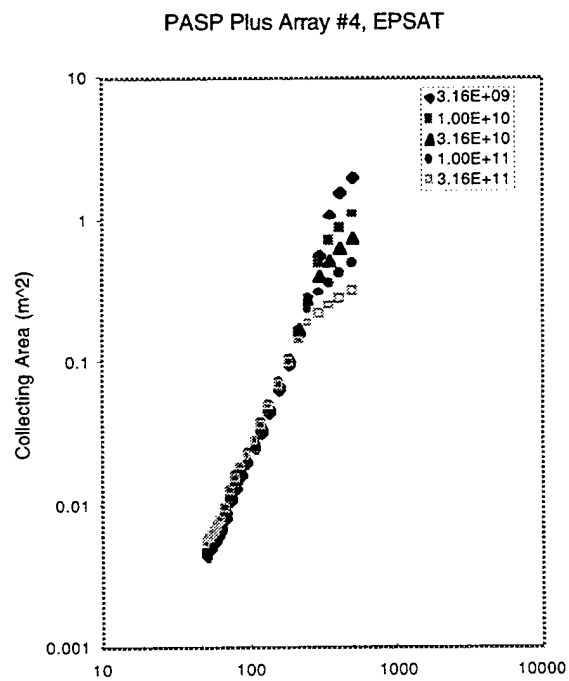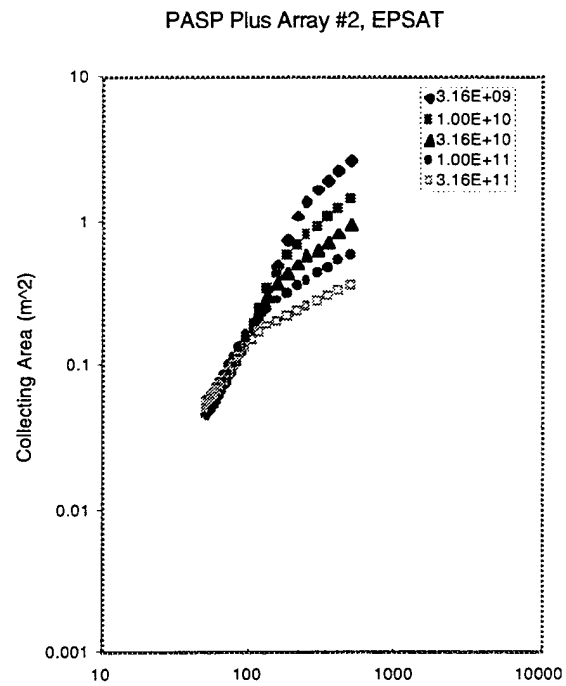
184

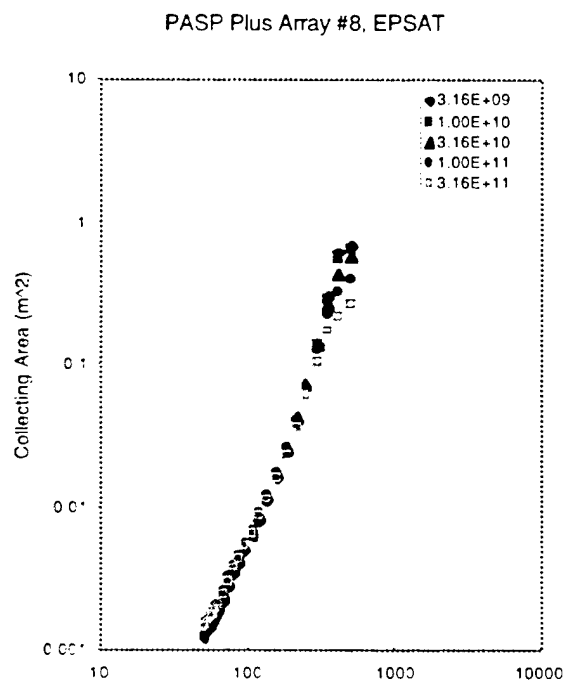Figure 3.—Computed collecting area versus applied bias curves.

PASP Plus Array #3, EPSAT

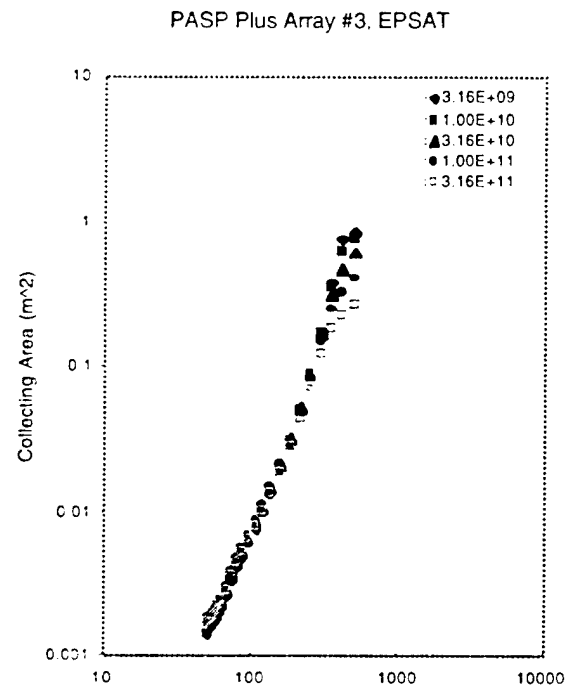PASP Plus Array #8, EPSAT

PASP Plus Array #11, EPSAT

Figure 3.—Computed collecting area versus applied bias curves.
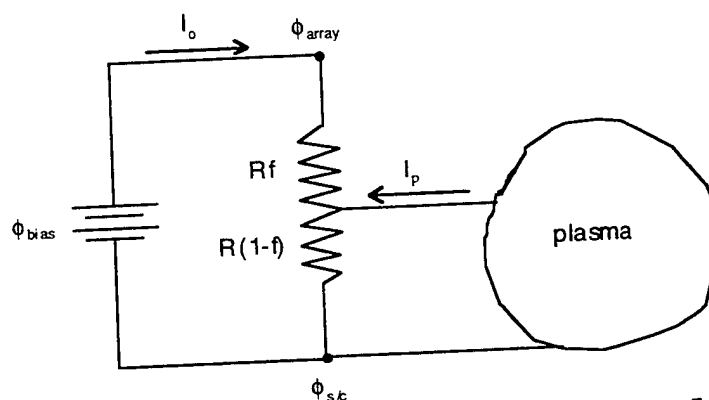
186
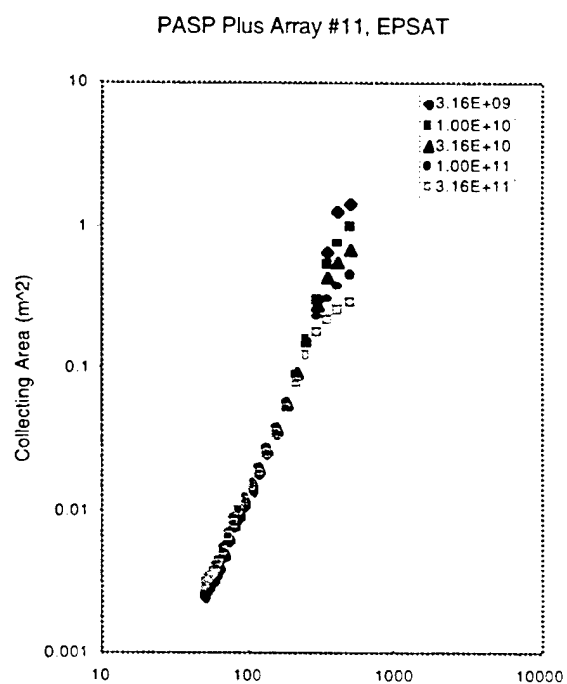
Figure 4.—Effective circuit for collection of current by array 5.

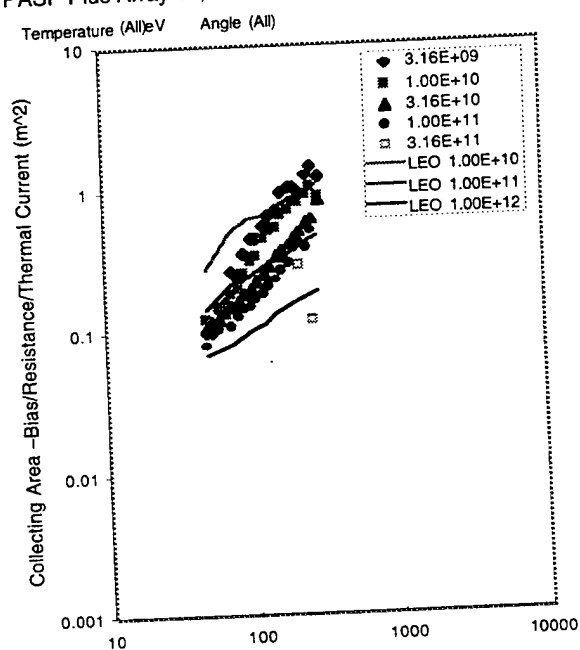PASP Plus Array #5, Ram, Emitter Off, Day 94215 to 95134

Figure 5.—Array 5 experimental collecting area connected for current through Germanium coating compared with NASCAP/LEO calculations.